Master's thesis

NTNU
Norwegian University of Science and Technology
Faculty of Engineering
Department of Marine Technology

Rosa Alexandra Cano Bravo

VORTEX-INDUCED MOTIONS (VIM) OF A SEMI-SUBMERSIBLE FLOATING OFFSHORE WIND TURBINE

Master's thesis in Nordic Master's Programme in Maritime Engineering with specialization in Ocean Structures
Supervisor: Svein Sævik
Co-supervisor: Bernt Leira, Elizabeth Passano, Decao Yin, Hua-Dong Yao
June 2024

NTNU
Norwegian University of Science and Technology

CHALMERS

Rosa Alexandra Cano Bravo

VORTEX-INDUCED MOTIONS (VIM) OF A SEMI-SUBMERSIBLE FLOATING OFFSHORE WIND TURBINE

Master's thesis in Nordic Master's Programme in Maritime Engineering with specialization in Ocean Structures
Supervisor: Svein Sævik
Co-supervisor: Bernt Leira, Elizabeth Passano, Decao Yin, Hua-Dong Yao
June 2024

Norwegian University of Science and Technology
Faculty of Engineering
Department of Marine Technology

MASTER THESIS SPRING 2024

for

Stud. Tech. Rosa Alexandra Cano Bravo

Vortex-induced Motions (VIM) of Floating offshore Wind Turbine

Virvelinduserte bevegelser av flytende vindturbiner

Background:
Floating offshore wind turbines (FOWT) with spar-type floaters have been proved to be successful concept (e.g. Hywind Demo/Scotland/Tampen). The submerged spar exposed to current and surface waves may experience cyclic vortex shedding forces, which induce harmful motions to FOWT – VIM. It is crucial to predict and evaluate the VIM responses.

The present master project focus on the alternative solution of applying a semisubmersible floater concept to support a 12 MW wind turbine. The work is to be carried out as a continuation of the project work conducted during Fall 2023. In January 2023, SINTEF Ocean performed model tests to address VIM behaviour during tow-out. The test results provide a starting point for the thesis work.

Proposed tasks:

1. Literature study on VIV/VIM, mechanics of FOWT, numerical prediction tools (including the relevant theories for the models that are going to be used in the work), and relevant standards.
2. Model test data analysis
3. Establish and report the necessary case scenarios
4. Establish SIMA models for correlation studies with model test and real life case scenario
5. Perform time domain VIM correlation and sensitivity studies with respect to test data
6. Conclusions and recommendation for further work

The work scope may prove to be larger than initially anticipated. Subject to approval from the supervisors, topics may be deleted from the list above or reduced in extent.

In the project report, the candidate shall present the personal contribution to the resolution of problems within the scope of the project work

Theories and conclusions should be based on mathematical derivations and/or logic reasoning identifying the various steps in the deduction.

The candidate should utilise the existing possibilities for obtaining relevant literature.

Project report format
The project report should be organised in a rational manner to give a clear exposition of results, assessments, and conclusions. The text should be brief and to the point, with a clear language. Telegraphic language should be avoided.

The report shall contain the following elements: A text defining the scope (including this text), preface, list of contents, summary, main body of thesis, conclusions with recommendations for further work, list of symbols and acronyms, references and (optional) appendices. All figures, tables and equations shall be numerated.

The supervisors may require that the candidate, in an early stage of the work, presents a written plan for the completion of the work.

The original contribution of the candidate and material taken from other sources shall be clearly defined. Work from other sources shall be properly referenced using an acknowledged referencing system.

The report shall be submitted in electronic format (.pdf):
- Signed by the candidate
- The text defining the scope shall be included (this document)
- Drawings and/or computer models that are not suited to be part of the report in terms of appendices shall be provided on separate (.zip) files.

Ownership

NTNU has according to the present rules the ownership of the project reports. Any use of the report has to be approved by NTNU (or external partner when this applies). The department has the right to use the report as if the work was carried out by a NTNU employee, if nothing else has been agreed in advance.

Thesis supervisors:

Prof. Svein Sævik & Prof. B.J. Leira, NTNU. Dr. E. Passano, Dr. D. Yin, SINTEF Ocean

Deadline: June , 2024, the exact date according to student web

Trondheim, January, 2024

Svein Sævik

Candidate – date and signature:

Rosa Alexandra Cano Bravo,
10-January-2024/Trondheim

Abstract

This thesis investigates the Vortex-Induced Motion (VIM) phenomenon in semi-submersible floating offshore wind turbines (FOWTs), specifically focusing on the 12 MW INO WINDMOOR model. VIM, caused by cyclic vortex shedding forces on submerged structures, can lead to significant and potentially damaging motions in FOWTs, making it critical to predict and evaluate these responses accurately.

The research begins with a comprehensive literature review on VIM and Vortex-Induced Vibrations (VIV), the mechanics of FOWTs, numerical prediction tools, and relevant industry standards. This foundation supports the development and application of advanced numerical models.

Experimental tests conducted by SINTEF Ocean in January 2024 on a Froude scale model of the INO WINDMOOR provide the data for this study. These tests focused on the VIM behaviour during two towing conditions and provided essential hydrodynamic parameters for further analysis.

A SIMA model was developed and validated using the experimental data, enabling correlation and sensitivity studies. The simulation results aligned closely with experimental observations, confirming the accuracy of the numerical models and hydrodynamic parameters used.

The findings of this research offer a deeper understanding of VIM in semi-submersible FOWTs, identifying critical design parameters and improving numerical modelling techniques. The thesis concludes with recommendations for future research, emphasising the importance of continued experimental validation and the advancement of simulation tools to enhance the predictability and mitigation of VIM effects in offshore wind turbines.

This study contributes to the offshore wind industry by providing validated insights and tools for designing and analysing semi-submersible platforms, supporting the development of more efficient and resilient FOWTs.

Sammendrag

Denne avhandlingen undersøker Vortex-Induced Motion (VIM)-fenomenet i semi-submersible flytende havvindmøller (FOWT), med spesielt fokus på 12 MW INO WINDMOOR-modellen. VIM, forårsaket av sykliske virvelshedningskrefter på nedsenkede strukturer, kan føre til betydelige og potensielt skadelige bevegelser i FOWT, noe som gjør det kritisk å forutsi og evaluere disse responsene nøyaktig.

Forskningen begynner med en omfattende litteraturgjennomgang om VIM og Vortex-Induced Vibrations (VIV), mekanikken til FOWT, numeriske prediksjonsverktøy og relevante industristandarder. Denne grunnleggende kunnskapen støtter utviklingen og anvendelsen av avanserte numeriske modeller.

Eksperimentelle tester utført av SINTEF Ocean i januar 2024 på en Froude-skalamodell av INO WINDMOOR gir dataene for denne studien. Disse testene fokuserte på VIM-adferden under to tauingsforhold og ga essensielle hydrodynamiske parametere for videre analyse.

En SIMA-modell ble utviklet og validert ved bruk av de eksperimentelle dataene, noe som muliggjorde korrelasjons- og følsomhetsstudier. Simuleringsresultatene stemte godt overens med eksperimentelle observasjoner, noe som bekreftet nøyaktigheten til de numeriske modellene og de brukte hydrodynamiske parameterne.

Funnene fra denne forskningen gir en dypere forståelse av VIM i semi-submersible FOWT, identifiserer kritiske designparametere og forbedrer numeriske modelleringsteknikker. Avhandlingen avsluttes med anbefalinger for fremtidig forskning, som understreker viktigheten av fortsatt eksperimentell validering og utvikling av simuleringsverktøy for å forbedre forutsigbarheten og avbøtningsstrategiene for VIM-effekter i havvindmøller.

Denne studien bidrar til offshore vindindustrien ved å gi validerte innsikter og verktøy for design og analyse av semi-submersible plattformer, noe som støtter utviklingen av mer effektive og motstandsdyktige FOWT.

Preface

This thesis is the final report resulting from completing my Master in the Nordic Master's Program in Maritime Engineering. After several years of experience as a Naval Architect in ship construction, refreshing my knowledge in the developing maritime industry has been fascinating over the past two years.

The journey began at Chalmers University in Sweden. Upon my arrival, I quickly understood the industry's new challenges and the continuous development led by Nordic countries. The coursework helped me better understand the hydrodynamic and structural responses of floating structures, and how this may influence the design.

As part of the Nordic Master program, I had the valuable opportunity to study my second year at the Department of Marine Technology at the Norwegian University of Science and Technology in Norway. Given the choice between several topics, wind turbines immediately captured my interest.

During the autumn semester of 2023, I was focused on understanding the wind turbines' operation through various disciplines. I engaged in experimental laboratories to study different hydrodynamic phenomena and attended classes on Integrated Dynamic Analysis of Wind Turbines to learn how these structures operate in such complex environments. I explored other subjects such as Design Methods and Risk Analysis to enhance my understanding of wind turbines.

The autumn semester concluded with an initial report that reviewed the most important theoretical backgrounds on the VIM phenomenon and conducted analyses in SIMA to understand the main operational characteristics of wind turbines. Using the Decay Test, we obtained the natural frequencies of the wind turbine. This process helped me gain a better understanding of the topic.

During the spring semester of 2024, my workload was entirely focused on performing a thorough analysis of the experimental results from a Froude scale model of the INO-WINDMOOR, conducted in January 2024 by SINTEF in the Ocean Basin. These results allowed us to determine the hydrodynamic parameters needed for the analysis in SIMA. A clear process was followed, and the results agreed with the experimental results. This thesis can be considered an important step to understanding the VIM phenomenon and limitations in SIMA.

Acknowledgements

"This is my command—be strong and courageous!
Do not be afraid or discouraged. For the Lord
your God is with you wherever you go"

Joshua 1:9

I extend my sincere gratitude to my supervisors: Prof. Svein Sævik and Prof. Bernt J. Leira from NTNU, Dr. Decao Yin and Dr. Elizabeth Passano from SINTEF Ocean, and Dr. Hua-Dong Yao from Chalmers University. Their consistent guidance, in-depth discussions, and unwavering commitment have been invaluable throughout this project. Their expertise in structural and hydrodynamics interaction, as well as Vortex-Induced Motion (VIM), has significantly enriched my understanding of the topic and played a pivotal role in completing this work.

I would like to thank FME NORTHWIND for providing the experimental data of the test carried out in January 2024. Also, I am grateful for SINTEF's collaboration on the towing test performed in the Ocean Basin, and for the permission to use the INO WINDMOOR NUMERICAL MODEL which provided relevant information to develop this project.

I want to express my appreciation to the professors from both universities for their unwavering dedication, valuable advice, and motivation during this journey, as well as to the administrative teams for their support.

I owe deep gratitude to my team at VARD for their strong support in achieving this goal and allowing me to develop my career.

Lastly, I want to extend my deepest appreciation to my family and friends, whose unwavering support sustained me during this transforming process.

Contents

Abstract . . . . . **vii**
Sammendrag . . . . . **viii**
Preface . . . . . **ix**
Acknowledgements . . . . . **x**
Contents . . . . . **xi**
Figures . . . . . **xiv**
Tables . . . . . **xxi**
Acronyms . . . . . **xxiii**
1 Introduction **1**
1.1 Objectives 3
1.2 Thesis structure 4
2 Theory **5**
2.1 VIV and VIM phenomenon. 5
2.2 Vibration in a system in 1DOF. 6
2.2.1 Forces on the cylinder in 1DOF 7
2.3 Vibration in a system with 2DOF. 8
2.4 Flow around a cylinder in a steady flow. 9
2.5 Vortex Shedding and Strouhal Number 12
2.6 Lock-in condition. 13
2.7 Main parameters to describe VIM 14
2.8 Vortex Induced Motions (VIM). 16
3 Numerical tools, Engineering practices, and relevant Standards **18**
3.1 Model Test. 18
3.2 Numerical prediction tools 19
3.2.1 Computational fluid dynamics 19
3.2.2 Semi-Empirical Frequency Domain model 20
3.2.3 Empirical Time Domain model 21
3.2.4 Semi-Empirical Time Domain model 22

3.3 The VIM design curve . . . 25
3.4 Relevant standards. . . . 25
4 SIMA model of the 12MW SS-FOWT. . . . 27
4.1 The Software . . . 28
4.2 The 12MW SS-FOWT INO-WINDMOOR model. . . . 28
4.2.1 INO-WINDMOOR model. Main characteristics. . . . 28
4.2.2 The TD-VIV model . . . 34
4.3 Mechanism of the 12MW SS-FOWT . . . 36
4.3.1 Environment . . . 36
4.3.2 Operational Characteristics of the Semi-submersible under Constant wind, no wave and no current . . . 36
4.3.3 Influence of Quadratic Drag under Constant wind, no wave and no current . . . 41
4.4 Decay Test of the 12MW SS-WT. . . . 45
5 Laboratory Test . . . 50
5.1 Model-Experiment to measure VIM response on a 12MW SS-FOWT . . . 50
5.1.1 Experimental Set-up . . . 51
5.1.2 Instrumentation during experiment . . . 53
5.1.3 Natural Periods of the Wind Turbine . . . 53
5.1.4 Selecting the towing speed . . . 56
6 The New Towing model in SIMA . . . 57
6.1 Main consideration for the new model . . . 57
6.1.1 The equivalent stiffness. . . . 59
6.1.2 Approximation of the Towing Frequency . . . 63
6.2 Establishing parameters of the new TD-VIV model. . . . 64
6.2.1 Analysis to establish parameters in the TD-VIV model . . . 65
6.3 Decay test in SIMA for the TD-VIV Towing model . . . 71
7 Results and Discussion . . . 72
7.1 Experimental Results . . . 72
7.2 Comparison of Experimental and SIMA results. . . . 75
7.2.1 Mean Towing Force . . . 75
7.2.2 Displacements . . . 77
7.2.3 Spectral Analysis . . . 80
7.2.4 Final comments about SIMA results . . . 87
7.2.5 Response Amplitude Ratio . . . 88
8 Conclusions . . . 91
Bibliography . . . 93
A Properties of the Tower in SIMA . . . 97

B Influence of Quadratic Drag. Motions in the 6DOF. **99**
C Selection of the Experimental data in the Single-Line (SL) Towing condition . . **101**
D Selection of the Experimental data in the Two-Bridle (2B) Towing condition . . **112**
E Displacements in the two towing conditions at different current speeds **124**
F Comparison of Matlab's functions for Spectral Analysis **127**
G Spectral Analysis of the Towing Force from Experimental data. **133**
H Spectral and Time Series comparison of the experimental Towing Force with SIMA's results. **136**
I Spectral Analysis of Displacements from Experimental data. **139**
J Spectral and Time Series comparison of experimental Sway and Roll with SIMA's results. **143**
K Additional Material **148**

Figures

2.1 a) Fluid-structure interaction due to alternative vortex shedding in a cylinder with 2DOF motion. b) VIM is a special case of VIV. Figure from [9] 5
2.2 Freely oscillation elastically mounted circular cylinder. Figure from [10] 6
2.3 Two degrees of freedom spring-mass-dashpot in a uniform free stream. Figure from [11] 8
2.4 Flow around a stationary circular cylinder including the vortex shedding phenomenon. Figure from [12] 9
2.5 Reynolds number at different flow regimes on a smooth circular cylinder in a steady current. Figure from [6] 9
2.6 Non-zero mean lift coefficient in the critical-flow regime. Figure from [1] 11
2.7 Transition of the boundary layer in a smooth circular cylinder in a steady flow from sub-critical to post-critical flow regimes. Figure from [9] 11
2.8 Mean drag coefficients on a circular cylinder as a function of Reynolds number and surface roughness ratio. Figure from [9] 12
2.9 Strouhal number vs the Reynolds number for smooth and rough surfaces. Figure from [6] 12
2.10 Schematic setup of a free vibration experiment with a bare cylinder. Figure from [2] 13

3.1 The incoming flow velocity decomposition and hydrodynamic forces at the cylinder. Figure from [32] 23
3.2 Phase angle relationship between the vortex shedding forces in CF direction and relative structure velocity in the local y-axis. Figure from [32] 24
3.3 Cross Flow Synchronisation. Figure from [32] 25
3.4 Typical VIM curve. Figure from [9] 26

4.1 The INO-WINDMOOR platform. Figure from [8] 27
4.2 Global and Local Coordinate system. Figure from [8] 29
4.3 Mooring system orientation for the INO-WINDMOOR. Figure from [8] 29

4.4 Nodal degrees of freedom for RIFLEX bar element. Figure from [6] 30
4.5 Nodal degrees of freedom for RIFLEX beam element. Figure from [6] 31
4.6 Platform modelled in WAMIT. Figure from[8] 34
4.7 Incoming Wind speed in the shaft and Rotor Speed on the 12MW SS-FOWT in Time series 37
4.8 Aero Force in the shaft and Blade Pitch, at different velocities on the 12MW SS-FOWT in Time series 37
4.9 Torque and Electrical Power Generator, at different velocities on the 12MW SS-FOWT in Time series 38
4.10 Performance curves of different Operational parameters vs wind speed of the 12MW SS-FOWT. Results are from OPEN FAST [39] and SIMA. 39
4.11 Translations and Rotations of the 12MWSS-FOWT under Constant wind, no wave, no current. 40
4.12 Motions in 6DOF for different models. The analysis was carried out at 10.6 m/s and 12 m/s. 42
4.13 Comparison of motions in Surge, Sway, and Yaw, for the three models at two constant wind speeds 44
4.14 Ramp and Constant Forces modelled in SIMA, and the oscillating curve in the time series of structure's response in the x-direction (surge). Figure is from [40] 45
4.15 Damped frequency of translations and P-Q parameters from the 12MW SS-FOWT, for both models with and without TD-VIV 47
4.16 Damped frequency of rotations and P-Q parameters from the 12MW SS-FOWT, for both models with and without TD-VIV 48

5.1 Experiment carried out in Ocean Basin during January 2024. Figure from[41] 50
5.2 Main dimension of Ocean Basin Towing Tank, and towing trajectory of the model during the experiment. Figure from[41] 51
5.3 Experimental set-up of the INO WINDMOOR towing test and coordinate system. Figure from[41] 52
5.4 Two towing heading conditions for measuring the VIM response. Figure from[41] . . 54
5.5 Towing configurations at model scale 55
5.6 Towing configurations at full scale 55

6.1 SIMA model of the 12MW SS-FOWT for the two towing configurations. 58
6.2 Connection between the wind turbine and the carriage during the experiment. The figure shows the equivalent system modelled as in-parallel/in-series springs connection. 60
6.3 SIMA model of the 12MW SS-FOWT for the Two-Bridle (2B) towing configuration. . . 63

6.4 SIMA results for the Mean Tension force in two Towing conditions. 66
6.5 SIMA results for the Amplitude of motion in CF direction. 68
6.6 SIMA results for the Amplitude of motion in IL direction. 69
6.7 Selection of the main parameters for the TD-VIV model in Single-Line (SL) towing conditions. Results are compared against experimental data. 70
6.8 Selection of the main parameters for the TD-VIV model in Two-Bridle (2B) towing conditions. Results are compared against experimental data. 71

7.1 Data selection for Single-Line (SL) towing condition. The Time Domain data includes towing speed, towing force, and displacements in the 6DOF at a mean towing speed of 2.0 m/s. 73
7.2 Data selection for Two-Bridle (2B) towing condition. The Time Domain data includes towing speed, towing force, and displacements in the 6DOF at a mean towing speed of 2.0 m/s. 74
7.3 Mean Towing Force vs Current Speed, in both towing conditions, i.e. the Single-Line (SL) and Two-Bridle (2B). The PoliFit is a second-order fitting curve. 76
7.4 Experimental and SIMA results of the mean Towing Force. Results are shown for Single-Line (SL) and Two-Bridle (2B) towing conditions. 76
7.5 Surge (X), Sway (Y), Roll (RX), and Yaw (RZ) displacements in both, Single-Line (SL) and Two-Bridle (2B) towing conditions, under three different current speeds. 77
7.6 Experimental and SIMA's results of Sway motion in the two towing conditions, at three different current speeds. 78
7.7 Experimental and SIMA TD-VIV Model results of Roll motion in the two towing conditions, at three different current speeds. 79
7.8 Power Spectral Density of the towing Force in the two towing conditions (SL: Single-Line, 2B: Two-Bridle), at the current speed of 2 m/s. The Force was analysed with the Powspec method. 81
7.9 Signal Spectra of Experimental and SIMA results of the Towing Force. Results are for the two towing conditions at 2.0 m/s. The graph also includes the Time Series Force of Experimental and SIMA results. 82
7.10 Power Spectral Density of the experimental Sway, and Roll in the two towing conditions (SL: Single Line, 2B: Two Bridle), at current speed U=2.0 m/s. 84
7.11 Power Spectral Density of the experimental Sway, and Roll in the two towing conditions (SL: Single Line, 2B: Two Bridle), at current speed U=2.8 m/s. 84
7.12 Spectral and Time Series comparison of experimental Sway with SIMA's results in the two towing conditions at 2.0 m/s. 85

7.13 Spectral and Time Series comparison of experimental Roll with SIMA's results in the two towing conditions at 2.0 m/s. 86
7.14 Time Series data and Signal Spectra of SIMA results in the Single-Line (SL) towing conditions at three different current speeds. 87
7.15 Time Series data and Signal Spectra of SIMA results in the Two-Bridle (2B) towing conditions at three different current speeds. 88
7.16 Amplitude of motion and the Response Amplitude Ratio in both, IL and CF direction, vs Current Speed. Results are from the two towing conditions, Single-Line (SL) and Two-Bridle (2B). The fitting curve is a first-order polynomial. 89
7.17 Experimental and SIMA TD-VIV Model results of the Amplitude Ratio in CF direction, vs Current Speed. 90

B.1 Motions in 6DOF for different models at two constant wind speeds 100

C.1 Data selection for Single-Line (SL) towing condition. The Time series data includes towing speed, towing force, and displacements in the 6DOF at a mean towing speed of 0.9 m/s. 102
C.2 Data selection for Single-Line (SL) towing condition. The Time series data includes towing speed, towing force, and displacements in the 6DOF at a mean towing speed of 1.0 m/s. 103
C.3 Data selection for Single-Line (SL) towing condition. The Time series data includes towing speed, towing force, and displacements in the 6DOF at a mean towing speed of 1.1.0 m/s. 104
C.4 Data selection for Single-Line (SL) towing condition. The Time series data includes towing speed, towing force, and displacements in the 6DOF at a mean towing speed of 1.6 m/s. 105
C.5 Data selection for Single-Line (SL) towing condition. The Time series data includes towing speed, towing force, and displacements in the 6DOF at a mean towing speed of 1.8 m/s. 106
C.6 Data selection for Single-Line (SL) towing condition. The Time series data includes towing speed, towing force, and displacements in the 6DOF at a mean towing speed of 2.0 m/s. 107
C.7 Data selection for Single-Line (SL) towing condition. The Time series data includes towing speed, towing force, and displacements in the 6DOF at a mean towing speed of 2.2.0 m/s. 108
C.8 Data selection for Single-Line (SL) towing condition. The Time series data includes towing speed, towing force, and displacements in the 6DOF at a mean towing speed of 2.4 m/s. 109

C.9 Data selection for Single-Line (SL) towing condition. The Time series data includes towing speed, towing force, and displacements in the 6DOF at a mean towing speed of 2.6 m/s. 110
C.10 Data selection for Single-Line (SL) towing condition. The Time series data includes towing speed, towing force, and displacements in the 6DOF at a mean towing speed of 2.8 m/s. 111

D.1 Data selection for Two-Bridle (2B) towing condition. The Time series data includes towing speed, towing force, and displacements in the 6DOF at a mean towing speed of 0.9 m/s. 113
D.2 Data selection for Two-Bridle (2B) towing condition. The Time series data includes towing speed, towing force, and displacements in the 6DOF at a mean towing speed of 1.0 m/s. 114
D.3 Data selection for Two-Bridle (2B) towing condition. The Time series data includes towing speed, towing force, and displacements in the 6DOF at a mean towing speed of 1.1.0 m/s. 115
D.4 Data selection for Two-Bridle (2B) towing condition. The Time series data includes towing speed, towing force, and displacements in the 6DOF at a mean towing speed of 1.6 m/s. 116
D.5 Data selection for Two-Bridle (2B) towing condition. The Time series data includes towing speed, towing force, and displacements in the 6DOF at a mean towing speed of 1.8 m/s. 117
D.6 Data selection for Two-Bridle (2B) towing condition. The Time series data includes towing speed, towing force, and displacements in the 6DOF at a mean towing speed of 2.0 m/s. 118
D.7 Data selection for Two-Bridle (2B) towing condition. The Time series data includes towing speed, towing force, and displacements in the 6DOF at a mean towing speed of 2.2.0 m/s. 119
D.8 Data selection for Two-Bridle (2B) towing condition. The Time series data includes towing speed, towing force, and displacements in the 6DOF at a mean towing speed of 2.4 m/s. 120
D.9 Data selection for Two-Bridle (2B) towing condition. The Time series data includes towing speed, towing force, and displacements in the 6DOF at a mean towing speed of 2.6 m/s. 121
D.10 Data selection for Two-Bridle (2B) towing condition. The Time series data includes towing speed, towing force, and displacements in the 6DOF at a mean towing speed of 2.8 m/s. 122

D.11 Data selection for Two-Bridle (2B) towing condition. The Time series data includes towing speed, towing force, and displacements in the 6DOF at a mean towing speed of 3.0 m/s. 123

E.1 Surge (X), Sway (Y), Roll (RX), and Yaw (RZ) displacements in both, Single-Line (SL) and Two-Bridle (2B) towing condition, at different current speeds. (1) 125

E.2 Surge (X), Sway (Y), Roll (RX), and Yaw (RZ) displacements in both, Single-Line (SL) and Two-Bridle (2B) towing condition, at different current speeds. (2) 126

F.1 Spectral and Time Series data of the Force, using three approaches for the analysis. Single-Line (SL) towing condition. 129

F.2 Spectral and Time Series data of the Force, using three approaches for the analysis. Two-Bridle (2B) towing condition. 130

F.3 Time Series and Spectral Surge, Sway, and Roll diagram using three approaches for the analysis. Single-Line (SL) towing condition 131

F.4 Time Series and Spectral Surge, Sway, and Roll diagram using three approaches for the analysis. Two-Bridle (2B) Towing Condition 132

G.1 Power Spectral Density (PSD) of the towing Force in the Single-Line (SL) towing condition, at various current speeds. The Force was analysed with the Powspec method. 134

G.2 Power Spectral Density (PSD) of the towing Force in the Two-Bridle (2B) towing condition, at various current speeds. The Force was analysed with the Powspec method. 135

H.1 Spectral Analysis of the Towing Force of Experimental and SIMA results. Results are for the Single-Line (SL) towing condition, at 3 different speeds. The graph also includes the Time Series Force of Experimental and SIMA results. 137

H.2 Spectral Analysis of the Towing Force of Experimental and SIMA results. Results are for the Two-Bridle (2B) towing condition, at 3 different speeds. The graph also includes the Time Series Force of Experimental and SIMA results. 138

I.1 Power Spectral Density (PSD) in Surge, Sway, and Roll in the two towing conditions (SL: Single-Line, 2B: Two-Bridle), at current speed U=1.0 m/s. 140

I.2 Power Spectral Density (PSD) in Surge, Sway, and Roll in the two towing conditions (SL: Single-Line, 2B: Two-Bridle), at current speed U=2.0 m/s. 141

I.3 Power Spectral Density (PSD) in Surge, Sway, and Roll in the two towing conditions (SL: Single-Line, 2B: Two-Bridle), at current speed U=2.8 m/s. 142

J.1 Spectral and Time Series analysis of experimental Sway and SIMA results, in Single-Line (SL) towing condition at different current speeds. 144

J.2 Spectral and Time Series analysis of experimental Roll and SIMA results, in Single-Line (SL) towing condition at different current speeds. 145
J.3 Spectral and Time Series analysis of experimental Sway and SIMA results, in Two-Bridle (2B) towing condition at different current speeds. 146
J.4 Spectral and Time Series analysis of experimental Roll and SIMA results, in Two-Bridle (2B) towing condition at different current speeds. 147

Tables

4.1 Anchor lines coordinate system. Data from [8] 29
4.2 Mooring line properties. Data from[8] 30
4.3 Mooring line segments modelled in SIMA. Data from[8] 30
4.4 Tower properties and main dimensions. Data from[8] 31
4.5 Main dimensions of the INO-WINDMOOR platform. Data from[8] 32
4.6 Full floating platform properties. Data from[8] 32
4.7 Added Mass Matrix of the SIMO body 33
4.8 Drag coefficient. Data from[8] 33
4.9 Rigid-body natural periods from decay test on SIMA model. Data from[8] 33
4.10 Tower frequencies. Data from[8] 34
4.11 Morison Coefficients and Vortex Shedding Parameters for model *VIM M1*. Data from [6] 35
4.12 Morison Coefficients and Vortex Shedding Parameters on model *VIM M2*. Data from [8] 41
4.13 Simulation parameters for decay test in SIMA. Data from [39] 45
4.14 Results from decay test: Damped period from Initial Model (no VIM) and VIM M1 Model 46

5.1 Main dimensions of the INO WINDMOOR prototype, at full scale. Data from[41] . . . 52
5.2 As-built condition of the INO WINDMOOR platform, at full scale. Data from[41] . . . 52
5.3 Specification of the towline and bridles. Data from[41] 53
5.4 Natural Periods of the Wind Turbine measured during the Towing test 56
5.5 Approximation of the towing velocity at full scale 56

6.1 Equivalent length and axial stiffness considering the geometrical arrangement during Experiment and SIMA model. 63
6.2 Approximate Towing frequency in the two towing conditions. 64
6.3 Suggested VIV parameters for pure CF-VIV presented in SIMA. Information is from [35] 64
6.4 Multi-variable parameters used in SIMA to assess the VIV phenomenon 65
6.5 Frequencies used in SIMA to assess the VIV phenomenon 65
6.6 Parameters on the SIMA model to assess the VIV phenomenon 67

6.7 Selected parameters for the TD-VIV model of the towing experiment. 70
6.8 Natural Periods of the Wind Turbine from the Towing Test in comparison to SIMA results 71

7.1 Experimental and SIMA results comparison of the mean towing force in both towing conditions 77
7.2 Mean and Standard deviation of the experimental Towing Force. 81
7.3 Mean and Standard deviation of the Towing Force from SIMA. 82

A.1 Tower model properties in Riflex. Data from[8] 98

F.1 Parameters for three Frequency Response methods. x represents the input signal. . 128
F.2 R value for the Force signal in Single-Line (SL) and Two-Bridle (2B) towing condition 128
F.3 R value for the Sway signal in Single-Line (SL) and Two-Bridle (2B) towing condition, with similar results for Surge and Roll. 128

Acronyms

$SS-FOWT$	Semi-Submersible Floating Offshore Wind Turbine
$S-FOWT$	Spar Floating Offshore Wind Turbine
VIV	Vortex Induced Vibration
VIM	Vortex Induced Motions
IL	In-line
CF	Cross-flow
g	Gravitational constant
DOF	Degree of freedom
ρ	Density of the fluid
ν	Kinematic viscosity
U	Mean stream velocity, current velocity
U_r	Nominal Reduced Velocity
S	Length of the cylinder
D	Diameter of the cylinder
Re	Reynolds number
Fn	Froude number
m	Mass
$m*$	Mass ratio.
m_a	Added mass
C_A	Added mass coefficient.
ϕ	Phase angle
k	System's stiffness.
c	Viscous damping coefficient
ζ	Damping ratio
A_p	Projected area
A/D	Response Amplitude ratio

A_R	Aspect ratio
T_n	Natural period
f_n	Natural frequency
ω_n	Natural angular frequency
f_{exc}	Vibration frequency
ω_{exc}	Excitation frequency
S_t	Strouhal number
f_{st}	Vortex shedding frequency
$\hat{f}$	Dimensionless frequency
$x, \dot{x}, \ddot{x}$	Motion, velocity and acceleration in x direction.
$y, \dot{y}, \ddot{y}$	Motion, velocity and acceleration in y direction.
A_x	Amplitude of motion in x direction
A_y	Amplitude of motion in y direction.
D	Drag force function
L	Lift force function
C_D	Mean drag coefficient
C_L	Mean Lift coefficient
C_{L_v}	Lift coefficient in terms of the velocity
C_{L_a}	Lift coefficient in terms of the acceleration
F_x	Mean drag force
F_y	Mean lift force
CQ_Y	Non-dimensional quadratic drag coefficient in the normal direction
CA_Y	Non-dimensional added mass per unit length in the normal direction
CV_{CF}	Non-dimensional vortex shedding force coefficient for the instantaneous CF load
FNULL	Non-dimensional natural CF vortex shedding frequency
FMIN	Non-dimensional minimum CF vortex shedding frequency
FMAX	Non-dimensional maximum CF vortex shedding frequency

Chapter 1

Introduction

Vortex-induced vibration (VIV) and Vortex-induced motion (VIM) are two concepts studied in fluid dynamics due to the motion induced to the bodies when interacting with external fluid flow.

VIM is considered a special case of VIV, experienced by slender structures with both a small mass ratio and aspect ratio, subjected to a high Reynolds Number (Re) and at least two degrees of freedom [1].

Vortex-induced vibration (VIV) is a phenomenon that has been known since ancient times. Greeks identified VIV in the strings on the harps when under certain wind velocities experienced vibration, producing acoustical tones.

Further studies by Strouhal in 1878 were done to analyse periodic lift forces associated with vortex shedding, and in 1912 Von-Kármán noticed the street formed by alternating vortices in the wake. The vortex street in the wake behind a cylinder under certain flow velocity is a topic that has been investigated by several disciplines including fluid dynamics, structural mechanics, vibration, and others, due to the relevance in engineering applications such as bridges, industrial chimneys, marine risers in the petroleum industry, and recently in wind turbines [2].

Rigid structures such as cylindrical structures, experience vibration under certain conditions causing the VIV phenomena [3], in Fluid dynamics, this concept is associated with the Reynolds Number (Re) around the cylinder. At a very low Re, the streamlines are perfectly symmetrical around the body as predicted by the potential flow theory, however, for a large Re, the flow becomes asymmetric, generating the so-called Kármán vortex street, resulting in the motion of the cylinder[4].

Most of the studies have been carried out to analyse VIV, but in the maritime industry, it is crucial to analyse also VIM phenomena, especially due to the mass production of wind turbines, and the component of the platforms are slender structures with small mass ratio, subjected to high Re.

Investigations at Re about 7.0×10^5 have been performed to analyse wave effect on the VIM

motion, both numerically and experimentally, to compare the response of different types of cylinders, with different lengths. Since 2004, experiments at model-scale have been carried out for VIV at sub-critical Re [3], to extract hydrodynamic coefficients such as added mass coefficient, excitation coefficient, and drag coefficient. Those parameters are used for VIM prediction in numerical tools such as VIVANA (SINTEF Ocean 2021).

According to Basu, Spar Floating Offshore Wind Turbine (S-FOWT) has several advantages in deep water [5], however, the submerged spar is exposed to current and surface waves, experiencing cyclic vortex shedding forces, which may induce harmful motions to the floating wind turbines, such as Vortex induced motion VIM [6].

Nowadays, another promising concept is under development in the offshore wind turbine market, such as Semi-Submersible Floating Offshore Wind Turbine (SS-FOWT), which uses a large water-plane projected area to ensure the stability of the structure, which usually means larger anchor loads and motions of the floater [7].

It is critical to predict and evaluate the VIM responses on wind turbine towers which in addition to increasing harmful motion, also induce fatigue of mooring elements and cables [3]. The prediction of VIM response will contribute to enhancing safe and cost-effective designs.

This thesis focuses on the VIM analysis of a Semi-Submersible Floating Offshore Wind Turbine (SS-FOWT) to compare analytical and experimental results from a towing experiment carried out by SINTEF Ocean. The analysis is done using the Time Domain Vortex-induced vibration (TD-VIV) model included in SIMA, to confirm the correct prediction of VIM phenomena. Also, the study includes the influence of the current direction on the response of the structure.

1.1 Objectives

The main objective of this thesis is to investigate the VIM response of a 12MW Semi-Submersible Floating Offshore Wind Turbine (SS-FOWT), under constant current flow, using a TD-VIV model.

The biggest challenge is to describe accurately the hydrodynamics parameters in the Semi-Submersible Floating Offshore Wind Turbine (SS-FOWT) model. Existing methods and research will provide the information, which will be compared with results from a towing experiment carried out by SINTEF. The following sub-tasks are proposed to reach this goal.

1. Literature study on VIV and VIM as an introduction to the fundamental aspects of the present thesis.
2. Overview of different numerical prediction tools, the TD-VIV model, and relevant standards.
3. Description of a 12MW SS-FOWT model for a VIM analysis in SIMA.
4. Review the mechanism of FOWT and computation of main characteristics, focus in:
    - Thrust, Power, Torque, and motion performance in the 6 DOF under constant wind and no wave/current.
    - Decay Test on Time series of surge, sway, heave, pitch, roll, and yaw, to predict the damped frequency and the P-Q parameters.
5. Model test of a 12MW SS-FOWT.
    - Establish the case scenarios and results.
    - Data analysis.
6. Time-domain VIM correlation.
    - Establish SIMA models for correlation studies with model tests.
    - Sensitivity studies concerning test data.
7. Conclusions and recommendations for further work.

1.2 Thesis structure

The thesis was divided into several chapters as follows:

- **Chapter 2**: provides the theoretical background on VIV and VIM. It includes some of the main parameters used to describe this phenomenon and contains fundamental aspects from several research to understand this topic. This chapter was structured so that any reader with basic knowledge of structural analysis and hydrodynamics may be able to build their understanding on VIM easily and fast.
- **Chapter 3**: describes the existing tools to predict the VIV, i.e. model test, computational fluid dynamics, semi-empirical frequency-domain models, empirical and semi-empirical time-domain approach. The semi-empirical time-domain model VIVANA-TD was used for VIM prediction and referenced in this document as the TD-VIV model. A briefly explanation of the theory and formulation behind the model was included in this chapter. In addition was added information about some engineering tools that are in practice nowadays.
- **Chapter 4**: describes the INO-WINDMOOR model which already is available in SIMA. It includes all the main characteristics of the wind turbine e.g. mooring system arrangement and material, main dimensions and weight of the platform, natural frequency of the wind turbine, etc. This model was used as a starting point to evaluate the response of the model. To do so, the main operational characteristics was compared with existing data of the wind turbine, in an environment with constant wind, no current and no wave. Finally, a Decay test was used to validate the natural frequencies presented in [8].
- **Chapter 5**: give a description of the experiment carried out in January 2024 by SINTEF in the Ocean Basin. The experiment was done in two towing directions to analysis the influence of the current direction. In this report is included geometries in each towing configuration, material characteristics, and selection of the towing velocities.
- **Chapter 6**: a new model was established based on the previous one, to account for the main particulars of the towing experiment. In this model the mooring configuration was change in geometry, also material characteristics changed according to the test. To validate the model the equivalent stiffness of the system was calculated taking into account each towing configuration. The selection of the VIV parameters was presented step by step in order to establish a methodology.
- **Chapter 7**: presents experimental results together with the main considerations during data processing. Later was analysed the towing force and main motions (i.e. surge, sway, and roll) in time domain and frequency domain to compare both outcomes and validate the results.
- **Chapter 8**: give the main findings, and provides conclusions and recommendations for further work.

Chapter 2

Theory

Vortex Induced Vibration (VIV) and Vortex Induced Motion (VIM), are related to the Reynolds number on a cylinder subjected to a steady flow. The main concepts and simplified models to analyse such complex phenomena are presented in this chapter. The fundamental theory is based on the book by Sumer and Fredsøe [1] and other research.

2.1 VIV and VIM phenomenon.

VIV is a hydrodynamic effect related to the vortex shedding phenomenon on cylindrical structures exposed to high-velocity fluids [9]. Due to the vortex shedding, the structure is forced to oscillate harmonically in a steady flow.

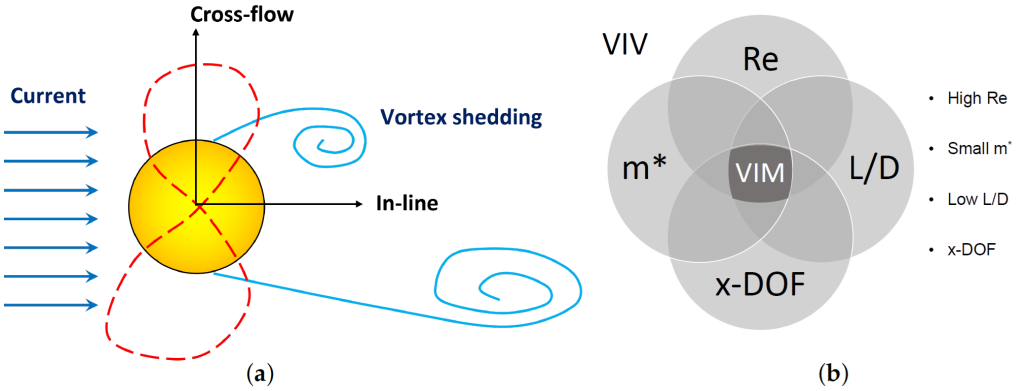

Figure 2.1: a) Fluid-structure interaction due to alternative vortex shedding in a cylinder with 2DOF motion. b) VIM is a special case of VIV. Figure from [9]

In slender marine structures when the fluid passes across-section, the energy provided by the fluid flow is balanced by the dissipated energy due to the damping acting on the structure.

Since the structure is free to move, the cylinder experiences a self-limited oscillation in both directions, Cross Flow (CF) and In Line (IL), reaching an amplitude near to the dimension of the

cross-section, with a vortex shedding frequency f_{st} near to the natural frequency [9].

VIM is a special case of VIV on slender structures that satisfy the following characteristics: low aspect ratio (A_R), small mass ratio (m*), body motion at least in 2 degrees of freedom (DOFs), at high Re. Both VIV and VIM are considered to be a resonant fluid-structure interaction phenomenon.

2.2 Vibration in a system in 1DOF.

For the analysis, let's consider a cylinder subjected to an incoming flow in the x direction, where the structure may experience motion in the y direction due to vortex shedding (see figure 2.2). The governing equation of motion in the cross-flow direction of a freely oscillating elastically mounted circular cylinder is presented in Equation 2.1.

$$m\ddot{y} + c\dot{y} + ky = L \tag{2.1}$$

The cylinder has mass m, the stiffness of the system is k, and the damping c. The force in the cross-flow direction, perpendicular to the fluid flow, is denoted by L in the previous equation. The natural frequency of the structure in vacuum as follows.

$$\omega_n = \sqrt{k/m} \tag{2.2}$$

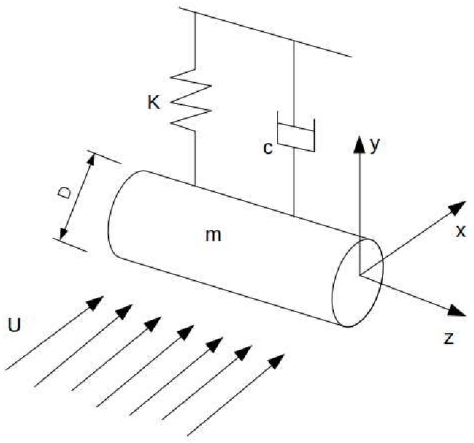

Figure 2.2: Freely oscillation elastically mounted circular cylinder. Figure from [10]

However, when the cylinder vibrates in a free stream of fluid, the acceleration will displace fluid around the body, resulting in a force on the cylinder that is in phase with the inertial force on the left-hand side of Equation 2.1, called the effective added mass force, defined by the Added

mass (m_a), this force also includes forces due to vortex shedding that acts in the wake. The added mass opposes the motion and is included in the system equation as follows:

$$m\ddot{y} + c\dot{y} + ky = L - m_a\ddot{y} \tag{2.3}$$

Considering the system with the newly added mass, the natural damped frequency of the system becomes:

$$\omega_n = \sqrt{k/(m + m_a)} \tag{2.4}$$

2.2.1 Forces on the cylinder in 1DOF

The motion in the y direction of the oscillating cylinder can be represented by a sinusoidal function, where A_y is the amplitude of motion, as follows:

$$y = A_y \sin \omega t \tag{2.5}$$

$$m_y\ddot{y} + c_y\dot{y} + k_y y = L \tag{2.6}$$

In equation (2.6), the lift force function L includes the effect of the added mass in the m_y term. The Lift function can be represented by a sinusoidal function (see equation 2.7).

$$L = F_y \sin(\omega t + \phi) = (F_y \cos \omega t) \sin \phi + (F_y \sin \omega t) \cos \phi \tag{2.7}$$

Where F_y represents the lift force amplitude, and ϕ is the phase angle between the motion and force. When the lift force is expressed in terms of sines and cosines two terms arise, the first in phase with the velocity and the second one in phase with the acceleration.

Usually, the lift force L is presented in terms of a non-dimensional form, known as the lift coefficient C_L, that is represented by the lift coefficient in terms of the velocity ($C_{L_v} = C_L \sin \phi$), and the lift coefficient in terms of the acceleration ($C_{L_a} = C_L \cos \phi$).

Formulation presented in [11], shows a relationship between those coefficients with the amplitude response and added mass coefficient.

$$A_y/D = \frac{U_r^2 C_{L_v}}{4\pi^3 (f_{exc}/f_n) m^* \zeta} \tag{2.8}$$

$$C_A = \frac{-C_{L_a}}{(1/4)\pi\rho D^2 S A_y \omega_{exc}^2} \tag{2.9}$$

From this, it is clear that the amplitude motion A_y is dependent on the reduced velocity, and lift coefficient in phase with the velocity, frequency ratio, mass ratio, and damping ratio. Whereas,

the added mass coefficient C_A is dependent on the lift coefficient in phase with acceleration, the amplitude A_y, the cylinder length S, and frequency ω_{exc}.

2.3 Vibration in a system with 2DOF.

A limited number of studies consider vibration in in-line (IL) and cross-flow (CF) direction, for an elastically mounted rigid cylinder. Moreover, the flexible cylinder introduces complexity to the VIV phenomenon and some simplifications are necessary to include for the analysis, as follows:

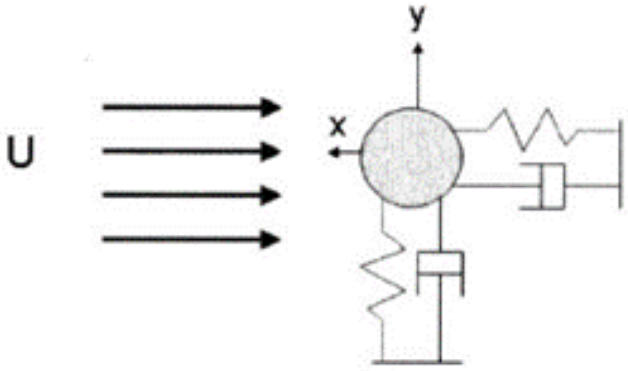

Figure 2.3: Two degrees of freedom spring-mass-dashpot in a uniform free stream. Figure from [11]

The oscillation of a cylinder free to move in 2 directions, can be treated as a spring-mass-dashpot system, very similar to the previous case. Motions are assumed to be harmonic, with θ as the phase angle between in-line and cross-flow motion.

$$x = A_x \sin(2\omega t + \theta) \tag{2.10}$$

$$y = A_y \sin(\omega t) \tag{2.11}$$

L and D are the fluctuating Lift and Drag fluid forces, denoted as follows:

$$m_x \ddot{x} + c_x \dot{x} + k_x x = D \tag{2.12}$$

$$m_y \ddot{y} + c_y \dot{y} + k_y y = L \tag{2.13}$$

Force parameters are calculated in the same manner as 1DOF, but the in-line motion frequency is used, which typically is twice the transverse frequency [11].

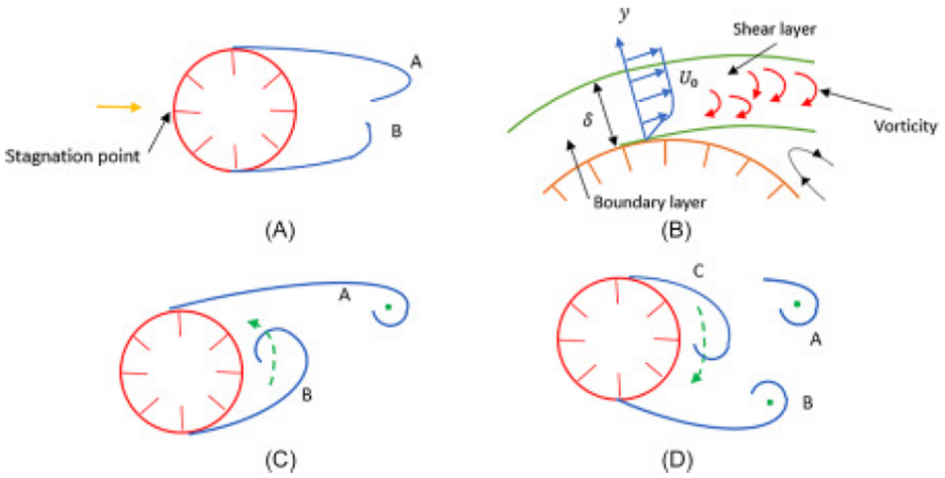

Figure 2.4: Flow around a stationary circular cylinder including the vortex shedding phenomenon. Figure from [12]

2.4 Flow around a cylinder in a steady flow.

At the cylinder surface, there is friction due to the viscosity of the fluid around the structure. Viscous forces develop because of the velocity gradient in the radial direction of the cylinder.

When the fluid is in contact with the cylinder surface, the no-slip boundary condition is satisfied all the time, consequently, the fluid at the cylinder surface will have zero velocity and increase up to the flow velocity when reaching the outer edge of the boundary layer. This boundary condition gives rise to a thin boundary layer (δ) around the cylinder.

Figure 2.4. shows the flow and different characteristics according to the Re regime, an illustration of the gradient velocity and the boundary layer developed at the cylinder surface is shown in Figure 2.4.B.

Reynolds number	Description
$Re < 5$	No separation. Creeping flow.
$5 \leq Re < 40$	A fixed pair of symmetric vortices.
$40 \leq Re < 200$	Laminar vortex street.
$200 \leq Re < 300$	Transition to turbulence in the wake.
$300 \leq Re < 3 \cdot 10^5$	**Subcritical**. Wake completely turbulent. Laminar boundary separation.
$3 \cdot 10^5 \leq Re < 3.5 \cdot 10^5$	**Critical (Lower transition)**. Laminar boundary layer separation on one side. Turbulent boundary layer separation, but laminar boundary layer on the other side.
$3.5 \cdot 10^5 \leq Re < 1.5 \cdot 10^6$	**Supercritical**. Turbulent boundary layer separation. Partly turbulent, partly laminar boundary layer.
$1.5 \cdot 10^6 \leq Re < 4.5 \cdot 10^6$	**Upper transition**. Boundary layer completely turbulent at one side.
$4.5 \cdot 10^6 \leq Re$	**Transcritical**. Boundary layer completely turbulent at both sides.

Figure 2.5: Reynolds number at different flow regimes on a smooth circular cylinder in a steady current. Figure from [6]

The understanding of different flow regimes is important to describe this topic. Figure 2.5 shows a description of different Reynolds number regimes around the cylinder.

For Re $<$ 5 there is no flow separation around the cylinder and the viscous forces dominate in this regime. Flow separation starts at Re $\approx$ 5. In this regime, the shear layer is formed at each side of the cylinder with vortices at the end.

For 5 $\leq$ Re $<$ 40, both vortices remain stable behind the cylinder in a surrounding laminar steady flow. This condition is known as Föppl vortices.

The unstable flow starts at Re $\approx$ 40, when one of the vortices grows larger than the other, and an adverse pressure gradient behind the cylinder. The opposite directions of both vortices generate at the vorticity of the largest vortex is cut off as the smaller vortex is approaching. In this condition, the vortex-shedding phenomenon appears when the largest vortex separates from the boundary layer. When the largest vortex is released downstream by the flow, a new vortex starts repeating the process alternating between both sides of the cylinder [13]. The alternating process gives the appearance of a vortex street defined by the two rows of vortices; this phenomenon is known as von Kármán vortex street.

For 40 $\leq$ Re $<$ 200, the vortex street remains in a laminar flow, and the shedding does not vary in transversal direction. [14]

For 200 $\leq$ Re $<$ 300, a transition to turbulent flow starts as the Reynolds number increases [15], and the vortex shedding becomes three-dimensional, the vortices appear in blocks in the span-wise direction [16]. At Re $\approx$ 300 the wake is completely turbulent and remains for all Re$>$300 with a completely turbulent wake.

For 300 $\leq$ Re $< 3 \cdot 10^5$ the regime is known as a sub-critical flow regime, with a laminar boundary layer over the cylinder in a turbulent wake. As the Reynolds number increases, the turbulence increases, and the boundary layer starts to develop turbulence as well.

For 3$\cdot 10^5 \leq$ Re $< 3.5 \cdot 10^5$ the regimen is known as a critical flow regime. On one side of the cylinder, at the separation point, the boundary layer becomes turbulent; on the other side of the cylinder, at the separation point, the boundary layer remains laminar. The asymmetry in the flow around the cylinder alternates and causes a non-zero mean lift force (F_y) a cross-flow (see Figure 2.6), that alternates with changes in direction [17]. As the Re increases, the boundary layer becomes turbulent at both sides of the cylinder, but the whole boundary layer around the cylinder is not completely turbulent. In some research, the critical regime for a smooth cylinder is considered to start at Re $\approx 2 \cdot 10^5$.

For 3.5$\cdot 10^5 \leq$ Re $< 1.5 \cdot 10^6$, the regime is known as the supercritical flow regime. The boundary layer is partially laminar (between the stagnation point to the separation point) and partially turbulent (from the separation point to downstream). Figure 2.7 illustrates the transition of the boundary layer for different Re regimes.

The post-critical regimen starts when Re $\approx$ 1.5$\cdot 10^6$. The boundary layer becomes fully tur-

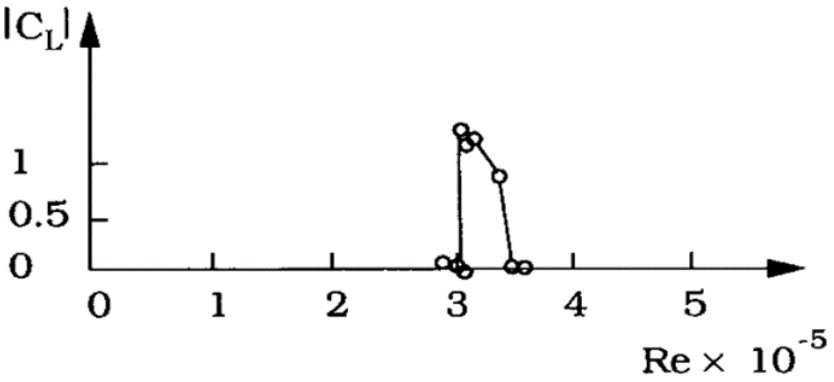

Figure 2.6: Non-zero mean lift coefficient in the critical-flow regime. Figure from [1]

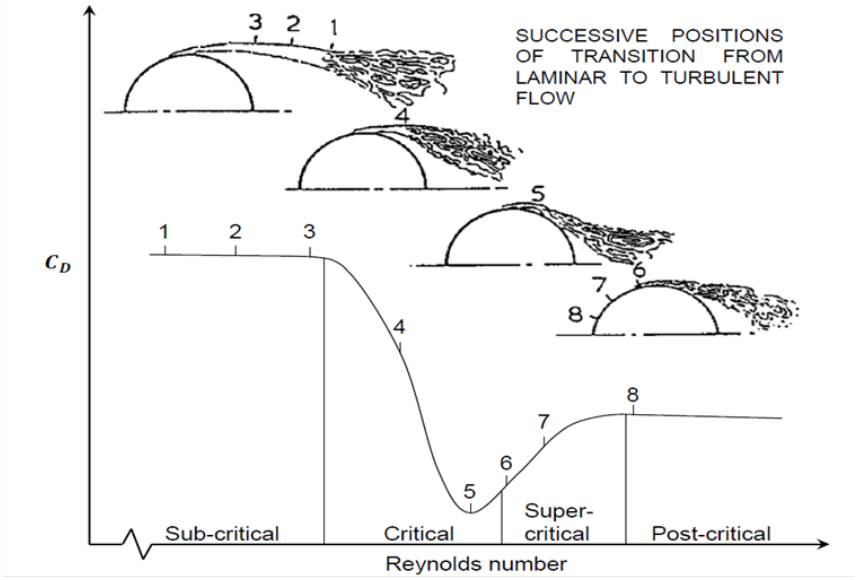

Figure 2.7: Transition of the boundary layer in a smooth circular cylinder in a steady flow from sub-critical to post-critical flow regimes. Figure from [9]

bulent on one side, while in the other side of the cylinder, it is partially laminar. This behaviour continues in the range of $1.5{\cdot}10^6 \leq \text{Re} < 4.5 \cdot 10^6$, which is known as the upper transition flow regime.

For $\text{Re} \geq 4.5 \cdot 10^6$, the regime is known as the trans-critical flow regime, characterised by a completely turbulent flow at the cylinder surface.

Figure 2.7 shows the so-called 'Drag crisis/bucket' when the boundary layer experiences the transition between a laminar regime (in the sub-critical region) to turbulent (in the post-critical region) in a fixed, smooth, circular cylinder. Figure 2.8 shows similar results for different surface conditions. The Reynolds number and the mean drag coefficient have a strong relation with the surface roughness [9].

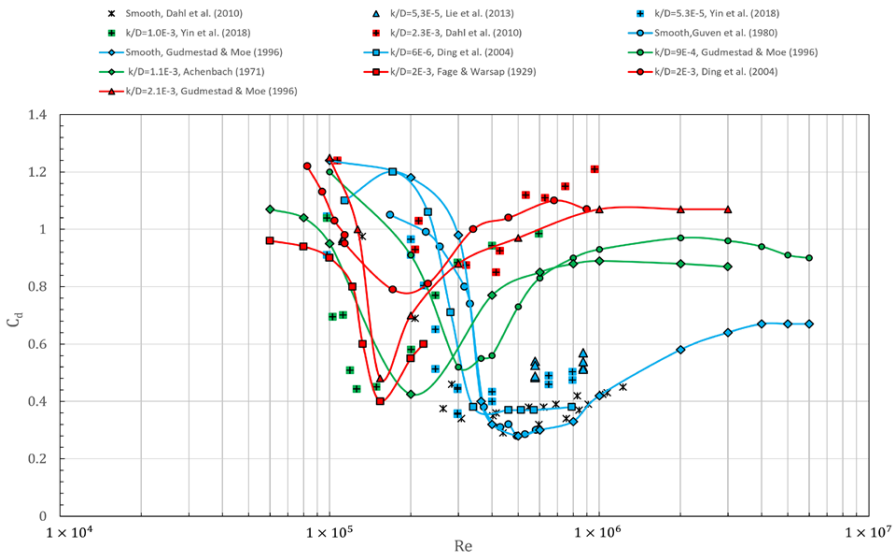

Figure 2.8: Mean drag coefficients on a circular cylinder as a function of Reynolds number and surface roughness ratio. Figure from [9]

2.5 Vortex Shedding and Strouhal Number

It was mentioned that vortex shedding arises as a consequence of the unstable fluid in the boundary layer at high Re. Since this is an alternating phenomenon, an important parameter is the vortex shedding frequency, f_{st}, which is described by the dimensionless parameter known as the Strouhal number S_t. This number depends on the free stream velocity (U) and the diameter of the cylinder (D) [9].

$$S_t = \frac{f_{st} D}{U} \tag{2.14}$$

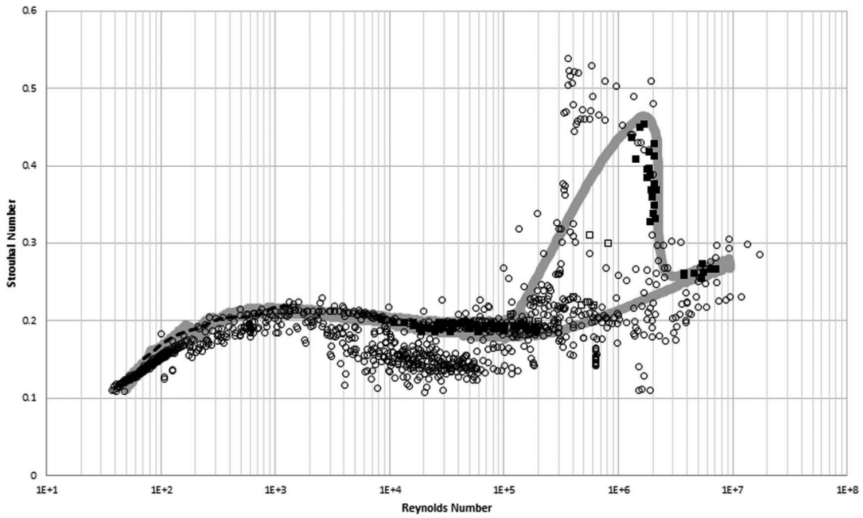

Figure 2.9: Strouhal number vs the Reynolds number for smooth and rough surfaces. Figure from [6]

The Strouhal number (S_t) is dependent on the Reynolds number and surface roughness. Figure 2.9 illustrates this relationship for circular cylinders. In the range of 300$\leq$Re$< 3 \cdot 10^5$, the Strouhal number (S_t) remains almost constant at 0.2 for a circular cylinder. The abrupt increase in the S_t number for smooth surfaces is called the *Camel Hump* and occurs at high values of Reynolds number, $1 \cdot 10^5 \leq$ Re $< 3 \cdot 10^6$, with values about 0.2 and beyond 0.4. Rough surfaces experience lower values with no abrupt changes during the whole range of velocities [2].

2.6 Lock-in condition.

The 'lock-in' term refers to the condition when the excitation frequency ω_{exc} is equal to the natural frequency of the structure (adjusted by the added mass) [11]. During this condition, resonant oscillations start and a high amount of energy is transferred from the wake to the structure resulting in large amplitude vibrations. The excitation frequency can be expressed in terms of the natural frequency and the dimensionless added mass C_A as follows.

$$\omega_{exc} = \omega_n \sqrt{\frac{m^*}{m^* + C_A}} \tag{2.15}$$

Usually, the frequency ratio is defined as the relation between the vibration frequency and the natural frequency (f_{exc}/f_n), in air this value is approximately 1. Figure 2.10 shows the results of a free oscillating 1DOF experiment carried out in air. As the flow velocity increases or decreases and the vortex shedding frequency reaches the vibration frequency, the lock-in condition starts [2].

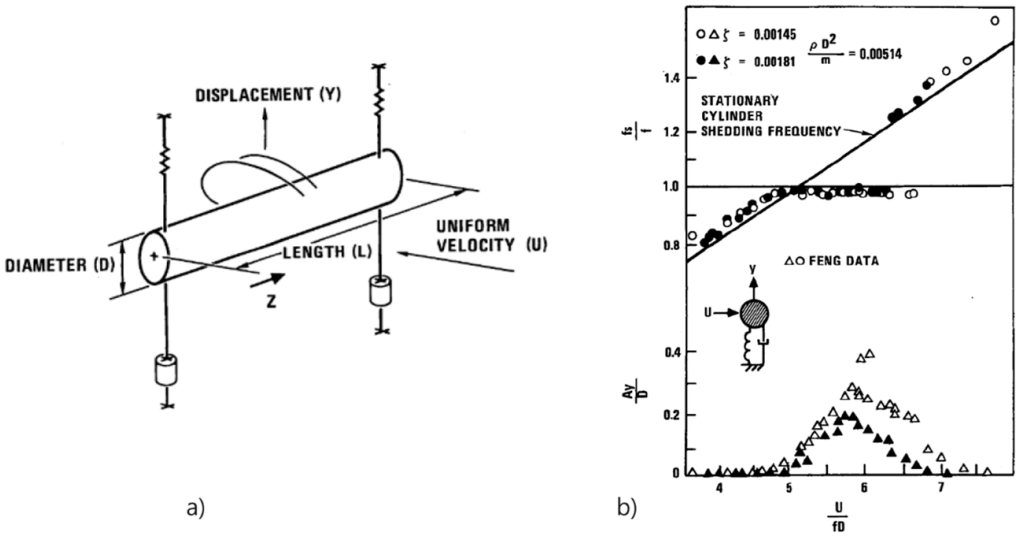

Figure 2.10: Schematic setup of a free vibration experiment with a bare cylinder. Figure from [2]

During lock-in, the dynamic equilibrium is reached and vortex shedding frequency reaches

the natural frequency of the structure $(f_{st}/f_n \approx 1)$. During a range of velocities, the cylinder vibration violates the Strouhal relationship and the vortex shedding frequency is similar to the natural vibration frequency of the cylinder. As the flow velocity increase or decrease, the cylinder returns to follow the Strouhal relationship [11].

2.7 Main parameters to describe VIM

Some of the main parameters used to describe VIM phenomena on FOWTs are presented below:

Froude number.

Surface waves are considered gravity-driven, and the Froude number is a dimensionless parameter measuring the ratio between inertial forces and gravitational forces. FOWTs experience both surface waves and the hydrodynamic effect on the submerged floater. The Froude Number depends on the flow velocity U, and the cylinder length S.

$$F_n = \frac{U}{\sqrt{gS}} \tag{2.16}$$

Reynolds number.

The Reynolds number describes the relationship between inertial forces and viscous forces, which is defined as:

$$Re = \frac{DU}{\nu} \tag{2.17}$$

Where D is the diameter of the cylinder, U is the flow velocity, and ν is the kinematic viscosity

Aspect ratio.

The ratio between the length and the diameter represents the dimensionless aspect ratio A_R.

$$A_R = S/D \tag{2.18}$$

FOWTs show relatively small aspect ratios in comparison with marine risers, pipelines, and cables. The Strouhal number increases with the aspect ratio (A_R), and vortex shedding was known to be valid for $A_R >$2.0 [9].

The critical $A_{R_{crit}}$ ≈2.0 has been suggested as an important parameter to consider during design, especially for floaters with low aspect ratios. Another effect that has been studied is the free end in floaters with a low aspect ratio, and the effect of trailing vortices on VIV on circular cylinders was significant for $A_R <$0.5.

Response Amplitude.

The ratio between the displacement in cross-flow or in-line direction to the cylinder diameter

represents the dimensionless response amplitude parameter.

$$(A/D)_{nom} = \frac{A_{(IL/CF)}}{D} = \frac{\sqrt{2}\sigma_{(IL/CF)}}{D} \tag{2.19}$$

Where $\sigma_{IL/CF}$ is the standard deviation of the displacement in the in-line or cross-flow direction [9].

Mass Ratio and Added mass ratio

The mass ratio defines the dimensionless mass, where m is the mass of the cylinder.

$$m^* = \frac{m}{(1/4\rho\pi D^2 S)} \tag{2.20}$$

Similarly, the added mass ratio can be expressed as

$$C_A = \frac{m_a}{(1/4\rho\pi D^2 S)} \tag{2.21}$$

Damping Ratio

The damping ratio ζ is a measure of the structural damping with respect to critical damping.

$$\zeta = \frac{c}{2m\omega_n} \tag{2.22}$$

Where c is the viscous damping coefficient, m is the total mass of the structure (including added mass), and the natural angular frequency (ω_n).

Damping on FOWTs is associated with a mixture of environmental-structural conditions such as aerodynamic damping, control damping, mass or liquid dampers, structure damping, hydrodynamic damping, and soil damping. Therefore, it's important to determine the structural damping to analyse the VIV and VIM response [9].

It is difficult to predict mathematically the system damping, however, Vondelen proposed a direct estimation of structural damping based on field measurement vibration data obtained from sensors mounted on OWTs [10].

For structural design purposes, various standards recommend a structural damping ratio within 1-5$\%$ of the critical damping, depending on the damping components. For fatigue design, it is recommended to consider a lower damping ratio.

Drag Coefficient and Lift coefficient.

The mean drag coefficient on a floating device is expressed by the relation between the mean drag force F_x, the density of the fluid ρ, the projected area ($A_p = DS$) and the mean velocity U in lock-in condition, as follows:

$$C_D = \frac{F_x}{1/2\rho U^2 DS} \tag{2.23}$$

Similarly, the mean Lift coefficient on a floating device is expressed by the relation between the mean lift force F_y, the density ρ, the projected area A_p and the velocity U:

$$C_L = \frac{F_y}{1/2\rho U^2 DS} \tag{2.24}$$

Nominal Reduced Velocity [11]

The Reduced Velocity (U_r) is the dimensionless parameter that compares the free stream velocity to the cylinder transverse velocity, it can be written as a function of the natural period (T_n) or the natural frequency (f_n).

$$U_r = \frac{UT_n}{D} = \frac{U}{Df_n} \tag{2.25}$$

Usually, the natural period in the cross-flow/in-line direction in still water is used to characterise the reduced velocity [9].

For design purposes, the VIM response amplitude ratio is usually presented as a function of the reduced velocity U_r (see figure 3.4). Figure 2.10 shows the response amplitude ratio in the cross-flow direction (A_y/D) vs the reduced velocity U_r. It is expected that VIM occurs at reduced velocities 4 to 6.

In free vibration with 1DOF, the peak amplitude motion of the cylinder is expected to reach one cylinder diameter at the reduced velocity of 6 [11]. However, defining the reduced velocity in a FOWT is difficult due to these structures undergoing 6-DOF motions, including a non-linear mooring system with hydro-static stiffness.

2.8 Vortex Induced Motions (VIM).

Vortex-induced motion (VIM) occurs due to the interaction between water and the cylinder when vortices are shed in the wake. In a flexible cylinder or a cylinder elastically mounted, its natural frequency can be triggered by vortex shedding phenomena. If the vortex shedding frequency reaches near to the natural frequency of the structure, large amplitude motions may occur [11].

During VIM, in the lift direction is expected the forcing frequency follow the vortex shedding frequency, while in the drag direction, this occurs at twice the lift frequency.

VIM occurs near the Strouhal frequency and is considered to be a stable and self-limiting vibration, with moderate amplitude. Typically, in the cross-flow direction, the fluctuating response motion results in a relatively large amplitude of about one cylinder diameter, whereas in the in-line direction, the amplitude is expected to be less than half of the cylinder diameter [11].

This type of vibration does not lead to catastrophic failures but may lead to fatigue of the anchoring system [11]. Ocean structures typically are designed to withstand more than 20 years, and the prediction of failure due to fatigue becomes extremely important.

Vortex shedding of large FOWT is complicated, the complete analysis must consider the interaction between different forces such as surface wave, current, and multi-directional current profiles.

On another hand, a low aspect ratio introduces an additional effect called *end effects* on vortex shedding, which is different from vortex shedding from a cross-section in an infinity-long cylinder. Semi-submersible structures face additional challenges [2], due to different headings of currents and waves, plus the wake interference between columns and pontoons.

Chapter 3

Numerical tools, Engineering practices, and relevant Standards

During recent years some tools have been developed to predict the VIM effect on structures. However, there is not a well-established analytical tool or procedure for the prediction of this phenomenon. There is therefore a need to improve methods to increase trust and efficiency, allowing at the same time cost reduction for the industry. Some methods for VIV/VIM prediction operate in the Frequency Domain (FD), while others have been developed in the Time Domain (TD). Current practice is based on model tests, that allow measurement and calibrate the current numerical methods. The models and tools that are used nowadays are reviewed in this chapter.

3.1 Model Test.

The wind turbine field is in development and model testing is recommended during design to determine amplitude response, frequency, and hydrodynamic coefficients such as drag/lift coefficients, mainly due to the limitations on information available.

Usually, this kind of test is carried out in towing tanks and there are two main types of testing, the first at sub-critical Re and the second at super-critical Re. Model tests for VIM have been performed with floating vertical structures, also with fully submerged structures positioned either vertically or horizontally.

Most of the research has been carried out during the last decades and recently by the industry focusing on renewable energy. The State-of-the-Art Review of Vortex-Induced Motions of Floating Offshore Wind Turbine Structures [9], presents the acquired knowledge of VIM from different model testing over the last years and represents a fundamental reference for this thesis.

Full-scale measurements are not so common, but there is available information that allows

us to validate numerical predictions and adjustments. Full-scale measurements from the Hywind Scotland wind park [6] are used in this thesis as a source of information and potential comparison.

3.2 Numerical prediction tools

Numerical predictions have been studied but are very limited. CFD studies have been done in spar types due to the simplicity of these structures, however, limitations on computational power are still a common problem.

To ensure a full prediction of the VIV effect on the structure, it is important to establish both, a structural model and a hydrodynamic model. The structural model will capture the structure response due to the hydrodynamic forces acting on the body, whereas the hydrodynamic model represents the loads acting on the structure. The most common tools are discussed in this part [6].

3.2.1 Computational fluid dynamics

An in-compressible flow that is flowing around a body can be described by the Navier-Stokes equation and the continuity equation. The continuity equation for an in-compressible flow is defined as:

$$\frac{\partial u}{\partial x} + \frac{\partial v}{\partial y} + \frac{\partial w}{\partial z} = 0 \tag{3.1}$$

$$or(\nabla \cdot u = 0) \tag{3.2}$$

Navier-Stokes equation is derived from Newton's second law and considers three types of forces acting in the fluid, such as pressure forces, gravitational forces, and viscous forces. In a Newtonian fluid, the equation system for an in-compressible flow is written as follows:

$$\frac{\partial u_i}{\partial t} + u_j \frac{\partial u_i}{\partial x_j} = -\frac{1}{\rho}\frac{\partial p}{\partial x_i} + \nu \frac{\partial^2 u_i}{\partial x_j^2} + f_i \tag{3.3}$$

Where $u_{i/j}$ represents the velocity vector with components in the three directions (i.e. u_x, u_y, u_z), p is the pressure, and f_i the external forces. Due to the complexity, Navier-Stokes equations have not been solved analytically, however, in the last century, computational tools have been developed to solve them. One of these tools is known as CFD, Computational Fluid Dynamics.

In the CFD method, the Navier-Stokes equations are discretized to calculate the flow around the object. Exists a variety of CFD classifications, the most known consider the following aspects: how it is considered the fluid, how the domain is discretized, and how the turbulence is modelled [**103**].

- Considering how the fluid is observed, the most common CFD classification are either Eu-

lerian or Lagrangian methods; most Eulerian methods utilise a mesh to describe the fluid domain whereas Lagrangian methods, do not use a mesh, but rather particles, which can move freely in space.

- Similarly, several methods differ in how the domain is discretized. Some types of discretization methods are: the finite difference method (FDM), the finite volume method (FVM), and the finite element method (FEM).
- Turbulence models include the effect of turbulence in the simulation of fluids. The most common models are Reynolds-averaged Navier-Stokes (RANS), large eddy simulation (LES), and direct numerical simulation (DNS). Some characteristics of these tools are summarised below:
    - RANS models are mathematical models based on average values of variables for the flow. Some models based on this method are the $k-l$ model, Spalart-Allmaras model, $k-\varepsilon$ model, and $k-\omega$ model.
    - LES is an average turbulence model where Navier-Stokes equations are used for large-scale eddies, while an appropriate model is used for smaller eddies.
    - DNS solves Navier-Stokes equations directly without using turbulence models, however, the entire space and time domain are discretized, requiring extreme fine mesh and small time step. Due to the increment in the number of degrees of freedom required to solve the flow, the computational cost increases from RANS to DNS. However, DNS and LES are generally applied to simple geometries and academic analysis, whereas RANS is applied to complex industrial problems.

Several studies are available using the CFD method to predict VIV, however, results from 2D-CFD simulations show that are less accurate than semi-empirical models. Studies in 3D-CFD simulations showed good agreement for both, the flow and structure response, therefore is considered that CFD can be a useful tool for VIV prediction.

The drawbacks of this method are the huge computational cost and actual limitations due to restrictions in computational power, this is an important feature since capturing the effect in the vortex shedding requires small resolution and small time steps.

3.2.2 Semi-Empirical Frequency Domain model

In the offshore industry, for analysis and VIV prediction, several semi-empirical tools are available. All the models use hydrodynamic coefficients (added mass, damping, and excitation) from experimental results. Some of the most common tools with a short description are presented below:

- VIVA [18], is a computational tool that predicts VIV and fatigue damage of marine risers in

shear flows based on strip theory. This model uses hydrodynamic data from experimental tests and mathematical models, on sectional force coefficients and correlation length.

- SHEAR7 [19], is a computational tool used for modelling natural frequencies, mode shapes, and the response of cables and beams, subjected to linearly varying tension, under any type of boundary condition. In SHEAR7, the cylinder is modelled as a one-dimensional structure, that may have variations in diameter. This program identifies the modes that are likely to be excited and estimates the cross-flow VIV response in steady, uniform, or sheared flows.
- VIVANA [20], is a computational tool used for the calculation of VIV, fatigue damage and drag amplification of slender marine structures such as risers, free-span pipelines, and cables subjected to ocean currents. The VIV analysis includes cross-flow, in-line, or both, cross-flow and in-line VIV effects.

Although FD models can be sufficient for some types of analysis, they do not handle effectively non-linearities showing a loss of accuracy. Some common non-linearities are time-varying boundary conditions, large responses, tension variations, and coupling between axial and lateral vibrations.

Moreover, in FD models, each frequency has to be considered individually, and this approach shows limitations under certain conditions when the interaction of different frequencies must be taken into account such as the case of varying sheared current. Another limitation arises from interaction with dynamic external loads. To correct this, the program includes a step-by-step time integration of the dynamic equilibrium equation, which is the basis for the Time Domain (TD) models.

3.2.3 Empirical Time Domain model

TD models solve the response of the structure by performing a step-wise time integration, allowing to capture of non-linearity effects. [21] has proven the effectiveness of this method for VIV prediction using ABAVIV code.

ABAVIV accounts for non-linearities and is suitable for calculating VIV response and fatigue damage on a catenary riser, considering sheared current profiles. In this model, the lock-in response is determined at each time step. Before and after lock-in, the lift force oscillates with Strouhal frequency, and when lock-in occurs, the lift force gradually changes its frequency towards being in phase with the frequency of the cylinder.

To approximate the nonlinear behaviour of the water, TD models are required to solve the wake flow behind the structure with some level of detail. Several models have been proposed to capture the interaction of the structural motions on the wake. Some researchers use the forced van der Pol oscillator equation to represent the self-exciting and self-limiting phenomenon ([22], [23]).

Another study using TD intended to apply neural network methods [22], by training the code using available data from tests on long-flexible-riser models, subject to uniform or sheared current. The program was trained given the velocity as input, allowing to reproduce the forces for different conditions in shear current. Results showed that the forces were well predicted at the lower current velocities, while the predictions were very poor at higher velocities, due to the complexity of the vortex-shedding interaction.

3.2.4 Semi-Empirical Time Domain model

In recent years, a very promising model has been developed by NTNU called VIVANA-TD. The model was presented for first time by [24], and including different improvements in subsequent publications ([25], [26], [27]), as part of the PhD work. Several improvements and changes have been done over the years with publications that validated the model, ([28], [29], [30], [31], [32], [33], [34]). A review of the main concepts is presented below.

Hydrodynamic formulation. [35]

The TD VIV formulation originates from the generalised Morison equation, which consists of three main terms, Froude-Kriloff force (F_{FK}), the added mass force (F_{M_a}) and the drag forces (F_D).

$$F = F_{FK} + F_{M_a} + F_D \tag{3.4}$$

$$F = \underbrace{\frac{1}{4}C_M \rho \pi D^2 \dot{\mathbf{u}}_n}_{\text{Froude-Kriloff force}} - \underbrace{\frac{1}{4}(C_M - 1)\rho \pi D^2 \ddot{\mathbf{r}}_n}_{\text{Added mass force}} + \underbrace{\frac{1}{2}C_D \rho D |\mathbf{v}_n| \mathbf{v}_n}_{\text{Drag force}} \tag{3.5}$$

In this equation, F is the total hydrodynamic force acting on the cylinder, C_D is the non-dimensional drag coefficient, C_M is the non-dimensional inertia coefficient, which is related to the added mass coefficient as follows: $C_M = C_A + 1$. The $\dot{\mathbf{u}}_n$ represents the fluid acceleration in the transverse direction, $\ddot{\mathbf{r}}_n$ the structure acceleration in the transverse direction, $\mathbf{v}_n$ is the relative velocity in the transverse direction. ($\mathbf{v}_n = \mathbf{u}_n - \dot{\mathbf{r}}_n$). Where $\mathbf{u}_n$ and $\dot{\mathbf{r}}_n$ represent the fluid velocity and structure velocity in the transverse direction, respectively.

Figure 3.1 shows the velocity vector decomposition and the hydrodynamic forces acting on the cross-section of the cylinder. Due to the model is based on strip theory, the incoming flow velocity must be decomposed into a tangential velocity to the cylinder ($\mathbf{u}_t$) and a normal velocity to the cylinder ($\mathbf{u}_n$). For the analysis, the tangential component of the velocity is neglected, and only the normal component contributes to the force in the strip theory.

Since vortex shedding forces are in phase with the relative structure velocity, then the relative velocity in the local x and y direction is defined as follows:

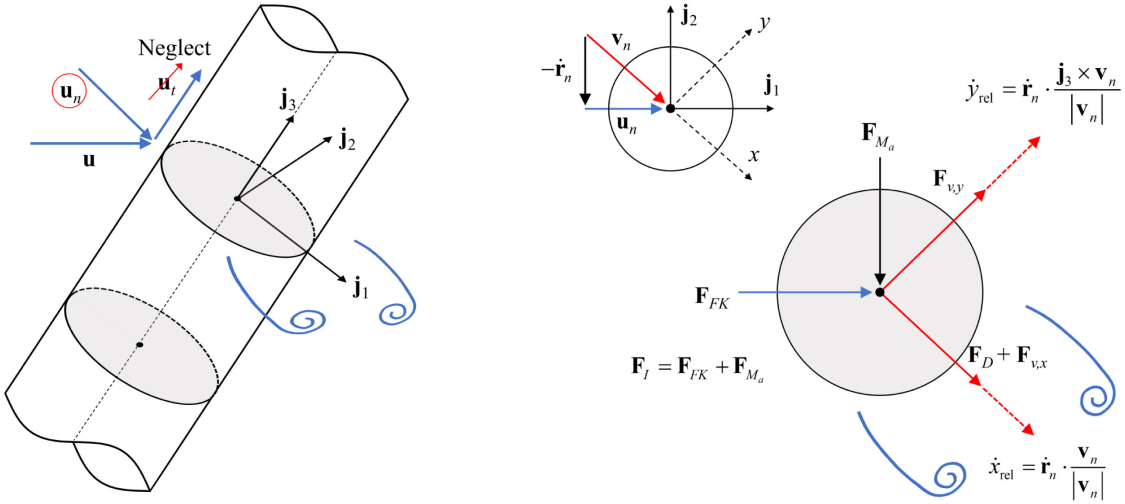

(a) 3D cylinder strip with an incoming flow (b) Hydrodynamic force terms at the cross-section

Figure 3.1: The incoming flow velocity decomposition and hydrodynamic forces at the cylinder. Figure from [32]

$$\dot{x}_{rel} = \dot{r}_n \cdot \frac{\mathbf{v}_n}{|\mathbf{v}_n|} \tag{3.6}$$

$$\dot{y}_{rel} = \dot{r}_n \cdot \frac{\mathbf{j}_3 \times \mathbf{v}_n}{|\mathbf{v}_n|} \tag{3.7}$$

The hydrodynamic model in VIVANA-TD includes two additional terms in the Morison equation, to include the contribution of the CF and IL vortex shedding forces, as follows:

$$F_n = F_{FK} + F_{M_a} + F_D + F_{v,x} + F_{v,y} \tag{3.8}$$

$$F_n = \overbrace{\underbrace{\frac{1}{4}C_M\rho\pi D^2\dot{\mathbf{u}}_n}_{\text{Froude-Kriloff force}} - \underbrace{\frac{1}{4}(C_M-1)\rho\pi D^2\ddot{\mathbf{r}}_n}_{\text{Added mass force}}}^{\text{Inertia forces}} + \underbrace{\frac{1}{2}C_D\rho D|\mathbf{v}_n|\mathbf{v}_n}_{\text{Drag force}} + \overbrace{\underbrace{\frac{1}{2}C_{v,x}\rho D|\mathbf{v}_n|\mathbf{v}_n\cos\phi_{\mathbf{exc},x}}_{\text{IL vortex shedding force}} + \underbrace{\frac{1}{2}C_{v,y}\rho D|\mathbf{v}_n|(\mathbf{j}_3\times\mathbf{v}_n)\cos\phi_{\mathbf{exc},y}}_{\text{CF vortex shedding force}}}^{\text{Vortex shedding forces}} \tag{3.9}$$

Morison's equation

Where F_n represents the total hydrodynamic force. The CF vortex shedding force ($F_{v,y}$) corresponds to a lift force in the local y-direction that is normal to the relative flow velocity vector $\mathbf{v}_n$, while the IL vortex shedding force ($F_{v,x}$) correspond to a drag force in the local x-direction that is aligned with the relative flow velocity vector $\mathbf{v}_n$. $\phi_{\mathbf{exc},x}$ and $\phi_{\mathbf{exc},y}$ are the IL and CF instantaneous phases of the vortex shedding forces, and $\mathbf{j}_3$ is the unit vector in the axial direction of the cylinder.

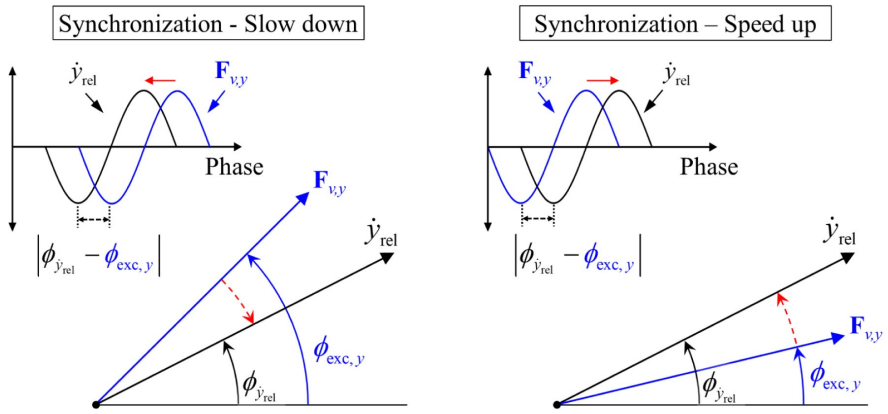

Figure 3.2: Phase angle relationship between the vortex shedding forces in CF direction and relative structure velocity in the local y-axis. Figure from [32]

Synchronisation of Vortex Shedding Forces

Synchronisation in the VIV model is a concept that describes the coupling between the force and the structure response during lock-in condition, represented by $\phi_{\mathbf{exc},x}$ and $\phi_{\mathbf{exc},y}$ in equation 3.9. Figure3.2 explains the CF synchronisation model.

When $\phi_{\mathbf{exc},y}$, the phase angle of the CF vortex shedding force, is in front of $\phi_{\dot{y}_{rel}}$, the phase angle of the relative structure velocity, then, the instantaneous vortex shedding frequency is reduced to minimise the difference, this procedure is known as slow down. For the opposite case, the instantaneous vortex shedding frequency is increased with the same objective, to minimise the difference, this is known as speed up [32].

$$\frac{d\phi_{\mathbf{exc},y}}{dt} = 2\pi f_{\mathbf{exc},y} = \frac{2\pi|\mathbf{v}_n|}{D}\widehat{f}_{\mathbf{exc},y} \tag{3.10}$$

Equation 3.10 shows the instantaneous frequency of vortex shedding force which can be changed to match the instantaneous frequency of the relative structure velocity.

$$\widehat{f}_{\mathbf{exc},y} = \widehat{f}_{\mathbf{0},y} + \Delta\widehat{f}_y \sin\theta_y \tag{3.11}$$

$$\theta_y = \phi_{\dot{y}_{rel}} - \phi_{\mathbf{exc},y} \tag{3.12}$$

In equation 3.11, θ_y is defined as the CF phase difference, between the CF relative structure velocity ($\phi_{\dot{y}_{rel}}$), and the CF vortex shedding force ($\phi_{\mathbf{exc},y}$). $\widehat{f}_{\mathbf{0},y}$ define the non-dimensional frequency of maximum energy transfer and $\Delta\widehat{f}_y$ determine the CF synchronisation range. The synchronisation range is determined based on experimental data, an example is shown in figure 3.3.

The formulation for IL synchronisation is similar to CF. $\widehat{f}_{\mathbf{0},x}$ define the IL non-dimensional fre-

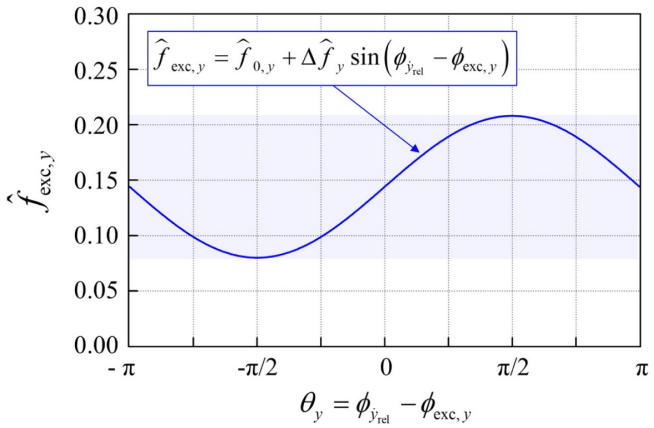

Figure 3.3: Cross Flow Synchronisation. Figure from [32]

quency of maximum energy transfer and $\Delta\widehat{f}_x$ the IL synchronisation range.

$$\frac{d\phi_{\mathbf{exc},x}}{dt} = 2\pi f_{\mathbf{exc},x} = \frac{2\pi|\mathbf{v}_n|}{D}\widehat{f}_{\mathbf{exc},x} \tag{3.13}$$

$$\widehat{f}_{\mathbf{exc},x} = \widehat{f}_{\mathbf{0},x} + \Delta\widehat{f}_x \sin\theta_x \tag{3.14}$$

$$\theta_x = \phi_{\dot{x}_{rel}} - \phi_{\mathbf{exc},x} \tag{3.15}$$

According to [32], in the case of in-line responses, a pure IL response and a combined IL-CF response. [11] mentioned, that in the case of combined IL-CF, the IL frequencies are usually twice of CF frequencies. Since this thesis is going to analyse the combined IL-CF response of the structure, this feature is included and the IL parameters ($\widehat{f}_{\mathbf{0},x}$, $\Delta\widehat{f}_x$) are set to be twice of CF parameters in SIMA models.

3.3 The VIM design curve

A practical method that has been used in the industry, refers to the VIM design curve. This method is often used during the early design phase as an initial criterion. The typical curve is shown in Figure 3.4. The curve allows us to predict the amplitude ratio, A/D, as a function of the reduced velocity.

3.4 Relevant standards.

VIM is partially treated in several standards, some of which are:

1. DNV-RP-C205 [36]. Environmental Conditions and Environmental Loads. This document includes guidance and recommendations about the environmental loads and conditions that

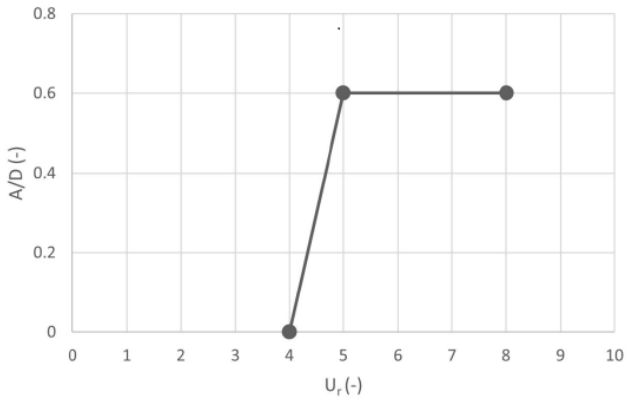

Figure 3.4: Typical VIM curve. Figure from [9]

must be included during modelling.

2. DNV-ST-0119 [37]. Floating wind turbine structures. This standard includes principles and requirements for the structural design of offshore wind turbines.
3. ISO 19901-7:2013 [38]. This document includes specific requirements for designing, analysing, and evaluating stationkeeping systems for floating structures used by the oil and gas industries.

Chapter 4

SIMA model of the 12MW SS-FOWT.

Figure 4.1: The INO-WINDMOOR platform. Figure from [8]

4.1 The Software

VIVANA-TD is a complete software that includes different tools to predict the response of the structure subjected to aero-hydrodynamic forces. Following are some descriptions of the modules that were used:

SIMO is a time domain tool for rigid body motion prediction of multi-body systems. This tool includes flexible modelling of station-keeping forces and connecting mechanisms such as anchor lines, ropes, fenders, etc.

RIFLEX is a time domain tool for global hydrodynamic and non-linear structural analysis of slender structures, the analysis includes static and dynamic responses. This tool includes wind turbine aerodynamic models for wind turbine analysis.

SIMA is a user interface software developed by SINTEF Ocean for simulations and analysis of marine and floating structures. SIMA applies SIMO and RIFLEX as the underlying tools for wind turbine analysis. The software allows SIMO and RIFLEX can be connected for coupled analysis at each time step when required, i.e. coupled analysis of mooring systems and floater response.

4.2 The 12MW SS-FOWT INO-WINDMOOR model.

The thesis studies a 12MW wind turbine, called INO-WINDMOOR that is available in SIMA with an aero-hydro-servo-elastic model and has been analysed in various research.

The model and parameters of the wind turbine are based on a report from SINTEF [8], describing the procedure for modelling the 12MW SS-FOWT INO-WINDMOOR.

The model consists of a rigid-body platform modelled in SIMO and coupled to a flexible tower - a wind turbine - mooring system modelled in RIFLEX. The wind turbine has a rated wind speed of 10.6 m/s and a cut-out wind speed of 25.0 m/s.

4.2.1 INO-WINDMOOR model. Main characteristics.

For modelling the INO-WINDMOOR the x-y plane coincides with the mean water level, with the z-axis positive upwards. Waves, winds, and current direction coincide with the positive x-direction. Loads and motions refer to the local coordinate system defined in figure 4.2.

The INO-WINDMOOR operates at 150m water depth and the sea bottom is assumed flat. The mooring system consists of three hybrid catenary lines (chain + polyester), the pretension is about 1050 kN, operating at 150m water depth. The fairleads are at the waterline. The orientation of the mooring system in SIMA is shown in the figure 4.3. The anchor lines coordinate system is presented in table 4.1.

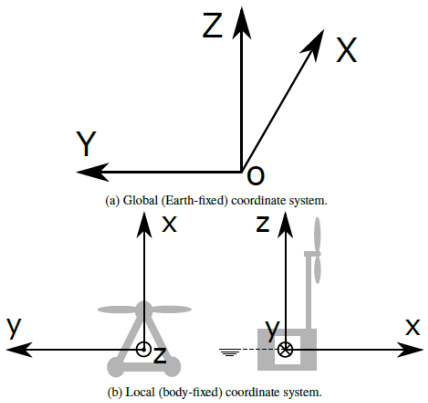

Figure 4.2: Global and Local Coordinate system. Figure from [8]

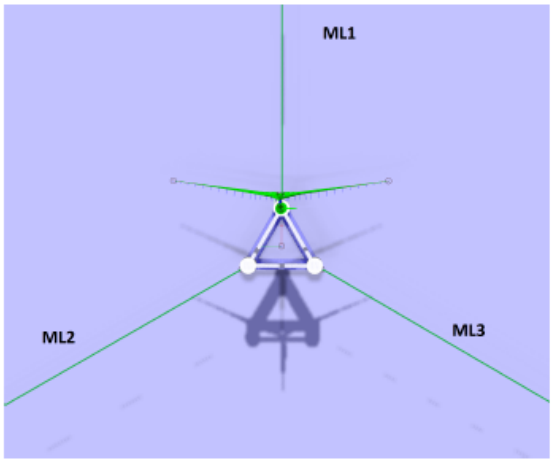

Figure 4.3: Mooring system orientation for the INO-WINDMOOR. Figure from [8]

The mooring system was modelled as bar elements in RIFLEX. Bar elements are assumed to be straight, with constant cross-section area A_o. In figure 4.4 L_o is the initial length, and L denotes the deformed length. 2 nodes with 3DOF define each bar element, therefore, bar elements have zero bending stiffness and only can take loads in the axial direction.

Each line of the mooring system consists of 4 segments, summarised in table 4.2. The equivalent diameter is used for the Morison formulation in SIMA. The mass/length ratio considers marine growth [8]. C_A is the added mass coefficient, C_Q is the quadratic drag coefficient.

In table 4.3 are listed the elements and segment characteristics. Super-nodes at the fairleads

	Fairlead			Anchor			
Mooring line	x(m)	y(m)	z(m)	x(m)	y(m)	z(m)	Azimuth (deg)
ML1	42.7	0.0	0.0	700.0	0.0	-150.0	180
ML2	-21.4	37.0	0.0	-350.0	606.2	-150.0	300
ML3	-21.4	-37.0	0.0	-350.0	-606.2	-150.0	60

Table 4.1: Anchor lines coordinate system. Data from [8]

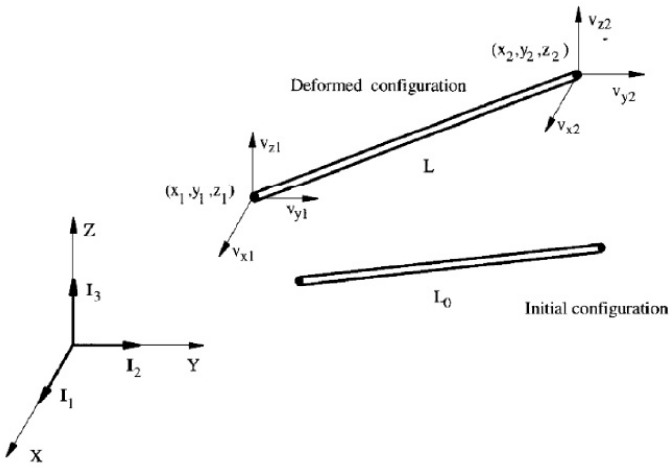

Figure 4.4: Nodal degrees of freedom for RIFLEX bar element. Figure from [6]

Segment-Type	Length (m)	Eqv.Dia. (m)	Mass/L (kg/m)	Ax-stiff. (MN)	CA_Y (-)	CA_X (-)	CQ_Y (-)	CQ_X (-)
#1-130mm std.chain	25.0	0.234	377.7	1443.0	1.0	0.5	6.1	2.9
#2-190mm polyester	85.0	0.190	60.7	228.0	1.0	0.0	2.5	0.1
#3-190mm polyester	85.0	0.190	46.0	228.0	1.0	0.0	1.8	0.1
#4-130mm std.chain	499.8	0.234	353.6	1443.0	1.0	0.5	4.2	2.0

Table 4.2: Mooring line properties. Data from[8]

are modelled slaves to the master super-node at the platform.

The tower is placed at the top of one of the platform's columns, at 15.5 m above the mean water level. Tower's properties and main dimensions are given in table 4.4.

The tower was modelled using 20 beam elements in RIFLEX. Beam elements have 6DOF in each node (see figure 4.5), which allows these elements to translate and rotate, consequently they can undergo bending.

The main assumptions that define beam elements in SIMA are listed below:

- The plane section of the beam, normal to the x-axis, remains plane and normal during deformations.
- Lateral contractions due to axial elongation are neglected.
- Strains on the beam are small.
- Shear deformations due to lateral loading are considered by modifying the bending stiffness.
- St. Venant torsion model is included, but Torsional warping is neglected.

Segment-Type	Length (m)	N. elements	Elem. Length (m)
#1-130 mm std.chain	25.0	5	5.0
#2-190 mm polyester	85.0	17	5.0
#3-190 mm polyester	85.0	9	9.44
#4-130 mm std.chain	499.8	45	11.11

Table 4.3: Mooring line segments modelled in SIMA. Data from[8]

Parameter	Units	Value
Diameter at top	(m)	5.97
Diameter at bottom	(m)	9.90
Thickness at top	(mm)	30.1
Thickness at the bottom	(mm)	90.0
Length	(m)	110.20
Mass	(t)	1161.6
ρ_{steel}	kg/m^3	7850
E_{steel}	Pa	$2.11x10^{11}$
CG_z from base	(m)	56.65

Table 4.4: Tower properties and main dimensions. Data from[8]

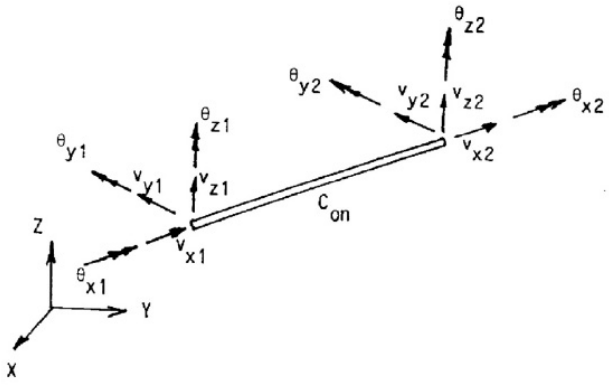

Figure 4.5: Nodal degrees of freedom for RIFLEX beam element. Figure from [6]

- Coupling between torsion and bending is considered by a second-order approximation of torsion and bending curvature. This coupling is not reflected in the stiffness matrix.

Two super-nodes were used to model the tower, one at the base and another at the top. The tower base is at (35.2,0.0,15.5), this is the connection point with the SIMO body (the platform) and this node was modelled as a slaved connection.

The axisymmetric cross-section of the tower was modelled with a decreasing diameter from the base to the top. Elements, length, and cross-sectional properties are described in Appendix A.

The semi-submersible platform is a steel structure, with three vertical cylinders each one connected by rectangular deck beams and submerged rectangular pontoons. The hull main dimensions of the platform are listed in table 4.5.

Properties of the full system including platform, tower, wind turbine, and mooring lines, are found in the INO-WINDMOOR Report [8].

To find the hydrodynamic coefficients, such as added mass, wave radiation damping, wave force, and drift force coefficients, a hydrodynamic diffraction-radiation analysis is required. According to Silva [8], WAMIT was applied to compute the hydrodynamic coefficients.

WAMIT is a 3D frequency domain panel code, that uses linear and second-order potential theory for diffraction radiation analysis of floating/submerged bodies. Results of the hydrodynamics

Parameter	Units	Value
Column diameter	(m)	15.00
Column height	(m)	31.00
Pontoon width	(m)	10.00
Pontoon height	(m)	4.00
Centre-centre distance	(m)	61.00
Deck beam width	(m)	3.50
Deck beam height	(m)	3.50
Total substructure mass	(t)	11974.00
Total substructure CG_x	(m)	-5.91
Total substructure CG_z	(m)	-9.70
Total substructure R_{xx}	(m)	23.66
Total substructure R_{yy}	(m)	18.63
Total substructure R_{xx}	(m)	28.10

Table 4.5: Main dimensions of the INO-WINDMOOR platform. Data from[8]

Parameter	Units	Value
Displacement	(t)	14176.1
Draft	(m)	15.5
CG_x^*	(m)	[-0.37,0.37]
CG_y^*	(m)	[-0.37,0.37]
CG_z^*	(m)	4.23
R_{xx}	(m)	43.67
R_{yy}	(m)	44.18
R_{zz}	(m)	30.26
Static heel angle at rated thrust	(deg)	6.40
Still water airgap to column top	(m)	15.50
Still water airgap to deck beam bottom	(m)	12.00
Still water airgap to blade tip	(m)	21.70
I_{xx}	(kg m^2)	2.7292·10^{10}
I_{yy}	(kg m^2)	2.7295·10^{10}
I_{zz}	(kg m^2)	1.2985·10^{10}

*CG_x and CG_y are dependent on the nacelle orientation.
For 0^o orientation CG_x=0.37m and CG_y=0.00m
For 90^o orientation CG_x=0.00m and CG_y=0.37m

Table 4.6: Full floating platform properties. Data from[8]

coefficients can be found in the INO-WINDMOOR Report Appendix A2 [8]. The added mass matrix A_{ii} is presented in table 4.7.

In SIMA, the platform was modelled as a SIMO body, subjected to loads from waves and RIFLEX structures. Equation 4.1, represents the equation of motion, which depends on (m) the rigid-body inertia matrix, (A_∞) the infinity-frequency added-mass matrix, (D_1) the linear external damping matrix, (K) the hydrostatic restoring matrix, (h) the retardation function, (q) is the vector containing all the external loads.

$$(m + A_\infty)\ddot{x} + D_1\dot{x} + Kx + \int_0^t h(t-\tau)\dot{x}(\tau)d\tau = q(t, x, \dot{x}) \tag{4.1}$$

$$q = -mg\widehat{k} \times r_g + \rho g V\widehat{k} \times r_b + q_{1st} + q_{2nd} + q_{vis,q} + q_{FE} \tag{4.2}$$

	$x(kg)$	$y(kg)$	$z(kg)$	$r_x(kgm)$	$r_y(kgm)$	$r_z(kgm)$
$x(kg)$	$5.41 \cdot 10^6$	0	-93.04	0	-3.05·10^7	0
$y(kg)$	0	5.41·10^6	0	3.05·10^7	0	647.0
$z(kg)$	-24.95	0	1.99 ·10^7	0	3137.8	0
$r_x(kgm)$	0	3.05·10^7	0	5.88·10^9	0	9288.1
$r_y(kgm)$	-3.05·10^7	0	4053.8	0	5.88·10^9	0
$r_z(kgm)$	0	610.1	0	16903	0	5.46·10^9

Table 4.7: Added Mass Matrix of the SIMO body

Equation 4.2, depends on (m) the total mass of the FWT, (ρ) the water density, (g) the gravity acceleration, (V) the displaced volume, ($\boldsymbol{r}_g$ and $\boldsymbol{r}_b$) the position vector of the gravity centre and buoyancy to the origin, (q_{1st}) is a vector containing the first-order wave loads, (q_{2nd}) is a vector containing the second-order wave loads, using Newman's approximation, (q_{FE}) are the loads imposed on the platform by the mooring lines and tower, ($q_{vis,q}$) contains all the viscous drag contributions from the columns and pontoons.

The drag force per unit length is defined as follows:

$$f = \frac{1}{2}\rho C_Q D u|u| \tag{4.3}$$

The characteristic length D, is the column diameter or the pontoon width/height. The relative velocity u includes the wave-particle kinematics and platform motion, and the C_Q is the non-dimensional drag coefficient.

Figure 4.6, shows the model defined in WAMIT [8]. Notice that z-axe coincides with the tangential direction, as it was defined according to strip theory in figure 3.1, therefore, the CQ_y and CQ_z coefficients are defined as follows:

	$C_{Q,y}$	$C_{Q,z}$
Column	1.0	1.0
Pontoon	2.3	1.4

Table 4.8: Drag coefficient. Data from[8]

Table 4.9 shows the natural periods of the platform [8]. During the platform's installation, it was registered the frequencies of the tower at rated speed considering the full system. (See Table 4.10).

	Surge	Sway	Heave	Roll	Pitch	Yaw
Nat. period (s)	97.3	98.0	16.3	29.5	31.4	88.0

Table 4.9: Rigid-body natural periods from decay test on SIMA model. Data from[8]

RIFLEX uses the Blade Element Momentum theory (BEM) for wind turbine analysis. In the FE model, the equilibrium is found with a blade discretization. Model corrections are used as follows: Øye's models for correction on dynamic stall and dynamic wake, Prandtl factor is used for

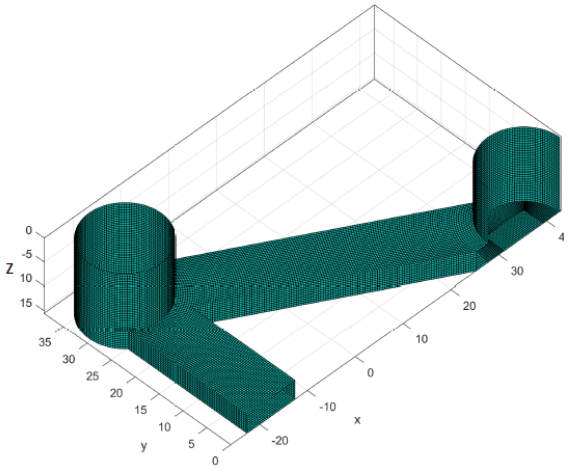

Figure 4.6: Platform modelled in WAMIT. Figure from[8]

1st Fore-Aft Bending Moment Frequency	3p Frequency	6p Frequency
0.641 Hz	0.39 Hz	0.56-0.78 Hz

Table 4.10: Tower frequencies. Data from[8]

correction due to hub and tip losses, and Glauert correction for high induction factors. The tower is considered by using potential theory.

The controller uses a variable-speed variable-pitch approach and a thrust-peak-shaving strategy near the rated speed. The blades are modelled with 18 elements using a double symmetric cross-section. Details about controller and blade properties are listed in the INO-WINDMOOR Report [8]

4.2.2 The TD-VIV model

SIMA includes the semi-empirical TD-VIV model, which has proven to be suitable for VIM analysis on Spar Wind Turbine models [6]. The time domain model is based on Morison formulation including the cross-flow and in-line vortex shedding force term. SIMA allows modelling pure in-line effect, pure cross-flow effect, also, the combination of in-line and cross-flow vortex shedding force.

This formulation is applied to beam elements under hydrodynamic forces, and it is required to make some changes to the initial model available on SIMA for the subsequent study.

- First, in this model the quadratic drag coefficient was removed from each column in the SIMO body, instead, the quadratic drag was considered in the TD-VIV model to prevent duplication of the drag effect on the structure.
- Second, to introduce the VIM effect in the SIMO body, it was used a fictitious element that coincides with each column. The fictitious element was modelled as a BEAM section with

the Load Formulation Time Domain VIV, using the following data:

- Mass coefficient 0.01
- Gyration Radius 0.01
- Hydrodynamic diameter: 15 m
- Axial Stiffness 1.0·10^{11} N
- Bending Stiffness 1.0·10^{11} Nm^2
- Torsional Stiffness 1.0·10^{11} Nm^2/rad

For each column, the fictitious elements have an independent cross-section, a line type, and a pair of nodes coinciding with the top and bottom of each column. To ensure these beam elements have the same motion as the whole structure, each pair of nodes was set up as slaves of the master node of the platform.

- Finally, in the TD-VIV formulation, the added mass coefficients are not considered since the SIMO body already includes the added mass matrix.

A first TD-VIV model is presented to carry out an initial analysis. This model includes vortex-shedding parameters in each column. The non-dimensional coefficients were taken from a Spar Wind Turbine model presented by [6],

	C_L	C_Q	C_A
Tangential direction	0.000	0.0739	0.000
Normal direction	0.000	1.0000	0.000

	C_v	f_0	f_{MIN}	f_{MAX}	Δf
IL	0.75	0.288	0.16	0.416	0.256
CF	0.85	0.144	0.08	0.208	0.128

Table 4.11: Morison Coefficients and Vortex Shedding Parameters for model *VIM M1*. Data from [6]

4.3 Mechanism of the 12MW SS-FOWT

4.3.1 Environment

During the thesis, is planned to study the responses of the 12MW SS-FOWT in two different scenarios.

1. **Constant wind, no wave no current**: for an initial model evaluation.
2. **No wind, no wave, constant current**: for the experimental analysis of the towing test.

4.3.2 Operational Characteristics of the Semi-submersible under Constant wind, no wave and no current

To start the analysis, it is important to mention that the present model includes TD-VIV only in the columns of the semi-submersible. It is considered that the pontoons do not contribute to VIM.

The first study was carried out with constant wind speed, no current, and no wave. This procedure was done to evaluate and set up the model. Some of the results were compared with information available from class notes in Integrated Dynamics Analysis of Wind Turbines [39].

Figure 4.7, Figure 4.8, and Figure 4.9 include results from two models. One of the models, called ***no VIM*** which doesn't include the TD-VIV formulation, whereas the other model, called ***VIM M1*** which includes the TD-VIV formulation on the columns. The analysis was done at three different speeds: below-rated wind speed (8.0 m/s), rated wind speed (10.6 m/s), and above-rated wind speed (12.0 m/s).

The main operational parameters such as rotor speed, aero-thrust, blade pitch, torque, and power were reviewed for assessing the performance of the wind turbine. In general, when we compare both models, very small differences are found.

Figure 4.10 shows results from OPEN FAST [39] of different operational parameters of the 12 MW SS-FOWT plotted against wind velocity, under similar conditions (no wave, no current, and constant wind). The graph also includes results from SIMA of both models, i.e. with and without TD-VIV formulation. The results show the mean values after reaching the steady state.

Results showed that exist small differences in results between SIMA and OPEN-FAST, which can be explained due to the computational approach of each program. Also, it is noticed that both models in SIMA have similar performance. This allows us to confirm that the operational behaviour of the wind turbine is not affected by introducing TD-VIV formulation on the model.

Motion performance in the 6-DOF describes the motion of the semi-submersible platform, under constant wind speed. Figure 4.11 shows results from the two SIMA models showing minimum variations of the amplitude response. In Surge, we cannot distinguish variations in the amplitude response at different wind speeds, while Sway displays variations in the amplitude response for the whole range of velocities. Heave, Roll, and Pitch didn't show variation between the models.

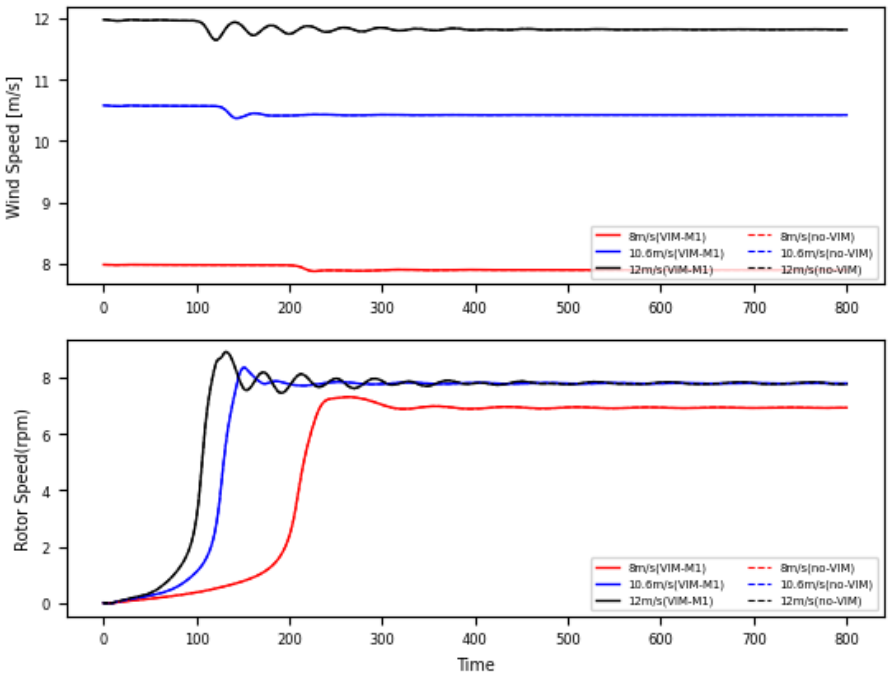

Figure 4.7: Incoming Wind speed in the shaft and Rotor Speed on the 12MW SS-FOWT in Time series

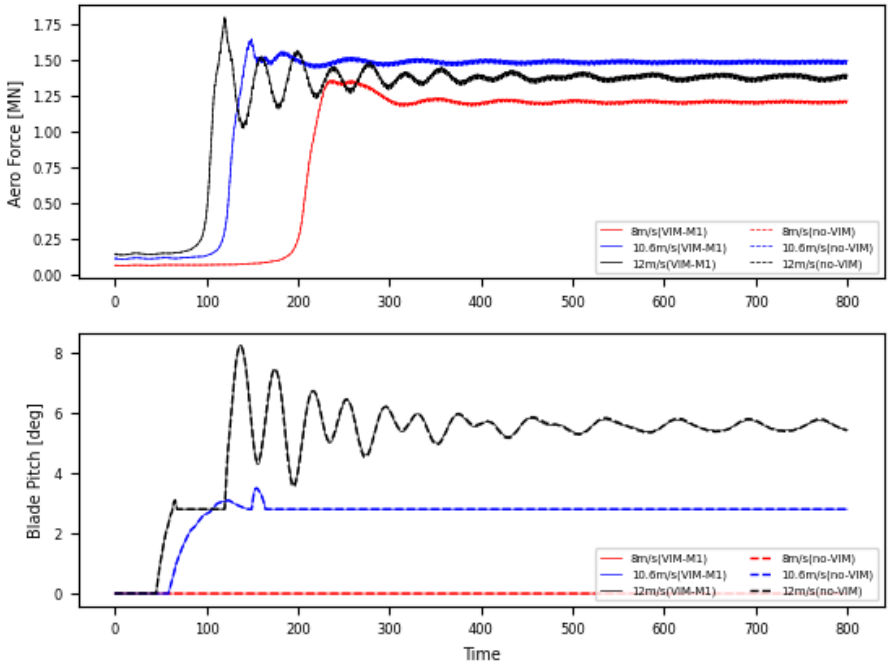

Figure 4.8: Aero Force in the shaft and Blade Pitch, at different velocities on the 12MW SS-FOWT in Time series

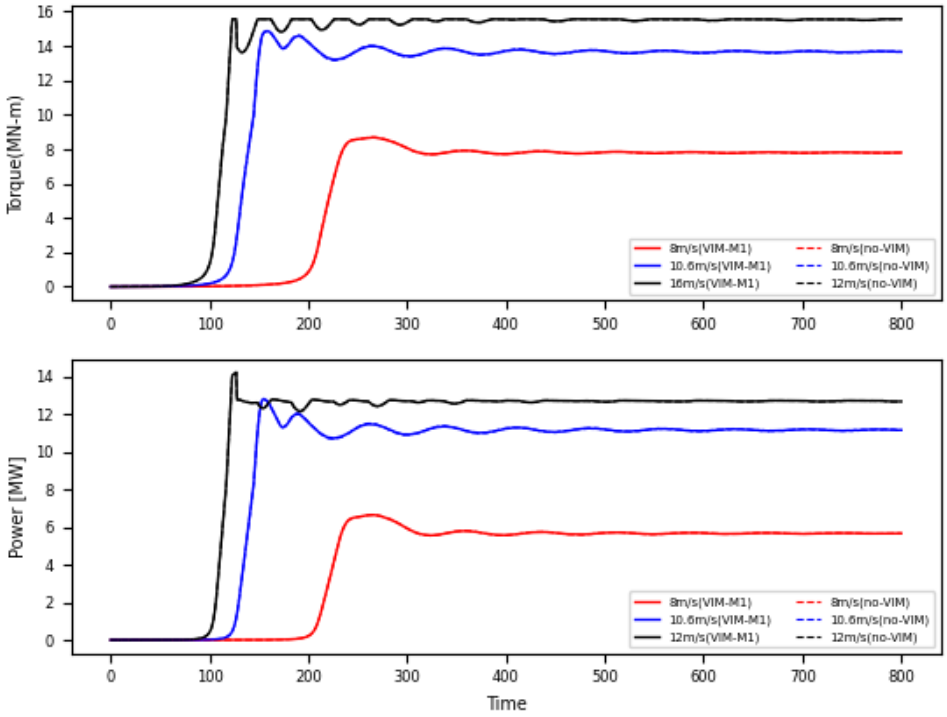

Figure 4.9: Torque and Electrical Power Generator, at different velocities on the 12MW SS-FOWT in Time series

However, the most important VIM effect in rotations is noticed in YAW, which was expected since the principal movements are in the x-y plane.

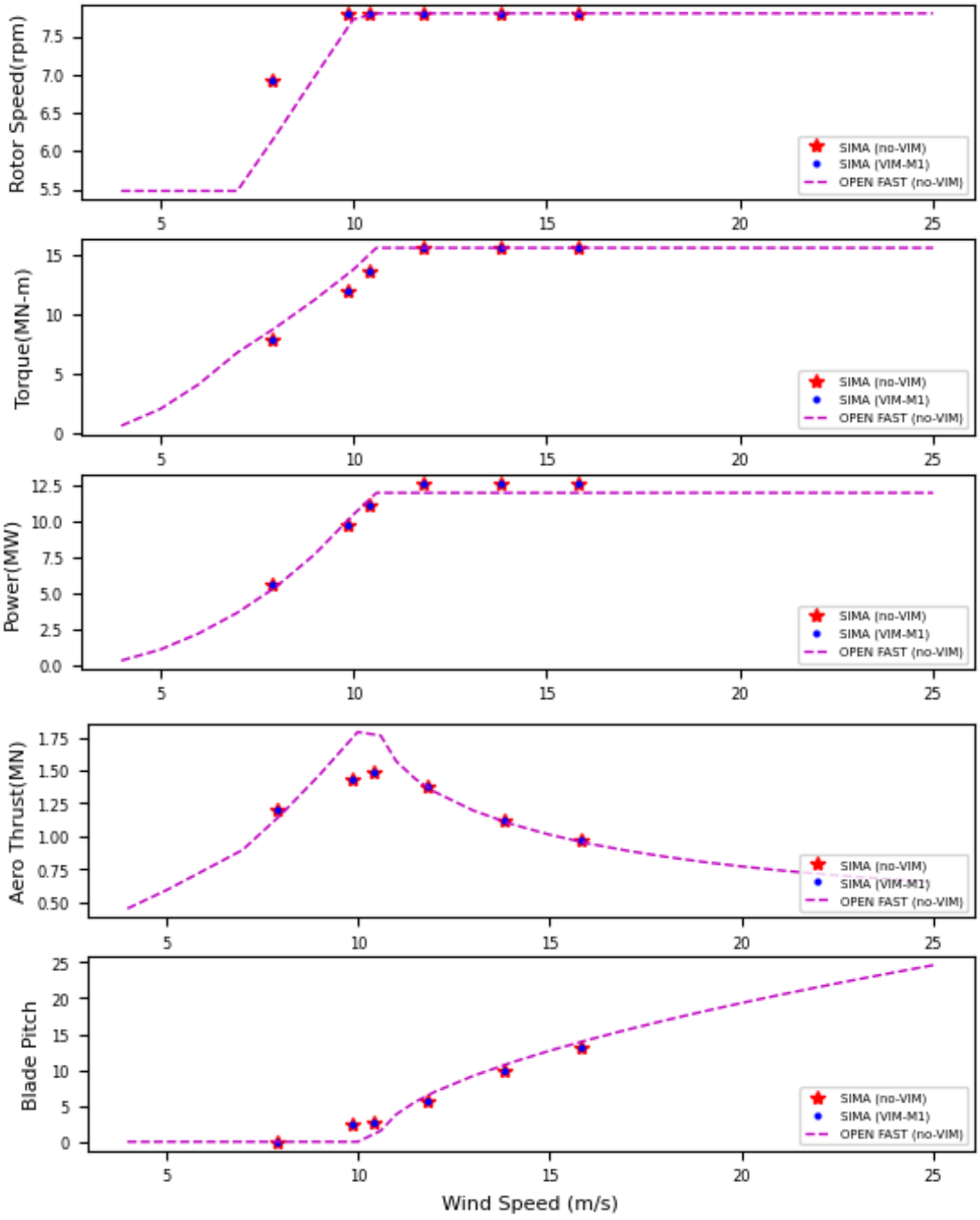

Figure 4.10: Performance curves of different Operational parameters vs wind speed of the 12MW SS-FOWT. Results are from OPEN FAST [39] and SIMA.

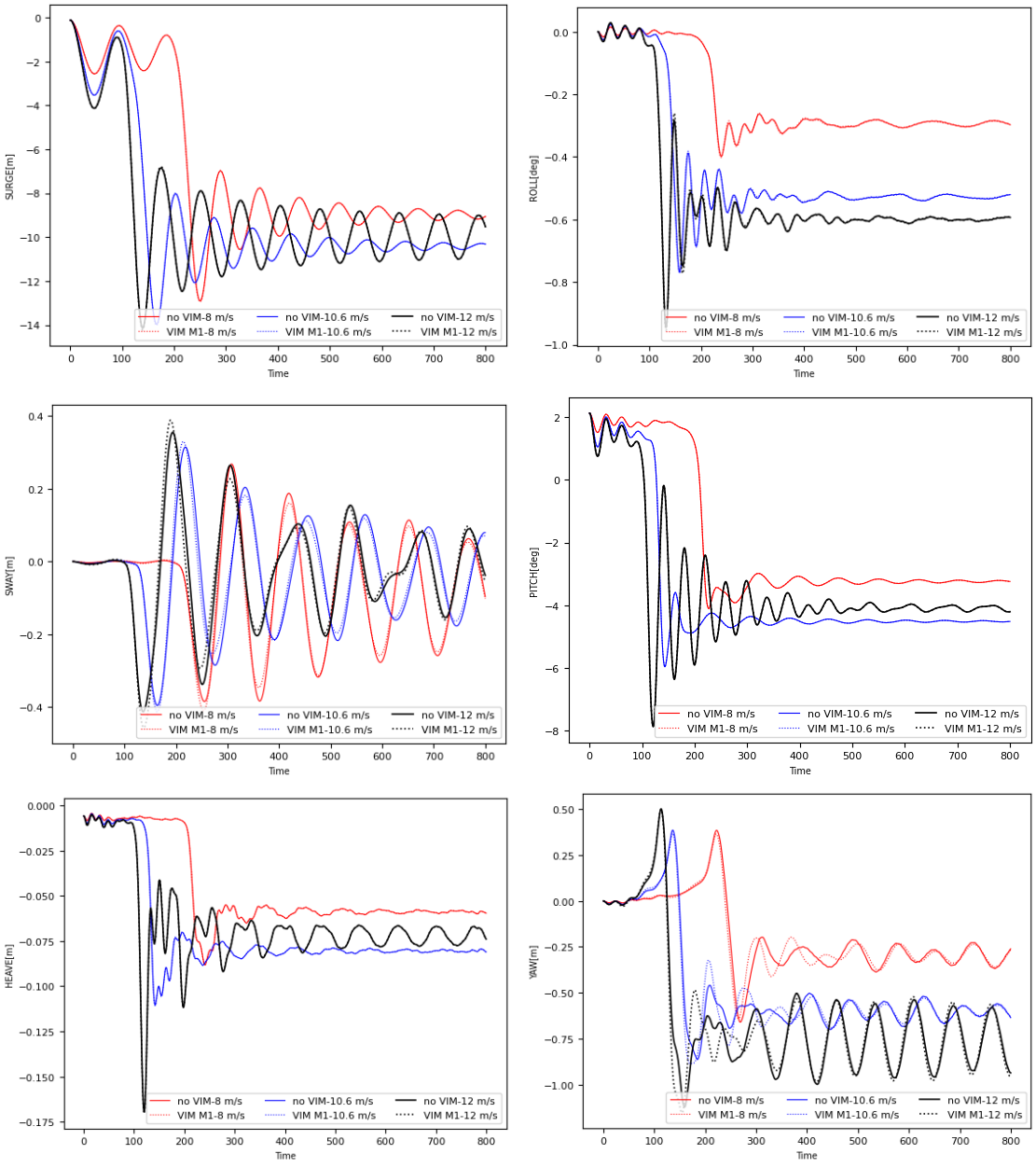

Figure 4.11: Translations and Rotations of the 12MWSS-FOWT under Constant wind, no wave, no current.

4.3.3 Influence of Quadratic Drag under Constant wind, no wave and no current

Two sets of parameters have been considered for assessing the influence of the tangential drag, on the structure response, in an environment with constant wind speed, no current, and no wave. The first set of parameters used the data from a spar wind turbine [6] presented in table 4.11, which was called the model ***VIM M1***. The second model uses hydrodynamic results from WAMIT in the SINTEF's report[8], this model is called ***VIM M2***.

	C_L	C_Q	C_A
Tangential direction	0.000	1.000	0.000
Normal direction	0.000	1.000	0.000

	C_v	f_0	f_{MIN}	f_{MAX}	Δf
IL	0.75	0.288	0.16	0.416	0.256
CF	0.85	0.144	0.08	0.208	0.128

Table 4.12: Morison Coefficients and Vortex Shedding Parameters on model *VIM M2*. Data from [8]

On ***VIM M2***, the quadratic drag coefficients acting on the columns are similar in tangential and normal direction (see table 4.8). According with the strip theory definition, it is noticed that the tangential direction coincides with the CQ_z, whereas the quadratic drag coefficient in the normal direction coincides with the CQ_y. Morison Coefficients and Vortex Shedding Parameters used on model ***VIM M2*** are presented in table 4.12.

In both models, the drag coefficient was modelled in the columns through the TD-VIV module. Also, the added mass was not considered in the TD-VIV formulation, since the SIMO body has included the added mass matrix in the model.

Figure 4.12 presents results for three different models, i.e. no-VIM model, Model 1, and Model 2, at two different wind speeds, i.e. 10.6 m/s the rated speed, and 12 m/s. Time series results showed that all motions look very similar between the models under these environmental conditions.

In figure 4.13 is presented surge, sway, and yaw at rated wind speed and at 12 m/s. Appendix B presents in detail motions in the 6DOF. These results allow some initial conclusions:

- Time series results showed that the amplitude of motion in TD-VIV models is slightly smaller than the amplitude response in the model that does not include TD-VIV, which means that the TD-VIV model is capturing the effect of vortex shedding in the columns.
- Amplitudes of the motions are similar between Model 1, and Model 2, which means that the magnitude of the drag coefficient in the tangential direction hasn't played a role in the VIM response under this environmental condition.
- Also, it is noticed that in the time series spectra, sway, and yaw motions showed the clearest

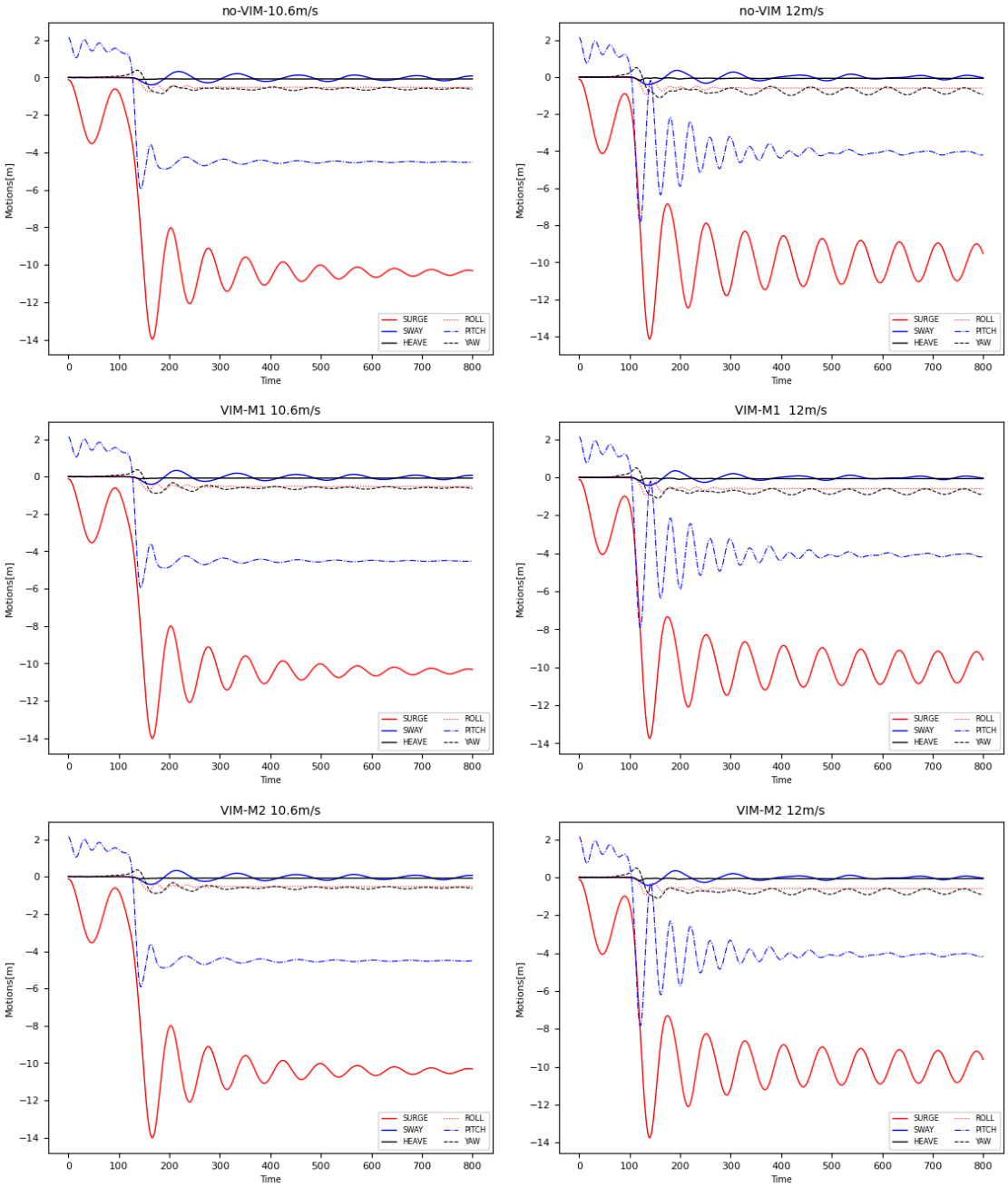

Figure 4.12: Motions in 6DOF for different models. The analysis was carried out at 10.6 m/s and 12 m/s.

difference in the vibration pattern when vortex-shedding is included under this environmental condition. This was expected since VIM is a phenomenon that occurs in the x-y plane. The difference in the vibration pattern can be related to the interaction between columns and the wake.

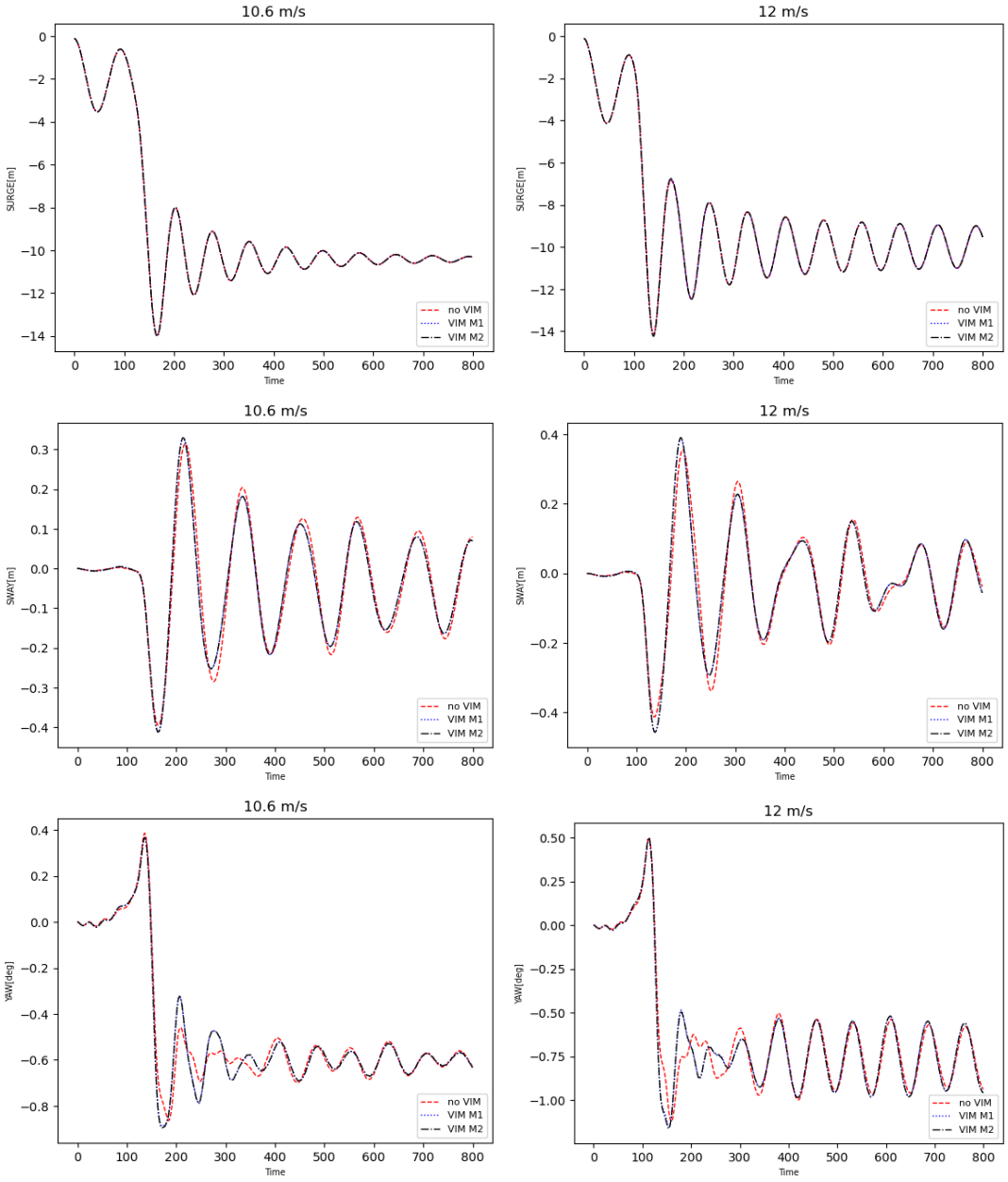

Figure 4.13: Comparison of motions in Surge, Sway, and Yaw, for the three models at two constant wind speeds

4.4 Decay Test of the 12MW SS-WT.

A decay test was performed, both experimentally and numerically, to estimate the dynamic coefficients for the equation of motion. This procedure is done in park conditions, i.e. the blades are not rotating and wind velocity is neglected.

To do a decay test, a force is applied to the system in a particular direction, to displace the structure a certain amount from the equilibrium, and then the force is released. This will allow us to capture the oscillating structure's response.

In SIMA, the decay test is simulated in two steps, firstly it is applied a ramp force or moment during a certain time, secondly, a constant force or moment is applied during some time, and then, the force or moment is released. A graph of the oscillating structure's response typically shows a decrement, because any source of damping acting on the system will release energy, as shown in figure 4.14.

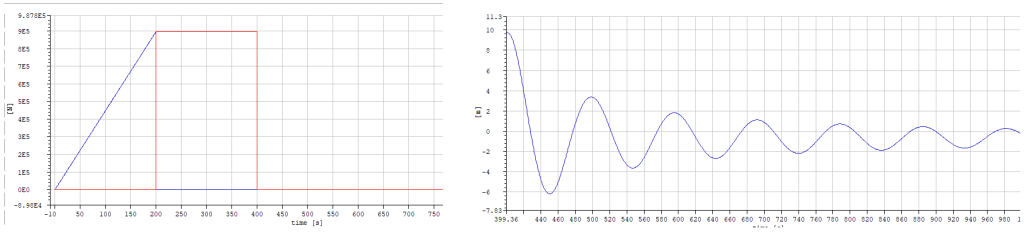

Figure 4.14: Ramp and Constant Forces modelled in SIMA, and the oscillating curve in the time series of structure's response in the x-direction (surge). Figure is from [40]

For the 12MW SS-WT, the decay test was performed with the parameters described in table 4.13, according to the class notes in Integrated Dynamics Analysis of Wind Turbines [39].

Motion	Force/Moment	Ramp duration (s)	Constant Force duration (s)
Surge	1700 KN	100 s.	200 s.
Sway	1700 KN	100 s.	200 s.
Heave	10000 KN	100 s.	200 s.
Pitch	220000 KNm	100 s.	100 s.
Roll	220000 KNm	100 s.	100 s.
Yaw	10000 KNm	100 s.	100 s.

Table 4.13: Simulation parameters for decay test in SIMA. Data from [39]

Figure 4.16 shows results from the decay test, of the motions in the 6 DOF, for the three established models. After removing the force, from the oscillating curve, the damped frequency and other parameters can be found following the next procedure.

The damped frequency (ω_d) is obtained from the structure's response curve, where t_d is the damped period.

$$\omega_d = \frac{2\pi}{t_{i+1} - t_i} = \frac{2\pi}{t_d} \tag{4.4}$$

The natural angular frequency (ω_n) may be calculated as follows:

$$\omega_n = \frac{\omega_d}{\sqrt{1-\zeta^2}} \tag{4.5}$$

If the structure is subjected to a small linear damping ($\zeta < 0.2$), and the quadratic damping is about zero, ζ can be expressed by the logarithmic decrement of the two subsequent peaks from the decay test, as follows:

$$\zeta \approx \frac{1}{2n\pi} ln\left(\frac{y_i}{y_{i+n}}\right) \tag{4.6}$$

This assumption can be confirmed with a P-Q analysis from the decay test. In the case of a system subjected to linear and quadratic damping, the estimation can be approximated by using the P-Q method [39]. Where, P is associated with quadratic damping and is represented by the slope of the curve, and Q is associated with linear damping and is represented by the intercept of the curve. Figure 4.15 and 4.16 includes the structure response and P-Q curve for all motions. Table 4.14 summarised the damped period from the decay test in SIMA.

Motion	INO MODEL [8]	INITIAL MODEL (no-VIM)	TD-VIV MODEL (VIM M1)	TD-VIV MODEL (VIM M2)
Surge	97.30	95.90	95.90	95.90
Sway	98.00	98.50	98.30	98.35
Heave	16.30	24.50	24.45	24.45
Roll	29.50	28.60	28.65	28.65
Pitch	31.40	98.30	97.90	97.90
Yaw	88.00	87.90	89.65	89.65

Table 4.14: Results from decay test: Damped period from Initial Model (no VIM) and VIM M1 Model

Surge, sway, roll, and yaw motions showed good agreement between the data from INO-MODEL [8] and results from the models on SIMA. Also, It was found that heave and pitch period from SIMA models are higher than the value reported in the reference [8].

Under this environmental condition, the damped period is similar between the SIMA models, i.e., no-VIM, VIM M1, and VIM M2. In all cases, the difference is less than 0.5$\%$, except for yaw, which the difference is almost 2$\%$.

In figure 4.16, yaw motion evidence the complexity of the VIM phenomenon. During the whole range of data, the oscillation period is varying. Also, there is variation in the damping. Only after 500 s., the damping is high enough that the structure experiences a rapid decrement in oscillation amplitude.

Also, it is noticed that when TD-VIV is included, sway displays a small increment in the oscillation amplitude, whereas, yaw shows a higher difference. In other types of motions, no evidence exists of changes in the oscillating amplitude, even for surge.

Generally, this type of wind turbine experiences high damping in sway, roll, and yaw, which is confirmed by the decay test. The P-Q curve in figure 4.16 represents the presence of linear and

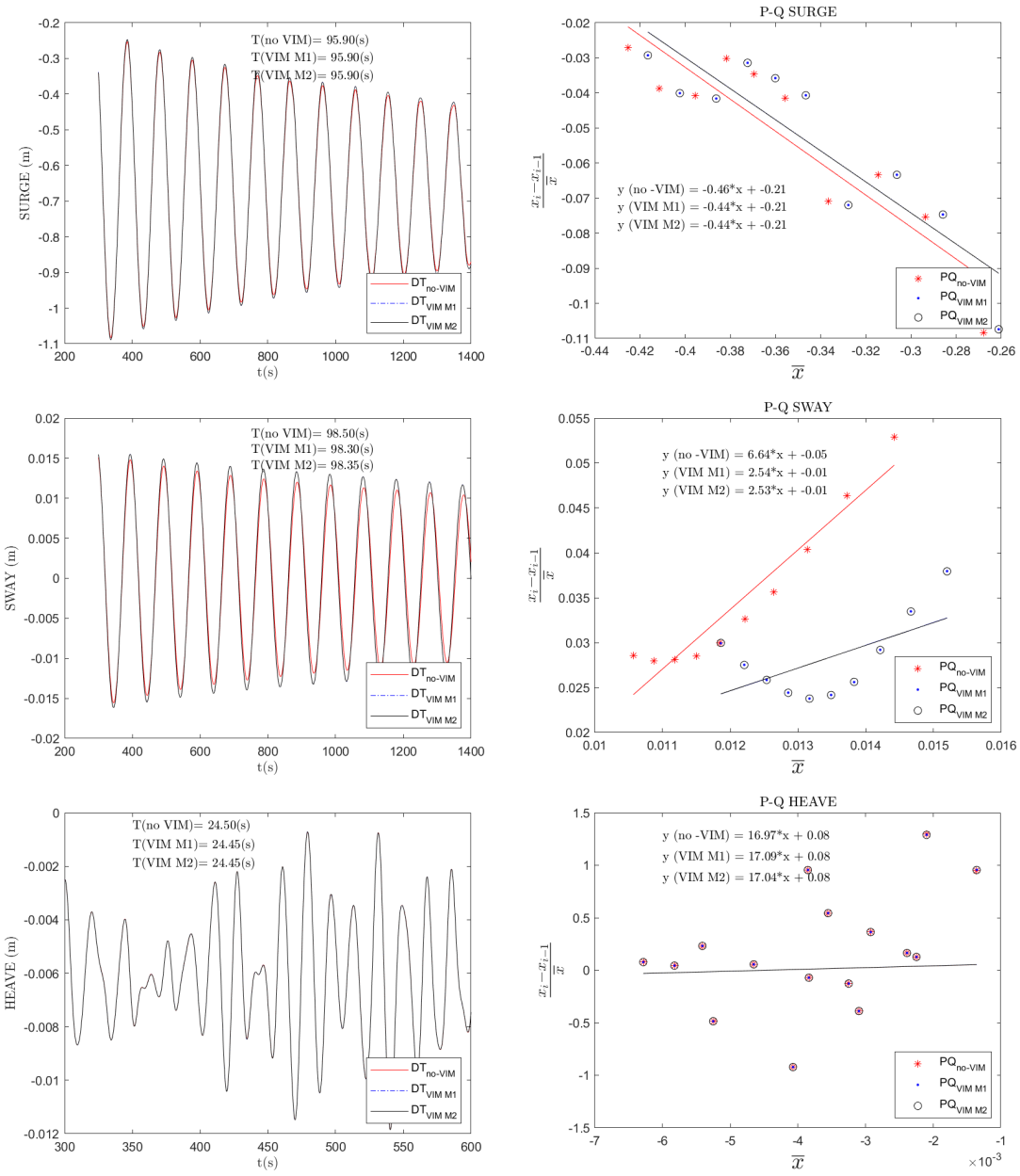

Figure 4.15: Damped frequency of translations and P-Q parameters from the 12MW SS-FOWT, for both models with and without TD-VIV

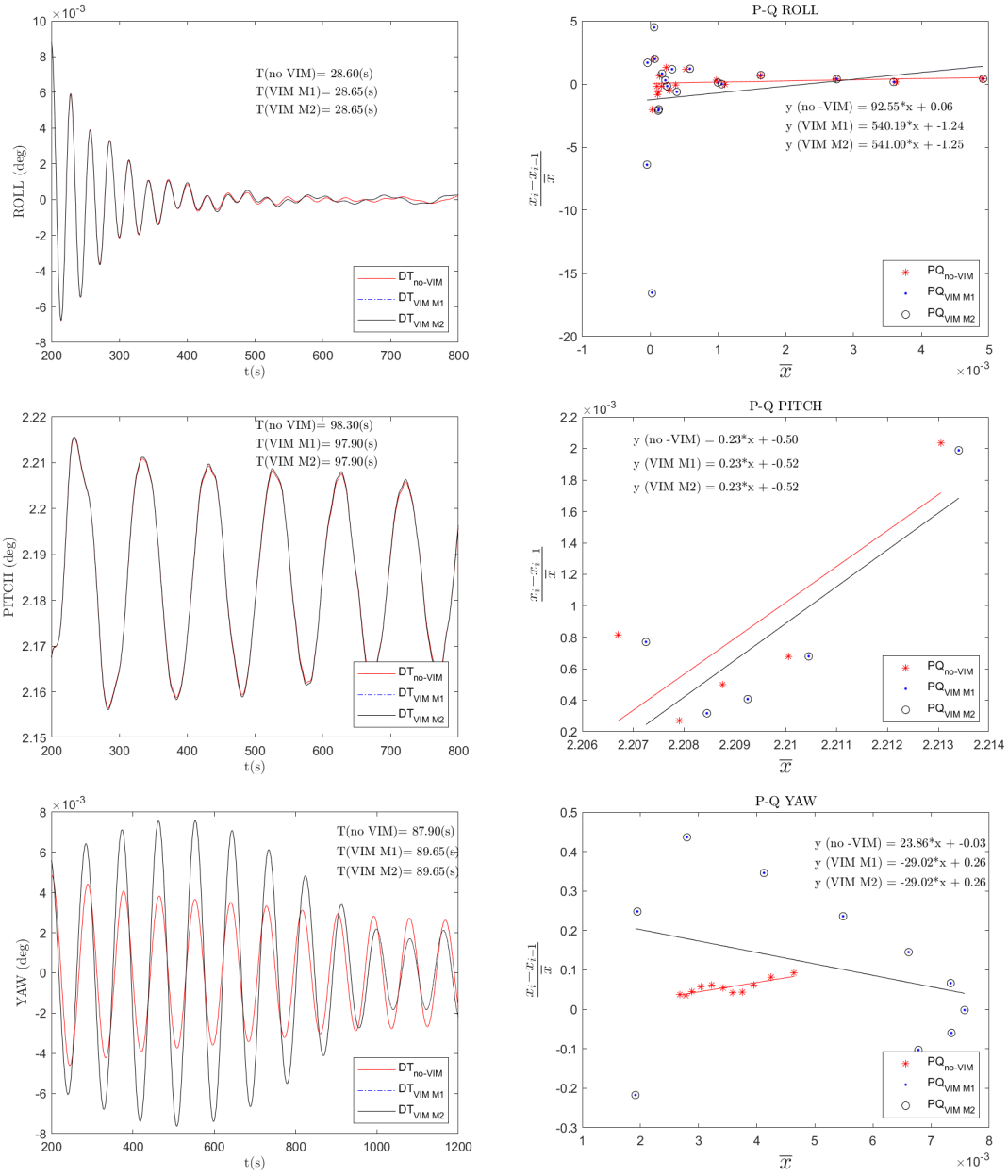

Figure 4.16: Damped frequency of rotations and P-Q parameters from the 12MW SS-FOWT, for both models with and without TD-VIV

quadratic damping in the system for all motions in the 6 DOF.

When the TD-VIV is considered, Surge and pitch experience variation in the linear damping. Whereas, for sway and yaw motions, quadratic damping is the one that experiences changes when vortex-shedding forces are considered. This is noticed in the slope of the P-Q curve, which decreased in both TD-VIV models.

Also, it is concluded that tangential drag doesn’t play a role in the VIM phenomenon, considering that under these environmental conditions, both models obtain very similar results in all motions.

Chapter 5

Laboratory Test

5.1 Model-Experiment to measure VIM response on a 12MW SS-FOWT

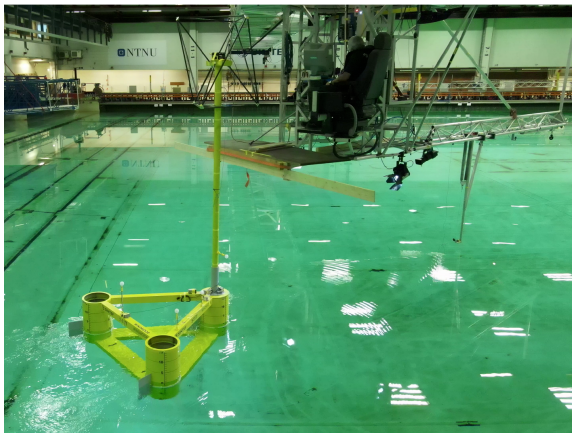

Figure 5.1: Experiment carried out in Ocean Basin during January 2024. Figure from[41]

SINTEF Ocean experimented in January 2024 with measuring the structure's response of a SS-FOWT at model scale (1:40). The experiment aims to analyse the VIM effect on the platform, and the consequence of the current direction. Also, it may be possible to study the interference between the three columns on the VIM effect. Further, the model test data will be used to validate numeral tools [41].

The experiment was carried out in the Ocean Basin, which is 80 m in length, 50 m in width, and a maximum depth of 10 m, which can be adjusted from 0 to 8.7 m, above the concrete floor of the basin. The towing tank counts with wave makers in both directions, transversal and longitudinal. The transversal unit is a hydraulic double flap (BM2), capable of generating long-crested irregular waves, as well as regular waves.

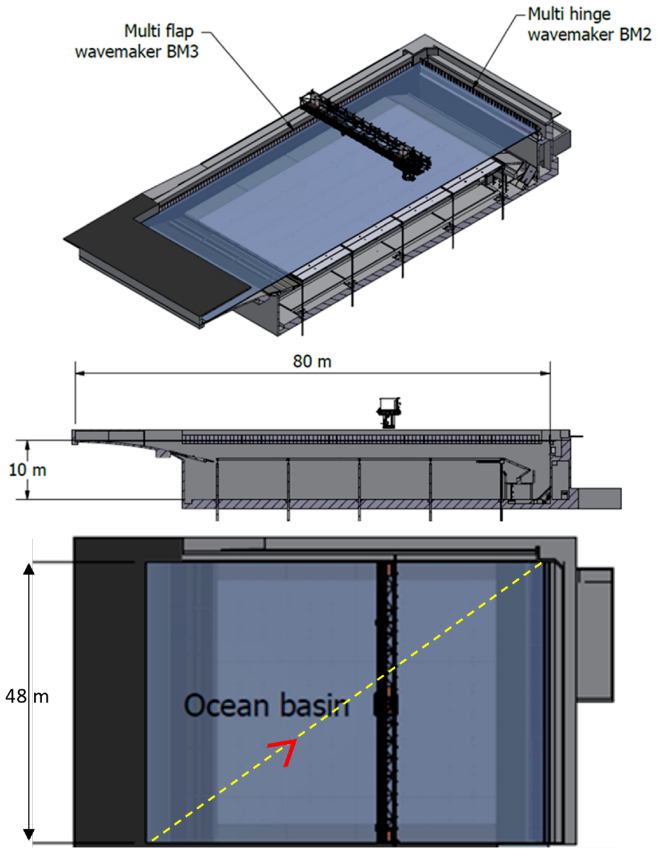

Figure 5.2: Main dimension of Ocean Basin Towing Tank, and towing trajectory of the model during the experiment. Figure from[41]

On the other hand, along the towing tank is found a multi-flap wave-maker (BM3), capable of generating short crested waves and oblique long-crested waves, by using 144 individual controlled flaps. Wave reflection is less than 5 $\%$ of the amplitude of the incoming waves, thanks to the parabolic wave absorption beaches along both, the long and short basin sides [41]. Figure 5.2 shows the main characteristics of the towing tank and the towing trajectory to measure the structure's response.

During the experiment, the wind turbine was towed in the diagonal direction of the towing tank, at velocities that match the VIM effect. During the experiment wind and waves were neglected, and the towing speed was considered constant.

5.1.1 Experimental Set-up

The test was done at 1:40 Froude scale. The main dimensions of the prototype, at full scale, are listed in table 5.1. The as-built condition is presented in table 5.2. It must be noticed that the model did not include the wind turbine during this test, therefore, the mass corresponds to the platform itself. Moreover, it was registered some differences in the main characteristics to the original semi-submersible, those values are listed in table 5.2.

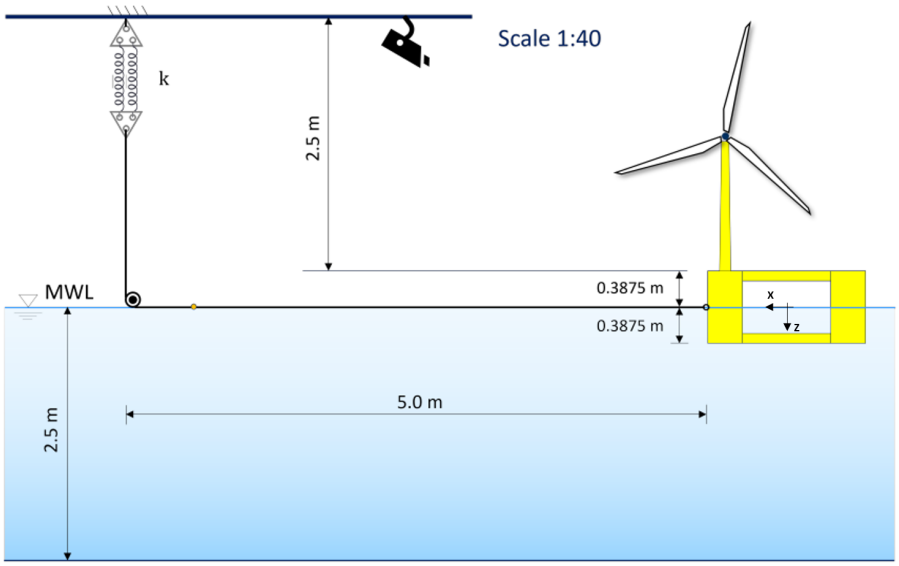

Figure 5.3: Experimental set-up of the INO WINDMOOR towing test and coordinate system. Figure from[41]

Parameter	Units	Value
Column diameter	(m)	15.00
Column height	(m)	31.00
Pontoon width	(m)	10.00
Pontoon height	(m)	4.00
Centre-centre distance	(m)	61.00
Deck beam width	(m)	3.50
Deck beam height	(m)	3.50
Draft	(m)	15.50
Column height ratio, H/D	-	2.07
Column distance ratio, L/D	-	4.07

Table 5.1: Main dimensions of the INO WINDMOOR prototype, at full scale. Data from[41]

Parameter	Units	Specified	As-built
Mass	(t)	11974	12129
COGx	(m)	-5.910	-5.800
COGy	(m)	0.000	0.000
KG	(m)	5.800	5.700
I_{xx}	(kg m^2)	6.703·10^9	6.664·10^9
I_{yy}	(kg m^2)	4.156·10^9	4.264·10^9
I_{zz}	(kg m^2)	9.455·10^9	9.684·10^9

Table 5.2: As-built condition of the INO WINDMOOR platform, at full scale. Data from[41]

Property	Unit	Full Scale	Model Scale
Tug's Bollard Pull	(t)	150	
Minimum Breaking Load (MBL) of bridle	(t)	340	0
Length between towing points	(m)	61.0	1.525
Apex angle	(deg)	60	60
Length of the bridle	(m)	61.0	1.525
WIRE (6x36- IWRC)			
d	(mm)	74.0	2.0
EA	(kN)	253461	3.86
Mass/Length	(kg/m)	21.9	0.0144
Single spring stiffness	(N/m)	-	261

Table 5.3: Specification of the towline and bridles. Data from[41]

The systems' origin was set up at the mean waterline and the geometrical centre of the platform. The Z-axis is pointed downwards and the X-axis coincides with the main wave and wind propagation direction (see figure 5.3). The prototype was towed in the diagonal direction of the towing tank in two different heading conditions (see figure 5.4).

Due to the towing conditions, two sets of towing line configurations were used during the experiment. The main dimensions at the model scale are presented in figure 5.5, and the equivalent configurations at full scale are presented in figure 5.6. For both configurations, the main towing line and bridles were steel wire.

It is shown in figure 5.3, that the towing configuration included two springs in the vertical direction of the towing carriage. Specification of the towline and bridles, as well as the material specification of the wire and springs are included in table 5.3

5.1.2 Instrumentation during experiment

The instrumentation included:

1. One Force transducer at the connection between the towing line and the WINDMOOR platform.

2. Reflexive markers at the platform and tower, for measurement of the motions using a motion tracking system, from cameras fixed at the basin.

3. One three-component accelerometer at the WINDMOOR platform.

4. Towing speed measurements from the towing carriage.

5.1.3 Natural Periods of the Wind Turbine

To start the towing test it was performed a decay test in the Ocean Basin to measure the natural periods of the platform, Table 5.4 shows those results.

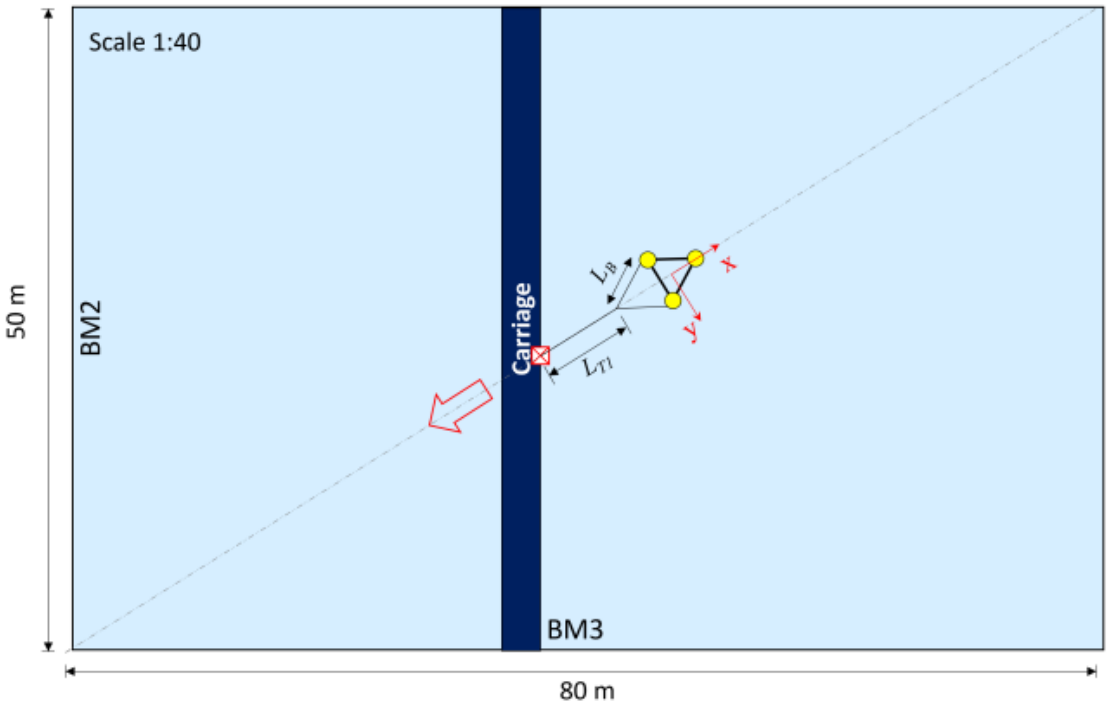

(a) $\alpha = 0°$.

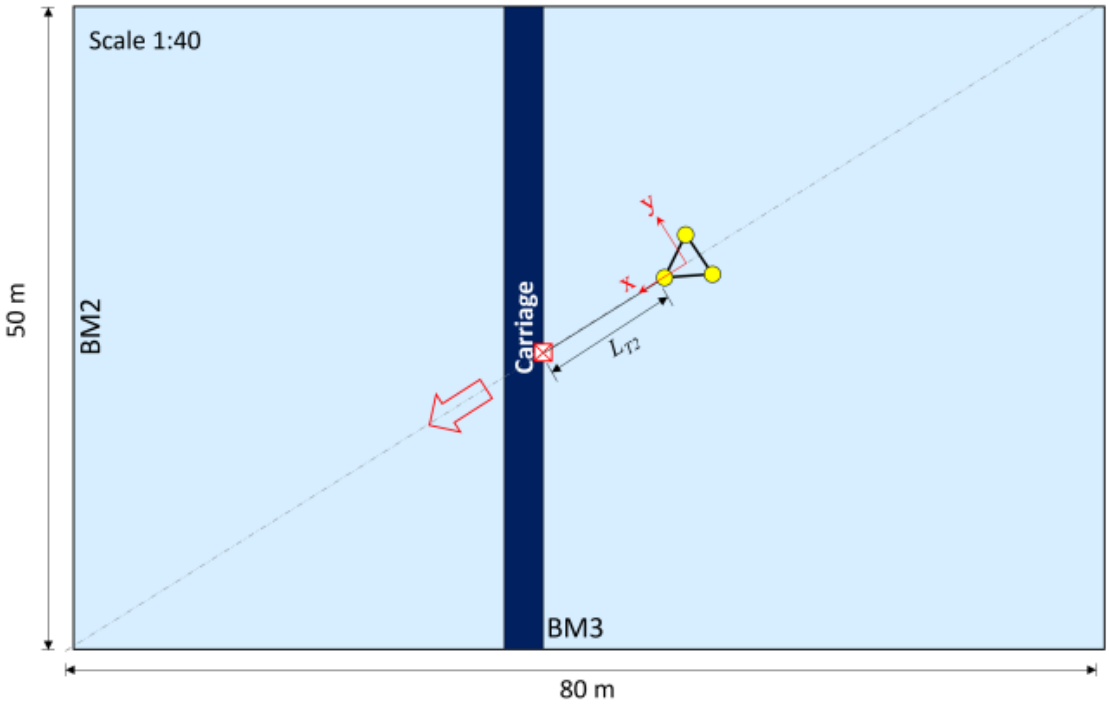

(b) $\alpha = 180°$.

Figure 5.4: Two towing heading conditions for measuring the VIM response. Figure from[41]

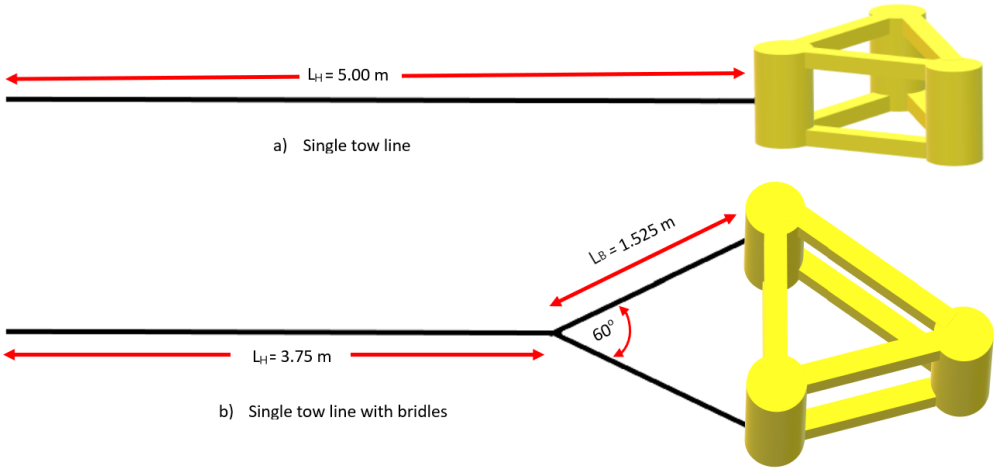

Figure 5.5: Towing configurations at model scale

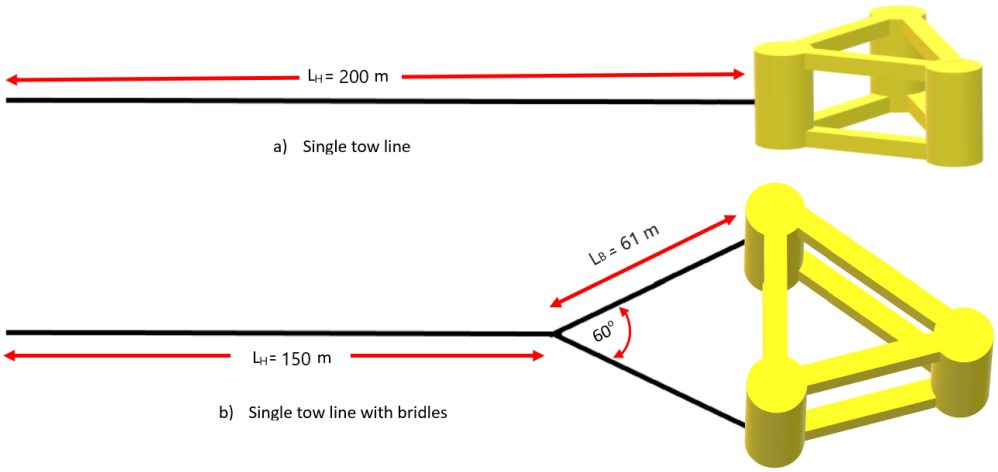

Figure 5.6: Towing configurations at full scale

DoF	Surge	Sway	Heave	Roll	Pitch	Yaw
T_n (s)	31.6	-	31.6	30.3	31.3	-

Table 5.4: Natural Periods of the Wind Turbine measured during the Towing test

5.1.4 Selecting the towing speed

Figure 2.9 shows the relationship between the Reynolds number and the Strouhal number. This relationship depends on the vortex-shedding frequency, the diameter of the cylinder, the surface roughness, and the stream velocity. The following considerations were taken into consideration for the towing velocity selection.

- The platform is composed of three columns with smooth surface.
- A first approximation of the vortex shedding frequency is to reach the same value as the natural frequency. The wind turbine's natural periods were measured during the towing test (see Table 5.4).
- Although there are three columns and three pontoons, it is considered that the Strouhal number will be between 0.2 and 0.3 for Re $2 \cdot 10^7$, similar Strouhal tendency as mono-cylinders showed in figure 2.9

Table 5.5 shows the approximated towing velocity at full-scale (U_F), under two conditions of Strouhal number, 0.2 and 0.3, it is also including the corresponding Reynolds number.

	Damped period s	Frequency Hz	$U_F = \frac{D \times f}{St_{0.2}}$ m/s	Re -	$U_F = \frac{D \times f}{St_{0.3}}$ m/s	Re -
Surge	31.60	0.032	2.373	$3.18 \cdot 10^7$	1.582	$2.12 \cdot 10^7$
Heave	31.60	0.032	2.373	$3.18 \cdot 10^7$	1.582	$2.12 \cdot 10^7$
Roll	30.30	0.033	2.475	$3.31 \cdot 10^7$	1.650	$2.21 \cdot 10^7$
Pitch	31.30	0.032	2.396	$3.20 \cdot 10^7$	1.597	$2.14 \cdot 10^7$

Table 5.5: Approximation of the towing velocity at full scale

$$U_M = U_F \sqrt{\frac{L_M}{L_F}} = \sqrt{\frac{1}{40}} \cdot U_F \tag{5.1}$$

A Froude scaling method shows a decrement in the full-scale velocity by a factor of 0.158. For practicality, the towing velocities at full-scale were selected between 0.9 m/s and 3.0 m/s. Experimental results are shown in the following chapters.

Chapter 6

The New Towing model in SIMA

6.1 Main consideration for the new model

The towing experiment was done at model scale, afterwards, the results were scaled up to full-scale, to allow the comparison with the full-scale model in SIMA. The initial model in SIMA of the 12MW INO WINDMOOR was changed according to the following considerations to match the conditions of the towing experiment.

- The towing speed was simulated with a constant current profile in the X direction. To simulate the two towing conditions, the direction of the current is modelled as follows: 180^o for the Single-Line (SL) towing condition and 0^o for the Two-Bridle towing experiment.
- SIMA models the current as a constant value over time, therefore the initial transient effect experienced by the platform during the test was not able to be modelled.
- In SIMA, the arrangement of the initial anchoring lines was changed to represent the towing line of the experiment (see Figure 6.1).
- The towing line was modelled as a single bar element, with the same dimensions, and material characteristics used during the test (see Table 5.3).
- At the end of the anchoring line, the boundary conditions were full-fixed at the water level (z=0), to simulate the same conditions as the towing experiment.
- Due to the towing configuration, it was necessary to find an equivalent stiffness to match the model in SIMA with the experiment, mathematical formulation is found in Section 6.1.1.
- There are some differences between the full-scale experimental dimensions and SIMA model, in the Two-Bridle configuration (see Table 6.1), this was considered for the stiffness in the towing line.
- The towing line was set with stiffness damping axial factor 1, and hydrodynamic parameters were turned off, to prevent interaction in the towing line which was at the water surface.
- Due to some limitations in SIMA, it was necessary to use a fictitious line with small stiffness,

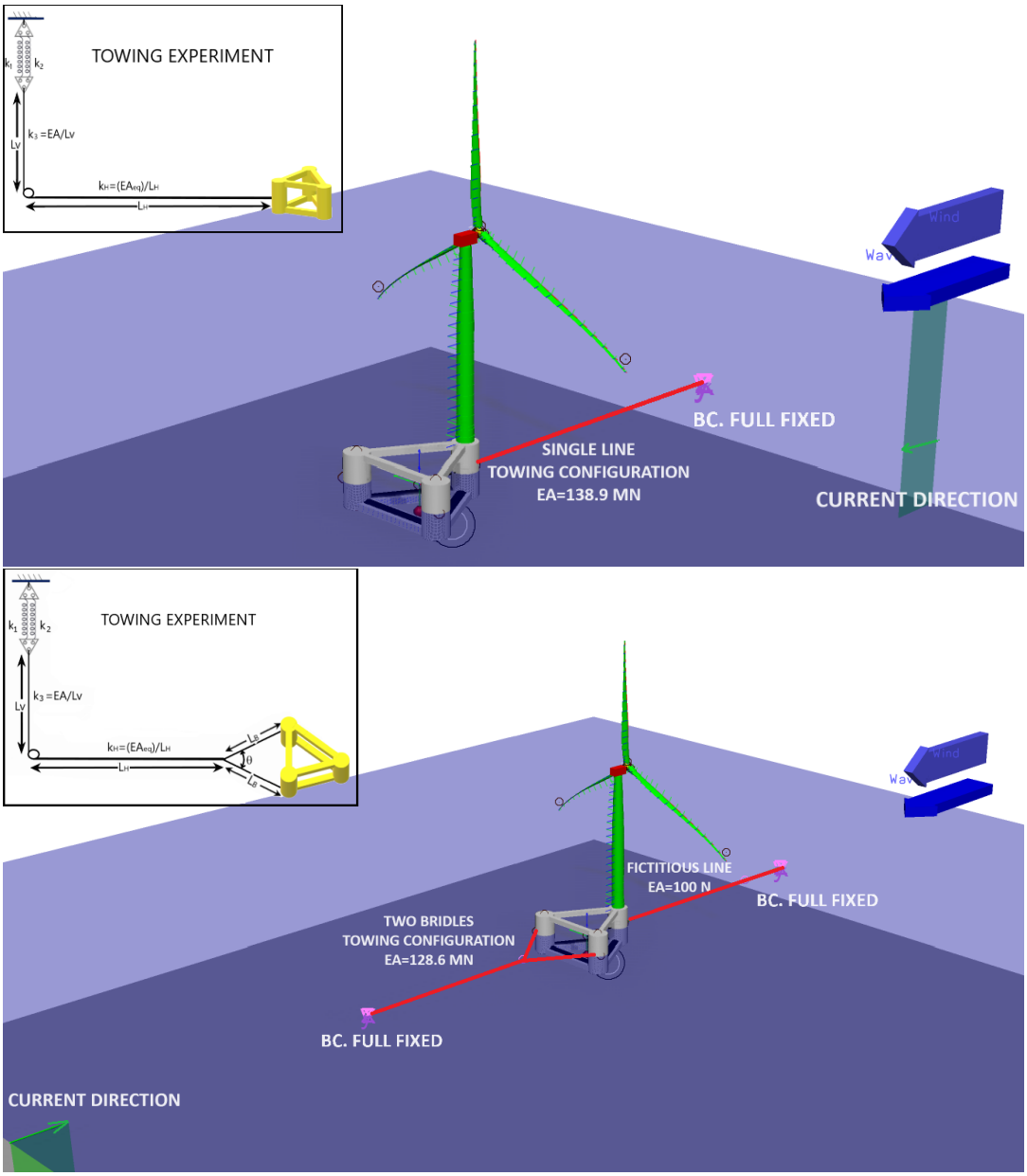

Figure 6.1: SIMA model of the 12MW SS-FOWT for the two towing configurations.

to model the Two-Bridle Towing condition. The tension in the fictitious line was controlled during each simulation, achieving values lower than 10 N, small enough to assume that this line was not influencing the results.

- During the analysis it was noticed that results from SIMA were influenced by the drag in the pontoons, amplifying the expected results in both, motions in the 6DOF, and tension. Therefore, linear and quadratic drag coefficients were set up as zero for both columns and pontoons in the SIMO-BODY. The drag effect in columns is considered in the TD-VIV model.
- The model included a new reference point, coinciding with the accelerometer position, which was placed at the basement of the platform, and the geometric centre. The reference point was simulated as a fictitious SIMO-BODY with zero mass and zero volume, with a slave connection to the system's reference point.

6.1.1 The equivalent stiffness.

During the experiment, two springs were connected between the carriage and the wind turbine. Therefore, each towing configuration requires finding an equivalent stiffness for the towing line. In SIMA, the equivalent stiffness is represented by the anchoring line's axial rigidity (EA). Figure 6.2 shows the connection of both configurations to the towing carriage and the equivalent spring connection diagram.

The system's equivalent stiffness is based on Newton's Law formulation, including the relationship between in-parallel and in-series springs. To achieve an approximation of the system's stiffness at full-scale, a lambda parameter (λ) is included in the formulation as follows:

- The net vertical force (F_V) includes the effect of the two in-parallel springs and the axial stiffness of the vertical wire.
    - At model-scale, the net force (F_{12}) and the equivalent stiffness (k_{12}), due to the two in-parallel springs with stiffness k_1 and k_2, are defined by:

$$F_{12} = -x_{12} \cdot k_{12}$$

$$k_{12} = k_1 + k_2 \tag{6.1}$$

      In Table 5.3, the material specifications shows that both springs have similar characteristics ($k_1 = k_2 = 261N/m$), therefore $k_{12} = 522N/m$.
    - The vertical wire is considered a bar element, allowing axial loading. The axial stiffness of the wire (k_3) is defined as:

$$k_3 = \frac{EA}{L_V} \tag{6.2}$$

      Where L_V is the length of the vertical wire of the towing experimental configuration.

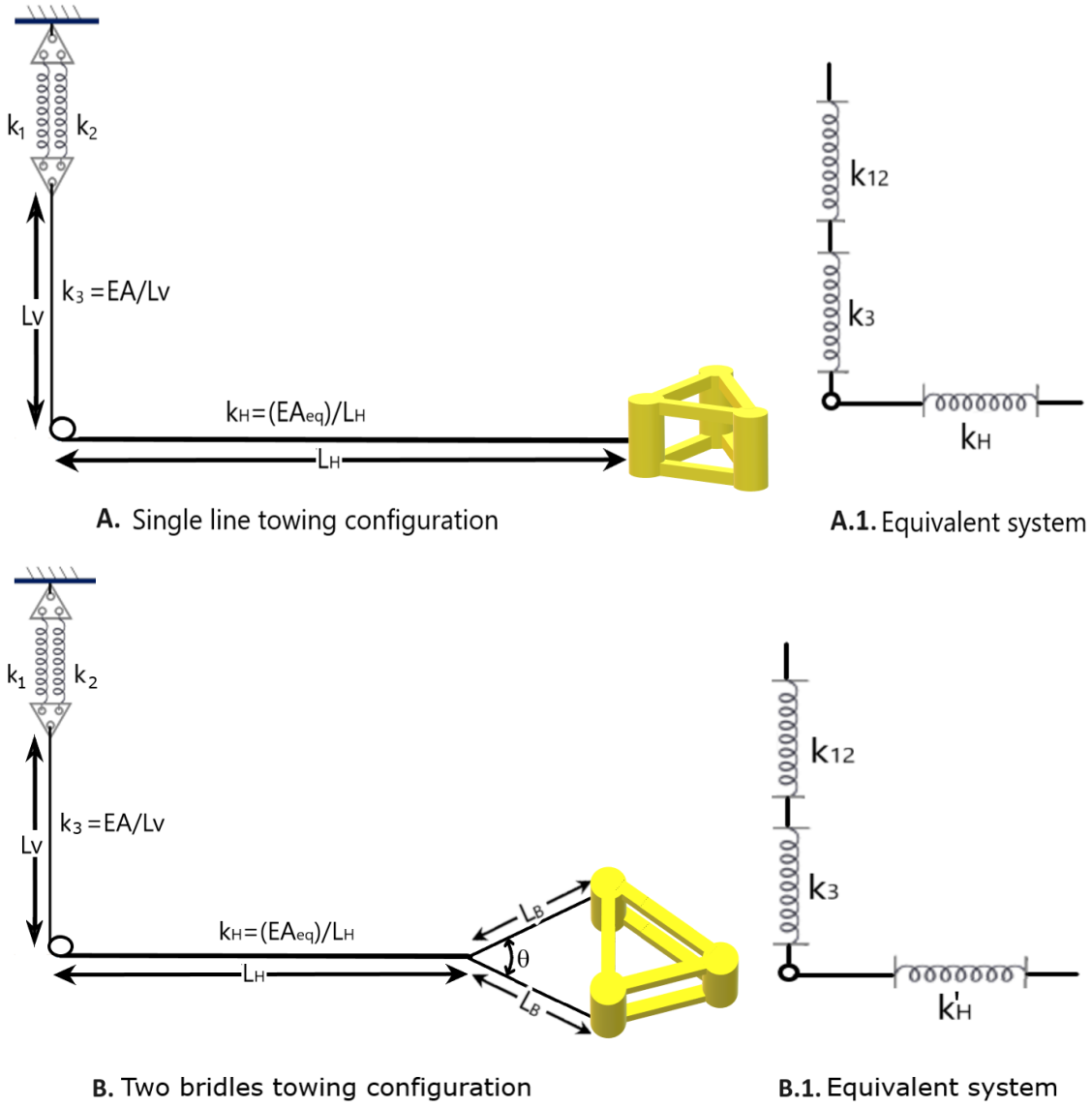

Figure 6.2: Connection between the wind turbine and the carriage during the experiment. The figure shows the equivalent system modelled as in-parallel/in-series springs connection.

This length was not registered during the towing experiment but has been defined as 60$\%$ of the total vertical length (L=2.8875 m). As result L_V=1.7325 m, and $k_3 = 2227.99N/m$ at model scale.

- To account for the axial stiffness of the wire (k_3), the system can be simplified as an in-series arrangement, between the two springs and the wire. The net vertical force (F_V) and the equivalent stiffness (k_V) of the vertical line, are defined as follows:

$$F_V = -x_V \cdot k_V$$

$$(k_V)_M = \frac{2(k_{spring}) \cdot k_{vert-wire}}{2(k_{spring}) + k_{vert-wire}} \tag{6.3}$$

The equivalent stiffness in the vertical direction at the model scale is $(k_V)_M = 422.9N/m$.

- It is assumed that the towing force in the horizontal direction is the same magnitude as the net vertical force. This is a reasonable assumption since the towing velocity is almost constant in the time window that was chosen for the analysis. Also, since the same wire was used along the connection, between the springs and the wind turbine, the same deformation is achieved in the horizontal and vertical directions. Consequently, the equivalent stiffness in the horizontal direction (k_H) will be similar to the equivalent stiffness in the vertical direction.

$$(k_V)_M = (k_H)_M \tag{6.4}$$

- For a system with a single towing line, the relationship between the stiffness at model-scale (k_M) and full-scale (k_F).

$$\frac{k_F}{k_M} = (\lambda)^{-1} \frac{(EA)_F}{(EA)_M} \tag{6.5}$$

Where $\lambda = L_F/L_M = 40$. Equation (6.5) shows the connection between both geometrical and material characteristics when the model is scaled up according to the Froude formulation.

- Using the previous equation, at full scale the equivalent stiffness in the horizontal direction (k_H), will be :

$$(k_H)_F = (k_H)_M \cdot (\lambda)^{-1} \frac{(EA)_F}{(EA)_M} \tag{6.6}$$

$$(k_H)_F = \frac{(EA_{eq})_F}{(L_H)_F} \tag{6.7}$$

Where (EA_{eq}) is the equivalent axial rigidity of the towing line in the horizontal direction and L_H is the length of the horizontal towing wire. Considering Equation (6.4),

Equation (6.6), and Equation (6.7), at full scale the equivalent axial rigidity becomes:

$$(EA_{eq})_F = (k_V)_M \cdot (\lambda)^{-1}(L_H)_F \cdot \frac{(EA)_F}{(EA)_M}$$

At full-scale $L_H = 200m$. Also, this equation can be rewritten as follows:

$$(EA_{eq})_F = (k_V)_M \cdot (L_H)_M \cdot \frac{(EA)_F}{(EA)_M}$$

In SIMA, the equivalent rigidity for a Single-Line towing condition is $(EA_{eq})_F = 1.389 \cdot 10^8 N$

- Similar analysis is carried out for the Two-Bridle towing condition, as follows:
  - The length of the single horizontal towing line is defined as L_H.
  - The length of the bridles (L_B) is assumed to be the same for both lines.
  - θ is the angle between the bridles.
  - The bridles are considered to be as in-parallel springs connected in-series to the horizontal wire. Therefore, the correspondent equivalent stiffness at the model scale of the horizontal towing line is defined by:

$$(k'_H)_M = EA \left[\frac{\frac{1}{L_H}\left(\frac{2\cdot\cos(\theta/2)}{L_B}\right)}{\frac{1}{L_H} + \frac{2\cdot\cos(\theta/2)}{L_B}} \right] = \frac{EA}{(L'_H)_M} \tag{6.8}$$

    where $(k'_H)_M$ is the horizontal equivalent stiffness and $(L'_H)_M$ an equivalent horizontal length, as a function of θ.
  - The relationship between the model and full-scale horizontal towing line, is defined as follows:

$$\frac{(k'_H)_F}{(k'_H)_M} = \frac{(L'_H)_M}{(L'_H)_F}\frac{(EA)_F}{(EA)_M} = (\lambda'_H)^{-1}\frac{(EA)_F}{(EA)_M} \tag{6.9}$$

    where (λ'_H) is the relation between full-scale and model-scale equivalent horizontal length in the Two-Bridle towing condition.
  - Assuming that the equivalent stiffness in the horizontal direction is similar to the stiffness in the vertical direction.

$$(k'_H)_M = (k_V)_M$$

    Then, the approximate equivalent axial rigidity at full-scale $(EA'_{eq})_F$ is:

$$(k'_H)_F = \frac{(EA'_{eq})_F}{(L'_H)_F} \tag{6.10}$$

$$\left(EA'_{eq}\right)_F = (k_V)_M \cdot (L'_H)_M \cdot \frac{(EA)_F}{(EA)_M} \tag{6.11}$$

The towing equivalent rigidity in both conditions depends on the arrangement of the vertical connection and the arrangement of the horizontal connection.

The position of the fairleads was different in SIMA's model in comparison to the full-scale test, therefore it was decided to keep the length of the horizontal towing line and the length of the bridle, but the angle between the bridles differed from the experiment. The system's equivalent length and the axial rigidity of the Two-Bridle towing condition are calculated as follows:

	$L_H(m)$	$L_B(m)$	$\theta(deg)$	$(L'_H)_F$ (m)	$EA_{eq}(N)$
Experimental data (full-scale)	150.00	61.00	60.00	185.22	$1.286 \cdot 10^8 N.$
SIMA	150.00	61.00	74.70	188.36	$1.286 \cdot 10^8 N.$

Table 6.1: Equivalent length and axial stiffness considering the geometrical arrangement during Experiment and SIMA model.

In SIMA, the equivalent rigidity for the Two-Bridle towing condition is $(EA'_{eq})_F = 1.286 \cdot 10^8 N.$

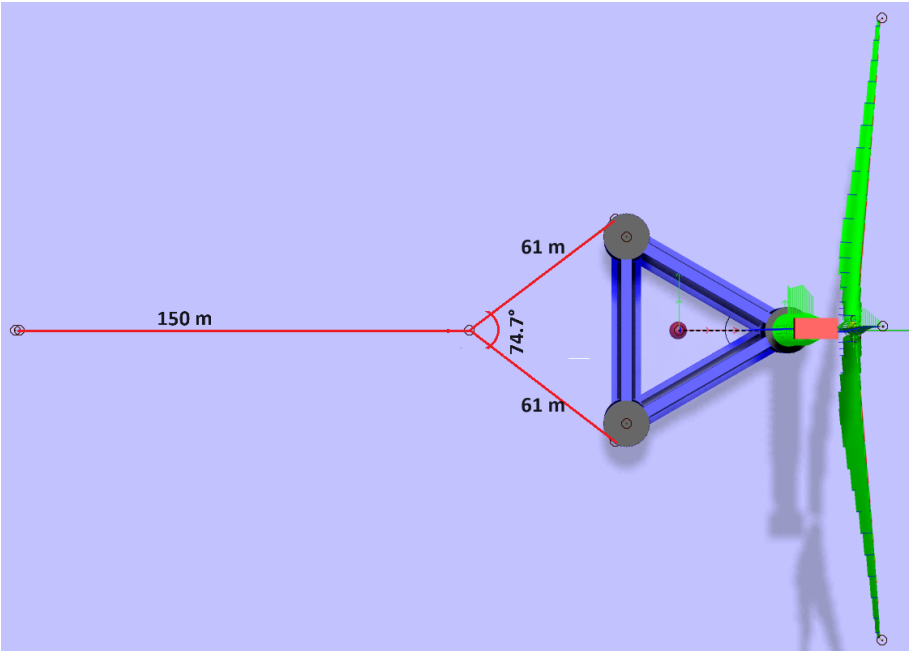

Figure 6.3: SIMA model of the 12MW SS-FOWT for the Two-Bridle (2B) towing configuration.

6.1.2 Approximation of the Towing Frequency

The platform is free to move and is expected to undergo 6DOF motions, Moreover, during the towing condition, the platform also experienced a pendulum behaviour in the x-y plane due to the type of 'anchoring'. Parameters such as the mass of the platform, the added mass effect in

the transversal direction, and the equivalent stiffness of the towing line, influence the system's period, as follows:

$$T = 2\pi\sqrt{\frac{(m + m_a)}{k}} \tag{6.12}$$

To approximate the period, the platform's mass was considered equal to the as-built full-scale condition of the experiment (see Table 5.2). On the other hand, the added mass under our interest is in the transversal direction $(m_a)_{22}$ and it is expected to be approximate as the values presented in the added mass matrix in Table 4.7.

It is important to remark that added mass values in Table 4.7 correspond to the complete wind turbine modelled in SIMA, therefore to approximate the towing frequency, the added mass in the transversal direction was established as 85% of the value shown in the matrix. This assumption represents an important uncertainty in the analysis.

	$m(kg)$	$(m_a)_{22}(kg)$	$EA_{eq}(N)$	$(L'_H)_F(m)$	$k(N/m)$	$T(s)$	$f(Hz)$
Single-Line	$1.21 \cdot 10^7$	$4.60 \cdot 10^6$	$1.389 \cdot 10^8$	200.00	$6.945 \cdot 10^5$	30.84	0.0324
Two-Bridle	$1.21 \cdot 10^7$	$4.60 \cdot 10^6$	$1.286 \cdot 10^8$	185.22	$6.943 \cdot 10^5$	30.84	0.0324

Table 6.2: Approximate Towing frequency in the two towing conditions.

The frequency in both towing conditions is approximately similar (0.0324 Hz).

6.2 Establishing parameters of the new TD-VIV model.

SIMA documentation [35] includes information about some VIV parameters used in different models. This information was considered as a source of information to calibrate the model. The suggested VIV empirical parameters are for Bare Risers sections and Bare Risers with buoyancy elements, under constant current subjected to pure CF-VIV phenomenon. The VIV parameters are listed in Table 6.3.

STRUCTURE TYPE	CV_{CF}	CQ_Y	CA_Y	FNULL	FMIN	FMAX
Bare Riser	1.3	1.0	1.0	0.13	0.10	0.26
Bare Riser w/buoyancy section $(L_b/L_r = 1/2)$	1.2	0.9	1.0	0.18	0.10	0.22
Bare Riser w/buoyancy section $(L_b/L_r = 1/1)$	0.8	1.2	1.0	0.18	0.10	0.26

Table 6.3: Suggested VIV parameters for pure CF-VIV presented in SIMA. Information is from [35]

The non-dimensional parameters are described as follows:

- CQ_Y is the quadratic drag coefficient in the normal direction,
- CA_Y is the added mass per unit length in the normal direction,
- CV_{CF} is the vortex shedding force coefficient for the instantaneous CF load,
- FNULL is the natural CF vortex shedding frequency,
- FMIN is the minimum CF vortex shedding frequency,

- FMAX the maximum CF vortex shedding frequency.

Parameters used for modelling the towed wind turbine were chosen in the range of the suggested information, however, as mentioned before the added mass parameters are not included in the TD-VIV model since the added mass matrix is already included in the SIMO-BODY.

CQY	0.68 - 1.20
CV_{CF}	0.20 - 1.30
CV_{IL}	0.01 - 0.2

Table 6.4: Multi-variable parameters used in SIMA to assess the VIV phenomenon

The analysis for the towed wind turbine included CF-VIV and the combined CF/IL-VIV. Pure CF effect is represented with CV_{IL}=0.01 since those values are completely similar to outcomes with CV_{IL}=0.

It is important to remark that is expected IL frequency doubles the CF frequency in a combined CF/IL-VIV phenomenon, thus the SIMA model follows this principle.

	FREQ (1)	FREQ (2)
CF	fnull=0.13;fmin=0.10;fmax=0.26	fnull=0.18;fmin=0.10;fmax=0.22
IL	2*$FREQ_{CF}$	2*$FREQ_{CF}$

Table 6.5: Frequencies used in SIMA to assess the VIV phenomenon

6.2.1 Analysis to establish parameters in the TD-VIV model

This was a multi-variable analysis with the parameters as presenting Table 6.4 and Table 6.5. 3D plots were used to represent the influence of the CQ_Y and the CV_{CF} parameters, on the Towing Force, and amplitude of motions in CF and IL direction.

As mentioned in previous lines, the model in SIMA varied CQ_Y between 0.68 and 1.20, whereas CV_{CF} was between 0.2 and 1.3. In addition, two sets of IL vortex-shedding coefficients ($CV_{IL} = 0.01; 0.2$) were used to analyse the pure CF and combined CF/IL effect. Further, the analysis includes the effect of two different frequency ranges, presented in Table 6.5.

Initially, those parameters were tested at 2.0 m/s in the two towing conditions, to calibrate the model. In the second stage, the model was tested in the full range of velocities.

Figure 6.4 contains results at 2.0 m/s of the mean tension (Fm) whereas Figure 6.5, and Figure 6.6 show amplitudes of motion in both, CF and IL directions. Figures include a 3D plot in the upper part, while the bottom displays the same results in 2D, to visualise the influence of both parameters, i.e. CQ_Y and the CV_{CF} on the Towing Force, and amplitude of motion. The 2D plots include limiting curves that come from results during the towing test.

Figure 6.4 shows the mean Towing force F_m at 2.0 m/s. Looking at the 2D plot F_m vs CV_{CF}, the mean towing force increases as CV_{CF} increases, and for different CQ_Y this trend repeats.

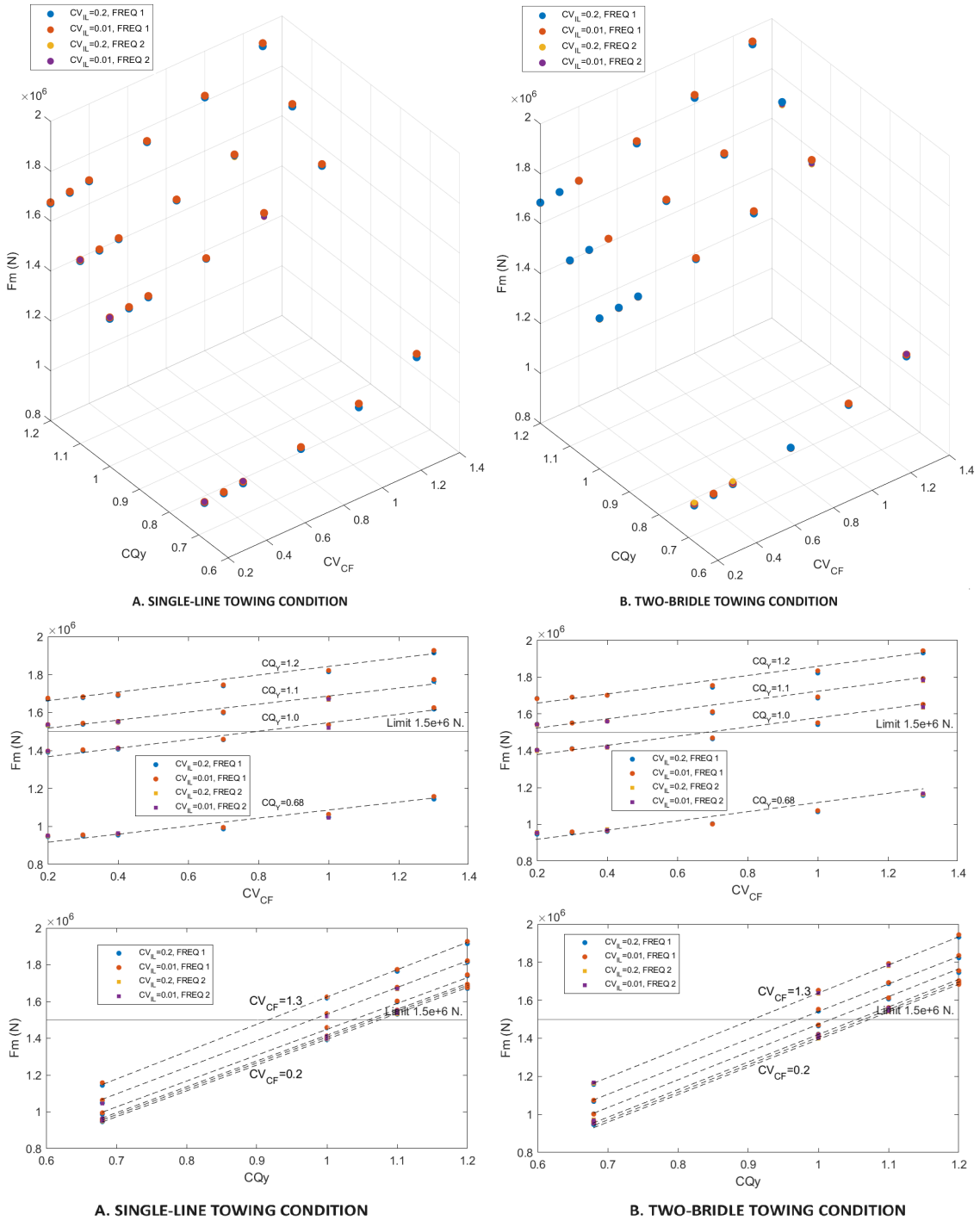

Figure 6.4: SIMA results for the Mean Tension force in two Towing conditions.

The 2D graph Fm vs CQ_Y showed a force response dominated by CQ_Y, this is noticeable with the steepest slope in the curve. The same trend repeats in the two towing conditions.

Since experimental results showed that the mean towing Force at 2.0 m/s is about 1.5 MN in both towing conditions, the limiting line exposes that CQ_Y is in the range of 1.0 and 1.1 to achieve the target mean force.

Figure 6.4 shows the Amplitude of motion in the CF direction. If we look at the graph A_{CF} vs CV_{CF}, the upper and lower limiting curves come from results during the towing test and the correspondent value from the tendency line (see Figure 7.16).

The plot shows a clear influence of the vortex shedding coefficient CV_{CF} in the amplitude in the CF direction. The impact of CV_{IL} is undetectable in this mode of motion, this is noticeable with similar results around the trend line. A similar effect is shown between the two types of frequency ranges.

From this graph, it was established the CV_{CF} in each towing condition. For the Single-Line (SL) condition, the range was set between 0.40 and 0.70, whereas for the Two-Bridle (2B) condition is within the range of 0.85 to 1.40.

Figure 6.6 shows the Amplitude of motion in the IL direction at 2.0 m/s. If we look at the graphs, the limit was set as 0.002 m for both towing conditions (see Figure 7.16), according to the towing test results.

The graph A_{IL} vs CV_{CF} indicates that CV_{IL}= 0.01 achieved the smallest amplitude response in several conditions. Therefore, it was established CV_{IL}= 0.01. It is important to mention that results for pure CF-VIV showed identical results to values at CV_{IL}= 0.01.

Then, the model was tested at different current speeds with the next range of parameters.

	Single-Line towing condition	Two-Bridle towing condition
CQ_Y	1.00 - 1.10	1.00 - 1.10
CV_{CF}	0.40 - 0.70	0.85 - 1.40
CV_{IL}	0.01	0.01
$FREQ_{CF}$	FREQ(1)	FREQ(1)
$FREQ_{IL}$	2*FREQ(1)	2*FREQ(1)

Table 6.6: Parameters on the SIMA model to assess the VIV phenomenon

Models in SIMA were tested with three values of CV_{CF} within the range established in Table 6.6, whereas CQ_Y varied from 1.0 to 1.1.

Figure 6.7 compares results from SIMA and experimental data, under current velocities from 0.90 to 3.00 for Single-Line (SL) towing conditions.

Results from the towing force showed a good agreement between the experimental and SIMA results. Nevertheless, the amplitude of motions does not fit the tendency line neither in the IL direction nor CF.

CF motions display two important facts, the first is that different parameters can get similar

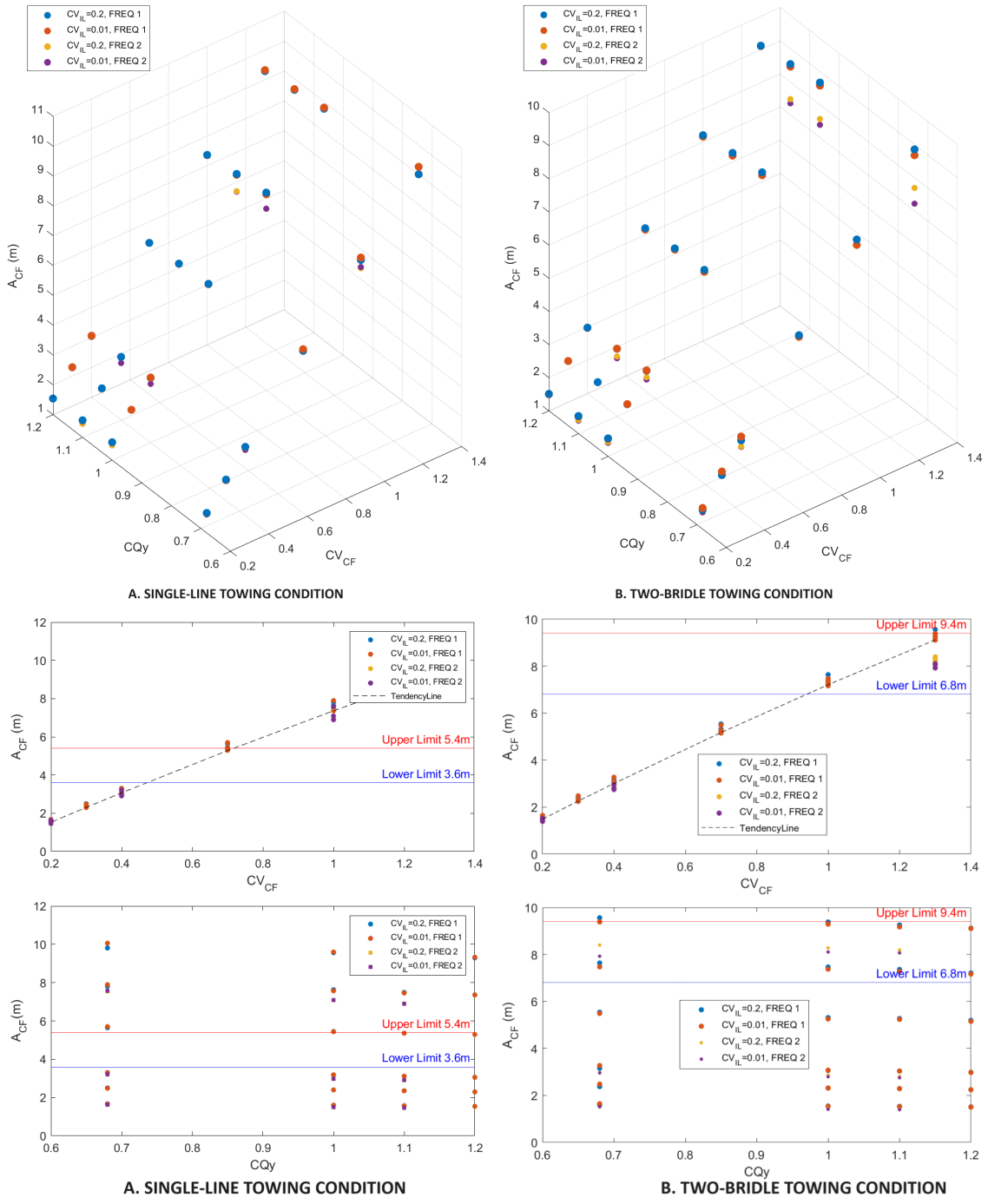

Figure 6.5: SIMA results for the Amplitude of motion in CF direction.

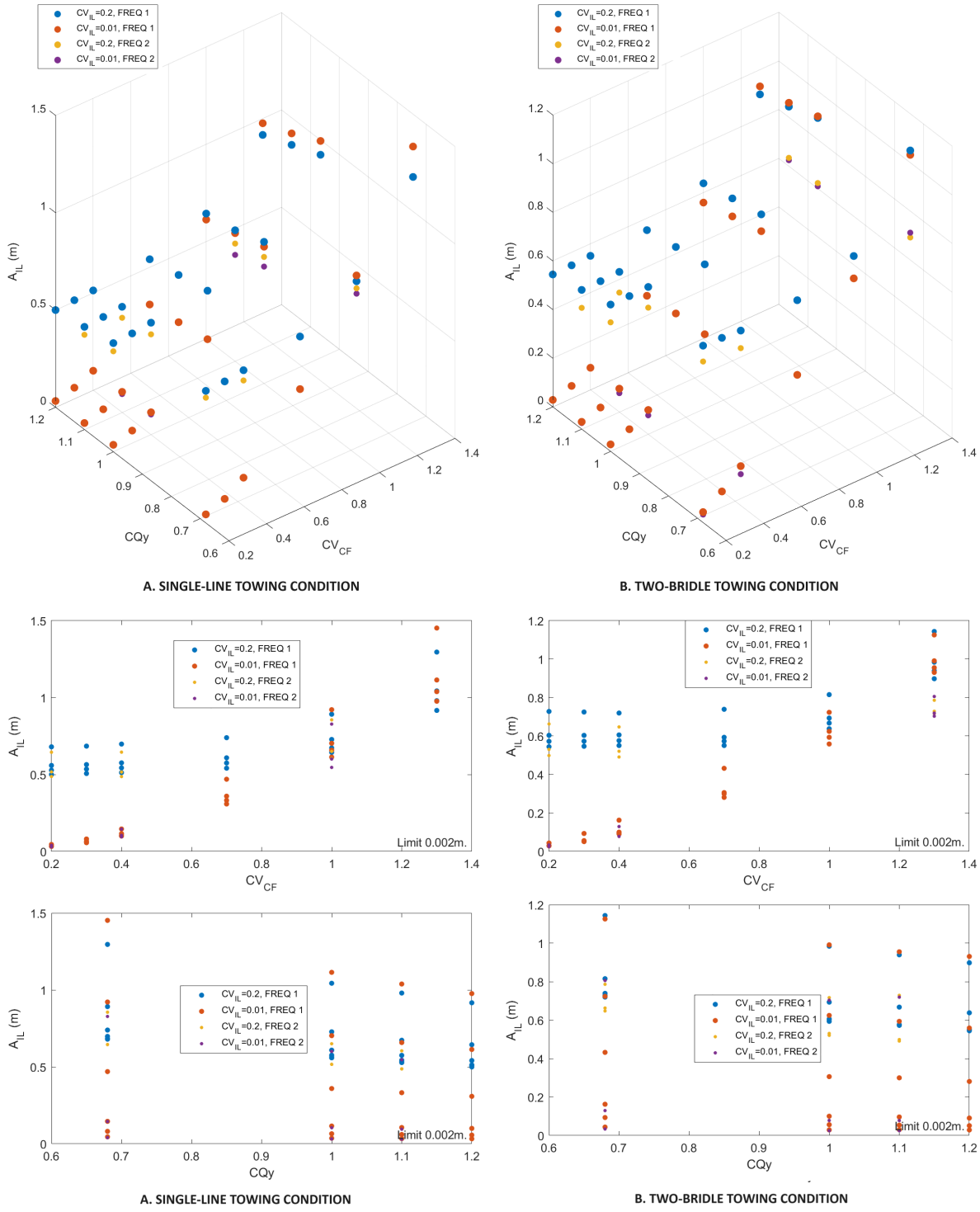

Figure 6.6: SIMA results for the Amplitude of motion in IL direction.

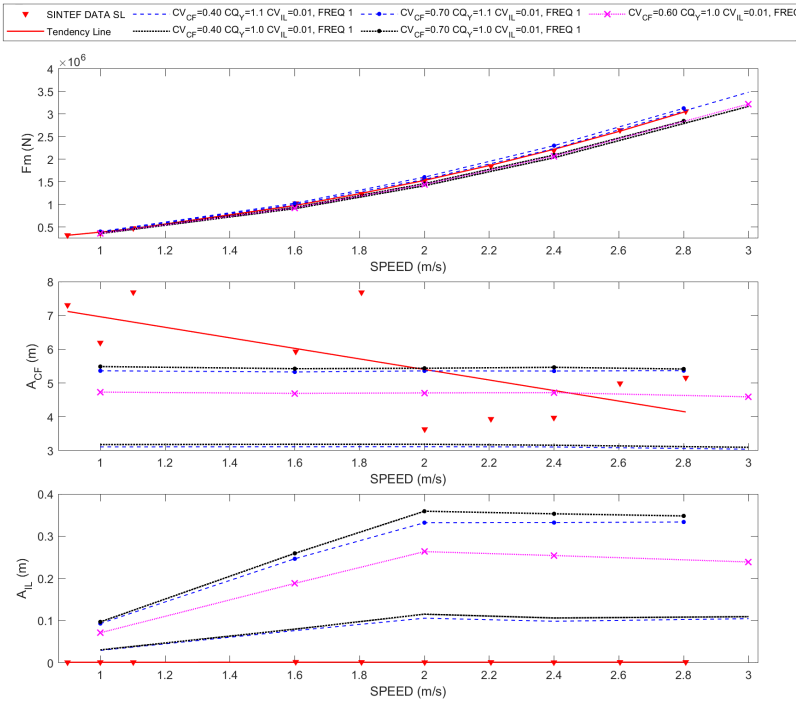

Figure 6.7: Selection of the main parameters for the TD-VIV model in Single-Line (SL) towing conditions. Results are compared against experimental data.

results. This is noticed in the two constant upper lines of the A_{CF} graph (see Figure 6.7 and Figure 6.8), with different CQ_Ys, results look similar.

The second fact is that the amplitudes of motions in the CF direction are almost constant within the range of velocities. Although SIMA results don't fit the tendency line we can observe that scatter values have similar tendencies in some range of velocities.

Motions in the IL direction reveal that SIMA overestimated the IL response. However, for our purpose, the IL response is not considered for further analysis since results from laboratory tests were smaller than 2 mm.

Figure 6.8 compares results from SIMA and experimental data, under current velocities from 0.90 to 3.00 for the Two-Bridle towing conditions. Results displayed similar tendencies as in Single-Line (SL) towing conditions.

Finally, the TD-VIV models were defined by the parameters presented in Table 6.7.

	Single-Line towing condition	Two-Bridle towing condition
CQ_Y	1.10	1.00
CV_{CF}	0.70	1.40
CV_{IL}	0.01	0.01
$FREQ_{CF}$	FREQ(1)	FREQ(1)
$FREQ_{IL}$	2*FREQ(1)	2*FREQ(1)

Table 6.7: Selected parameters for the TD-VIV model of the towing experiment.

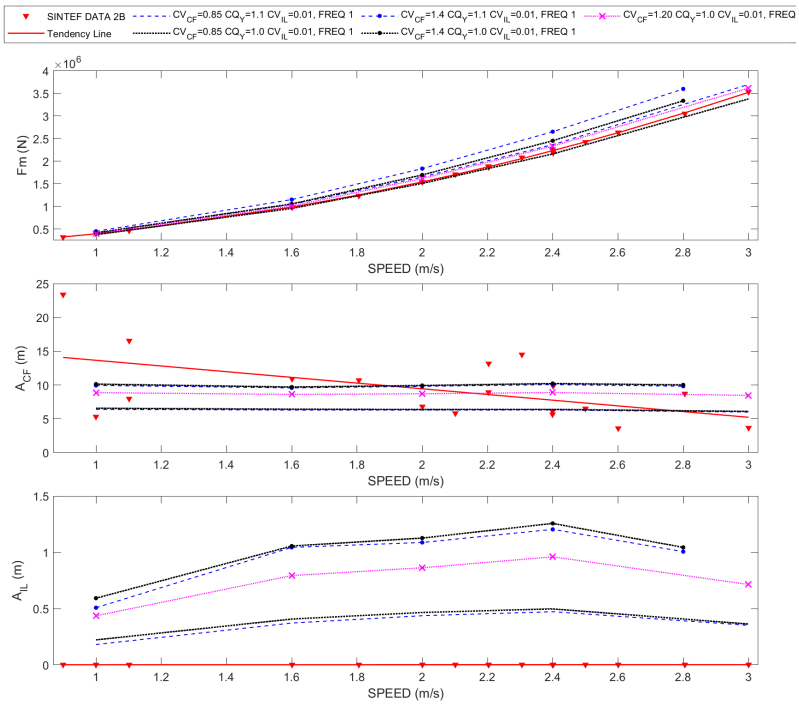

Figure 6.8: Selection of the main parameters for the TD-VIV model in Two-Bridle (2B) towing conditions. Results are compared against experimental data.

6.3 Decay test in SIMA for the TD-VIV Towing model

It was performed a decay test in SIMA to compare the natural periods of the platform. Results are presented for Surge, and Roll in Table 6.8.

DoF	SINTEF	SIMA	Deviation
Surge	31.6	37.2	17.7%
Roll	30.3	28.9	4.6%

Table 6.8: Natural Periods of the Wind Turbine from the Towing Test in comparison to SIMA results

Chapter 7

Results and Discussion

7.1 Experimental Results

Experimental data used to study the VIM effect includes the x,y, and z positioning data, rotations around the x,y, and z direction, tension in the towline, and speed of the prototype during towing. Those parameters were measured in time steps of 0.0316 seconds.

Figure 7.1 show the time series diagrams of the towing force, the towing speed, and motions in the 6DOF for a mean towing speed of about 2.0 m/s, results are for the Single-Line (SL) towing condition. Figure 7.2 displays values for the Two-Bridle (2B) towing condition. Appendix C and Appendix D contain results at different speeds.

SINTEF provided the results in two sets. The first set included the results of the full experiment, while the second set contained data within a selected time window. The time-window selection was based on the speed diagram, initiated after the platform reached the mean target speed, and finalised before decreasing the speed to stop the test.

In Figure 7.1 and Figure 7.2, the full range of data is presented on the left side of the graphs, where the two dotted red lines show the time window selection. On the right side of the plot is shown the selected data. The following points were considered during the processing of the towing experiment's results:

- The data used for the VIM analysis corresponds to the selected data within the time window.
- Figure 5.4 evidence that the X-axis coincided with the direction of the towing velocity, therefore the original data in the X direction, required a deduction of the equivalent displacement due to the towing velocity to get the real displacement in the X direction.
- According to the measurements, once the platform reached the target speed, the velocity showed small fluctuations, with a standard deviation less than 3% in all conditions. Therefore, this thesis considers the towing velocity as a constant value during each experiment.
- After processing the data, the towing speed is referred to as current velocity indistinctly.

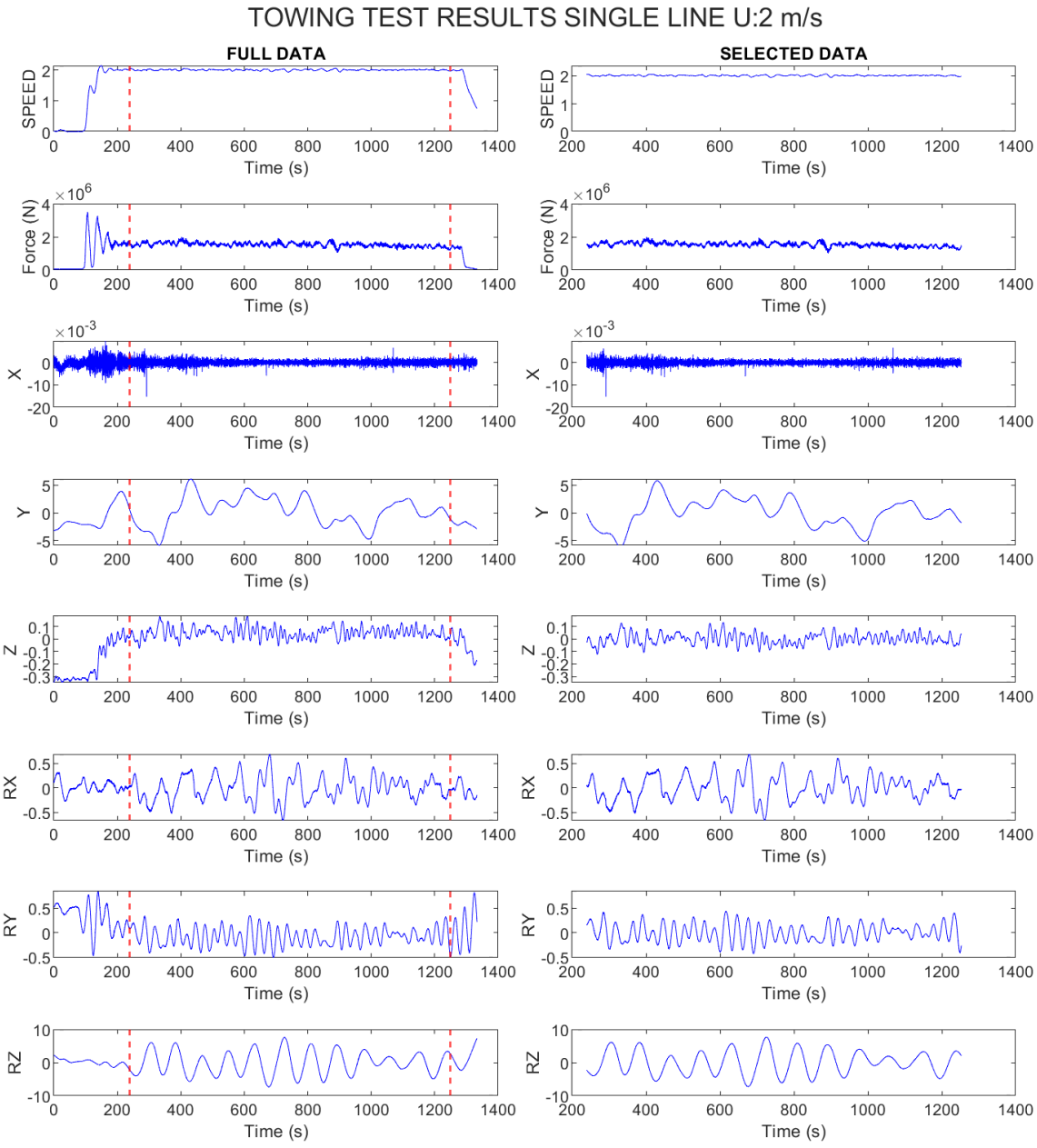

Figure 7.1: Data selection for Single-Line (SL) towing condition. The Time Domain data includes towing speed, towing force, and displacements in the 6DOF at a mean towing speed of 2.0 m/s.

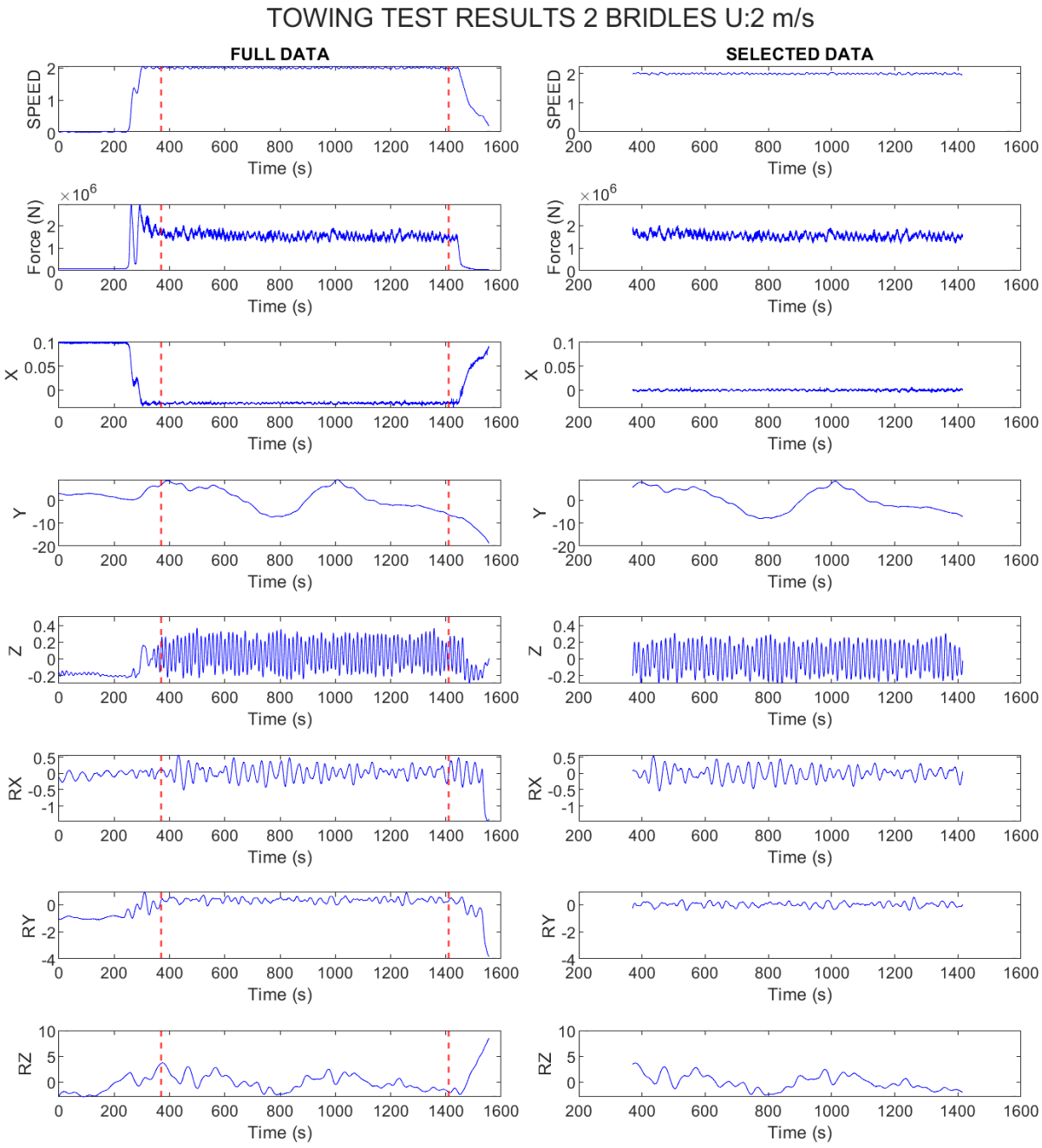

Figure 7.2: Data selection for Two-Bridle (2B) towing condition. The Time Domain data includes towing speed, towing force, and displacements in the 6DOF at a mean towing speed of 2.0 m/s.

Results from the full data show an initial period with instability in the platform motion, followed by a stable period when the platform reached the mean target speed.

Displacements in Surge (X-direction) were in the order of $1 \cdot 10^{-3}$ m, those results are considered small in comparison with Sway displacements (Y-direction), which were larger than 3.0 m in different conditions. The same behaviour was evident in all ranges of current velocities (see Appendix C and Appendix D).

Heave presented small displacements, in the order of $1 \cdot 10^{-1}$ m. Rotations were significantly small, less than 10 deg. The higher values were registered in Yaw (RZ).

7.2 Comparison of Experimental and SIMA results.

Results from different parameters of the towing experiment will be reviewed in the following lines, also including the comparison with results from the TD-VIV model.

7.2.1 Mean Towing Force

Figure 7.1 and Figure 7.2 showed that the towing Force reached a mean value, almost constant when the target speed was achieved.

A valuable way to understand the results is to plot the mean Towing Force at the correspondent current speed. Figure 7.3 shows the mean Force vs the towing speed in each towing condition, also the graph includes the second-order polynomial fitting curve.

Results showed a quadratic dependency between the towing force and the current speed. Moreover, a clear similitude in outcomes from both towing conditions is noticed.

Although the triangular shape of the platform changed according to the heading position, the graph shows that the magnitude of the mean force is identical in both directions. Therefore, it is considered that the towing force is not sensitive to the towing direction.

Comparison of the experimental Towing Force with results from SIMA.

Figure 7.4 compares the mean Towing Force from experimental data with SIMA results in both towing conditions. SIMA results show a similar trend to the experimental data. The outcomes were similar to experimental results with errors less than 10%, in any case. In general, the highest difference was found in the Two-Bridle (2B) towing condition (see Table 7.1).

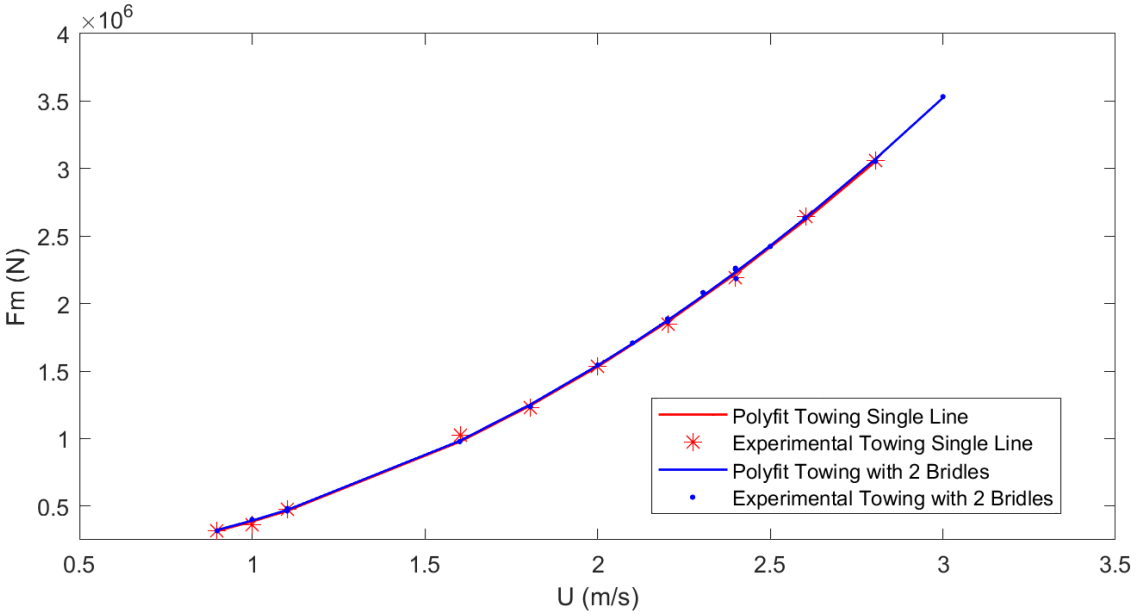

Figure 7.3: Mean Towing Force vs Current Speed, in both towing conditions, i.e. the Single-Line (SL) and Two-Bridle (2B). The PoliFit is a second-order fitting curve.

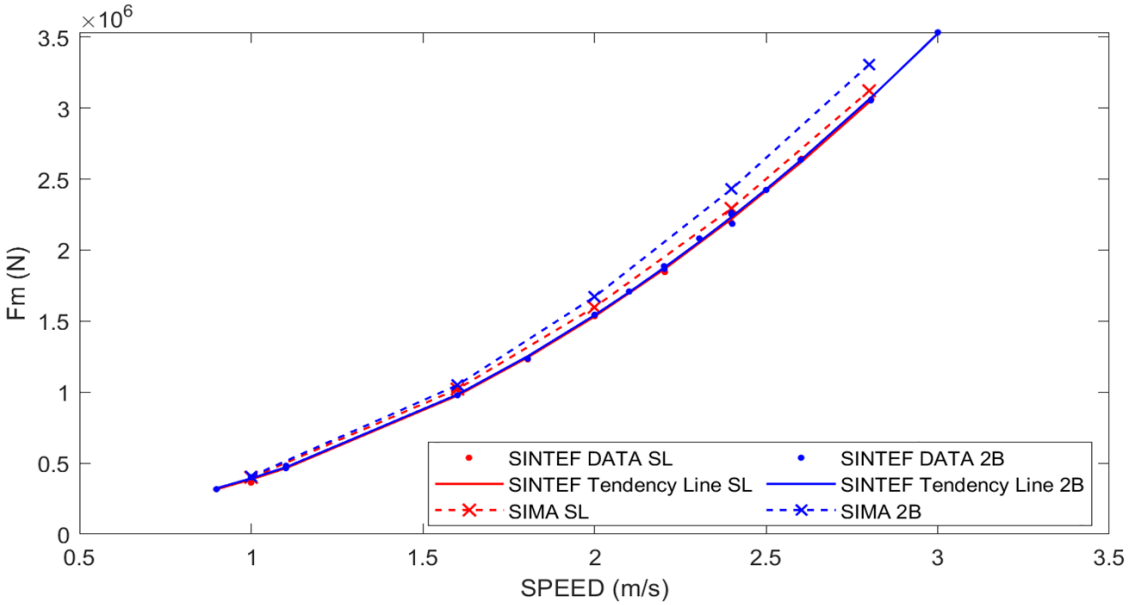

Figure 7.4: Experimental and SIMA results of the mean Towing Force. Results are shown for Single-Line (SL) and Two-Bridle (2B) towing conditions.

	Single-Line			Two-Bridle		
U (m/s)	Fm (N) Experimental	Fm (N) SIMA	Deviation %	Fm (N) Experimental	Fm (N) SIMA	Deviation %
1.0	$0.363 \cdot 10^6$	$0.397 \cdot 10^6$	9.5	$0.401 \cdot 10^6$	$0.407 \cdot 10^6$	1.6
1.6	$1.022 \cdot 10^6$	$1.020 \cdot 10^6$	0.2	$0.978 \cdot 10^6$	$1.048 \cdot 10^6$	7.1
2.0	$1.535 \cdot 10^6$	$1.597 \cdot 10^6$	4.1	$1.545 \cdot 10^6$	$1.670 \cdot 10^6$	8.1
2.4	$2.193 \cdot 10^6$	$2.294 \cdot 10^6$	4.6	$2.252 \cdot 10^6$	$2.430 \cdot 10^6$	7.9
2.8	$3.060 \cdot 10^6$	$3.120 \cdot 10^6$	1.9	$3.053 \cdot 10^6$	$3.305 \cdot 10^6$	8.3

Table 7.1: Experimental and SIMA results comparison of the mean towing force in both towing conditions

7.2.2 Displacements

Figure 7.5 compares Surge, Sway, Roll, and Yaw under both towing conditions, i.e. Single-Line (SL) and Two-Bridle (2B), at current speeds of about 1.0 m/s, 2.0 m/s, and 2.8 m/s. Appendix E shows results at different current speeds.

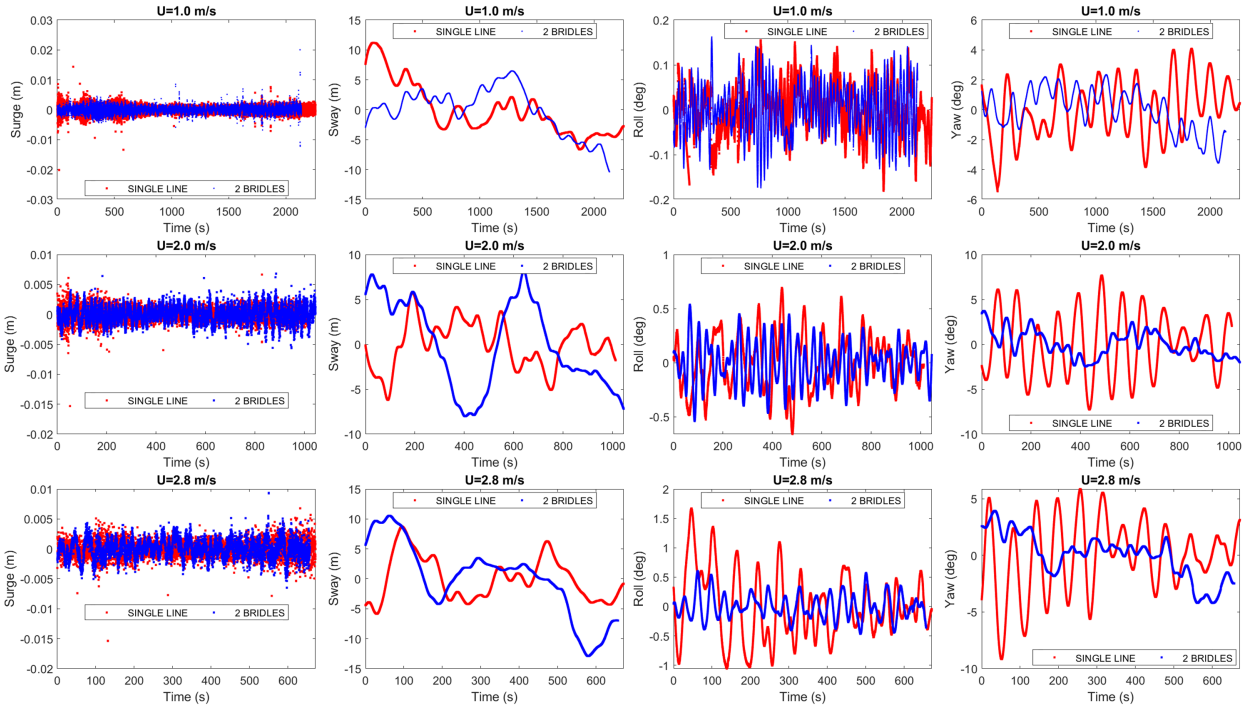

Figure 7.5: Surge (X), Sway (Y), Roll (RX), and Yaw (RZ) displacements in both, Single-Line (SL) and Two-Bridle (2B) towing conditions, under three different current speeds.

This comparison revealed that during the experiment the platform found similar motions at different current speeds in the two towing conditions. In Surge, motions showed similar amplitudes for both towing conditions, at different current speeds.

Similarly, the amplitude of motions in Sway (Y) and Roll (RX) were equivalent when we compared both towing conditions, except at 2.8 m/s when Roll motions were very small in the Two-Bridle condition. Yaw showed a different behaviour, motions have higher amplitudes in a Single-

Line (SL) towing condition than in the Two-Bridle condition, at different current speeds.

During the experiment, the platform experienced larger changes in motion just before finishing the test, even so, it was not possible to do further investigation on it due to limitations on the length of the towing tank.

Time Series comparison of experimental Sway and Roll with results from SIMA

Figure 7.6 and Figure 7.7 compare experimental Sway and Roll motion in the two towing conditions, i.e. Single-Line (SL) and Two-Bridle (2B), with results from the TD-VIV model.

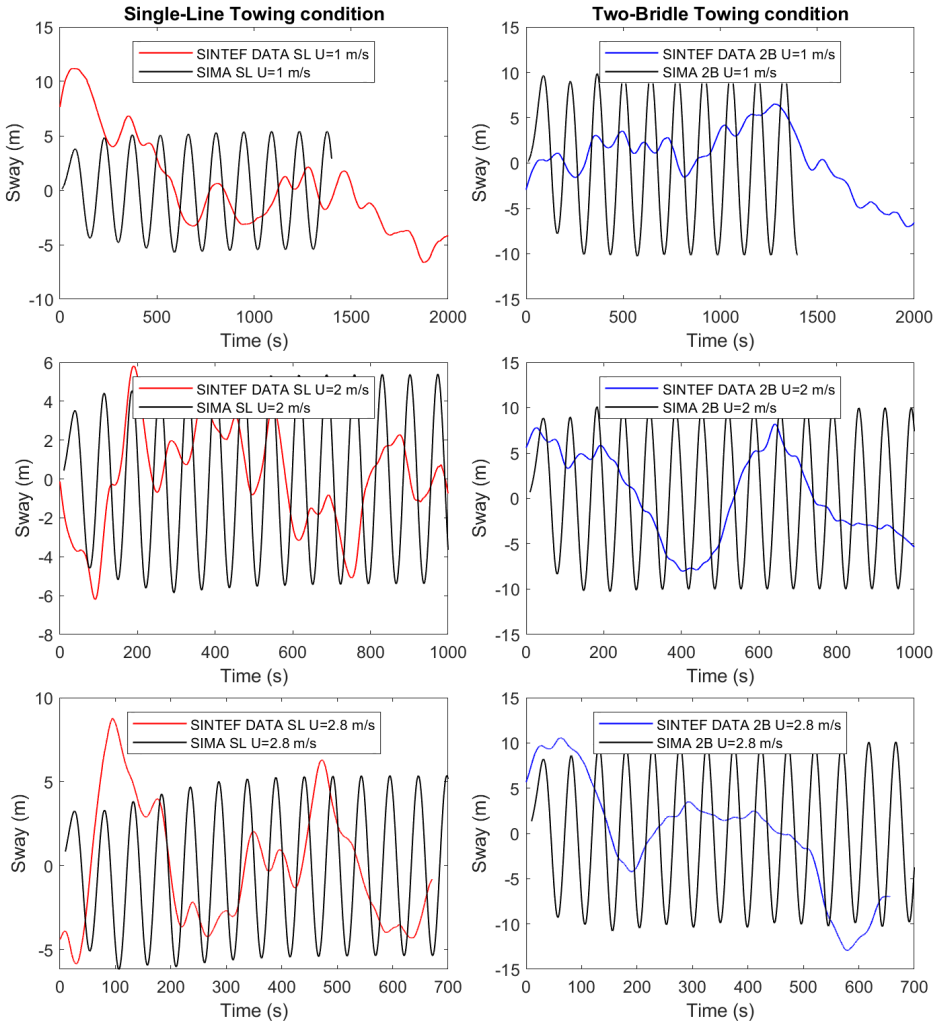

Figure 7.6: Experimental and SIMA's results of Sway motion in the two towing conditions, at three different current speeds.

Figure 7.6 display Sway motions with noticeable differences. Graphs reveal that the SIMA motions vibrate with a constant period while experimental results display an undefined pattern, dominated by a motion with a long period plus motions with shorter periods. This can be observed in both towing conditions.

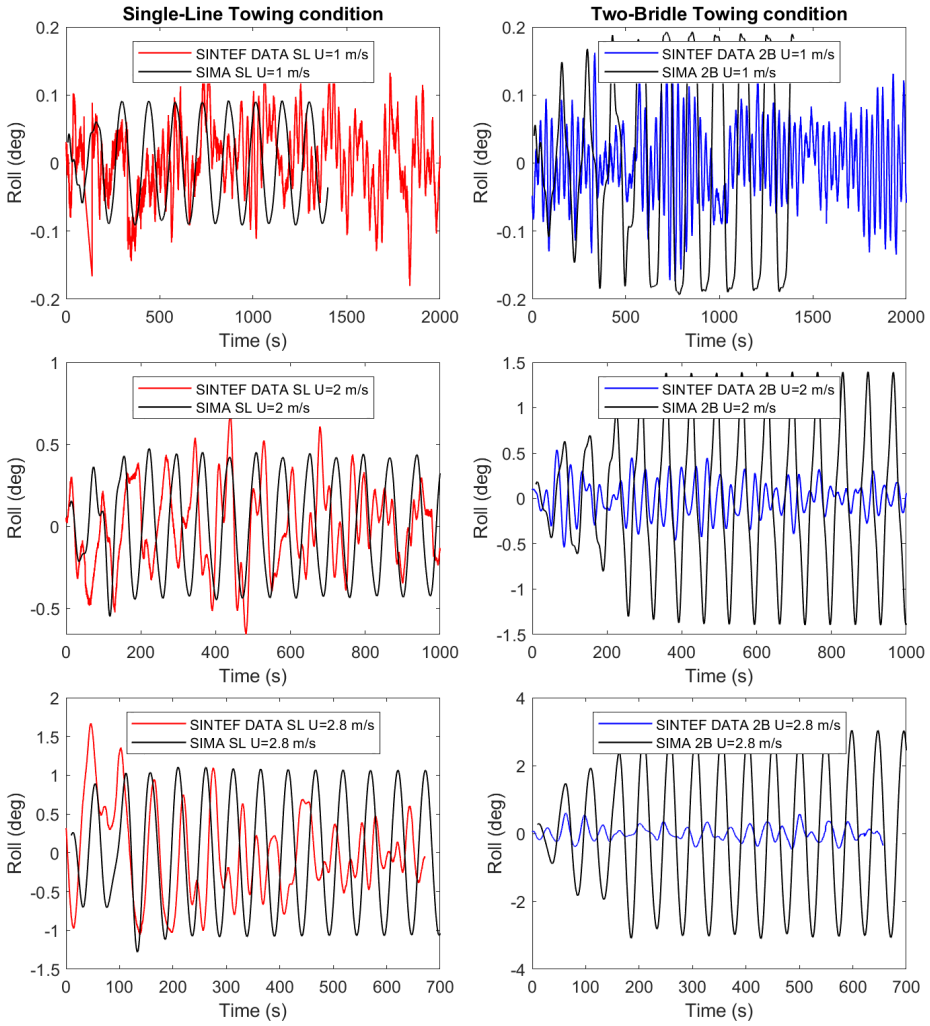

Figure 7.7: Experimental and SIMA TD-VIV Model results of Roll motion in the two towing conditions, at three different current speeds.

However, in Figure 7.7 is noticed that in Roll motion there is a better fit for the period in both towing conditions. Nevertheless, there is an important difference in the amplitude of motion with SIMA results. In the Single-Line (SL) towing condition, the amplitude of Roll motion was captured almost correctly, while in the Two-Bridle conditions, SIMA overestimated the Roll amplitude. This observation repeats at different velocities.

At this stage, it is important to emphasise the differences and uncertainties in our model. First, the SIMA model includes the wind turbine, resulting in mass differences between the SIMA model and the towed experiment. Also, the model in SIMA does not consider the effect of the drag on the pontoons and does not include the VIV effect on those elements. In addition, SIMA formulation is based on the assumption of a long aspect ratio, while the aspect ratio of the platform is near to one.

7.2.3 Spectral Analysis

A spectral analysis was carried out to have a better understanding of the structure response during the towing test. To do so, the displacements in Surge, Sway, and Roll were filtered using different methods, but it was noticed that several frequencies were involved in the motions and this idea was dismissed.

A second approach was to analyse the signal spectra (without filtering). Appendix F compares the Periodogram-Rectangular window, Periodogram-Hamming window, and Powspec methods for frequency response. The three methods were used to analyse the Force, Surge, Sway, and Roll motion at 2.0 m/s.

Spectral Analysis of the experimental Towing Force

Spectral Frequency response of the towing test showed good agreement with the Periodogram methods and the Powspec approach. The evaluation was done using the parameter R which must be about 1 to satisfy the Power Spectral Density (PSD).

Figure 7.8 shows the PSD of the experimental Towing Force vs frequency, at current speeds of 2.0 m/s, in the two towing conditions. The spectral analysis was performed using the Powspec method. Appendix G shows the PSD of the experimental Towing Force vs frequency, at current speeds 1.0 m/s, 2.0 m/s, and 2.8 m/s.

Plots include dotted lines marking the frequencies at the three highest PSD values, the approximated towing frequency found in Section 6.1.2, and the wind turbine's natural frequency in Surge and Roll motion measured during the towing test Section 5.1.3.

Signal spectra of the Force confirm the presence of different frequencies with some prominent peaks. At 1.0 m/s, the dominant frequencies are about 0.027 Hz, close to the natural frequencies, i.e. Surge, Roll and Towing frequency. This condition is similar in both towing directions.

At 2m/s there is a different behaviour on the Force spectra when comparing both towing conditions. In the Single-Line towing condition, the dominant frequency is about 0.024 Hz, whereas in the Two-Bridle condition, at 0.07 Hz, beyond the natural frequencies of the platform.

A similar condition was found at 2.8 m/s, the dominant frequency in the Single-Line towing condition was below the Roll frequency, whereas in the Two-Bridle condition, the dominant frequency was above the Roll frequency.

The approximate Towing Frequency coincides in some conditions with one of the peaks in the curve. However, it never meets the dominant frequency in any condition.

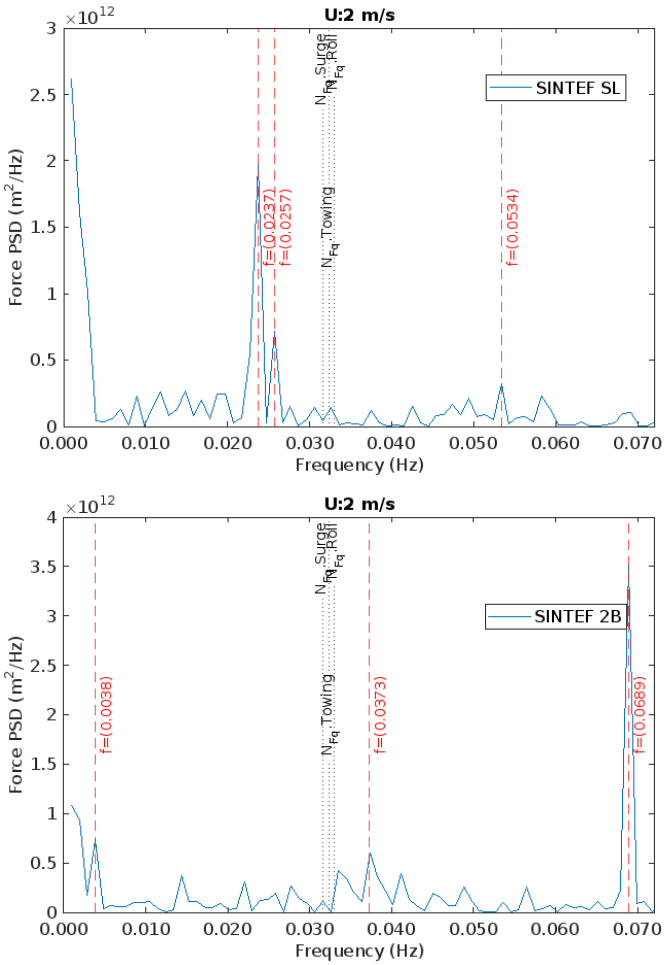

Figure 7.8: Power Spectral Density of the towing Force in the two towing conditions (SL: Single-Line, 2B: Two-Bridle), at the current speed of 2 m/s. The Force was analysed with the Powspec method.

Comparison of the Spectral experimental Towing Force and SIMA results

Figure 7.9 shows the Spectral comparison of the Experimental Towing Force and the TD-VIV model at 2.0 m/s. Appendix H includes results for other speeds.

The graph also includes the Time Series Experimental Towing Force and SIMA results. Since the mean value was deducted before performing the spectral analysis, those values represent the dynamic part of the towing force i.e. the standard deviation of the towing force. The mean Force and the standard deviation are presented in Table 7.2 and Table 7.3

Speed m/s	Force (SL) Mean $\pm$ Std Deviation	Force (2B) Mean $\pm$ Std Deviation
1.0	$0.36 \cdot 10^6 \pm 0.04 \cdot 10^6$	$0.40 \cdot 10^6 \pm 0.04 \cdot 10^6$
2.0	$1.53 \cdot 10^6 \pm 0.13 \cdot 10^6$	$1.54 \cdot 10^6 \pm 0.13 \cdot 10^6$
2.8	$3.06 \cdot 10^6 \pm 0.26 \cdot 10^6$	$3.05 \cdot 10^6 \pm 0.16 \cdot 10^6$

Table 7.2: Mean and Standard deviation of the experimental Towing Force.

Speed m/s	Force (SL) Mean ± Std Deviation	Force (2B) Mean ± Std Deviation
1.0	$0.40 \cdot 10^6 \pm 0.03 \cdot 10^6$	$0.40 \cdot 10^6 \pm 0.14 \cdot 10^6$
2.0	$1.60 \cdot 10^6 \pm 0.16 \cdot 10^6$	$1.69 \cdot 10^6 \pm 0.53 \cdot 10^6$
2.8	$3.12 \cdot 10^6 \pm 0.14 \cdot 10^6$	$3.32 \cdot 10^6 \pm 0.46 \cdot 10^6$

Table 7.3: Mean and Standard deviation of the Towing Force from SIMA.

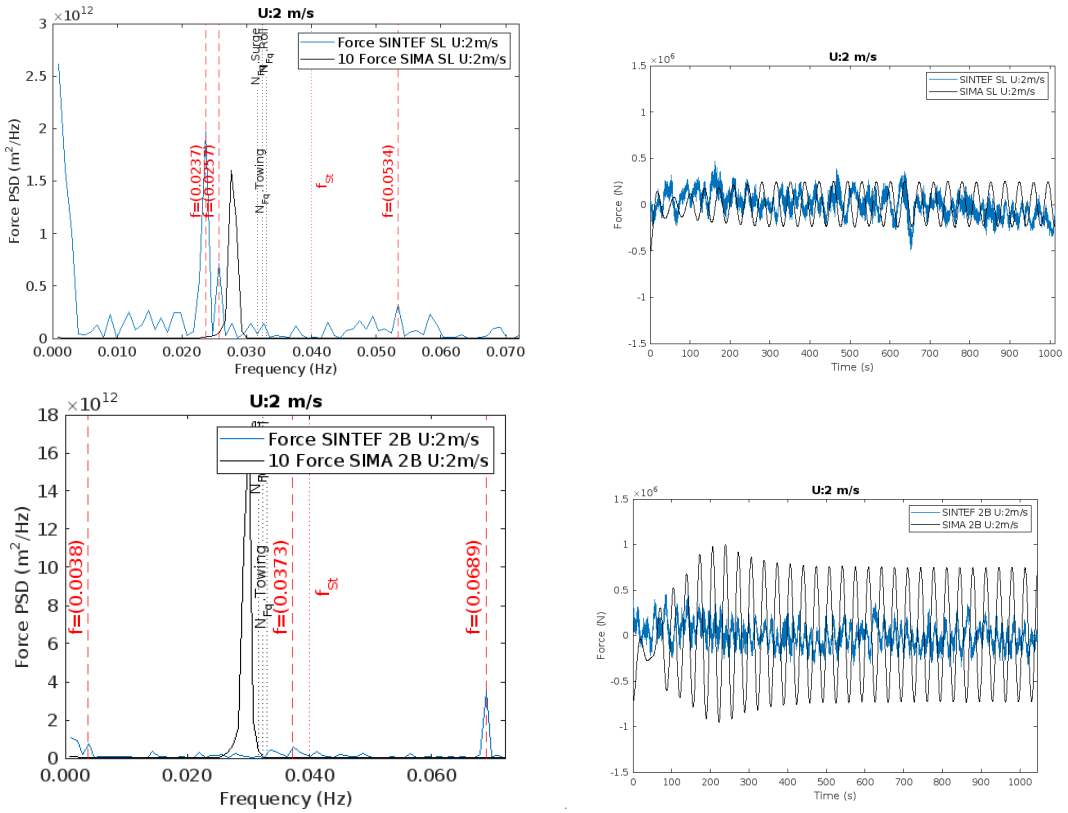

Figure 7.9: Signal Spectra of Experimental and SIMA results of the Towing Force. Results are for the two towing conditions at 2.0 m/s. The graph also includes the Time Series Force of Experimental and SIMA results.

In the Single-Line towing condition, the prediction is close to the experimental results, however, in the Two-Bridle towing condition is noticed that SIMA overestimates the towing force. Table 7.3 illustrates the difference in the standard deviation compared to the standard deviation of the experimental data. This is also reflected in the PSD plot, showing a high peak in the PSD curve.

On the other hand, results from SIMA reveal differences in the frequency response compared to experimental data. Figure 7.9 shows that the SIMA´s towing frequency is very close to one of the dominant frequencies from experimental values. This is more noticeable in the Single-Line towing condition at 2.0 m/s and 2.8 m/s. Whereas, in the Two-Bridle condition, results from SIMA do not coincide with experimental results.

Another important finding is that SIMA frequency in the Single-Line (SL) towing condition is

similar to results from the Two-Bridle (2B) condition. These results are opposite to experimental data. Figure G.1 and Figure G.2 showed the differences in the dominant frequencies in each towing condition.

These findings suggest an interaction between columns and pontoons that SIMA is not capturing, amplifying the structure response.

Spectral Analysis of Surge, Sway and Roll

Appendix F presented the results of the three methods to approximate the motion frequency response. From the assessment, all three methods performed well enough to predict the frequencies involved during the test.

Motions spectral analysis was carried out using the Periodogram with Rectangular window approach, and results are presented in Appendix I, for Surge, Sway, and Roll at three representatives' current speeds, i.e. 1.0 m/s, 2.0 m/s, and 2.8 m/s.

Figure 7.10 shows the PSD of the experimental Sway and Roll vs frequency, in the two towing conditions, at a current speed of 2.0 m/s, while Figure 7.11 presents results at 2.8 m/s. Plots include frequencies of the three biggest PSD peaks, the approximated towing frequency (0.0324 Hz), and the natural frequencies in Surge and Roll from the Decay test of the wind turbine.

The signal spectra of the experimental Sway, and Roll, show a variety of frequencies acting in the platform during the towing test. When comparing each mode of motion, there are differences in the frequency response between the two towing conditions, which repeats in all ranges of speeds.

Sway presents the lowest dominant frequencies, with values between 0.0009 Hz at 1.0 m/s up to 0.003 Hz at 2.8 m/s in the Single-Line (SL) towing condition, whereas in the Two-Bridle (2B) condition, the frequency variation is from 0.0005 Hz. up to 0.003 Hz. This confirms that Sway motions are dominated by long-period motions, with the influence of additional small-period motions. This fact is similar in both towing conditions.

On the other hand, Roll motions are dominated for higher frequencies (or small periods) than Sway. Also, it is noticed that in the Two-Bridle conditions, the frequency increases more than twice in comparison to frequencies in the Single-Line condition. In addition, experimental results for Roll motion indicate coupling with Sway motion, this is frequently noticed in the Single-Line condition.

In a VIM phenomenon, it is expected to find an IL motion smaller than in CF, however, it is important to analyse the IL frequency because it can be twice the CF frequency, responsible for large fatigue damage as mentioned [42]. Appendix I displays results for Surge showing dominant frequencies higher than the dominant Sway's frequency, more than double as was expected. Surge frequencies suggest accumulation of fatigue damage in the towing line. This repeats at both towing conditions.

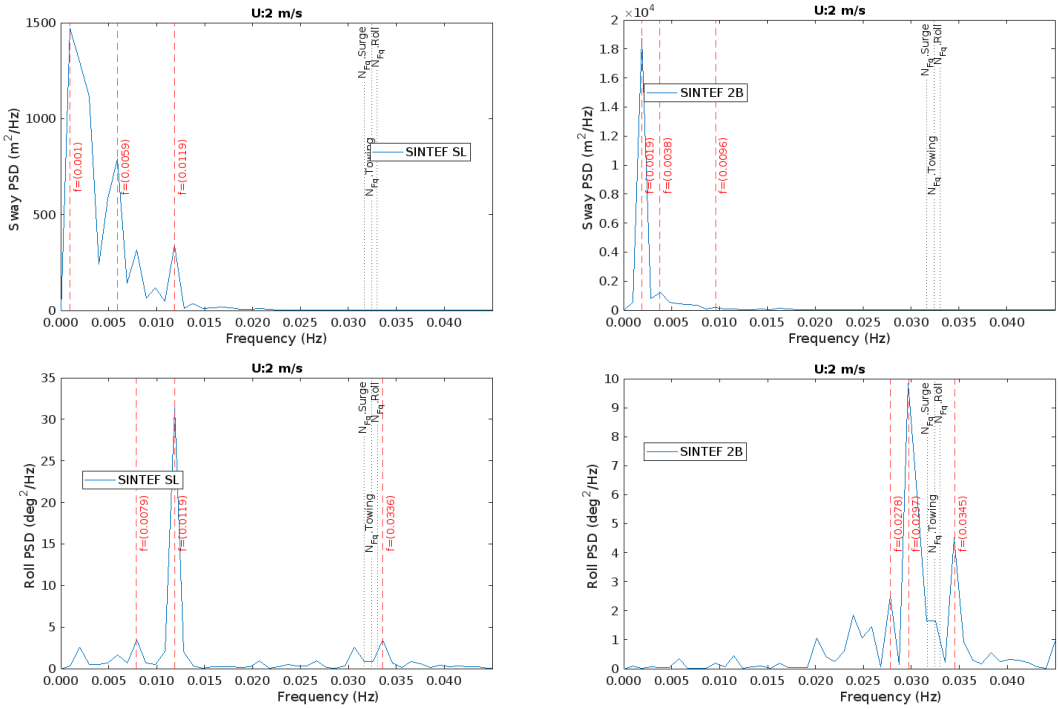

Figure 7.10: Power Spectral Density of the experimental Sway, and Roll in the two towing conditions (SL: Single Line, 2B: Two Bridle), at current speed U=2.0 m/s.

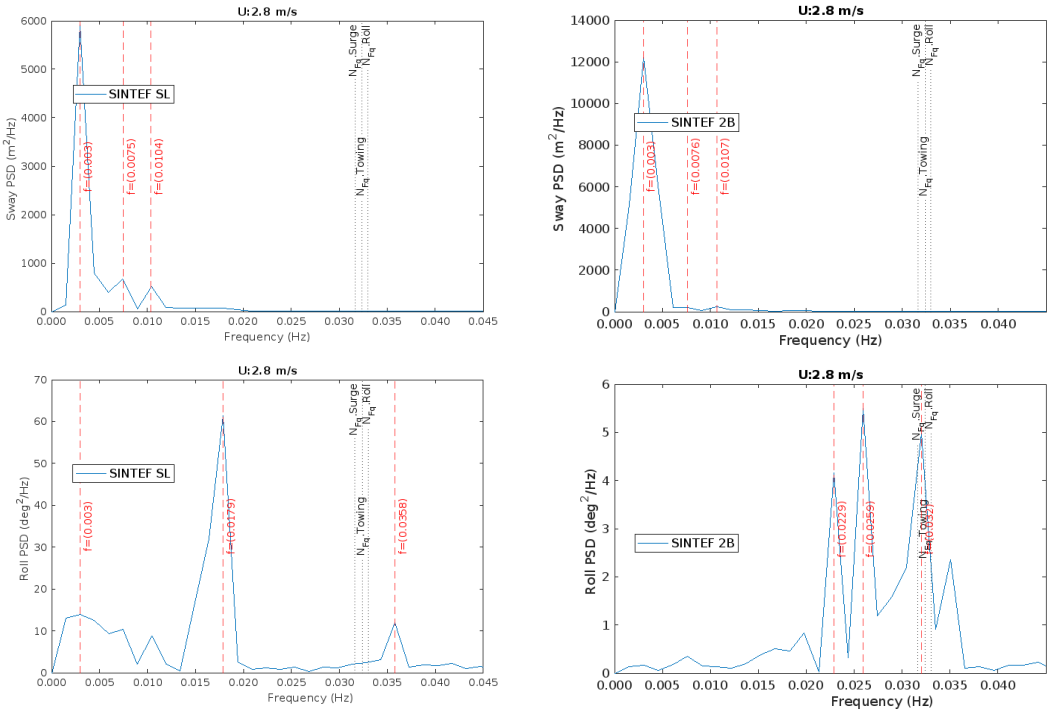

Figure 7.11: Power Spectral Density of the experimental Sway, and Roll in the two towing conditions (SL: Single Line, 2B: Two Bridle), at current speed U=2.8 m/s.

Spectral and Time Series comparison of experimental Sway and Roll with SIMA's results

Figure 7.12 presents the spectral and time series comparison of Sway motions. The results are at current speed 2.0 m/s for the two towing conditions. Whereas, Figure 7.13 shows results in Roll under similar conditions. Appendix J presents results for Sway, and Roll motions, under three different velocities i.e. 1.0 m/s, 2.0 m/s and 2.8 m/s.

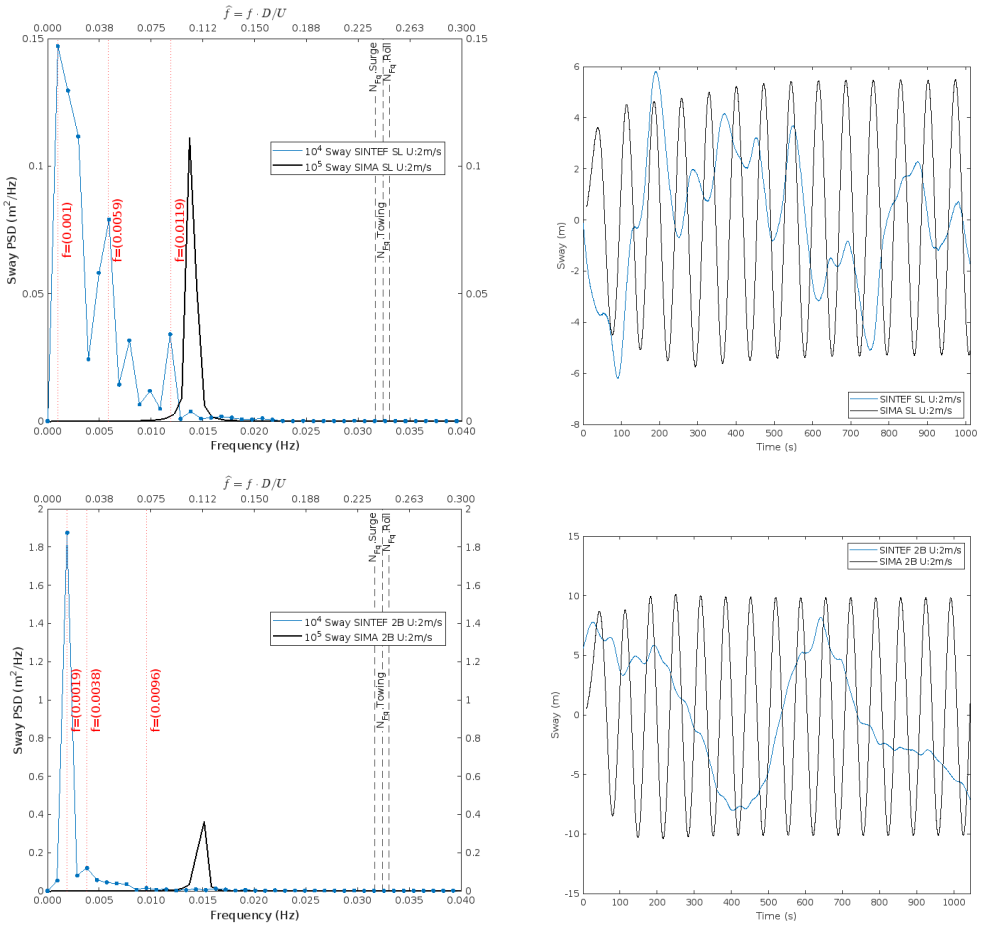

Figure 7.12: Spectral and Time Series comparison of experimental Sway with SIMA's results in the two towing conditions at 2.0 m/s.

According to research, cylinders with smooth surfaces may experience VIM in environments with current velocities that induce the vortex-shedding frequency at Strouhal number between 0.2 to 0.5.

Since towing velocities were calculated in the range of Strouhal number 0.2 to 0.3, these graphs included a second axis in the upper part marking the dimensionless frequency $\hat{f}$, defined as follows:

$$\hat{f} = \frac{f \cdot D}{U} \tag{7.1}$$

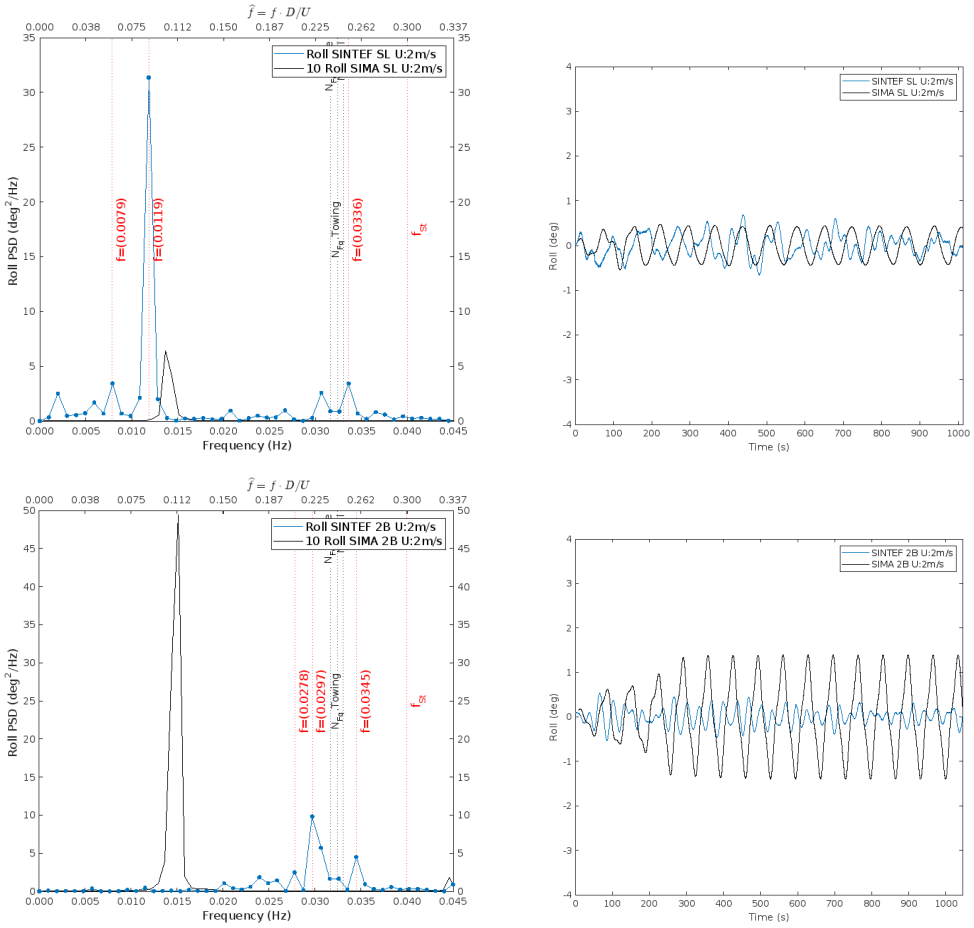

Figure 7.13: Spectral and Time Series comparison of experimental Roll with SIMA's results in the two towing conditions at 2.0 m/s.

When the dimensionless frequency is 0.3, the frequency is equivalent to the vortex-shedding frequency at Strouhal number 0.3. From the results, it is noticed that in any case, the Sway motion has reached the theoretical vortex-shedding frequency.

When we compare results, it is noticed difference between the experimental dominant frequencies and SIMA's result. In the Single-Line (SL) towing condition, SIMA's frequency prediction in Sway was higher than experimental results in all velocities. Nevertheless, when we look at the results in Roll, the frequency prediction showed good agreement in this mode of motion.

On the other hand, for the Two-Bridle (2B) towing condition neither Sway nor Roll results match the experimental outcomes. As we mentioned before, the Sway motion differs because SIMA predicts a Sway motion dominated by a constant period while experimental results showed motions influenced by both short and long-period motions.

In Roll motion, SIMA overestimates the response amplitude. Moreover, in any case, SIMA found the experimental frequency that dominates this motion.

7.2.4 Final comments about SIMA results

Figure 7.14 and Figure 7.15 shows the time series and spectral results from SIMA of three modes of motion (i.e. Surge, Sway and Roll). The PSD values of Surge and Roll were magnified to allow the comparison.

Plots show that in the Single-Line (SL) towing condition, the Surge frequency is exactly the double of the Sway frequency. This is a non-implicit condition that was introduced when parameters were chosen for the TD-VIV model. Also, SIMA formulation includes this assumption based on information from several research on single cylinders with an aspect ratio higher than 1. The model in SIMA tends to follow this approach, showing a limitation of the formulation.

In addition, it is surprising that SIMA encounters coupling with Roll motion, showing similar results as the experiment in Single-Line conditions. Nevertheless, SIMA showed this similar tendency in the Two-Bridle conditions and these results differ from experimental outcomes.

The fact that Two-Bridle conditions do not fit with experimental results is a clear piece of information. There is an interaction between columns and pontoons which is not modelled by SIMA.

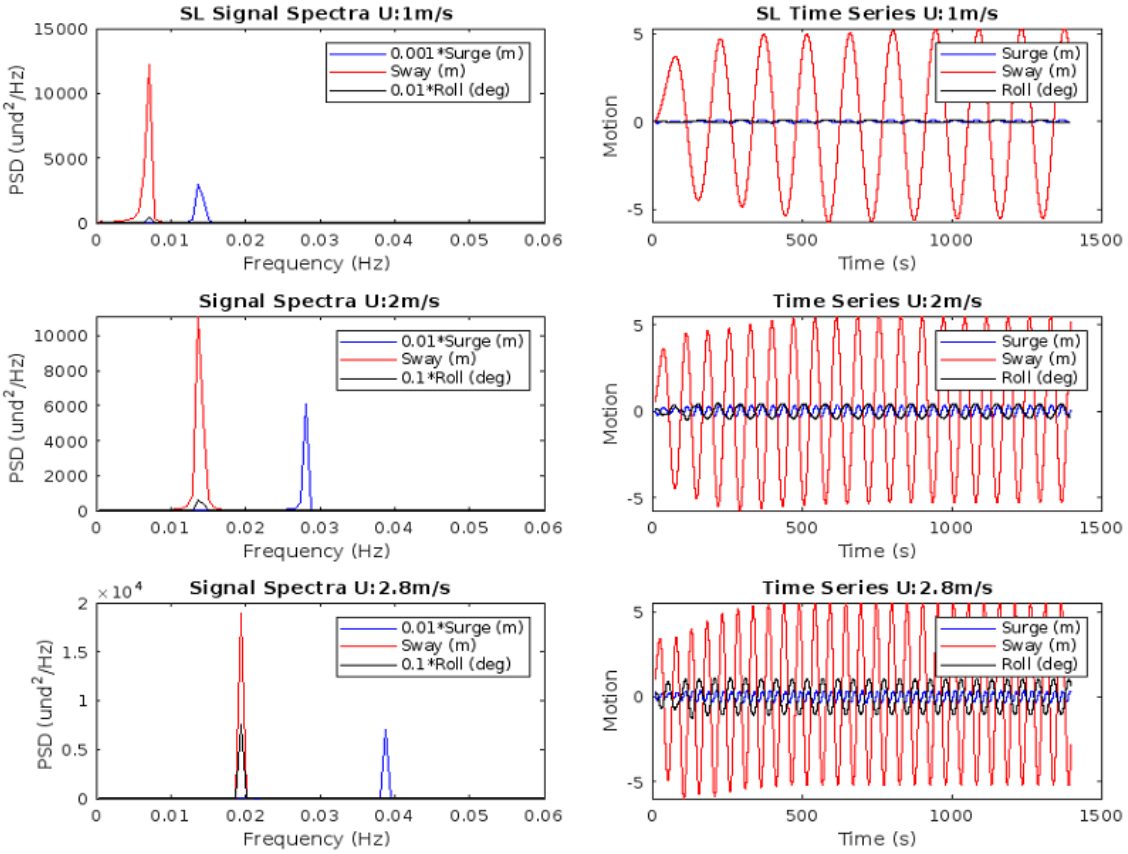

Figure 7.14: Time Series data and Signal Spectra of SIMA results in the Single-Line (SL) towing conditions at three different current speeds.

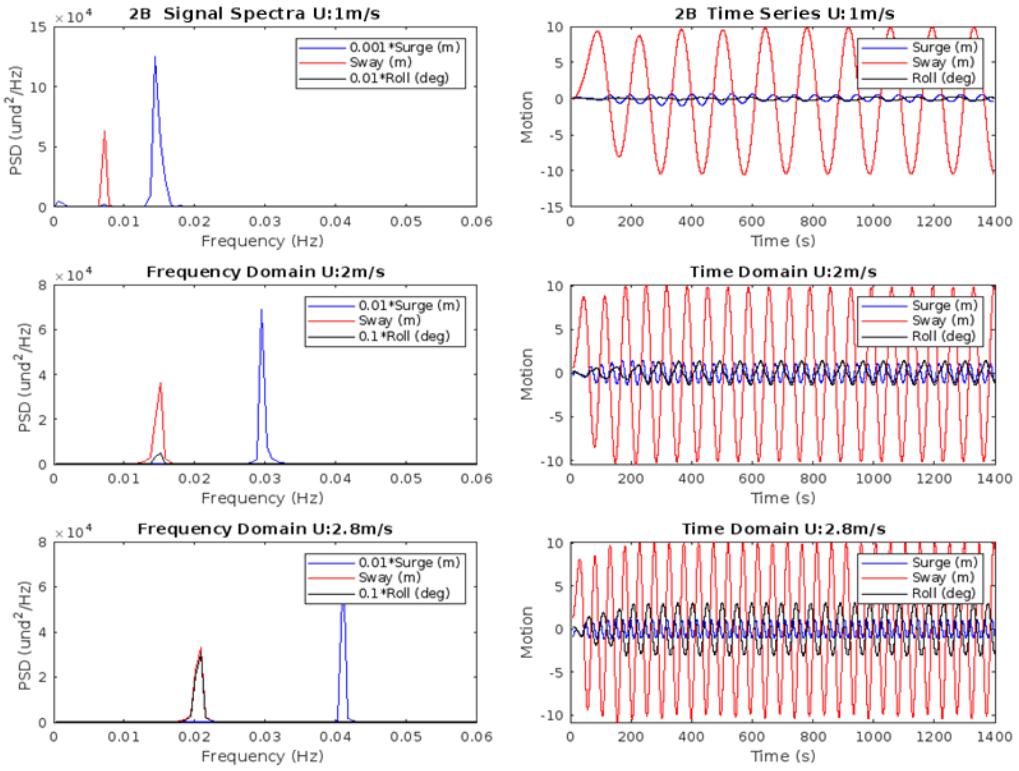

Figure 7.15: Time Series data and Signal Spectra of SIMA results in the Two-Bridle (2B) towing conditions at three different current speeds.

7.2.5 Response Amplitude Ratio

The response amplitude ratio is an important parameter that describes the VIM phenomenon. Usually, this parameter is plotted against the reduced velocity U_r, as was presented in the VIM design curve in Figure 3.4.

Figure 7.16 shows the amplitude of motion in the X-direction (A_{IL}) and Y-direction (A_{CF}) vs the current speed in both towing conditions, i.e. Single-Line (SL) and Two-Bridle (2B). The experimental data was plotted with the first-order polynomial fitting curve.

Also, on the right side, the graph includes the correspondent amplitude ratio in IL and CF vs speed. This allows us to make some comparison of the results in the two towing conditions.

As we mentioned before, the amplitude of motion in the X-direction is smaller than the amplitude in the Y-direction. This is intelligible looking closer to the A_{IL} and the A_{CF} graphs in Figure 7.16.

From the fitting curves, it can be distinguished that motions in the CF direction for the Single-Line (SL) towing condition, showed a slighter decreasing trend as the current speed increased, whereas, in the Two-Bridle (2B) towing condition, there is a decreasing trend with a higher slope.

Furthermore, it is noticed that the platform found a higher amplitude of motion in the Two-Bridle (2B) towing condition than in the Single-Line (SL) towing condition.

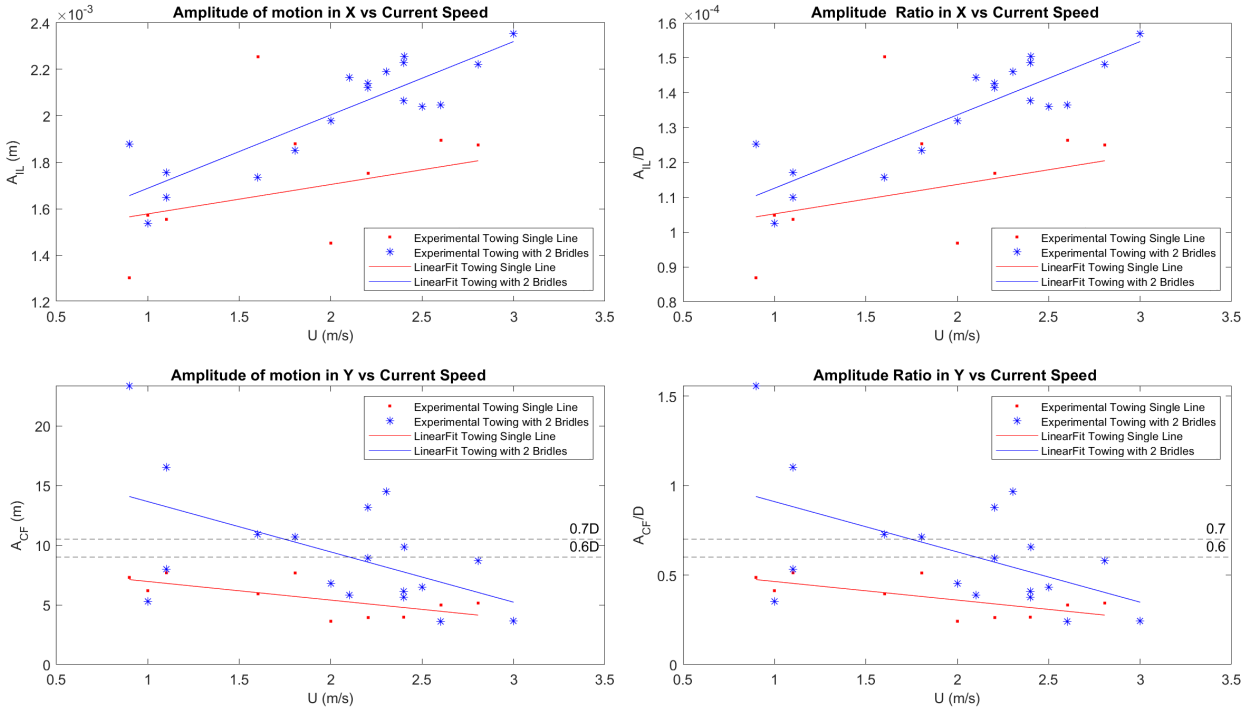

Figure 7.16: Amplitude of motion and the Response Amplitude Ratio in both, IL and CF direction, vs Current Speed. Results are from the two towing conditions, Single-Line (SL) and Two-Bridle (2B). The fitting curve is a first-order polynomial.

Comparison of experimental CF Response Amplitude Ratio with SIMA´s results

Figure 7.17 compares results from the TD-VIV model in SIMA and the experimental results. Those results are presented for both towing conditions, i.e. Single-Line (SL) and Two-Bridle (2B).

Results from SIMA show differences in the amplitude response for each towing condition. The highest amplitudes were found in the Two-Bridle (2B) towing condition. Also, it is noticed that the amplitude ratio is almost constant in the full range of velocities, a similar trend follows both towing conditions.

Figure 7.17 reveals the differences between SIMA results and the fitting lines of experimental results, in both conditions. Nevertheless, looking closer at the experimental data it is noticed that in some ranges of velocities, experimental results also follow the same constant tendency as results on SIMA, allowing some inferences.

- SIMA results show good agreement with experimental results, which validates the parameters that were chosen for the model.
- The constant trend line from SIMA suggests that amplitudes of motions are independent of the speed, however, it depends on the current direction, at least in this case of a triangular platform.

Yin [9] mentioned that for mono-column floaters with low aspect ratio under high Re condi-

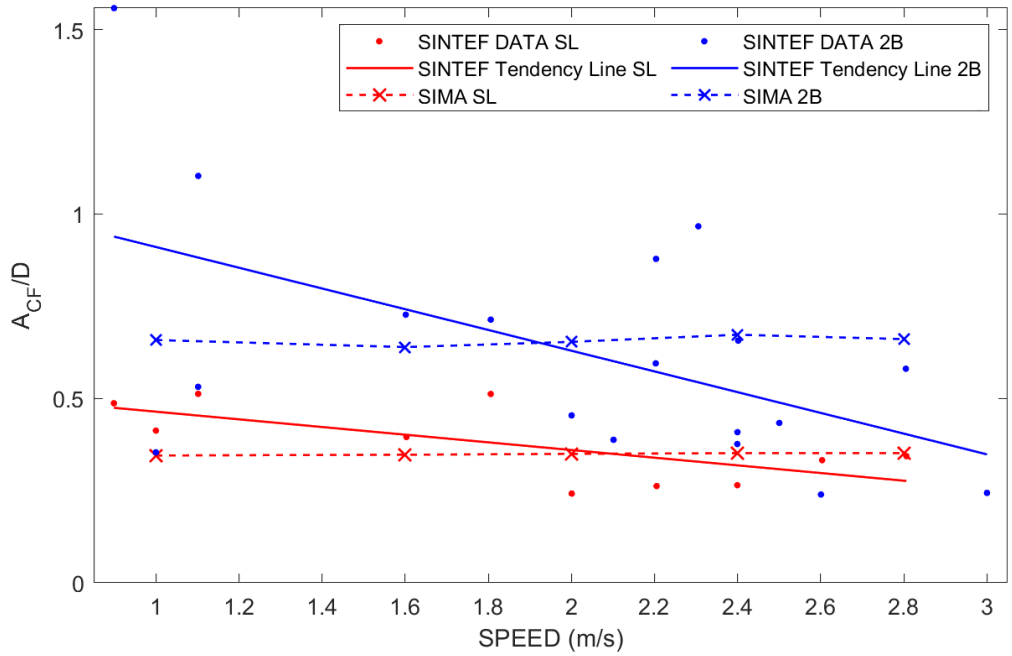

Figure 7.17: Experimental and SIMA TD-VIV Model results of the Amplitude Ratio in CF direction, vs Current Speed.

tions, the amplitude response in IL and CF decreased in comparison to results at lower Re. In addition, it is mentioned that experimental results from free oscillation tests on mono-circular cylinder showed that at high Re the expected A_{CF} is around 0.6D and 0.7D, while, the A_{IL} is about 0.2A_{CF}.

Columns on the 12 MW-SSWT have a low aspect ratio ($A_r = 1.03$), and the Reynolds number is in the post-critical regime ($Re > 6 \cdot 10^6$). Results from the towing test suggested that the A_{IL} is very small, lower than expected for a mono-floater circular cylinder in free oscillation.

On the other hand, A_{CF} is about 0.4D - 0.5D for a Single-Line (SL) towing condition, while for the Two-Bridle (2B) towing condition, the A_{CF} is about 0.5D - 1.0D. These results can suggest:

- During the experiment, the expected vortex-shedding frequency was not reached, which suggest not presence of VIM but pure CF motion with large amplitudes.
- A dependency of the amplitude of motion with the current direction. Larger amplitudes were experienced in the Two-Bridle condition, above 0.5D.

Chapter 8

Conclusions

The amplitude of motions from experimental tests showed a decreasing trend when the current speed increased. However, these results are not considered conclusive, the main ideas behind these are:

- Experimental data showed very complex motions. Although it was possible to capture cycling motion, in some cases was not able to distinguish more than one cycle, therefore is difficult to predict motions that suggest VIM (see Appendix E).
- Appendix C and Appendix D show the results of the towing test. The length of the towing tank was about 94m. In some trials, the platform experienced big changes in motion at the end of the test. This indicates the probability that the platform was starting to develop its motion at that point. Therefore, it is suggested to extend the experiment length in the towing tank to validate the results.

Although the platform was free to move in the 6-DOF, the CF motion was the one that achieved higher amplitudes in all ranges of velocities, this behaviour can be associated with a VIM in pure CF. However, the complexity of this phenomenon does not allow a clear definition of VIM. For example, the platform did not reach the expected vortex-shedding frequency defined at St=0.3. But, this assumption is based on data from single bare cylinders, with smooth surfaces and an aspect ratio higher than one, which differs from our platform, having three cylinders with an aspect ratio of about 1.03. Therefore, there is a necessity for establishing parameters to define VIM in this type of structure.

Results suggested that there was not a combined VIM effect in the platform. This is supported by the fact that SIMA and experimental results, did not achieve the expected conditions. According to [9], at high Re the expected A_{CF} is about 0.6D, while, the A_{IL} is about 0.2A_{CF}. Moreover, the dominant frequencies in Sway did not reach the f_{ST}, and the IL frequencies are higher than twice the CF frequency.

The TD-VIV model was able to capture some effects on the platform. Results showed a clear quadratic dependency between the towing force and the current speed. Moreover, similitude in outcomes from both towing conditions is noticed. Therefore, it is considered that the towing force is not sensitive to the towing direction. Nonetheless, results show a dependency of amplitude response in the CF to the current direction.

Results from the TD-VIV model in SIMA showed good agreement with experimental results of the Single-Line towing condition, nevertheless, presented differences with the Two-Bridle conditions. Experimental results showed a variety of frequencies, some of them are high frequencies that can suggest an interaction between the pontoons and columns, and this condition is not captured by SIMA.

During the experiment was also noticed galloping. SIMA formulation does not include this effect, and results suggest that exist some structure-hydrodynamic interactions that are not captured by SIMA. This topic is not included in the scope of this thesis and was not investigated.

In such a complex phenomenon, it is not easy to explain the combined effect of VIM and Galloping. It is suggested further investigation in that direction. It may be suggested to continue the investigation in this area, probably including CFD modelling to explain the interaction between columns and pontoons.

To ensure capturing the effects, either VIM, galloping, or the combined effect, it is suggested to extend the length and duration of future experiments.

Bibliography

[1] J. Fredsøe and B. Sumer, *Hydrodynamics Around Cylindrical Structures (Revised Edition)., World Scientific Publishing Company*. 2006.

[2] D. Livanos, *Investigation of Vortex-Induced Vibrations on Wind Turbine Towers, Delft University.* 2018.

[3] E. P. et al., *Simulation of Vim of an Offshore Floating Wind Turbine,DOI: 10.1115/ OMAE2022-79006.* 2022.

[4] T. F. E. Wikipedia, *Vortex-Induced Vibration [En línea]. Available: https:// en.wikipedia. org/w / index.php?title=vortex-induced-vibration*. 2023.

[5] V. Dinh and B. Basu, *On the Modelling of Spar-Type Floating Offshore Wind Turbines, In Damage Assessment Of Structures X, In Key Engineering Materials, Vol. 569, Trans Tech Publications Ltd, Pp. 636–643. DOI:10.4028 /WWW. SCIENTIFIC.NET/KEM.5, Oct.* 2013.

[6] H. Mørkeseth, *Time Domain Vortex-Induced Motion Prediction of Spar-Type Floating Wind Turbine, Master's Thesis, NTNU,* 2023.

[7] B. D. Renty, *Gradient-based design optimization of a semi-submersible floating wind turbine, Master's thesis in Marine Structures, NTNU,* 2020.

[8] C. E. Silva de Souza, *Definition of the INO WINDMOOR 12 MW base case floating wind turbine*. 2021.

[9] D. Yin, E. Passano, F. Jiang, H. Lie, J. Wu, N. Ye, S. Sævik and B. Leira, *State-of-the-Art Review of Vortex-Induced Motions of Floating Offshore Wind Turbine Structures. J. Mar. Sci. Eng. 2022, 10, 1021. https://DOI.ORG/10.3390 /JMSE10081021*. 2022.

[10] W. V. Vondelen, *Damping identification of offshore wind turbines using operational modal analysis: a review, Wind Energy Science, https://wes.copernicus.org/ articles/7/161/2022/, DOI: 10.5194/wes-7-161-2022, pp. 161–184*. 2022.

[11] J. Dahl, *Vortex-Induced Vibration of a Circular Cylinder with Combined In-line and Cross-flow Motion, Massachusetts Institute of Technology*. 2008.

[12] S. Chandrasekaran, *Vortex-induced vibration, Woodhead publishing series in civil and structural engineering: Design of marine risers with functionally graded materials, edited by Chandrasekaran S, chap. 3, pp. 59–90. Woodhead Publishing.* 2021.

[13] J. Gerrard, *The mechanics of the formation region of vortices behind bluff bodies., Journal of Fluid Mechanics. 1966; 25(2):401–413. DOI: 10.1017/ S00 22112066001721.* 1966.

[14] C. Williamson, *Oblique and parallel modes of vortex shedding in the wake of a circular cylinder at low Reynolds numbers., Journal of Fluid Mechanics. 1989;206:579–627.DOI:10.1017/ S0022112089002429.* 1989.

[15] M. Bloor, *The transition to turbulence in the wake of a circular cylinder., Journal of Fluid Mechanics. 1964;19(2):290–304. DOI: 10.1017/S0022112064000726.* 1964.

[16] C. Williamson, *The existence of two stages in the transition to three-dimensionality of a cylinder wake., The Physics of Fluids. 1988;31(11):3165–3168. DOI: 10.1063/1.86 6925.* 1988.

[17] G. Schewe, *On the force fluctuations acting on a circular cylinder in crossflow from subcritical up to transcritical Reynolds numbers., Journal of Fluid Mechanics. 1983;133:265–285. DOI:10.1017/S0022112083001913*. 1983.

[18] T. Michael, *Triantafyllou George, Tein, Y. S. David, and Bill D. Ambrose. Pragmatic Riser VIV Analysis. Paper presented at the Offshore Technology Conference, Houston, Texas, DOI: https://DOI.org/10.4043/10931-MS*. 1999.

[19] J. K. Vandiver and L. Li, *SHEAR7 V4.4 Program Theoretical Manual, Department of Ocean Engineering, Massachusetts Institute of Technology*. 2005.

[20] O. SINTEF, *SVIVANA 4.20.2 Theory Manual. April 18, 2021.* 2022.

[21] Y. Cheng and, *Time Domain Computation of Riser VIV From Vessel Motions. Proceedings of the 25th International Conference on Offshore Mechanics and Arctic Engineering. Volume 4: Terry Jones Pipeline Technology; Ocean Space Utilization; CFD and VIV Symposium. Hamburg, Germany. pp. 829-838. ASME. https://DOI.org/10.1115/OMAE2006-92432*. 2006.

[22] P. Mainçon, *A Wiener-Laguerre Model of VIV Forces Given Recent Cylinder Velocities, Mathematical Problems in Engineering, vol. 2011, Article ID 414702, 43 pages. https://DOI.org / 10. 1155/2011/414702*. 2011.

[23] W. Xu, X. Gao and J. Du, *The prediction on in-line vortex-induced vibration of slender marine structures. Acta Mech Sin 28, 1303–1308. https://DOI.org/ 10.1007/s10409-012-0098-3*. 2012.

[24] M. Thorsen, S. S and L. CM., *A simplified method for time domain simulation of cross-flow vortex-induced vibrations. Journal of Fluids and Structures. 2014;49:135–148. DOI: 10.1016/j.jfluidstructs.2014.04.006.* 2014.

[25] M. Thorsen, S. S and L. CM., *Fatigue damage from time domain simulation of combined in-line and cross-flow vortex-induced vibrations. Marine Structures. 2015;41:200–222. DOI: 10.1016/j.marstruc.2015.02.005.* 2015.

[26] M. Thorsen, S. S and L. CM., *Time domain simulation of vortex-induced vibrations in stationary and oscillating flows. Journal of Fluids and Structures. 2016;61:1–19. DOI: 10.1016/ j.jfluidstructs.2015.11.006.* 2016.

[27] M. Thorsen, S. S and L. CM., *Non-linear time domain analysis of cross-flow vortex-induced vibrations. Marine Structures. 2017;51:134–151. DOI: 10.1016 /j.marstruc.2016.10.007.* 2017.

[28] J. Ulveseter, S. S and L. CM., *Time domain model for calculation of pure inline vortex-induced vibrations. Journal of Fluids and Structures. 2017;68:158–173. DOI: 10.1016/ j. jfluidstructs.2016.10.013.* 2017.

[29] J. Ulveseter, M. Thorsen, S. S and L. CM., *Stochastic modelling of cross-flow vortex-induced vibrations. Marine Structures. 2017;56:260–280. DOI: 10.1016 /j.marstruc.2017.08.001.* 2017.

[30] J. Ulveseter, M. Thorsen, S. S and L. CM., *Time domain simulation of riser VIV in current and irregular waves. Marine Structures. 2018;60:241–260. DOI: 10.1016/j.marstruc.2018.04.001.* 2018.

[31] J. Ulveseter, M. Thorsen, S. S and L. CM., *Simulating fundamental and higher harmonic VIV of slender structures. Applied Ocean Research. 2019;90. Article 101856. DOI: 10.1016/ j.apor.2019.101856.* 2019.

[32] S. Kim, S. S, W. J and L. BJ, *Time domain simulation of marine riser vortex-induced vibrations in three-dimensional currents. Applied Ocean Research. 2022;120. Article 103057. DOI: 10.1016/j.apor.2022.103057.* 2022.

[33] S. Kim, S. S, W. J and L. BJ, *Prediction of deepwater riser VIV with an improved time domain model including non-linear structural behavior. Ocean Engineering. 2021;236. Article 109508. DOI: 10.1016/j.oceaneng.2021.109508.* 2021.

[34] S. Kim, S. S, W. J and L. BJ, *Simulating high-mode vortex-induced vibration of a riser in linearly sheared current using an empirical time-domain model. Journal of Offshore Mechanics and Arctic Engineering. 2021;143(4). Article 041901. DOI: 10.1115/1.4049246.* 2021.

[35] S. O. AS., 'Sima documentation: Riflex component data,' 2024.

[36] DNV, *DNV-RP-C205 Environmental conditions and environmental loads*. 2021.

[37] DNV, *DNV-ST-0119 Floating wind turbine structures*. 2021.

[38] ISO, *ISO 19901-7:2013, Petroleum and natural gas industries Specific requirements for offshore structures, Part 7: Station keeping systems for floating offshore structures and mobile offshore units*. 2013.

[39] E. E. Bachynski-Polic, ‘Lecture note: Assessing the results from decay tests,’ 2021.

[40] L. Eliassen, ‘How to model an offshore wind turbine in sima,’ 2014.

[41] D. Yin, ‘Windmoor towing test,’ 2024.

[42] D. Yin, H. Lie and R. Baarholm, ‘Prototype reynolds number vortex-induced vibration tests on a full-scale rigid riser.,’ 2017.

[43] T. M. Inc., ‘Matlab library: Periodogram power spectral density estimate.,’ 2024.

Appendix A

Properties of the Tower in SIMA

Element	Length (m)	Diameter (m)	Thickn (mm)	Mass coeff. (kg/m)	EA (N)	EI (N/m^2)
1	4.00	9.90	90.0	21873.5	5.91x10^{11}	7.24x10^{12}
2	4.00	9.50	90.0	20985.7	5.67x10^{11}	6.39x10^{12}
3	2.00	9.10	90.0	20097.9	5.43x10^{11}	5.62x10^{12}
4	5.89	9.00	74.3	16423.1	4.43x10^{11}	4.49x10^{12}
5	5.89	9.00	70.2	15529.1	4.19x10^{11}	4.24x10^{12}
6	5.89	9.00	66.1	14612.6	3.94x10^{11}	3.99x10^{12}
7	5.89	9.00	62.0	13717.8	3.70x10^{11}	3.75x10^{12}
8	5.89	9.00	57.9	12820.1	3.46x10^{11}	3.50x10^{12}
9	5.89	9.00	53.8	11904.9	3.21x10^{11}	3.25x10^{12}
10	5.89	9.00	49.7	11008.8	2.97x10^{11}	3.00x10^{12}
11	5.89	9.00	45.6	10090.3	2.72x10^{11}	2.75x10^{12}
12	5.89	9.00	41.5	9193.4	2.48x10^{11}	2.51x10^{12}
13	5.89	9.00	37.4	8290.5	2.23x10^{11}	2.26x10^{12}
14	5.89	8.82	34.7	7535.0	2.03x10^{11}	1.98x10^{12}
15	5.89	8.40	34.0	7029.7	1.89x10^{11}	1.67x10^{12}
16	5.89	7.96	33.3	6536.8	1.76x10^{11}	1.40x10^{12}
17	5.89	7.54	32.6	6052.4	1.63x10^{11}	1.16x10^{12}
18	5.89	7.11	31.9	5586.4	1.50x10^{11}	0.95x10^{12}
19	5.89	6.68	31.3	5137.4	1.38x10^{11}	0.77x10^{12}
20	5.89	6.25	30.6	4705.5	1.27x10^{11}	0.62x10^{12}

Table A.1: Tower model properties in Riflex. Data from[8]

Appendix B

Influence of Quadratic Drag.

Motions in the 6DOF.

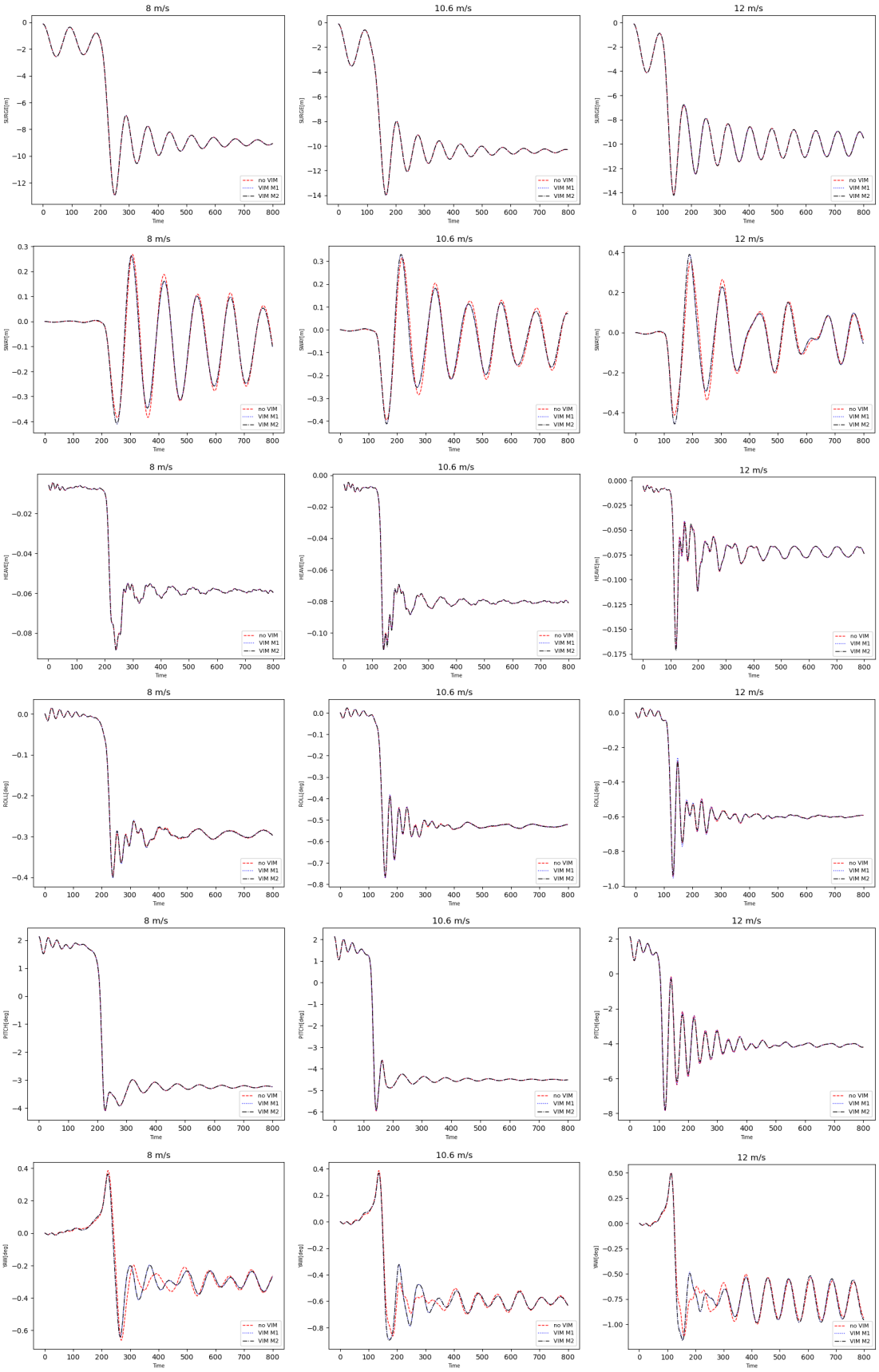

Figure B.1: Motions in 6DOF for different models at two constant wind speeds

Appendix C

Selection of the Experimental data in the Single-Line (SL) Towing condition

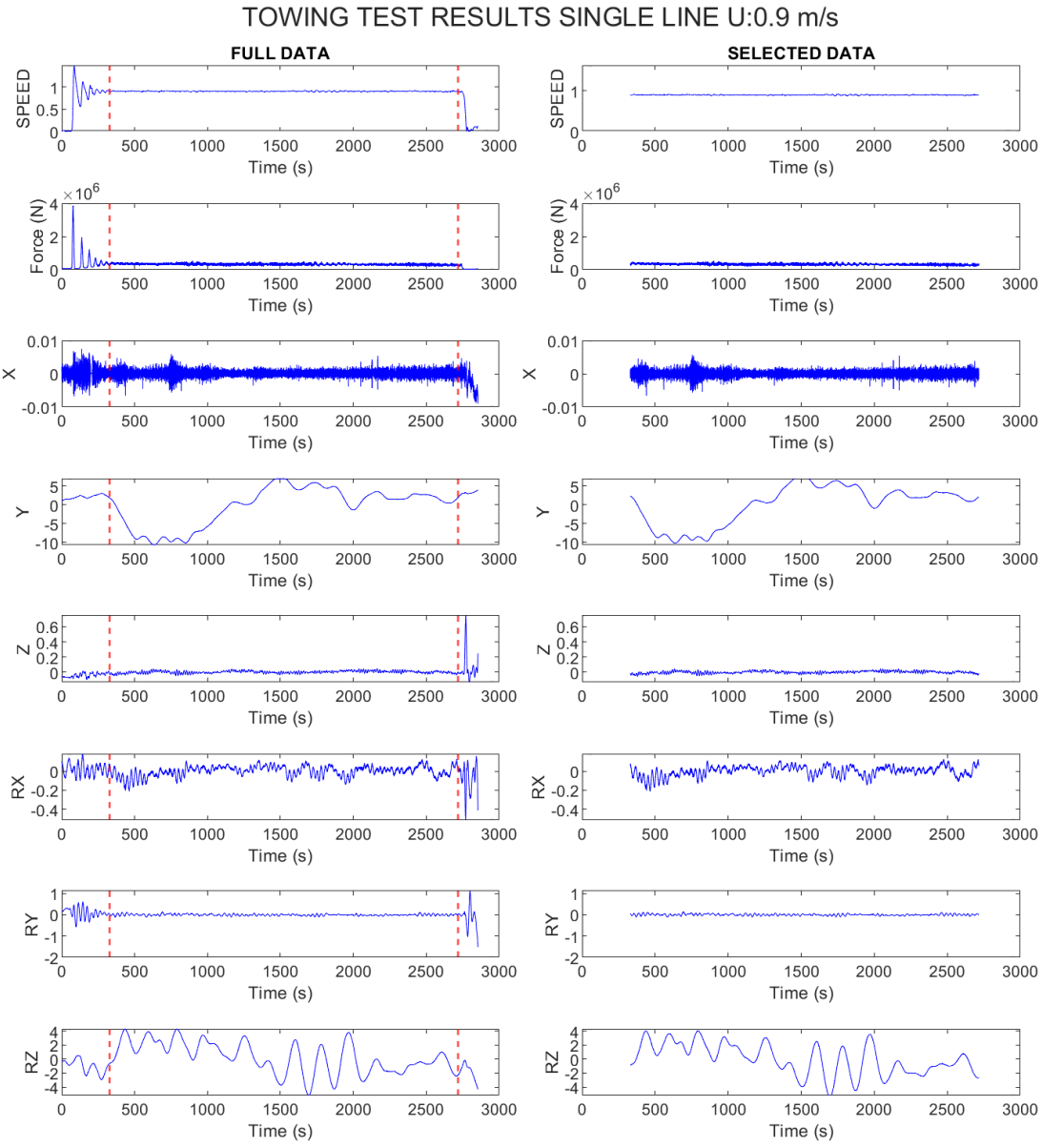

Figure C.1: Data selection for Single-Line (SL) towing condition. The Time series data includes towing speed, towing force, and displacements in the 6DOF at a mean towing speed of 0.9 m/s.

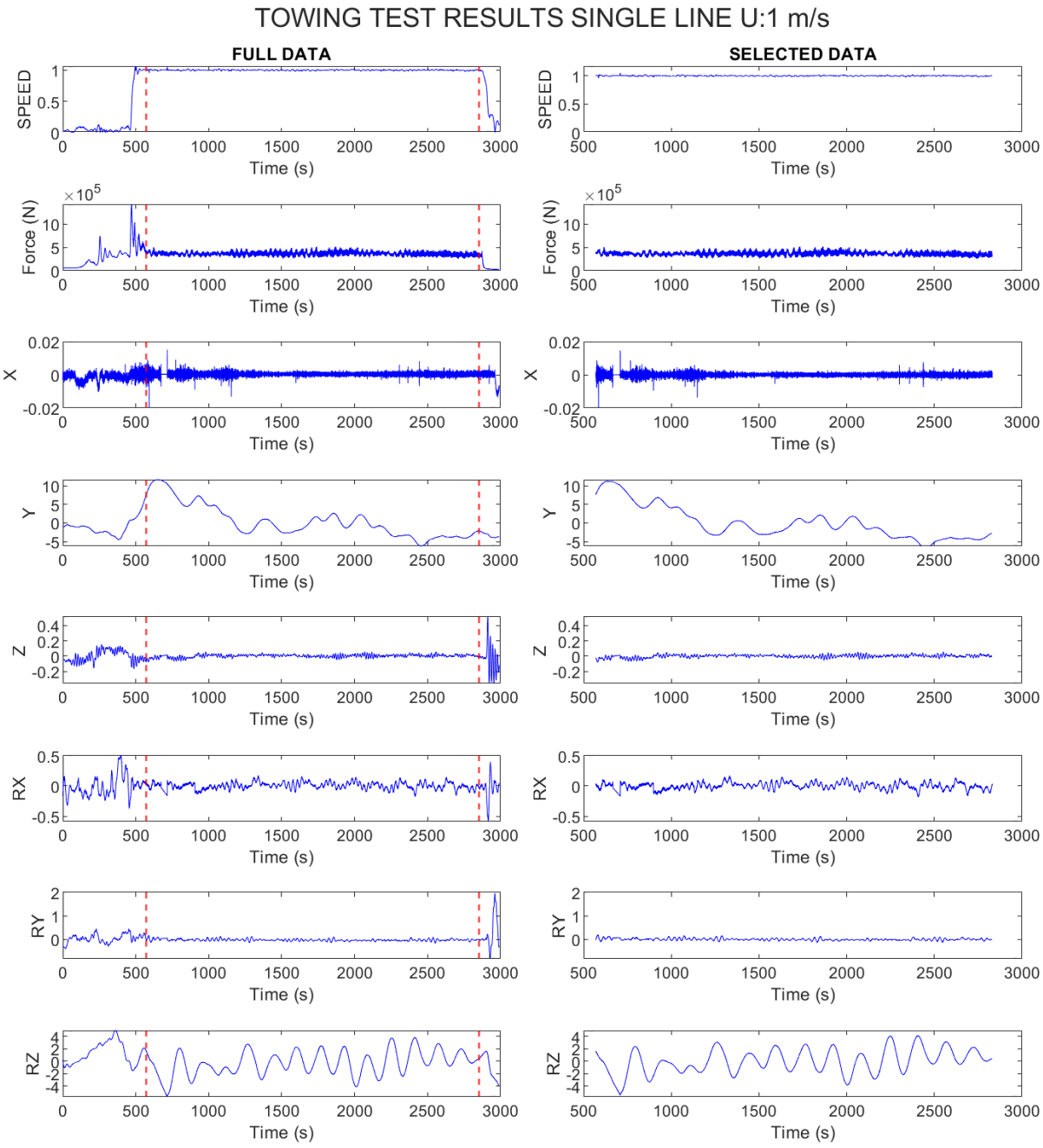

Figure C.2: Data selection for Single-Line (SL) towing condition. The Time series data includes towing speed, towing force, and displacements in the 6DOF at a mean towing speed of 1.0 m/s.

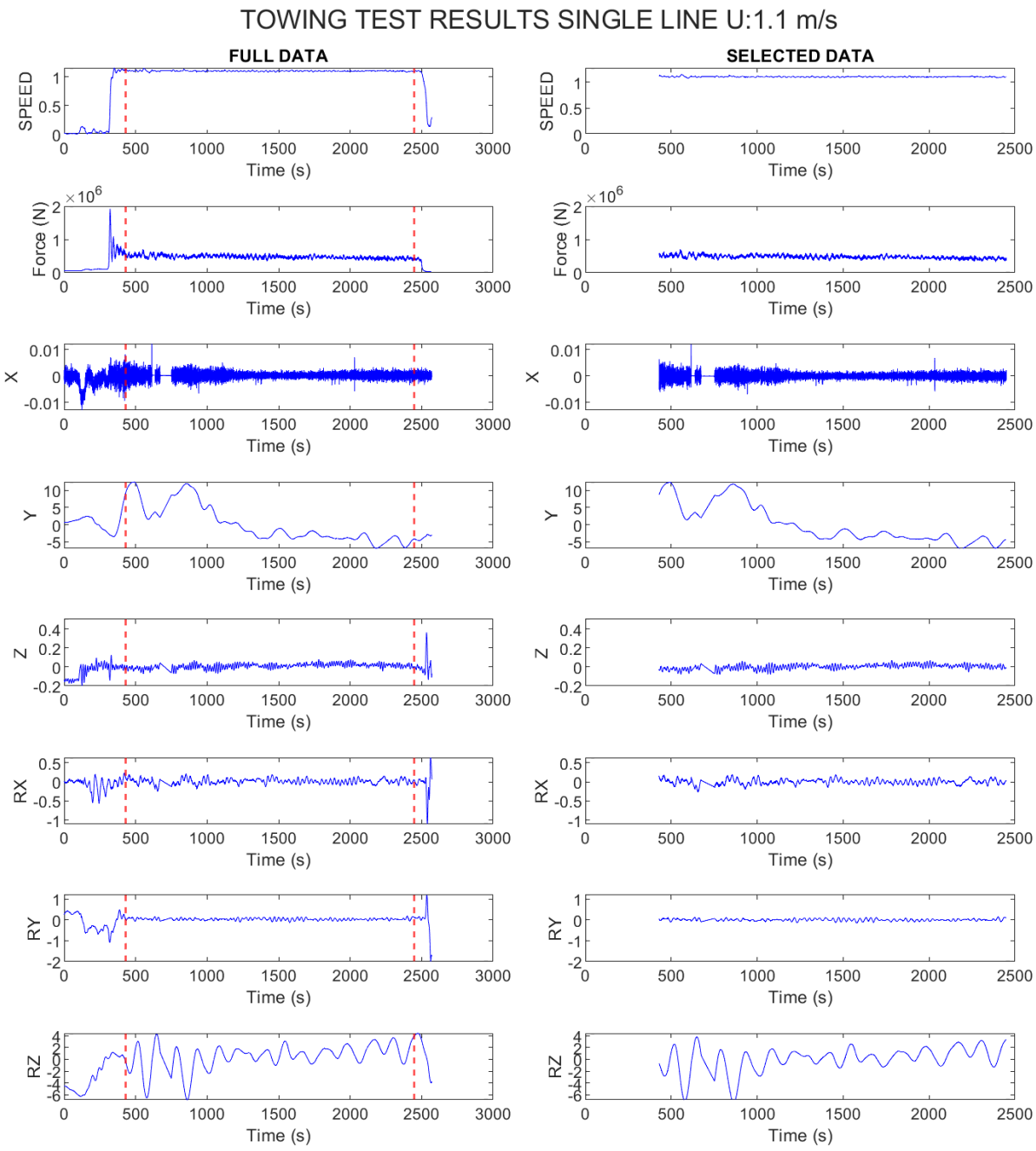

Figure C.3: Data selection for Single-Line (SL) towing condition. The Time series data includes towing speed, towing force, and displacements in the 6DOF at a mean towing speed of 1.1.0 m/s.

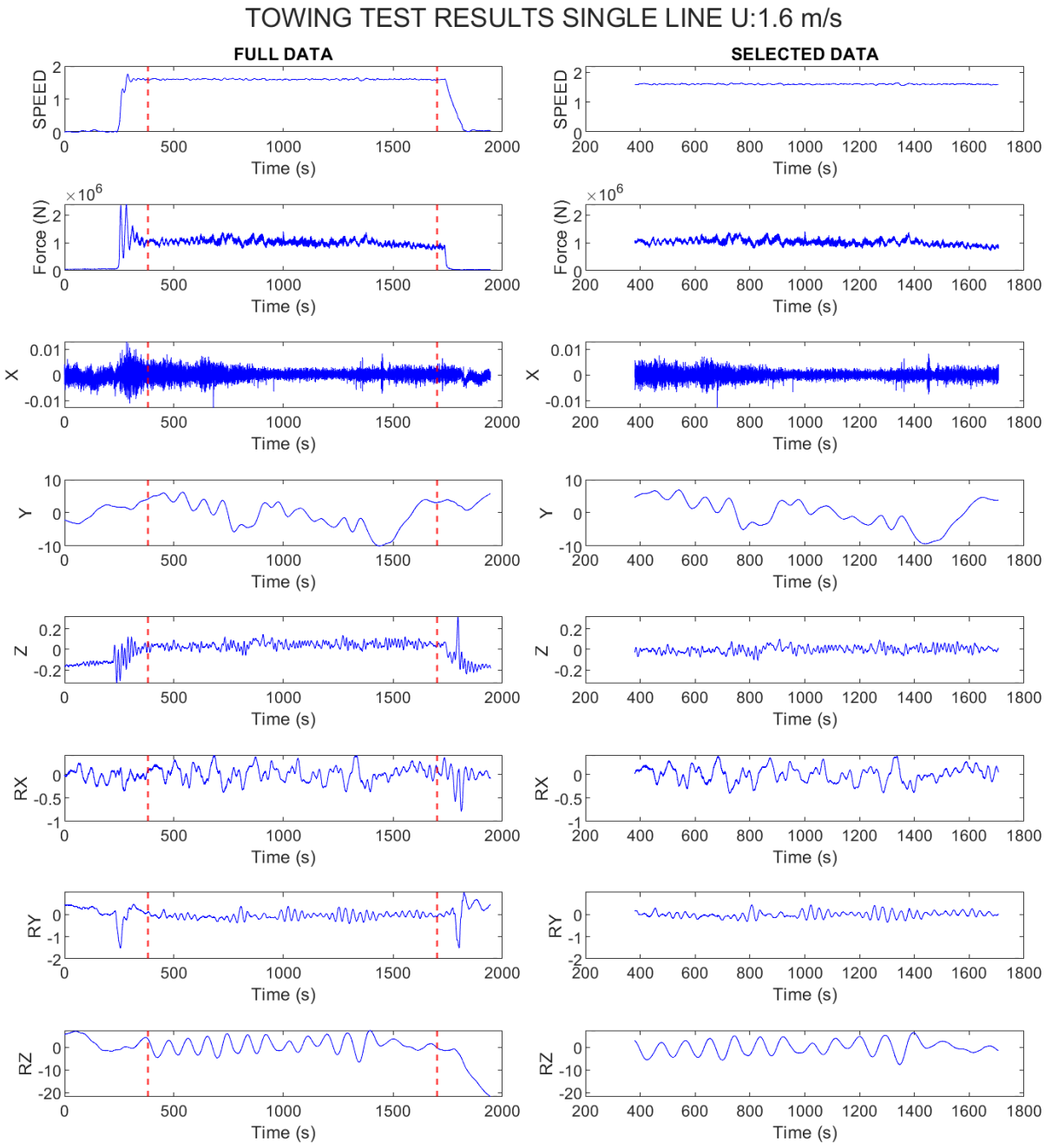

Figure C.4: Data selection for Single-Line (SL) towing condition. The Time series data includes towing speed, towing force, and displacements in the 6DOF at a mean towing speed of 1.6 m/s.

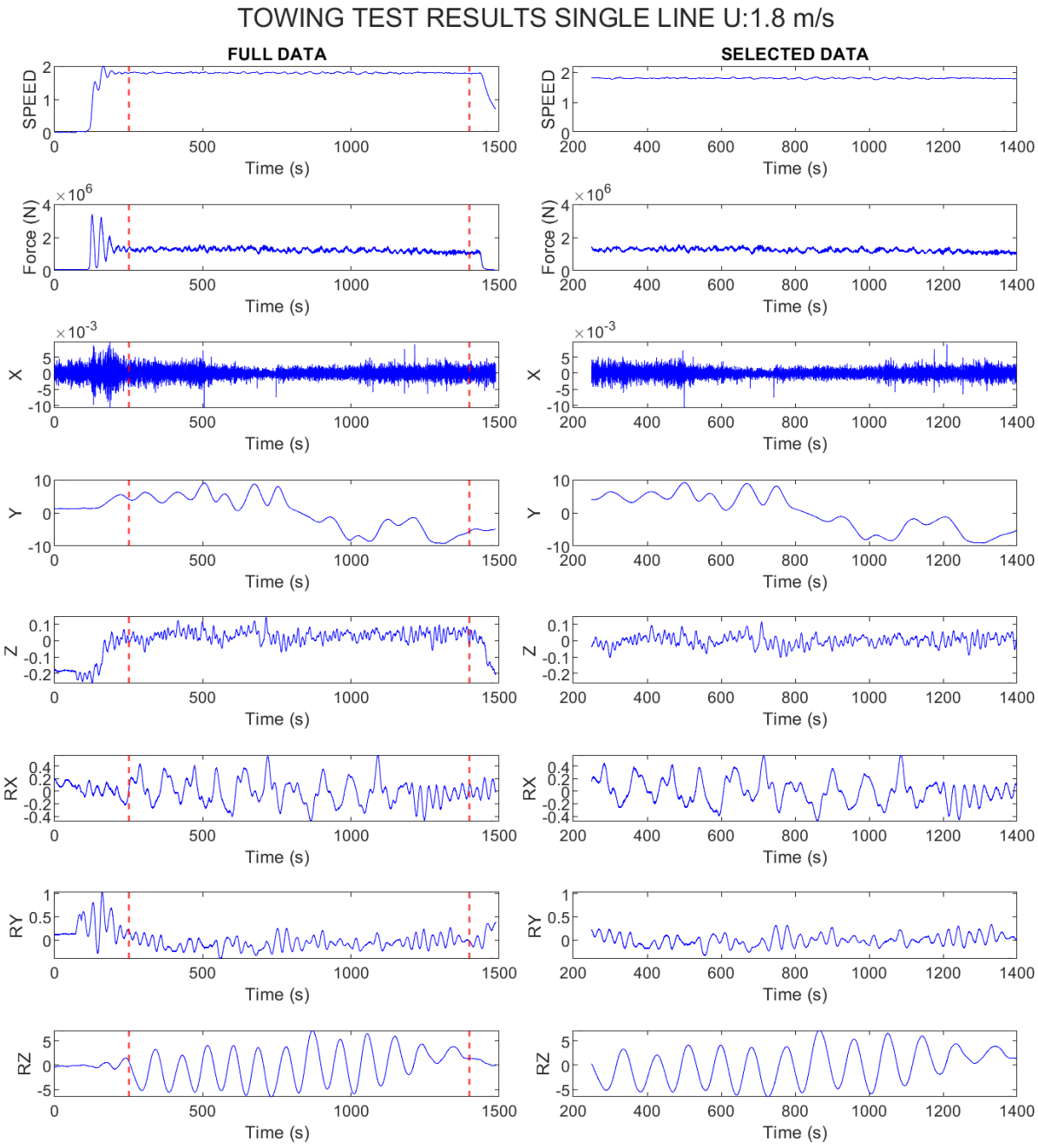

Figure C.5: Data selection for Single-Line (SL) towing condition. The Time series data includes towing speed, towing force, and displacements in the 6DOF at a mean towing speed of 1.8 m/s.

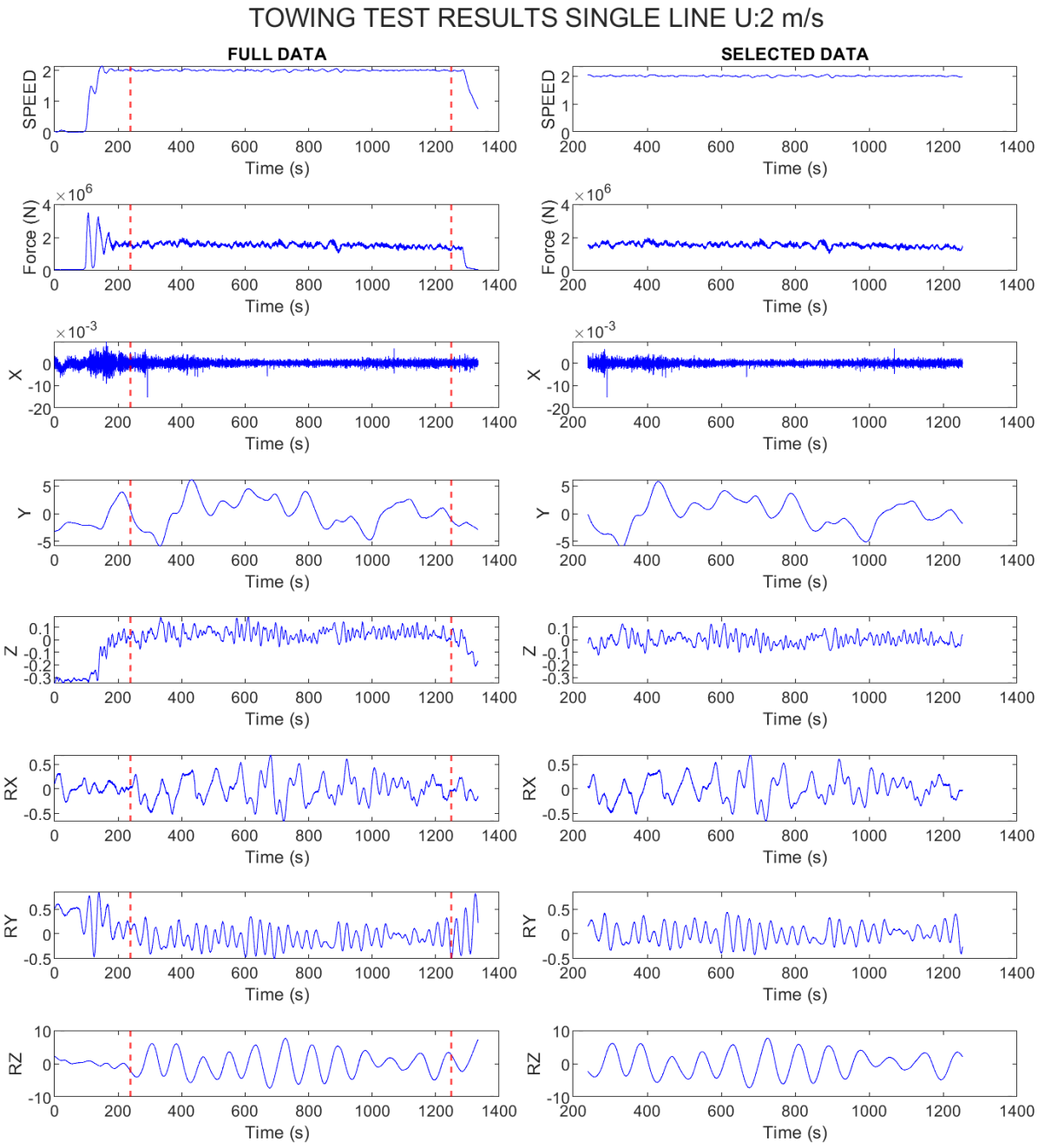

Figure C.6: Data selection for Single-Line (SL) towing condition. The Time series data includes towing speed, towing force, and displacements in the 6DOF at a mean towing speed of 2.0 m/s.

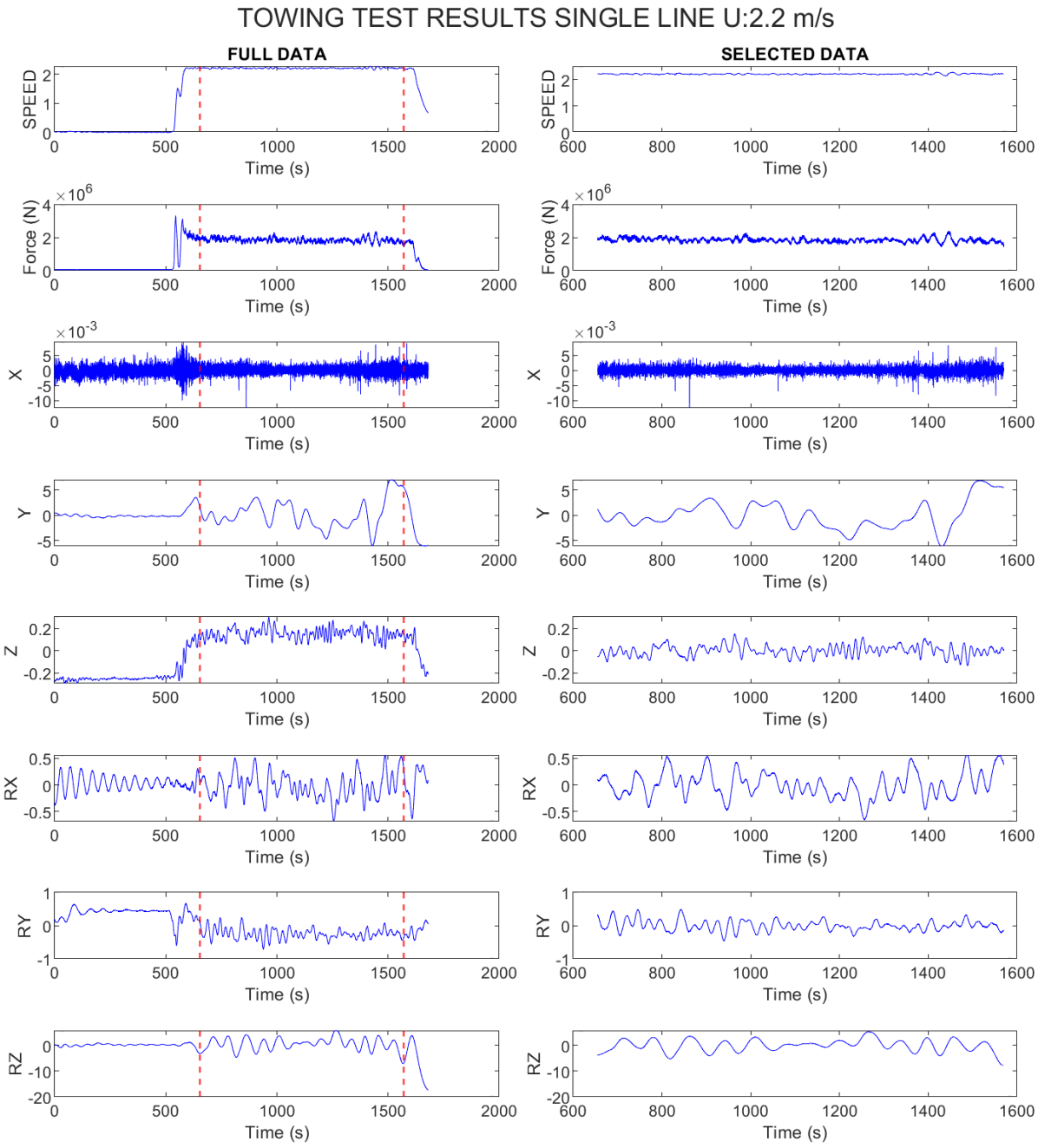

Figure C.7: Data selection for Single-Line (SL) towing condition. The Time series data includes towing speed, towing force, and displacements in the 6DOF at a mean towing speed of 2.2.0 m/s.

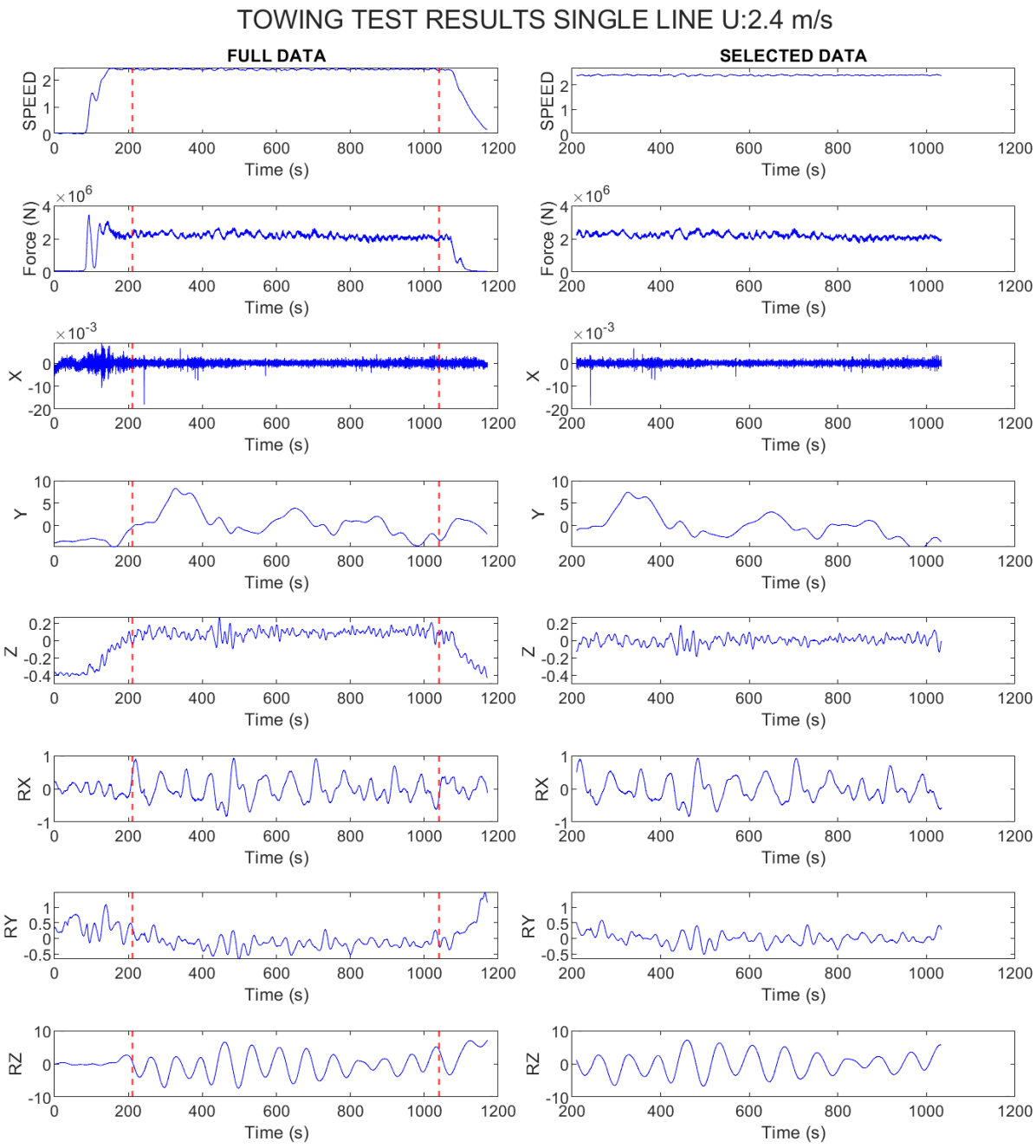

Figure C.8: Data selection for Single-Line (SL) towing condition. The Time series data includes towing speed, towing force, and displacements in the 6DOF at a mean towing speed of 2.4 m/s.

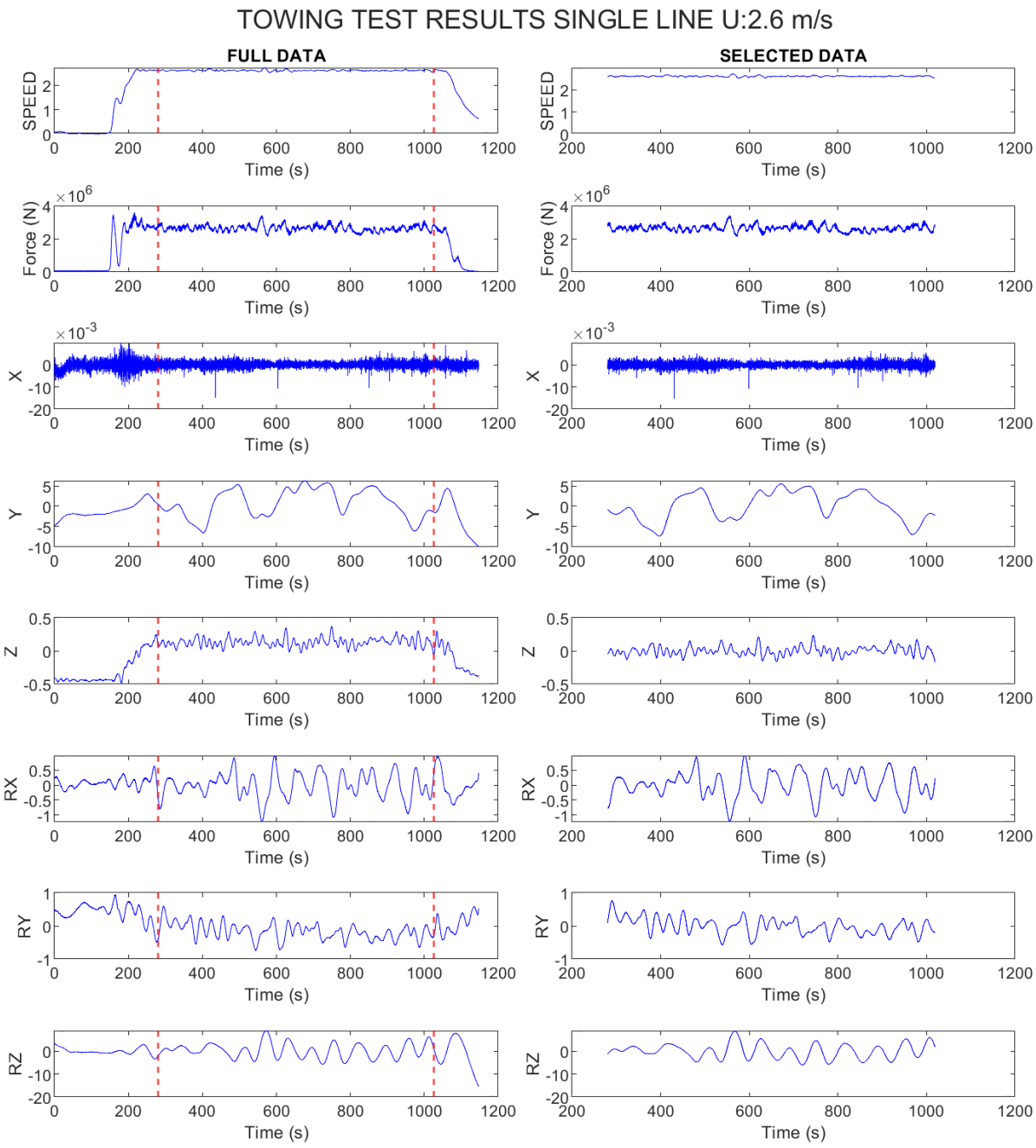

Figure C.9: Data selection for Single-Line (SL) towing condition. The Time series data includes towing speed, towing force, and displacements in the 6DOF at a mean towing speed of 2.6 m/s.

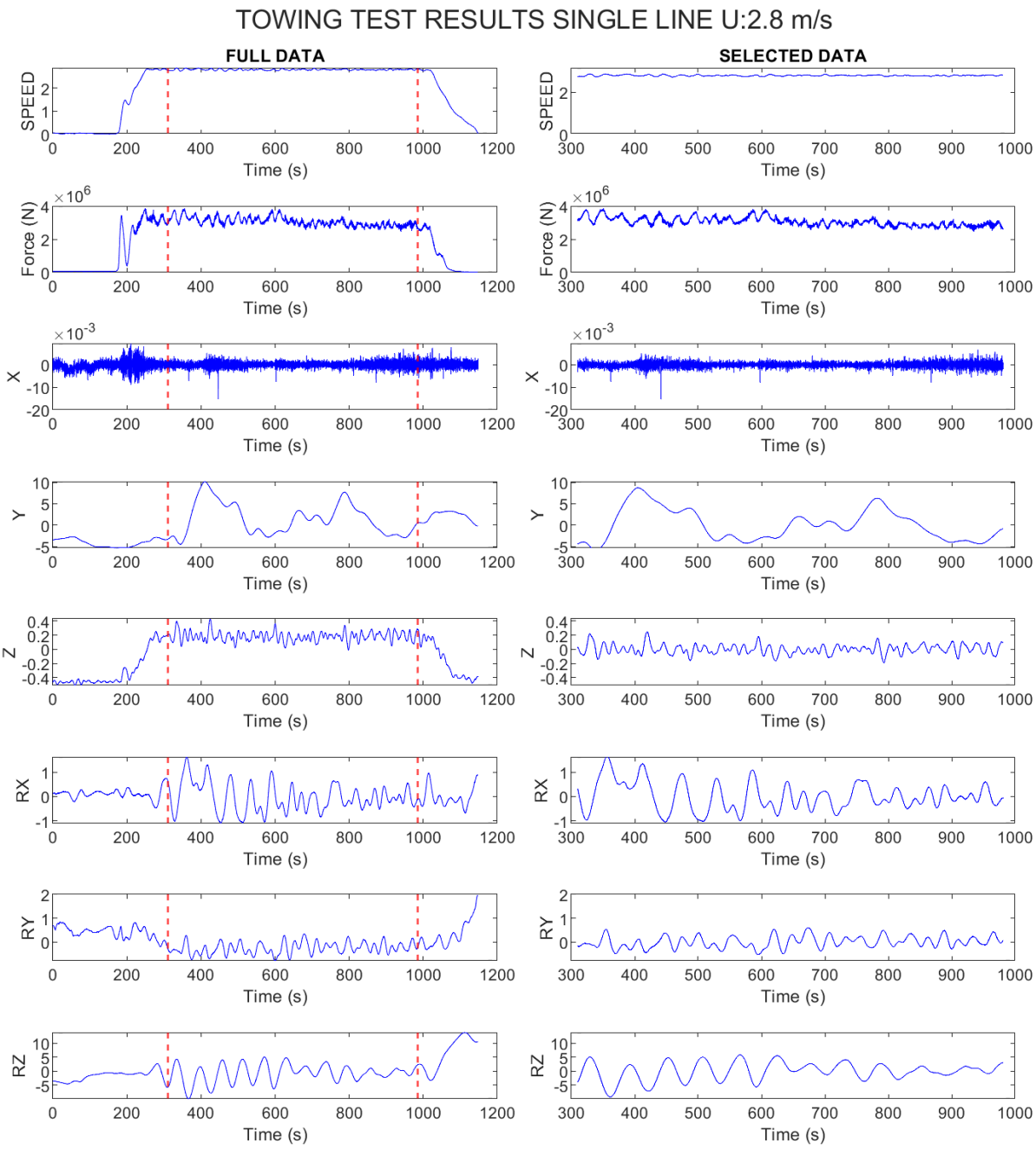

Figure C.10: Data selection for Single-Line (SL) towing condition. The Time series data includes towing speed, towing force, and displacements in the 6DOF at a mean towing speed of 2.8 m/s.

Appendix D

Selection of the Experimental data in the Two-Bridle (2B) Towing condition

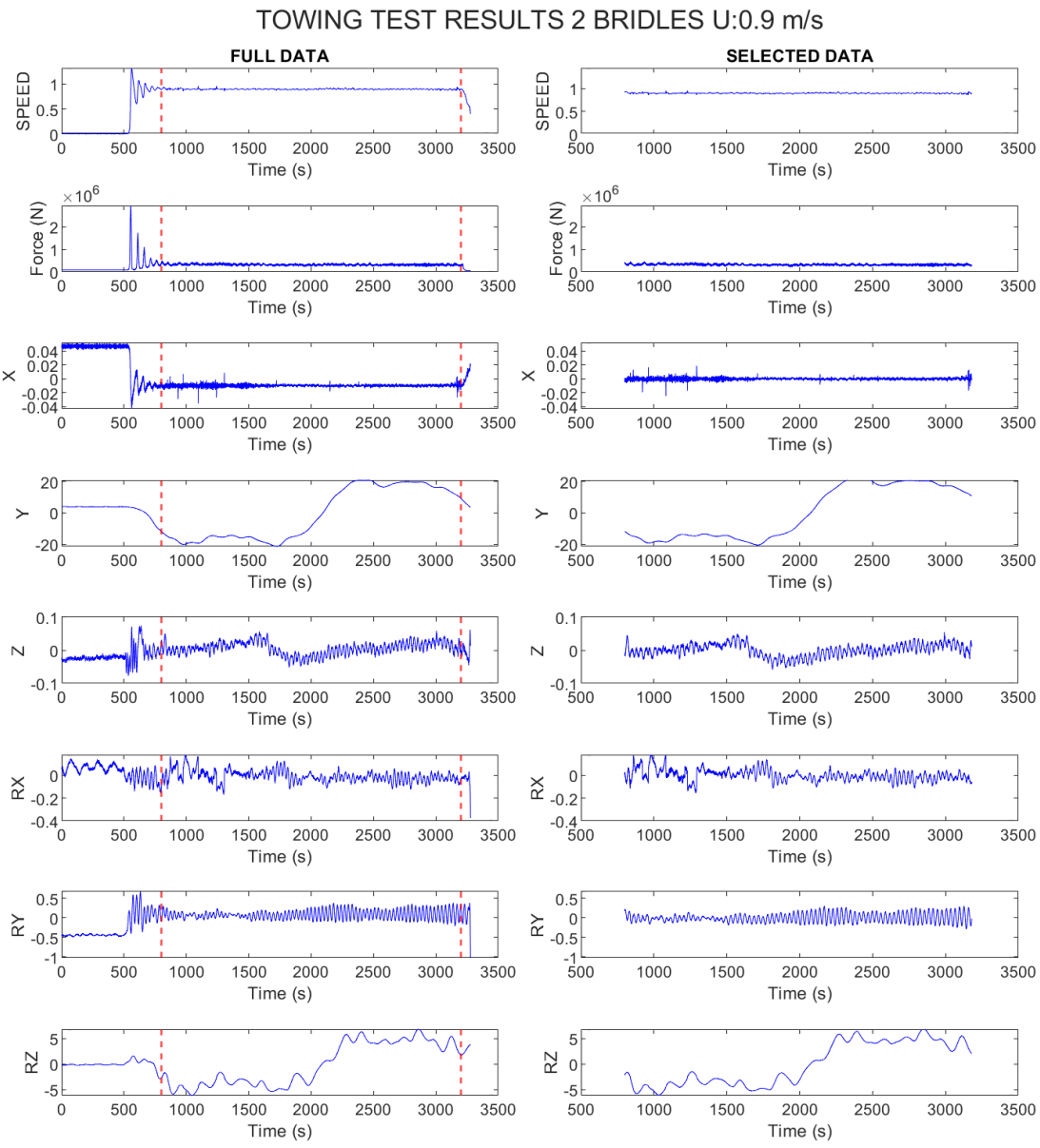

Figure D.1: Data selection for Two-Bridle (2B) towing condition. The Time series data includes towing speed, towing force, and displacements in the 6DOF at a mean towing speed of 0.9 m/s.

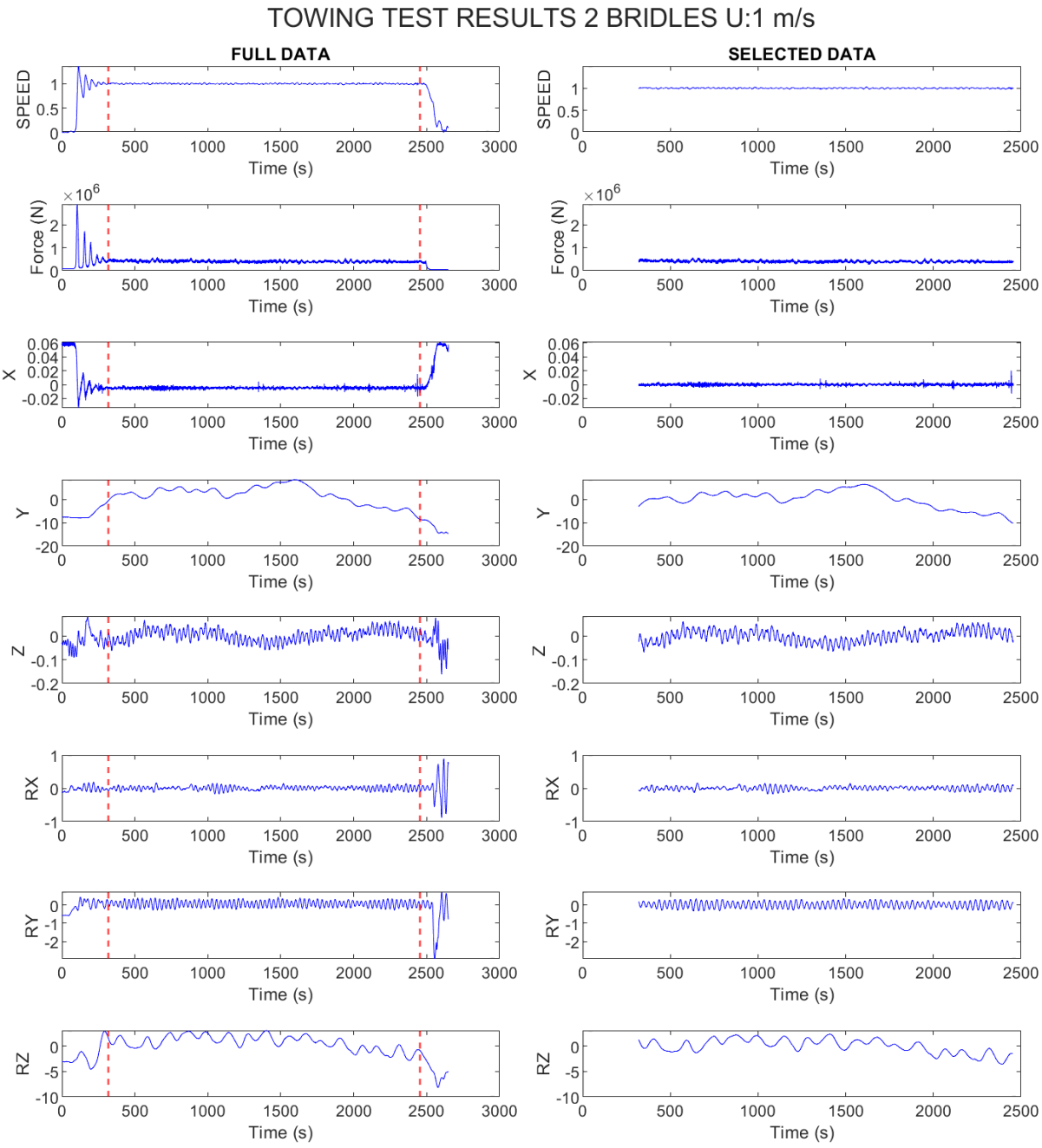

Figure D.2: Data selection for Two-Bridle (2B) towing condition. The Time series data includes towing speed, towing force, and displacements in the 6DOF at a mean towing speed of 1.0 m/s.

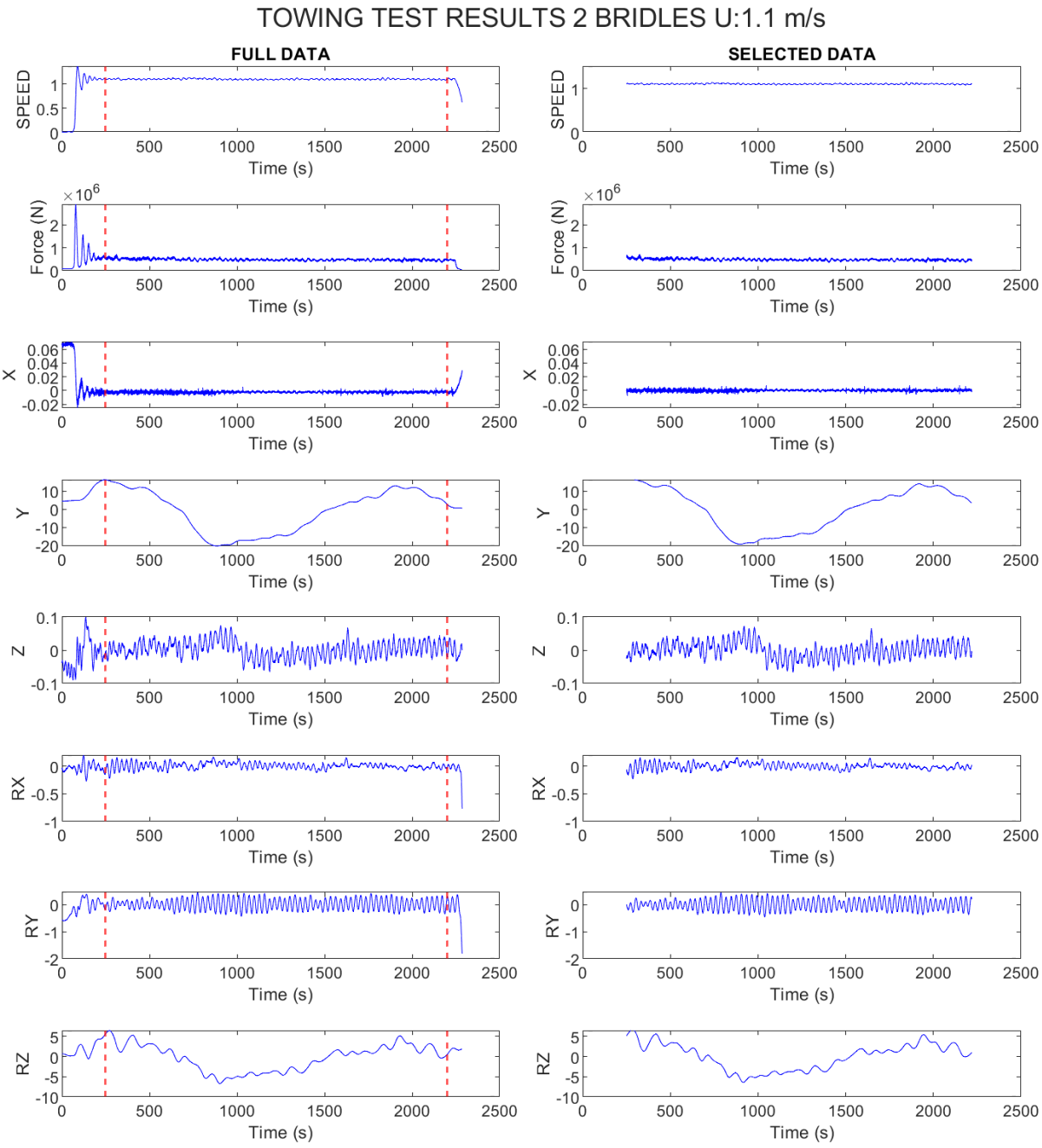

Figure D.3: Data selection for Two-Bridle (2B) towing condition. The Time series data includes towing speed, towing force, and displacements in the 6DOF at a mean towing speed of 1.1.0 m/s.

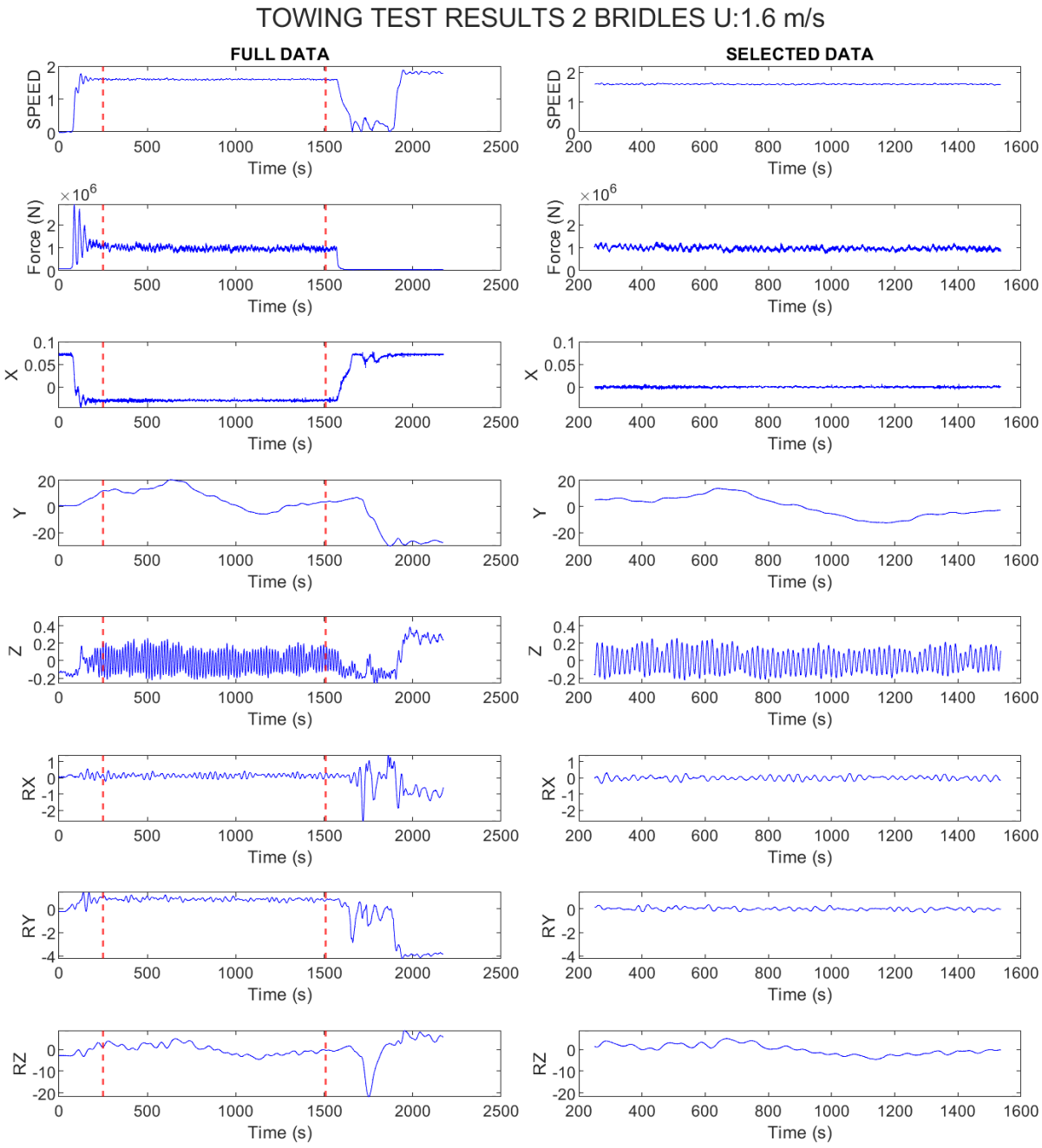

Figure D.4: Data selection for Two-Bridle (2B) towing condition. The Time series data includes towing speed, towing force, and displacements in the 6DOF at a mean towing speed of 1.6 m/s.

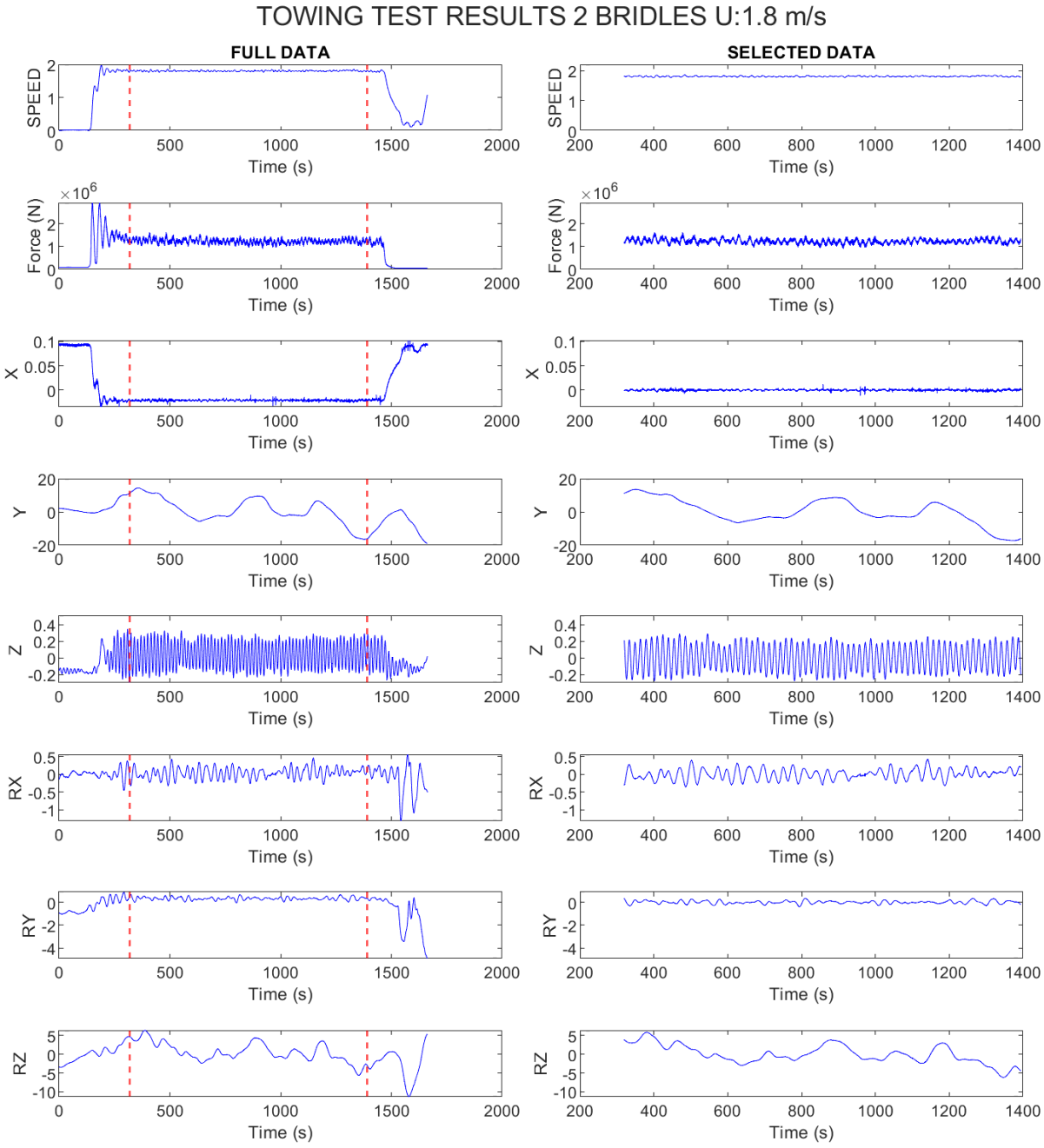

Figure D.5: Data selection for Two-Bridle (2B) towing condition. The Time series data includes towing speed, towing force, and displacements in the 6DOF at a mean towing speed of 1.8 m/s.

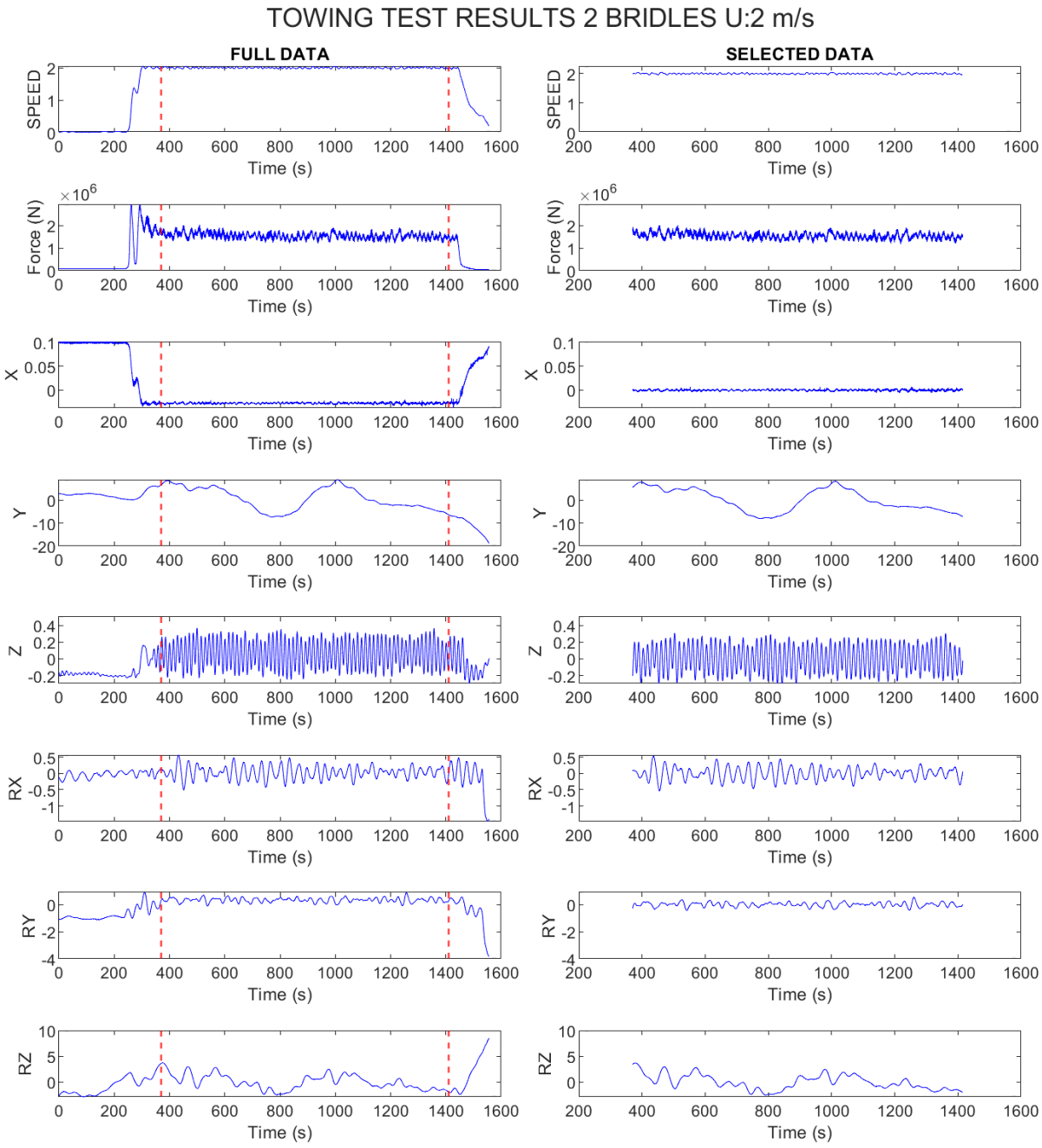

Figure D.6: Data selection for Two-Bridle (2B) towing condition. The Time series data includes towing speed, towing force, and displacements in the 6DOF at a mean towing speed of 2.0 m/s.

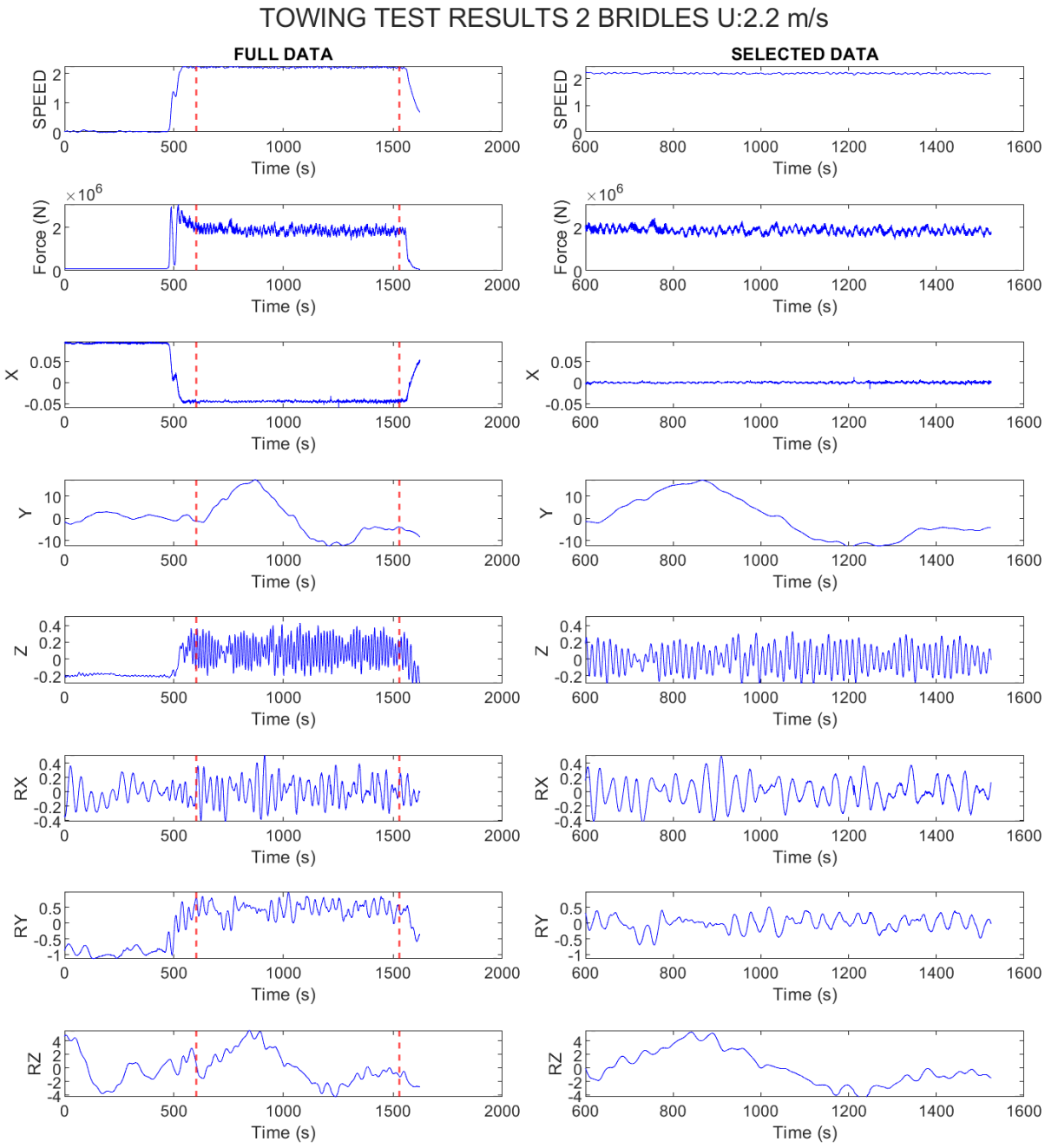

Figure D.7: Data selection for Two-Bridle (2B) towing condition. The Time series data includes towing speed, towing force, and displacements in the 6DOF at a mean towing speed of 2.2.0 m/s.

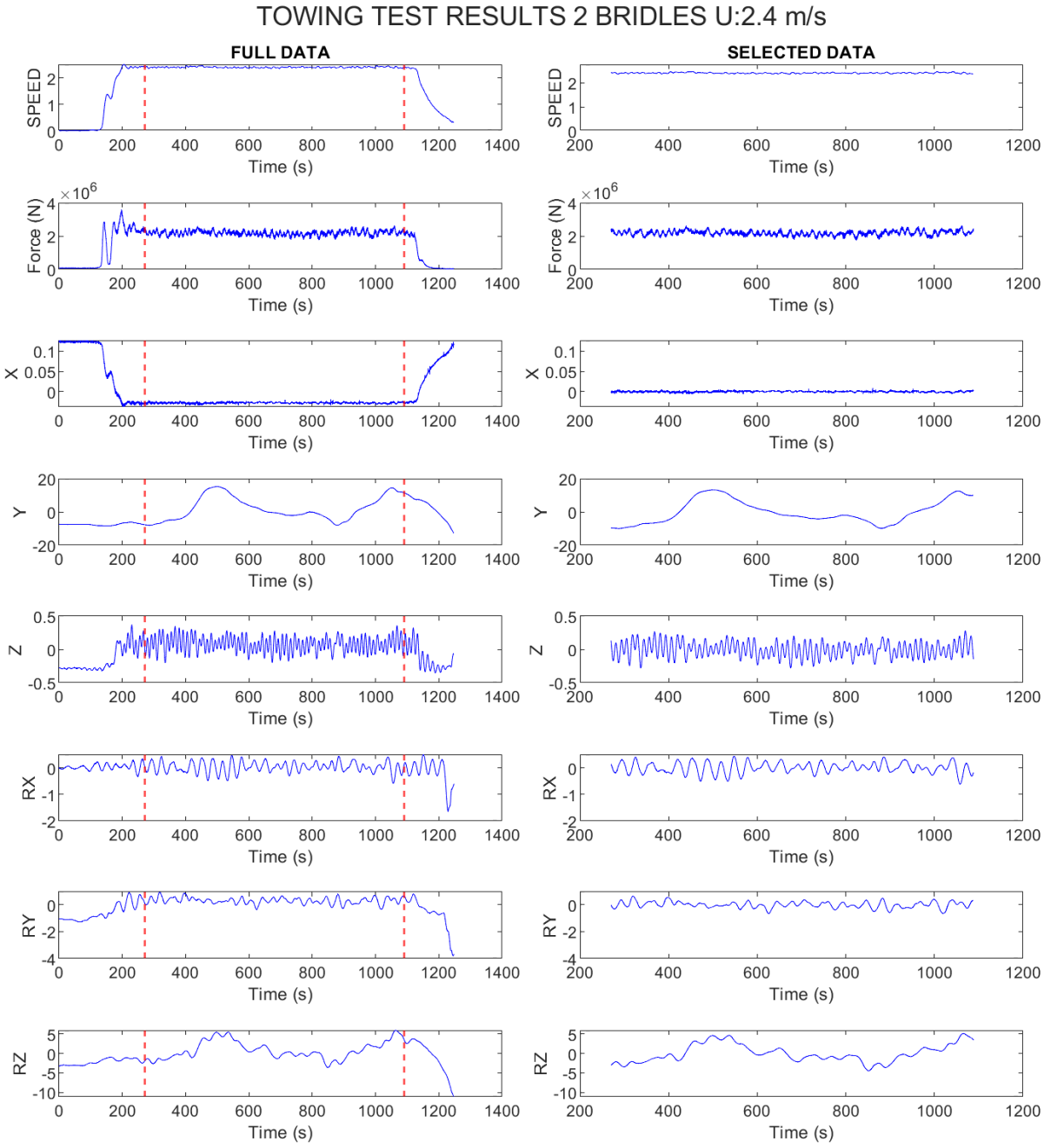

Figure D.8: Data selection for Two-Bridle (2B) towing condition. The Time series data includes towing speed, towing force, and displacements in the 6DOF at a mean towing speed of 2.4 m/s.

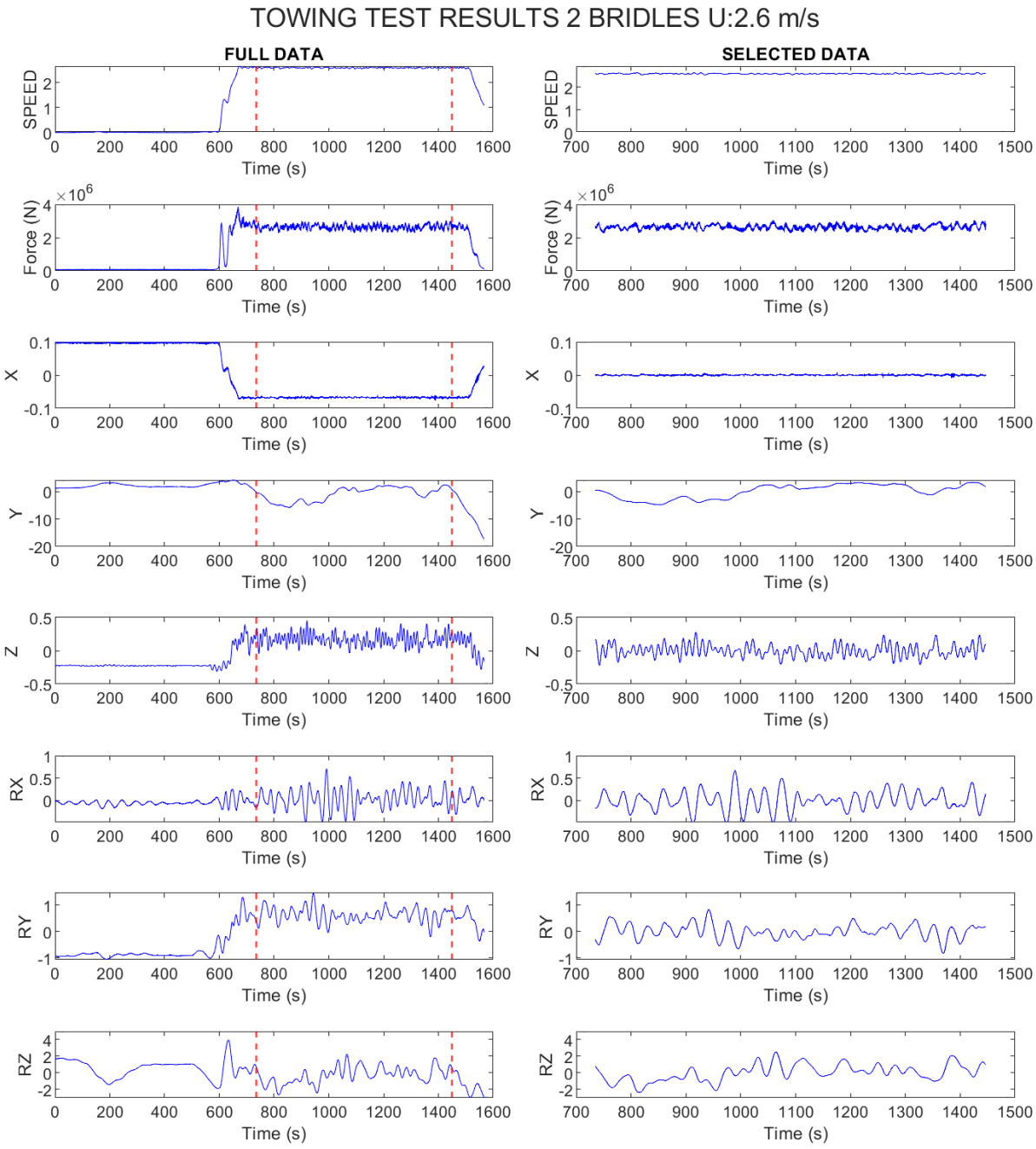

Figure D.9: Data selection for Two-Bridle (2B) towing condition. The Time series data includes towing speed, towing force, and displacements in the 6DOF at a mean towing speed of 2.6 m/s.

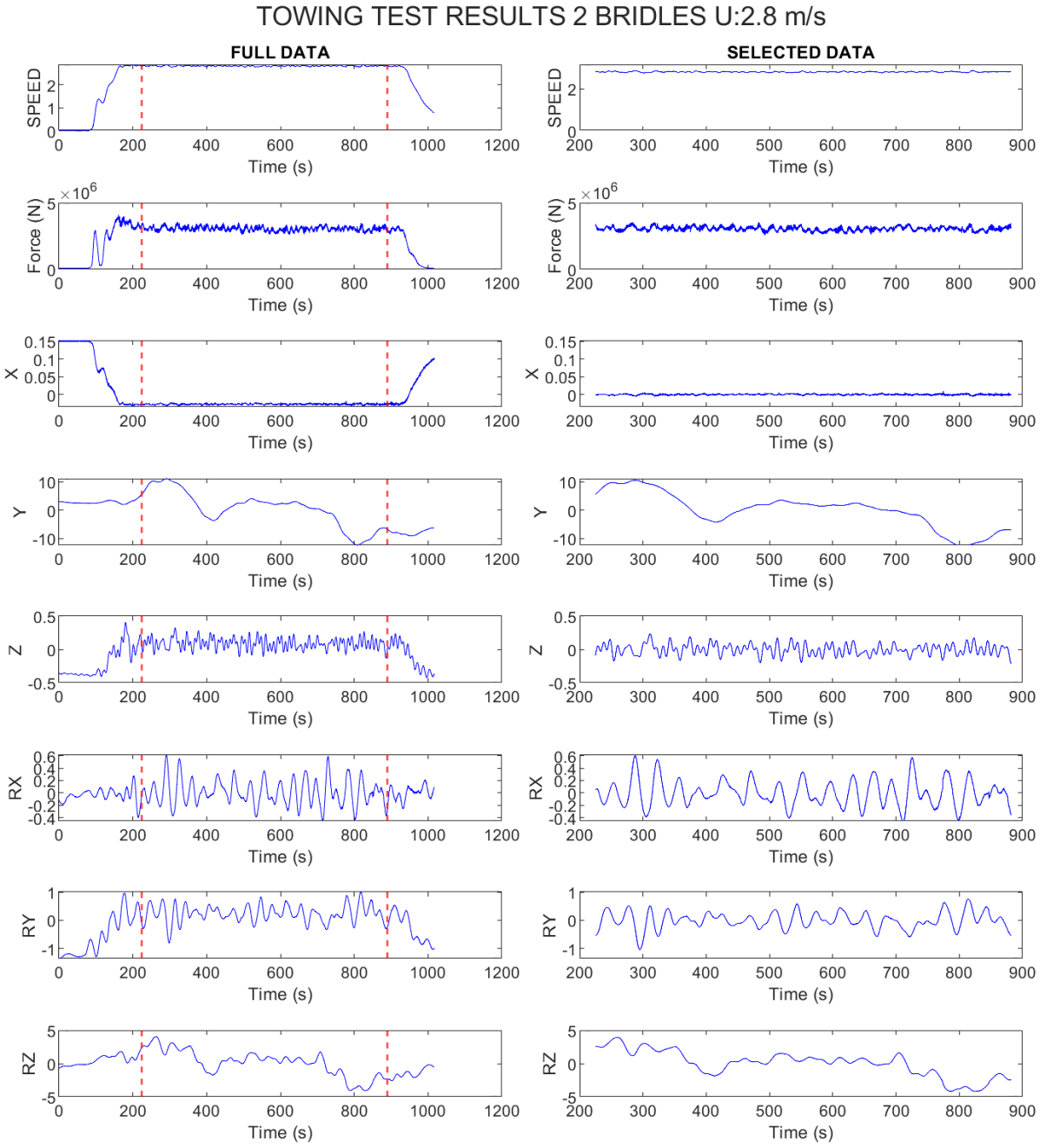

Figure D.10: Data selection for Two-Bridle (2B) towing condition. The Time series data includes towing speed, towing force, and displacements in the 6DOF at a mean towing speed of 2.8 m/s.

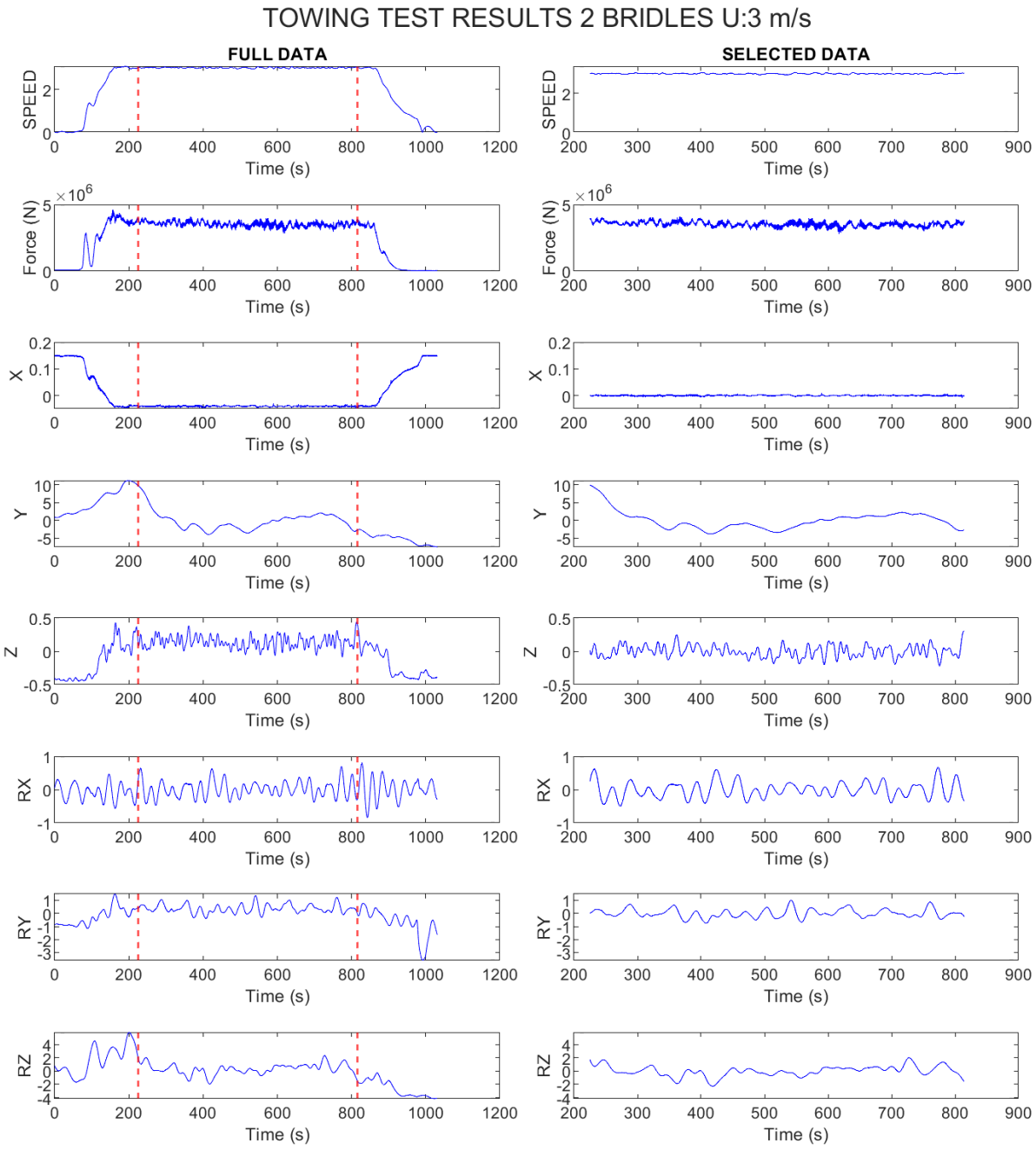

Figure D.11: Data selection for Two-Bridle (2B) towing condition. The Time series data includes towing speed, towing force, and displacements in the 6DOF at a mean towing speed of 3.0 m/s.

Appendix E

Displacements in the two towing conditions at different current speeds

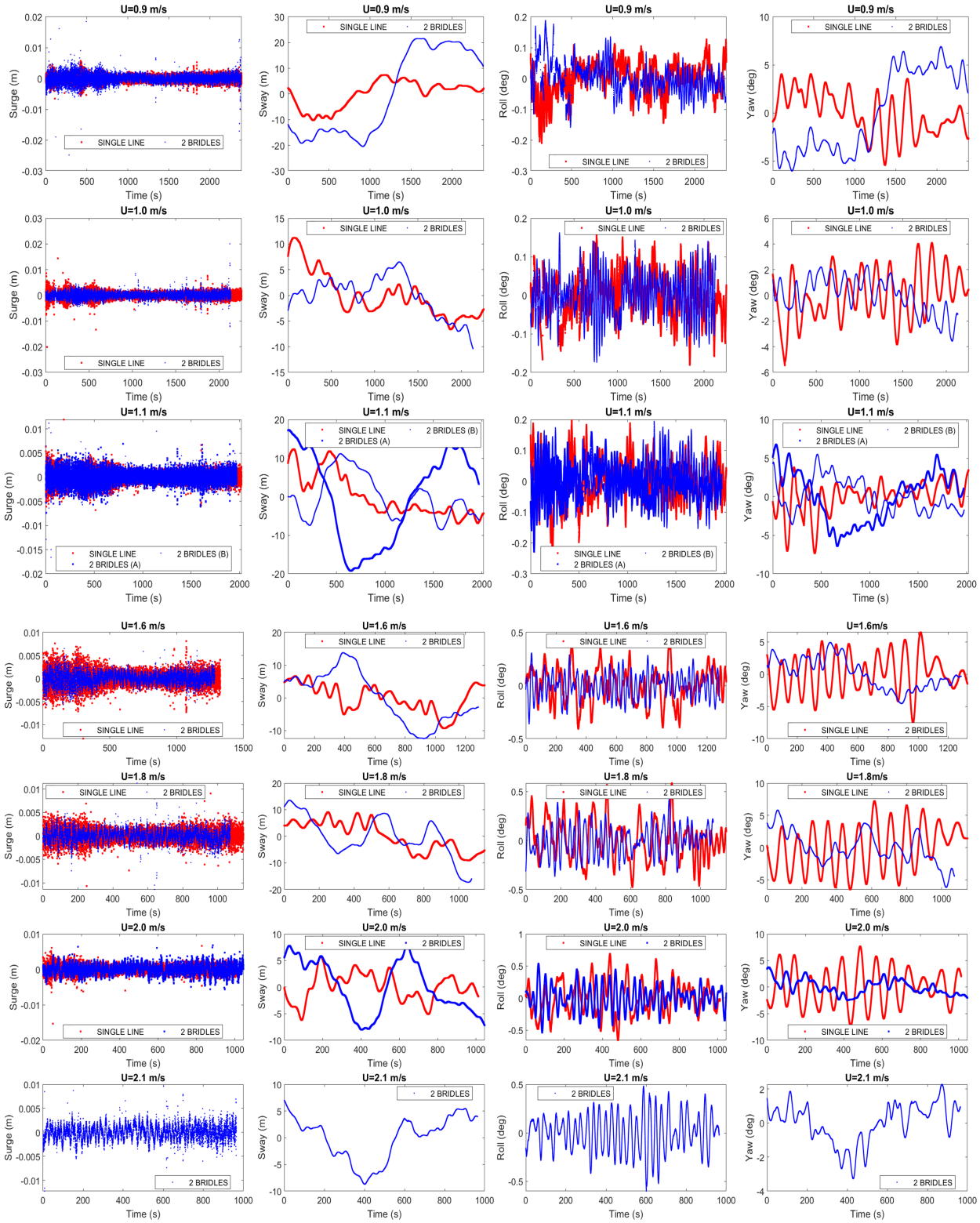

Figure E.1: Surge (X), Sway (Y), Roll (RX), and Yaw (RZ) displacements in both, Single-Line (SL) and Two-Bridle (2B) towing condition, at different current speeds. (1)

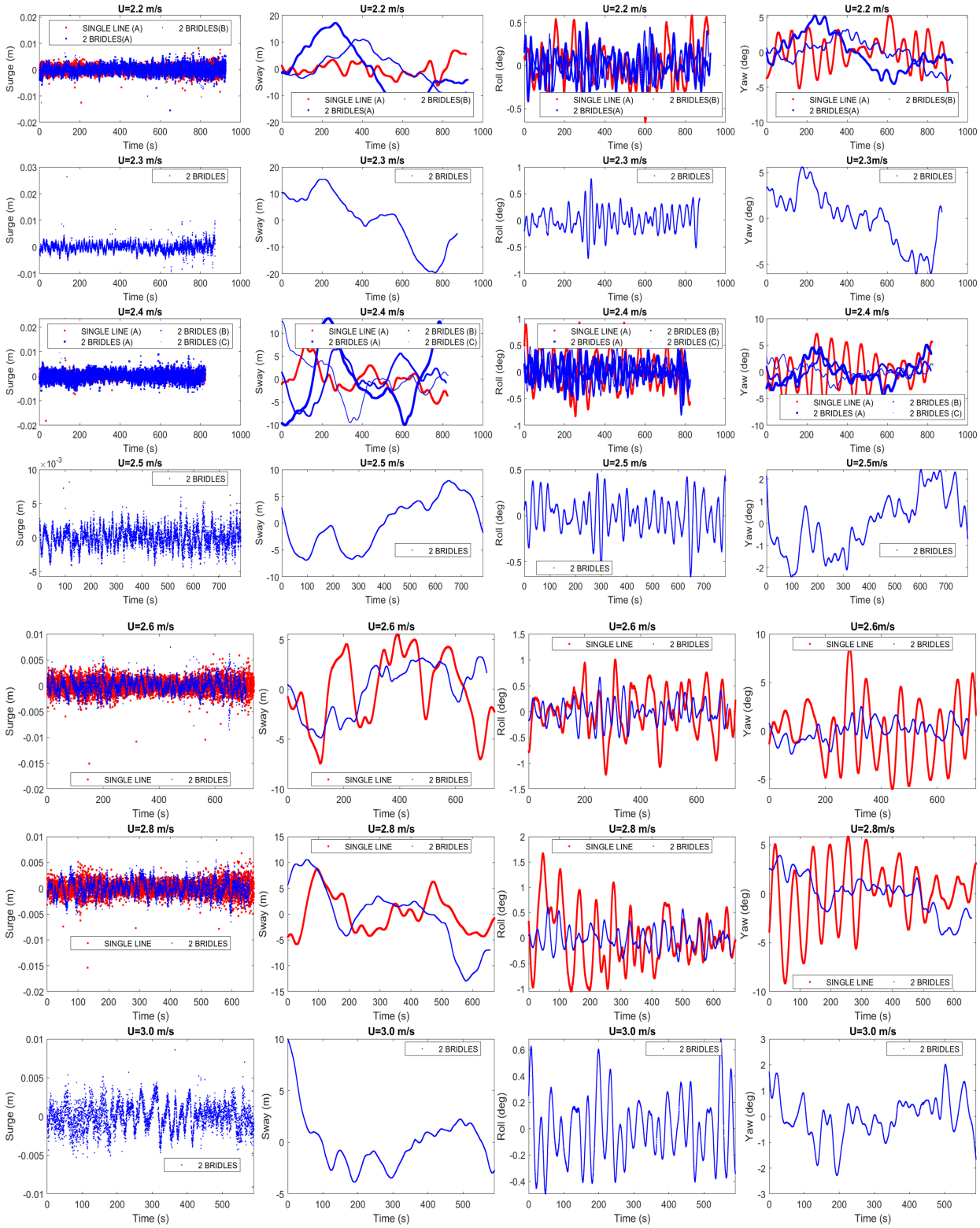

Figure E.2: Surge (X), Sway (Y), Roll (RX), and Yaw (RZ) displacements in both, Single-Line (SL) and Two-Bridle (2B) towing condition, at different current speeds. (2)

Appendix F

Comparison of Matlab's functions for Spectral Analysis

After processing the results, a frequency response analysis is required to determine the frequencies from the 6DOF motion and the towing force.

In Matlab, there are various signal processing tools, one of them is the Periodogram method which allows the identification of dominant frequencies from time series data. When the function is called as $[pxx, f] = periodogram(x, window, fo, fs)$, it returns the Power Spectral Density (PSD) (PSD) estimate pxx and a frequency vector f. The PSD is in squared magnitude units of the time series data per unit frequency (u^2/Hz), and f in samples per unit time (Hz) [43]. The input parameters are as follows:

- x is the input vector,
- $window$ is a parameter used to divide the signal into segments, according to the Periodogram approach. Several options of windows are available, and for the analysis, two types were tested, the so-called rectangular window, and the Hamming window, with segments equal to the length of the input signal.
- fo represents the points of the Discrete Fourier transform (DFT). The default value is 256 or the maximum is found with the function of the next power of two (2^p) where $p = log_2(length(x))$. For this analysis, the length was chosen similar to the length of the input vector x.
- fs is the sample rate in unit time (Hz). As mentioned before, the sample rate during the test was 0.0316s or 31.65Hz.

SINTEF uses a similar approach to analyse the frequency of time series data. This method uses the Fast Fourier Transform (FFT) to calculate the one-sided Power Density Spectrum of the vector containing the signal.

The function is called $[S, df] = powspec(x, dt)$, where x is the input vector and dt is the sample

Method	window	f_o	f_s	dt
Periodogram	Rectangular	$length(x) * 2$	$1/0.0316$	-
Periodogram	Hamming	$length(x) * 1$	$1/0.0316$	-
Sintef Powspec	-	-	-	0.0316

Table F.1: Parameters for three Frequency Response methods. x represents the input signal.

rate of the test in unit time (s). The result is the vector S which is the one-sided Power Spectral Density (PSD) (PSD) estimate, and the frequency df at S(1), the so-called zero-frequency value of the power density [43].

As a definition, the integral of the spectrum is equivalent to the variance of the input vector x [43]. Also, it is important to mention that before the analysis, the mean value of the input vector x must be reduced, therefore, only the dynamic part of the signal is analysed in the spectral analysis.

In this thesis, R is the ratio between the integral of the PSD curve and the variance. This parameter allowed the evaluation of the three methods to determine the effectiveness for subsequent analysis.

$$\left(R = \frac{PSD_{Area}}{variance(x)}\right) \tag{F.1}$$

The assessment was done to the Force, Surge, Sway, and Roll in the two towing conditions at 2.0 m/s. Table F.2 shows the R parameter of the PSD curve for the towing force in the two towing conditions. Sintef Powspec's approach shows a good agreement with the Periodogram-Rectangular window method for the frequency response of the towing force.

Method	R_{SL}	R_{2B}
Periodogram Rectangular window	1.00	1.00
Periodogram Hamming window	0.88	0.88
Sintef Powspec	0.92	0.97

Table F.2: R value for the Force signal in Single-Line (SL) and Two-Bridle (2B) towing condition

Table F.3 shows the R parameter of the PSD curve for the Sway response in the two towing conditions, results showed good agreement between all methods. Similar results were found for Surge and Roll.

Method	R_{SL}	R_{2B}
Periodogram Rectangular window	1.00	1.00
Periodogram Hamming window	0.87	1.15
Sintef Powspec	0.89	0.99

Table F.3: R value for the Sway signal in Single-Line (SL) and Two-Bridle (2B) towing condition, with similar results for Surge and Roll.

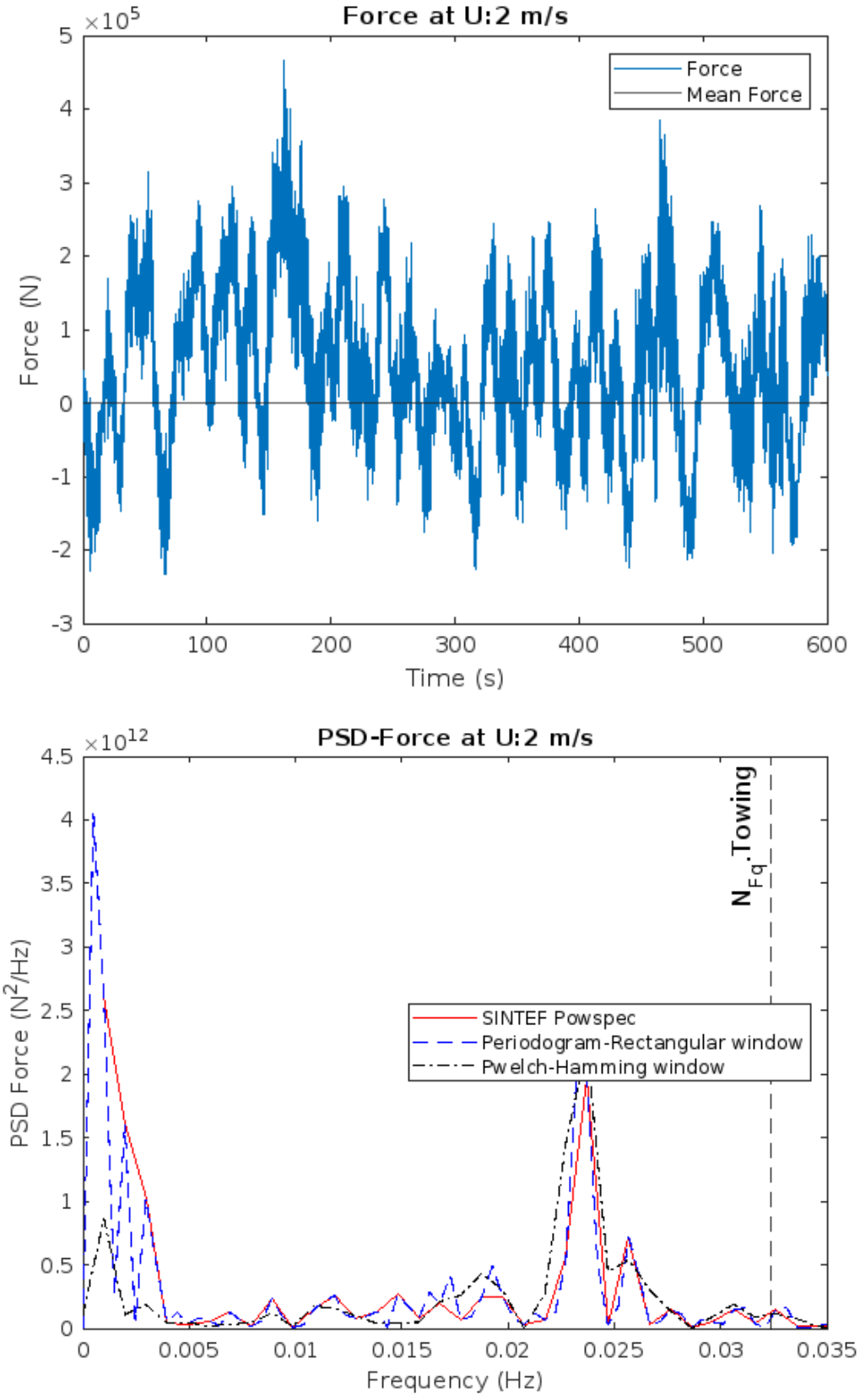

Figure F.1: Spectral and Time Series data of the Force, using three approaches for the analysis. Single-Line (SL) towing condition.

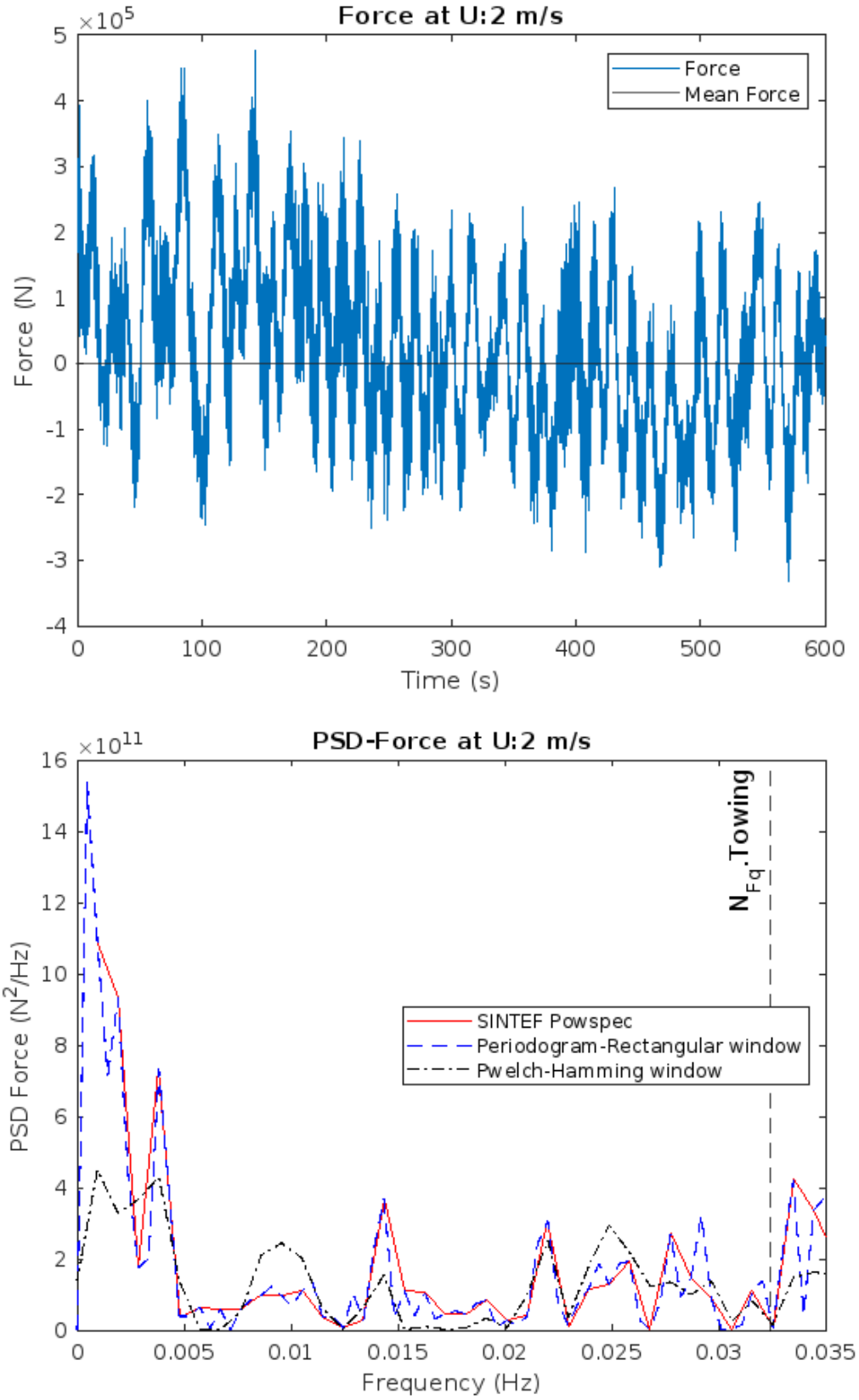

Figure F.2: Spectral and Time Series data of the Force, using three approaches for the analysis. Two-Bridle (2B) towing condition.

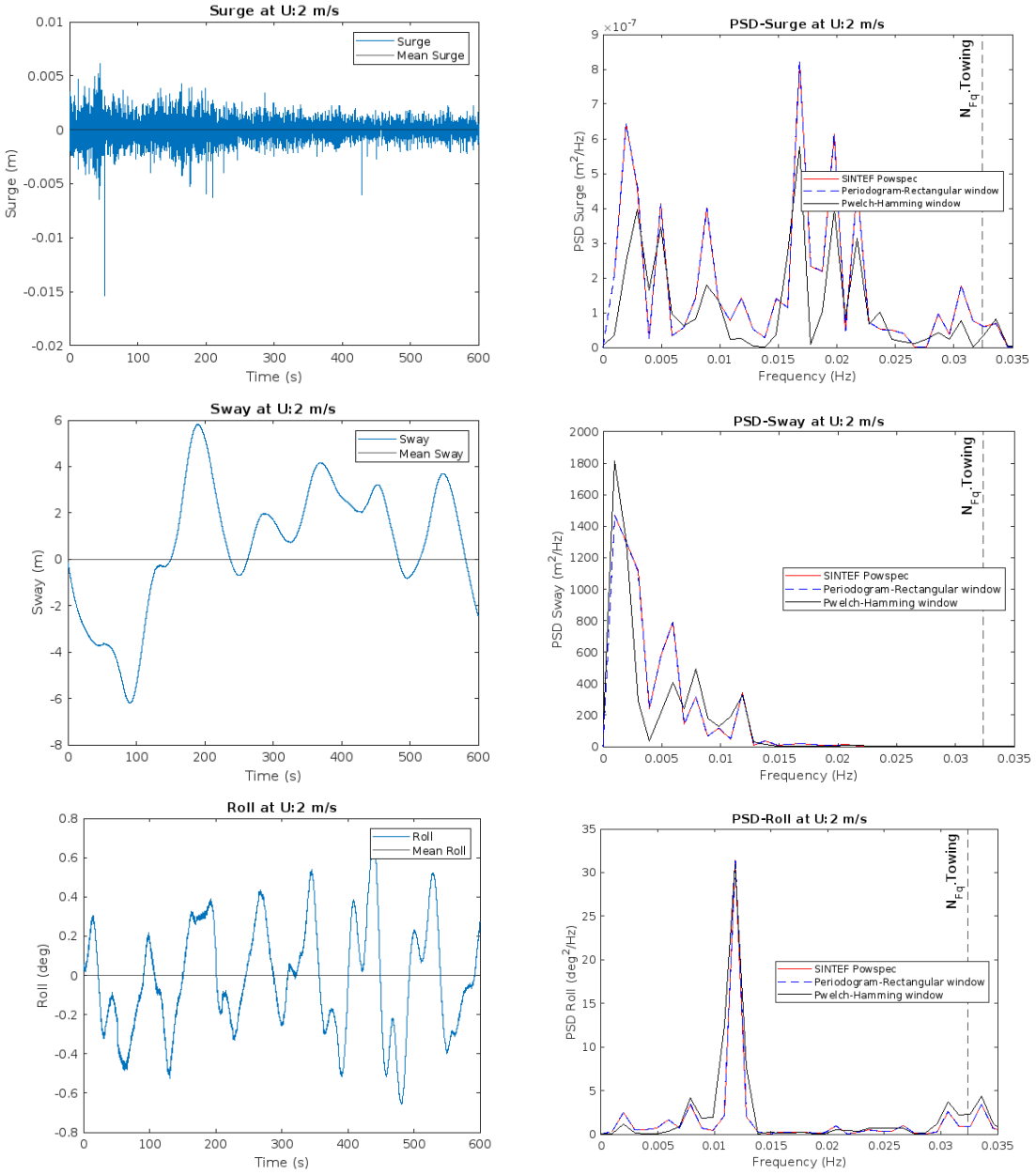

Figure F.3: Time Series and Spectral Surge, Sway, and Roll diagram using three approaches for the analysis. Single-Line (SL) towing condition

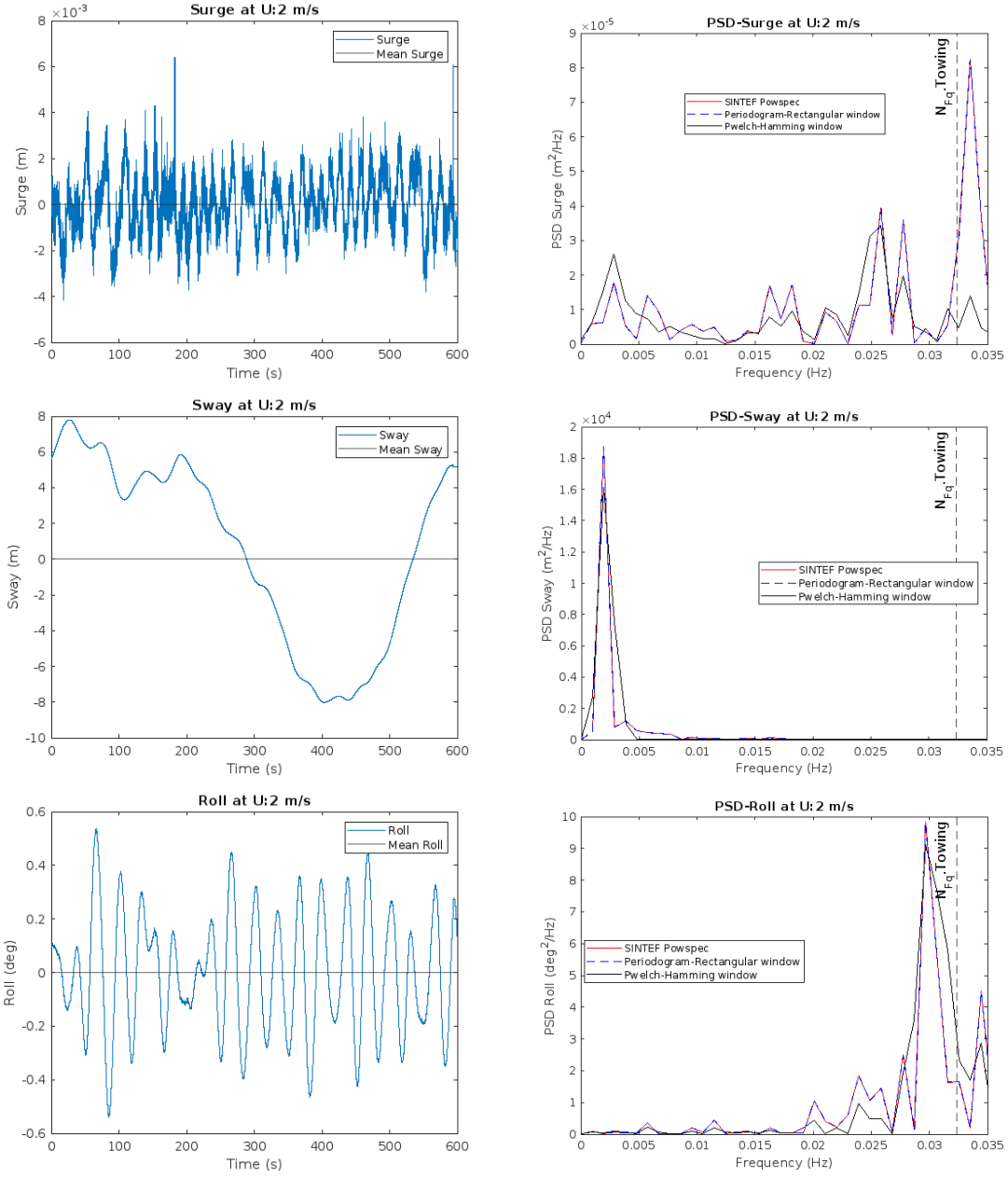

Figure F.4: Time Series and Spectral Surge, Sway, and Roll diagram using three approaches for the analysis. Two-Bridle (2B) Towing Condition

Appendix G

Spectral Analysis of the Towing Force from Experimental data.

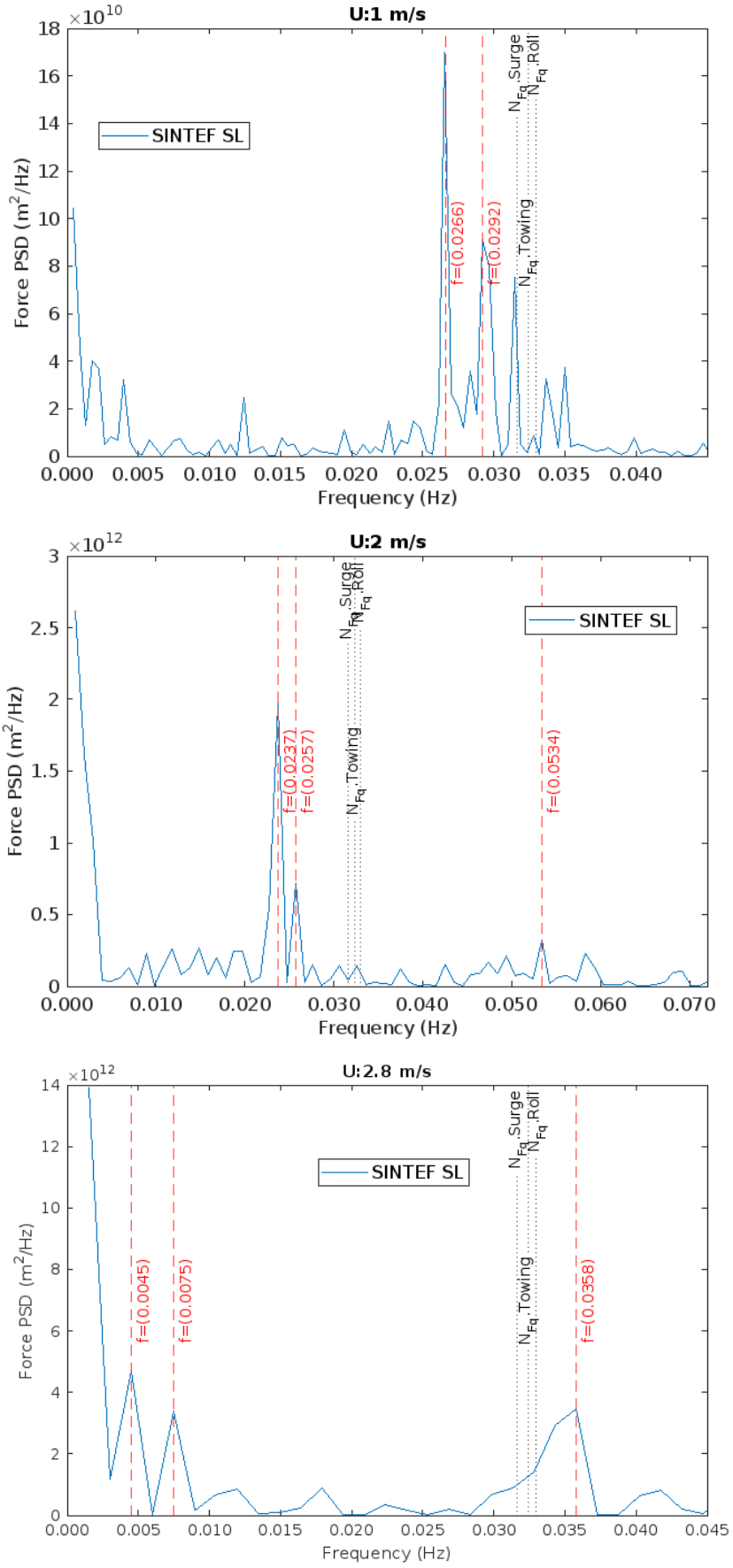

Figure G.1: Power Spectral Density (PSD) of the towing Force in the Single-Line (SL) towing condition, at various current speeds. The Force was analysed with the Powspec method.

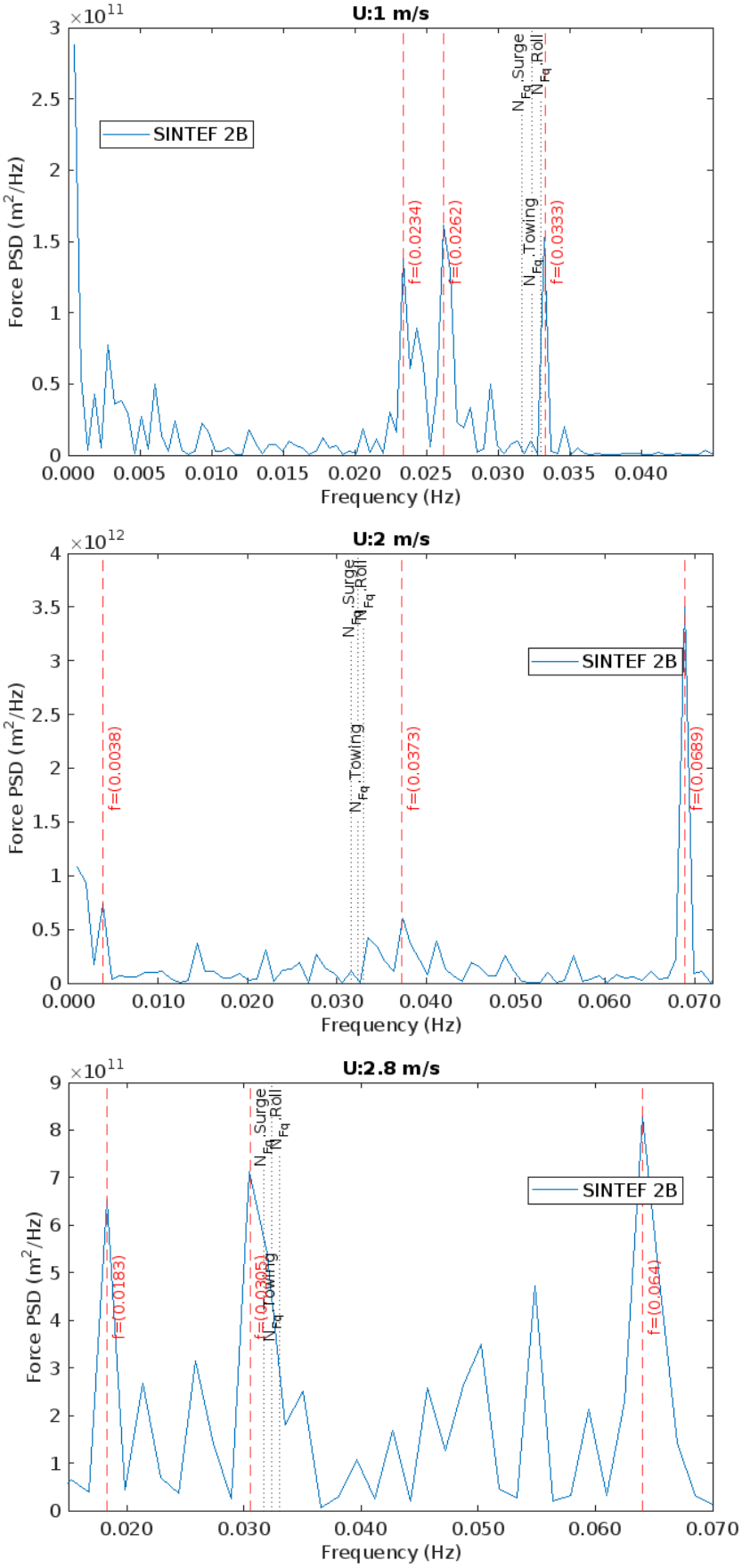

Figure G.2: Power Spectral Density (PSD) of the towing Force in the Two-Bridle (2B) towing condition, at various current speeds. The Force was analysed with the Powspec method.

Appendix H

Spectral and Time Series comparison of the experimental Towing Force with SIMA’s results.

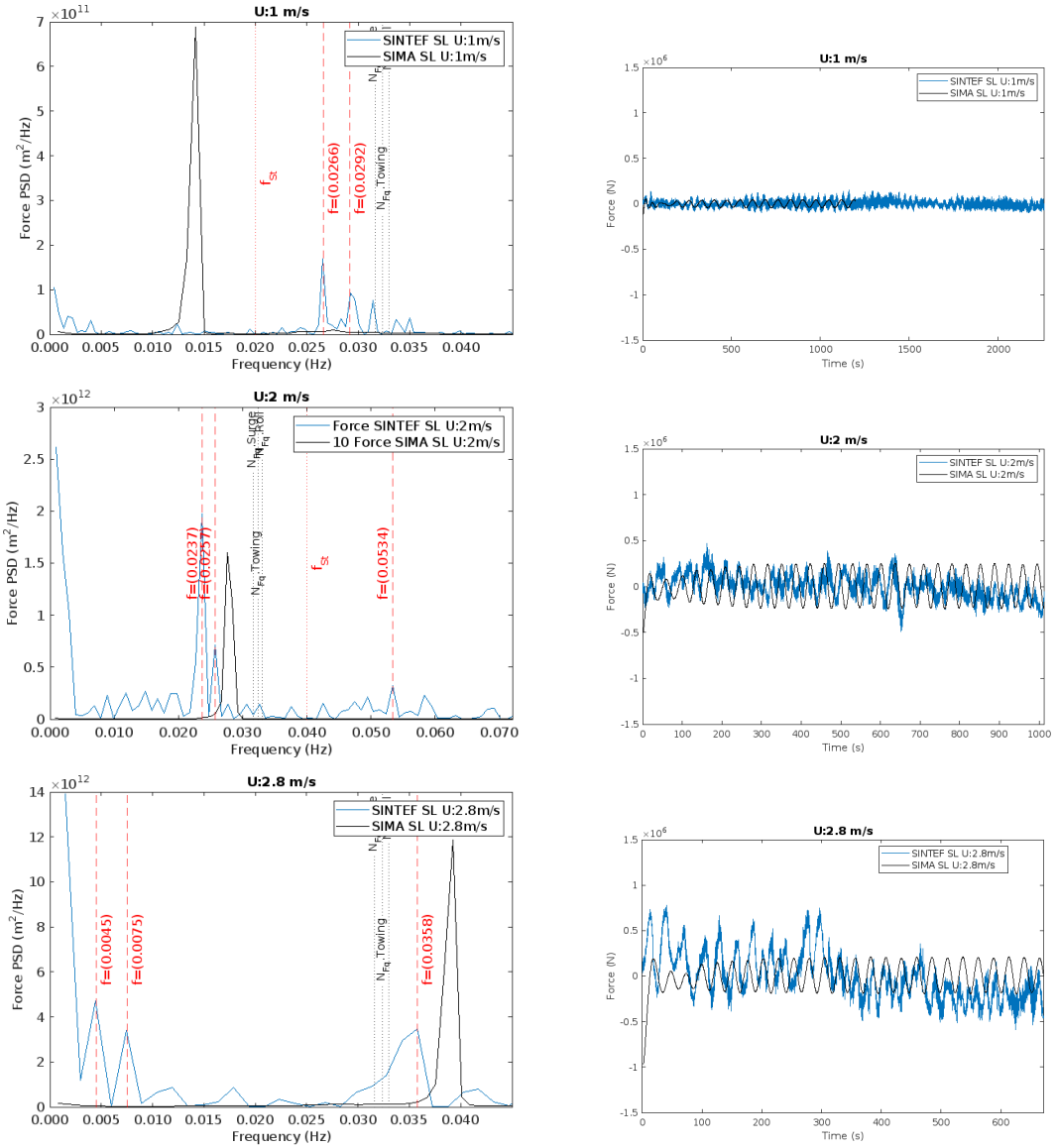

Figure H.1: Spectral Analysis of the Towing Force of Experimental and SIMA results. Results are for the Single-Line (SL) towing condition, at 3 different speeds. The graph also includes the Time Series Force of Experimental and SIMA results.

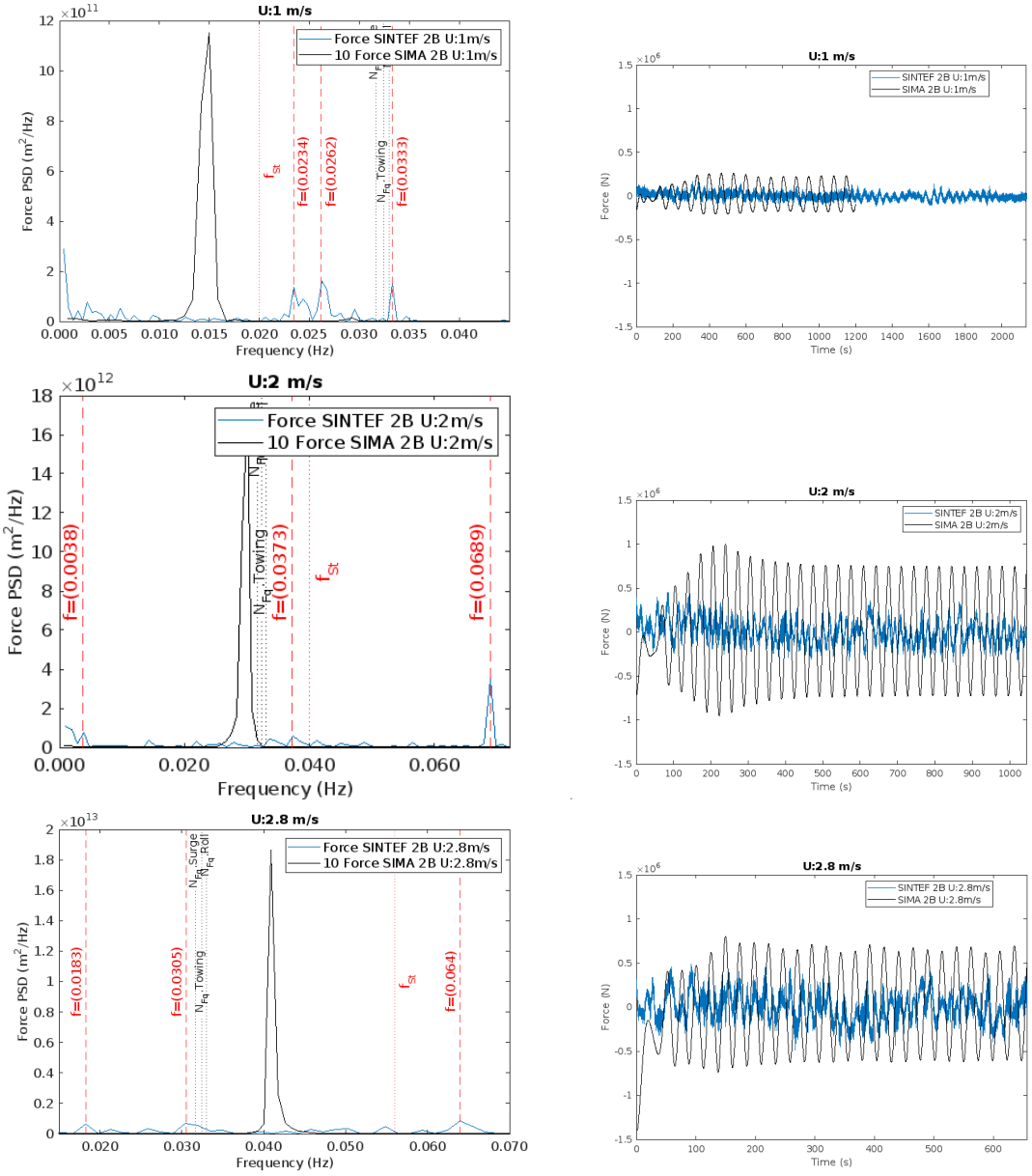

Figure H.2: Spectral Analysis of the Towing Force of Experimental and SIMA results. Results are for the Two-Bridle (2B) towing condition, at 3 different speeds. The graph also includes the Time Series Force of Experimental and SIMA results.

Appendix I

Spectral Analysis of Displacements from Experimental data.

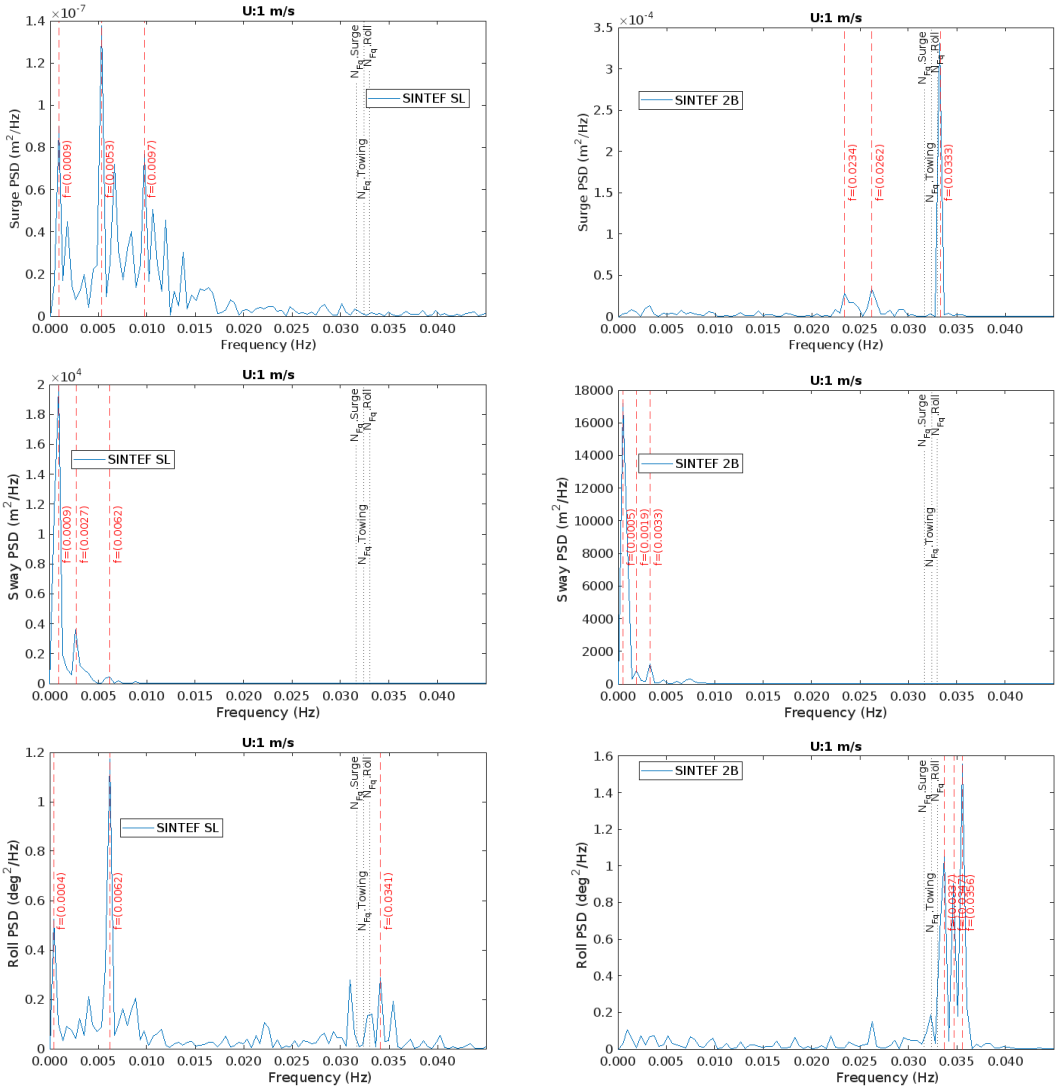

Figure I.1: Power Spectral Density (PSD) in Surge, Sway, and Roll in the two towing conditions (SL: Single-Line, 2B: Two-Bridle), at current speed U=1.0 m/s.

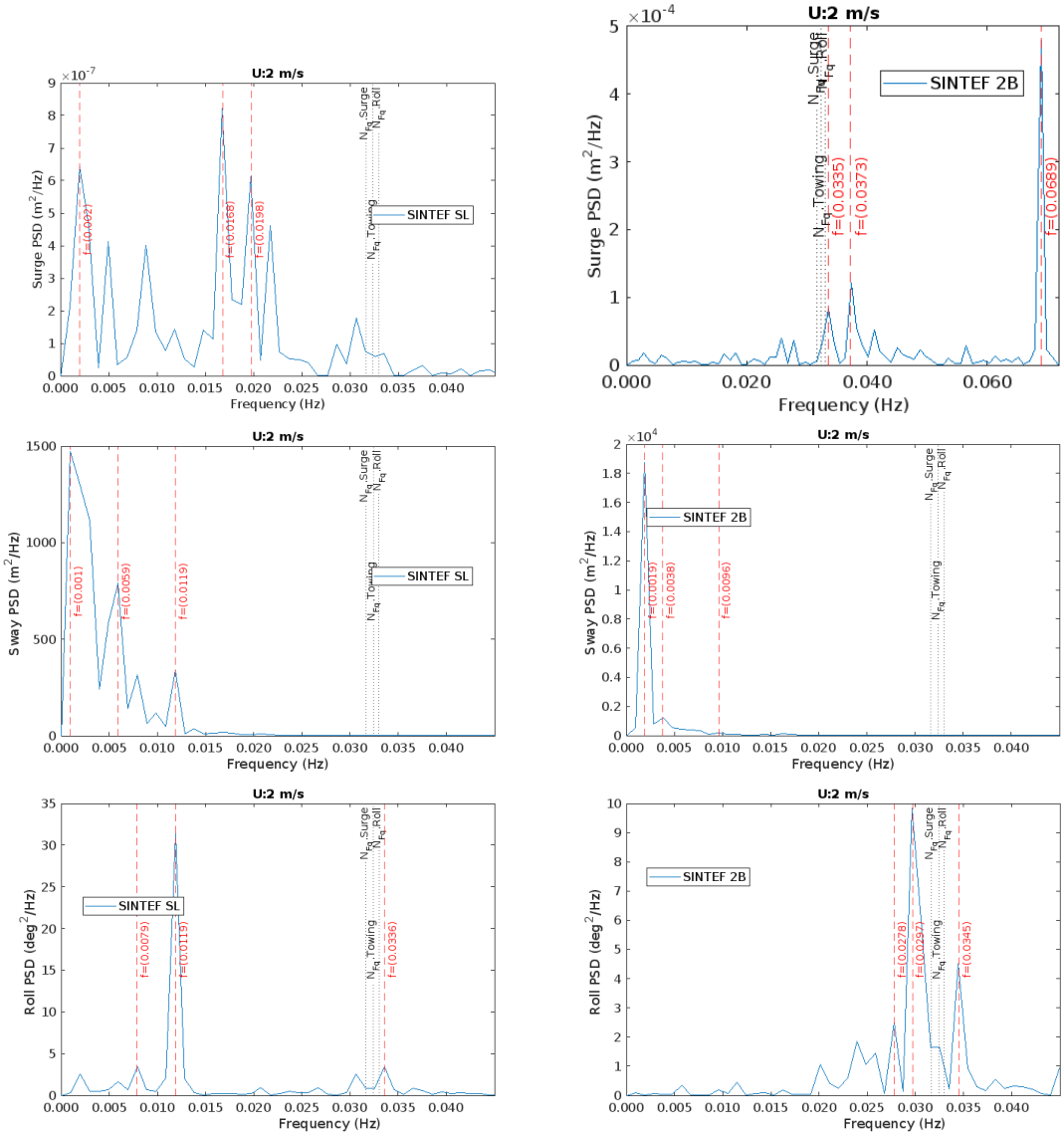

Figure I.2: Power Spectral Density (PSD) in Surge, Sway, and Roll in the two towing conditions (SL: Single-Line, 2B: Two-Bridle), at current speed U=2.0 m/s.

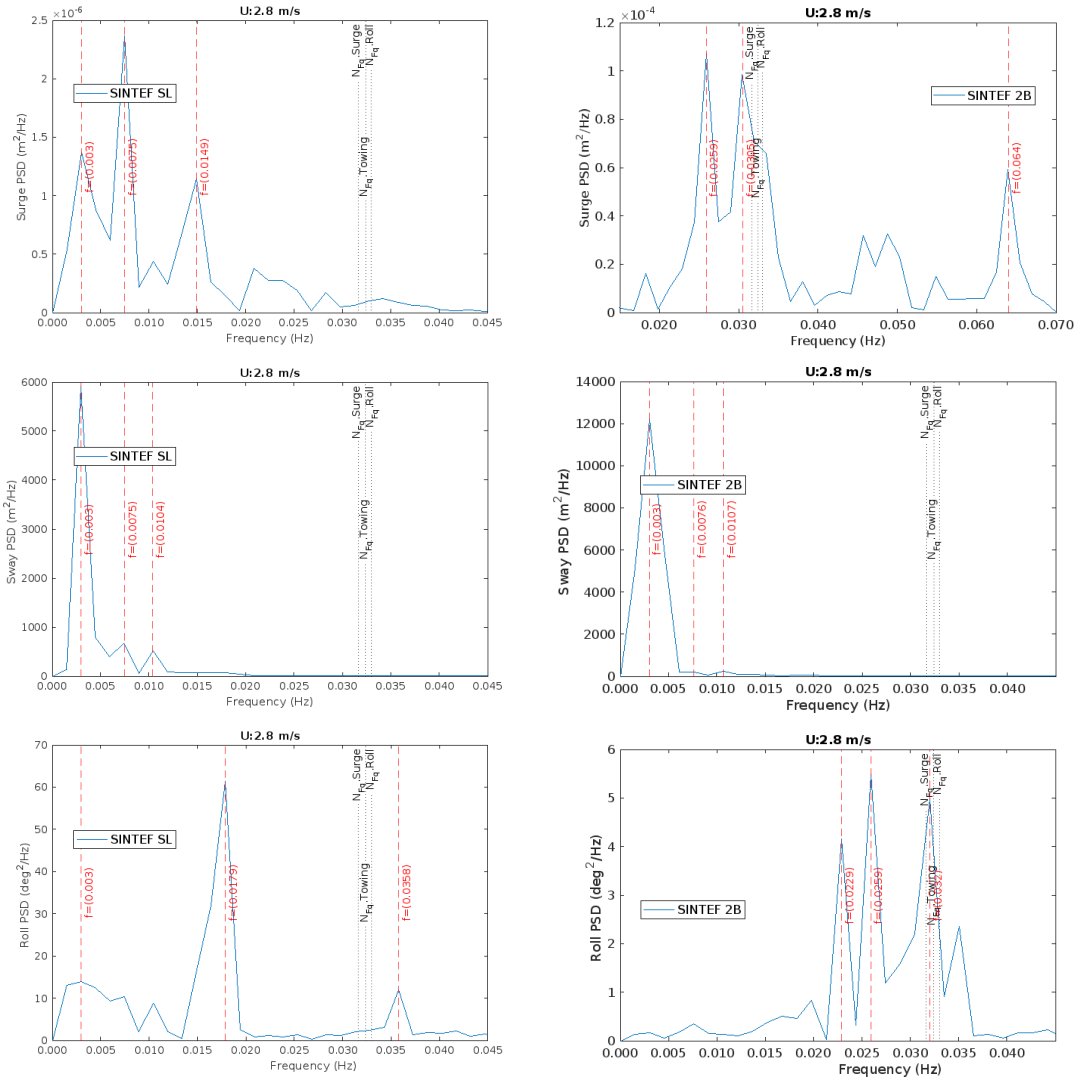

Figure I.3: Power Spectral Density (PSD) in Surge, Sway, and Roll in the two towing conditions (SL: Single-Line, 2B: Two-Bridle), at current speed U=2.8 m/s.

Appendix J

Spectral and Time Series comparison of experimental Sway and Roll with SIMA’s results.

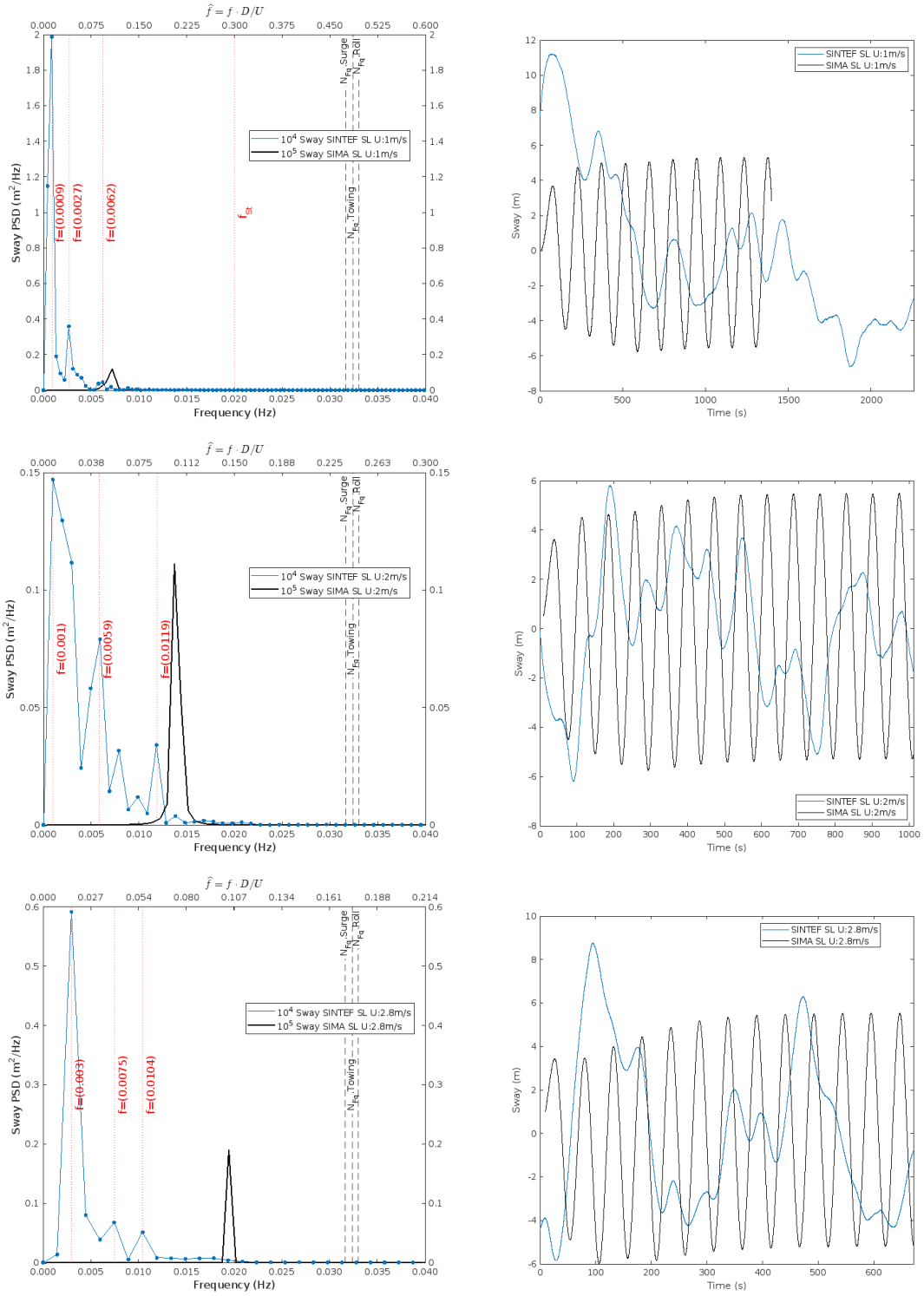

Figure J.1: Spectral and Time Series analysis of experimental Sway and SIMA results, in Single-Line (SL) towing condition at different current speeds.

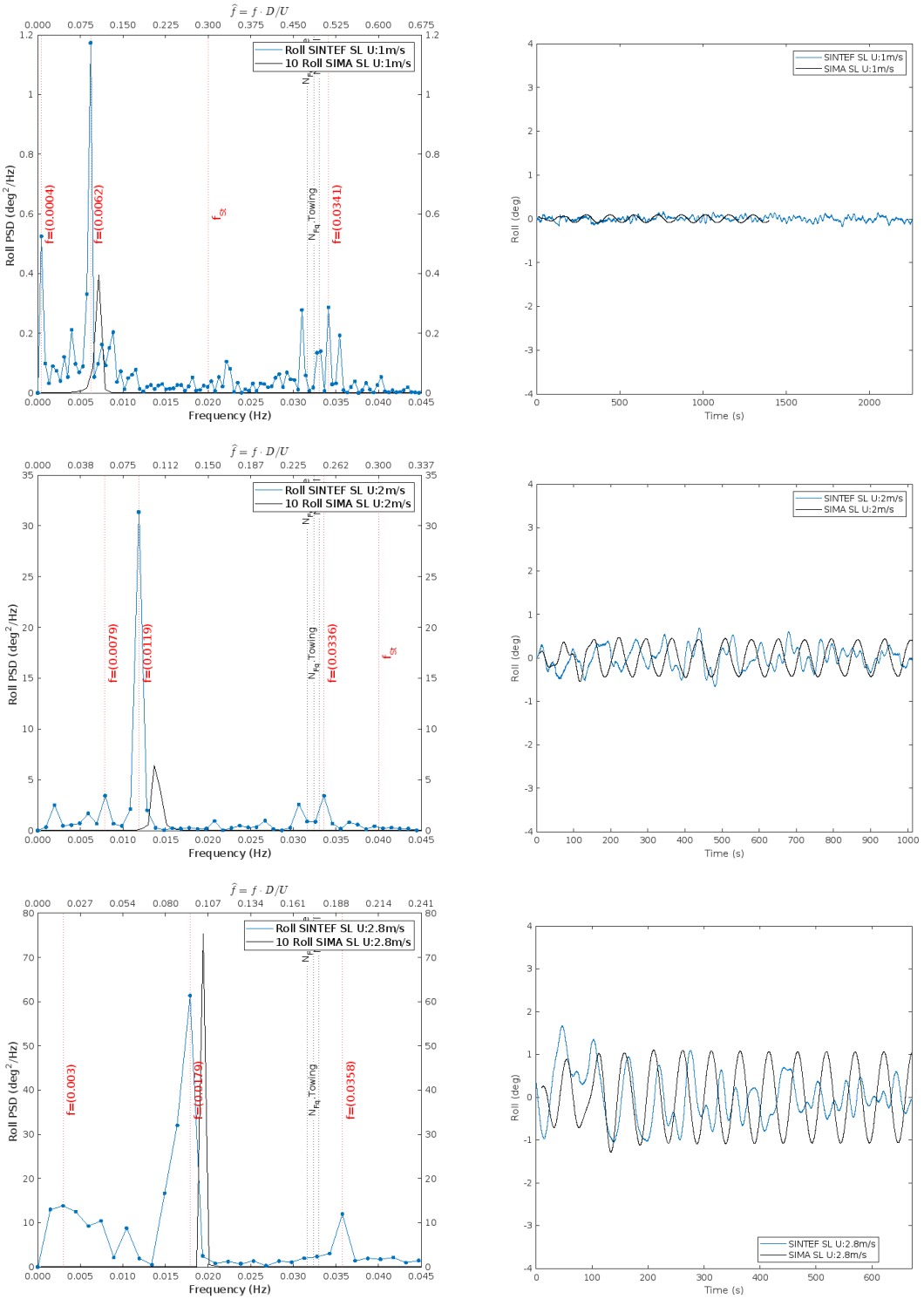

Figure J.2: Spectral and Time Series analysis of experimental Roll and SIMA results, in Single-Line (SL) towing condition at different current speeds.

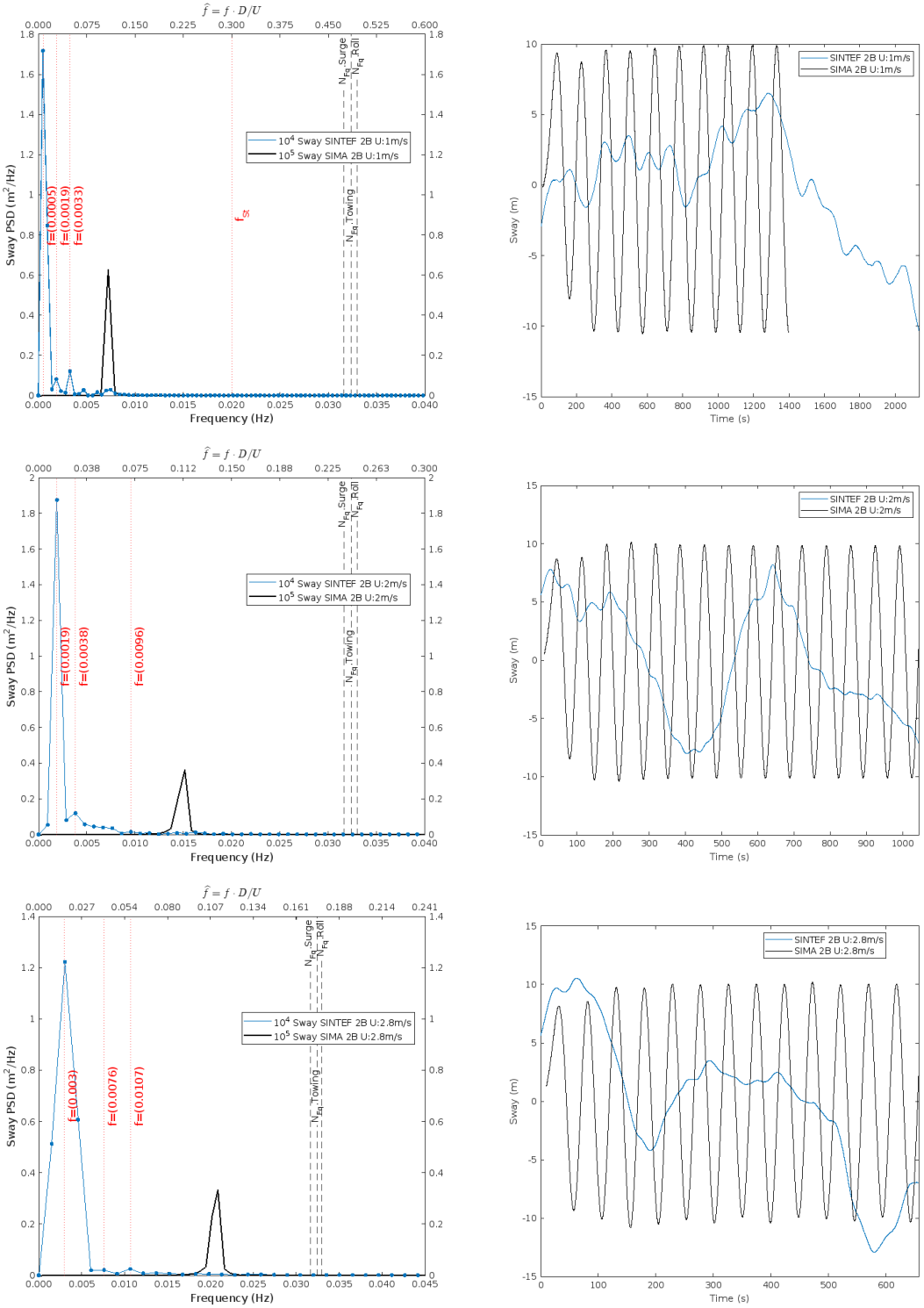

Figure J.3: Spectral and Time Series analysis of experimental Sway and SIMA results, in Two-Bridle (2B) towing condition at different current speeds.

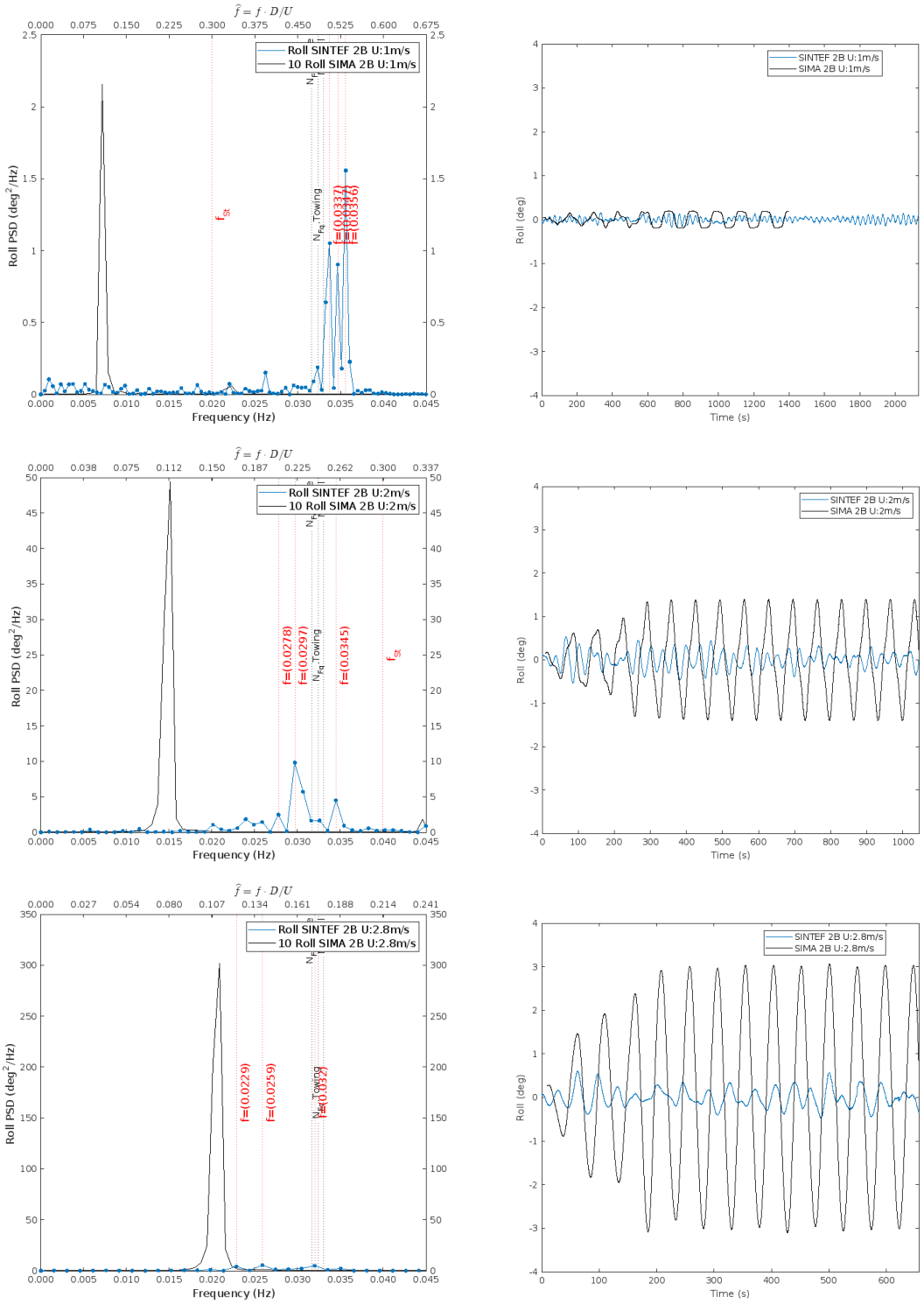

Figure J.4: Spectral and Time Series analysis of experimental Roll and SIMA results, in Two-Bridle (2B) towing condition at different current speeds.

Appendix K

Additional Material

VORTEX-INDUCED MOTIONS (VIM) OF A SEMI-SUBMERSIBLE FLOATING OFFSHORE WIND TURBINE

Rosa A. Cano[a], Svein Sævik[a], Bernt J. Leira[a], Elizabeth Passano[b], Decao Yin[b]
[a] Department of Marine Technology,Trondheim, Norway,[b] SINTEF Ocean,Trondheim, Norway
rosacano84@gmail.com, svein.savik@ntnu.no, decao.yin@sintef.no

Introduction

Rigid structures such as cylindrical structures, experience vibration under certain conditions causing the VIV phenomena [1], this is associated with high Reynolds Number (Re) around the cylinder. In the maritime industry, it is crucial to analyze also VIM phenomena, especially due to the mass production of wind turbines, and because the platforms are made of slender structures with small mass ratio, subjected to high Re. It is critical to predict and evaluate the VIM responses which in addition to increasing harmful motion, also induce fatigue of mooring elements and cables [1]. The prediction of VIM response will contribute to enhancing safe and cost-effective designs.

Objective

This thesis focuses on the VIM analysis of a SS-FOWT to compare analytical and experimental results from a towing experiment carried out by SINTEF Ocean at Froude Scale 1:40, using the INO WINDMOOR model. The analysis was done with the Time Domain Vortex-Induced Vibration (TD-VIV) model included in SIMA. Also, the study includes the influence of the current direction on the response of the structure.

Theoretical Background

Vortex-induced vibration (VIV) and Vortex-induced motion (VIM) are two concepts studied in fluid dynamics due to the motion induced to the bodies when interacting with external fluid flow. VIM is considered a special case of VIV, experienced by slender structures.

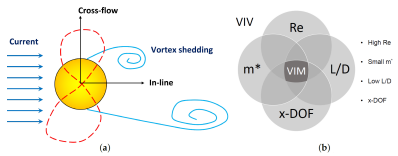

Figure 1: a) Fluid-structure interaction due to alternative vortex shedding. b) VIM is a special case of VIV. Figure from [5]

At large Re, the flow becomes asymmetric, generating the so-called Kármán vortex street, resulting in the motion of the cylinder[3]. The abrupt increase in the S_t number for smooth surfaces is called the *Camel Hump* and occurs at high values of Reynolds number, $1 \cdot 10^5 \leq \mathrm{Re} < 3 \cdot 10^6$ [2].

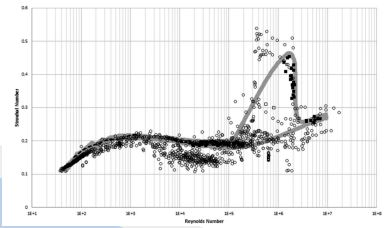

Figure 2: Strouhal number vs the Reynolds number for smooth and rough surfaces on circular cylinders. Figure from [5]

Towing Experiment in the Ocean Basin of SINTEF Ocean

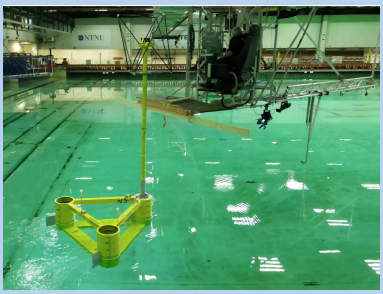

Figure 3: Experiment carried out in Ocean Basin. Figure from[4]

SIMA model of Towing Experiment

The towing equivalent rigidity in both conditions depends on the arrangement of the experiment connection.

$$(k_V)_M = \frac{2(k_{spring}) \cdot k_{vert-wire}}{2(k_{spring}) + k_{vert-wire}} \quad (1)$$

$$(EA_{eq})_F = (k_V)_M \cdot (L_H)_M \cdot \frac{(EA)_F}{(EA)_M} \quad (2)$$

$$\left(EA'_{eq}\right)_F = (k_V)_M \cdot (L'_H)_M \cdot \frac{(EA)_F}{(EA)_M} \quad (3)$$

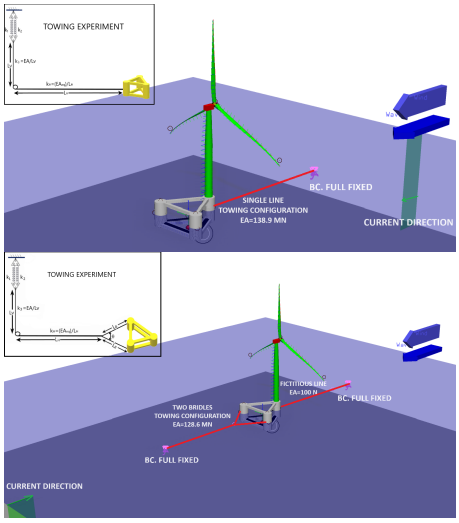

Figure 4: SIMA model of the 12MW SS-FOWT for the two Towing configurations.

A multi-variable assessment focused on the mean towing force and A_{CF} was carried out for parameter selection on the SIMA model. Variables such as CQ_Y, CV_{CF}, and CV_{IL}, show a particular effect either in the Towing force or the IL/CF motions.

	SL Towing	2B Towing
CQ_Y	1.10	1.00
CV_{CF}	0.70	1.40
CV_{IL}	0.01	0.01
$FREQ_{CF}$	Fnull=0.13;Fmin	=0.10;Fmax=0.26
$FREQ_{IL}$	Fnull=0.26;Fmin	=0.20;Fmax=0.52

Table 1: Final parameters used on the TD-VIV model..

Results

Results in figure 5 showed the quadratic dependency between the towing force and the current speed. Also, a clear similitude in experimental outcomes from both towing conditions is noticed. Moreover, SIMA's results showed good agreement with experimental data.

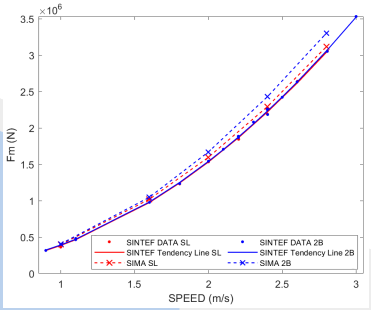

Figure 5: Mean Towing Force vs Current Speed, in both towing conditions. The graph includes TD-VIV results from SIMA.

Experimental displacements in Surge were less than 2mm, in contrast, Sway displacements were larger than 3 m. The same behavior was evident in all ranges of current velocities and towing conditions. During analysis, a variety of frequencies involved in the motion was noticed. The comparison with SIMA results confirmed this observation. From figure 7), it is clear that SIMA captures at least one of the frequencies, however, it cannot capture the combination of different frequencies as occurred in the towing experiment.

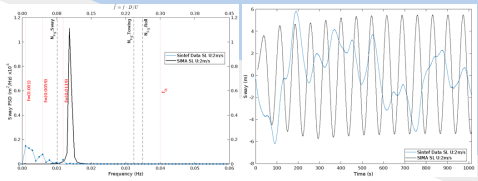

Figure 6: Experimental and SIMA TD-VIV in Sway-SL at 2 m/s.

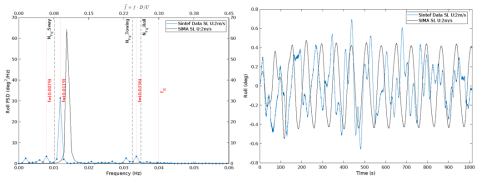

Figure 7: Experimental and SIMA TD-VIV of Roll-SL at 2 m/s.

SIMA's results showed a linear tendency for the A_{CF} amplitude ratio within the speed range. Although those results do not fit with the tendency line, it is observed that in some speed ranges experimental results display similar linear tendency.

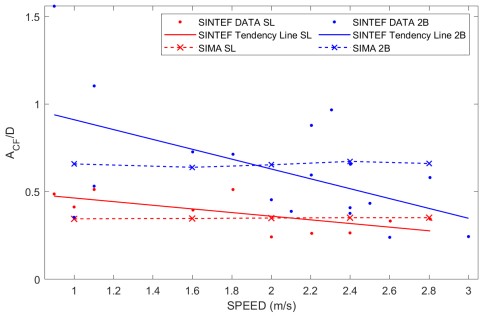

Figure 8: Experimental and SIMA TD-VIV results of the Amplitude Ratio in CF direction, vs Current Speed. .

Conclusion

The TD-VIV model was able to capture some effects on the wind turbine. However, results suggested that there was not a combined VIM effect in the platform. This is supported by the fact that SIMA and experimental results, did not achieve the expected conditions. According to [5], at high Re the expected A_{CF} is around 0.6D and 0.7D, while, the A_{IL} is about $0.2A_{CF}$. Moreover, main frequencies did not reach the f_{ST}

There was noticed a variety of frequencies during the experiment, some of them are high frequencies that can suggest an interaction between the pontoons and columns. Further, it was noticed galloping during the experiment, this topic is not included in the scope of this thesis and was not investigated.

In such a complex phenomenon, it is not easy to explain the combined effect of VIM and Galloping. It is suggested further investigation in that direction, with long term experiments.

References

[1] E. P. et al. *Simulation of Vim of an Offshore FWT.* 2022.

[2] D. Livanos. *Investigation of Vortex-Induced Vibrations on Wind Turbine Towers, Delft University.* 2018.

[3] Wikipedia. *Vortex-Induced Vibration. Available: https://en.wikipedia.org/w/index.php? title=vortex-induced-vibration.* 2023.

[4] D. Yin. Test report, windmoor towing test. 2024.

[5] D. Yin, E. Passano, F. Jiang, H. Lie, J. Wu, N. Ye, S. Sævik, and B. Leira. *State-of-the-Art Review of Vortex-Induced Motions of Floating Offshore Wind Turbine. J.Mar.Sci.Eng.2022,10.* 2022.

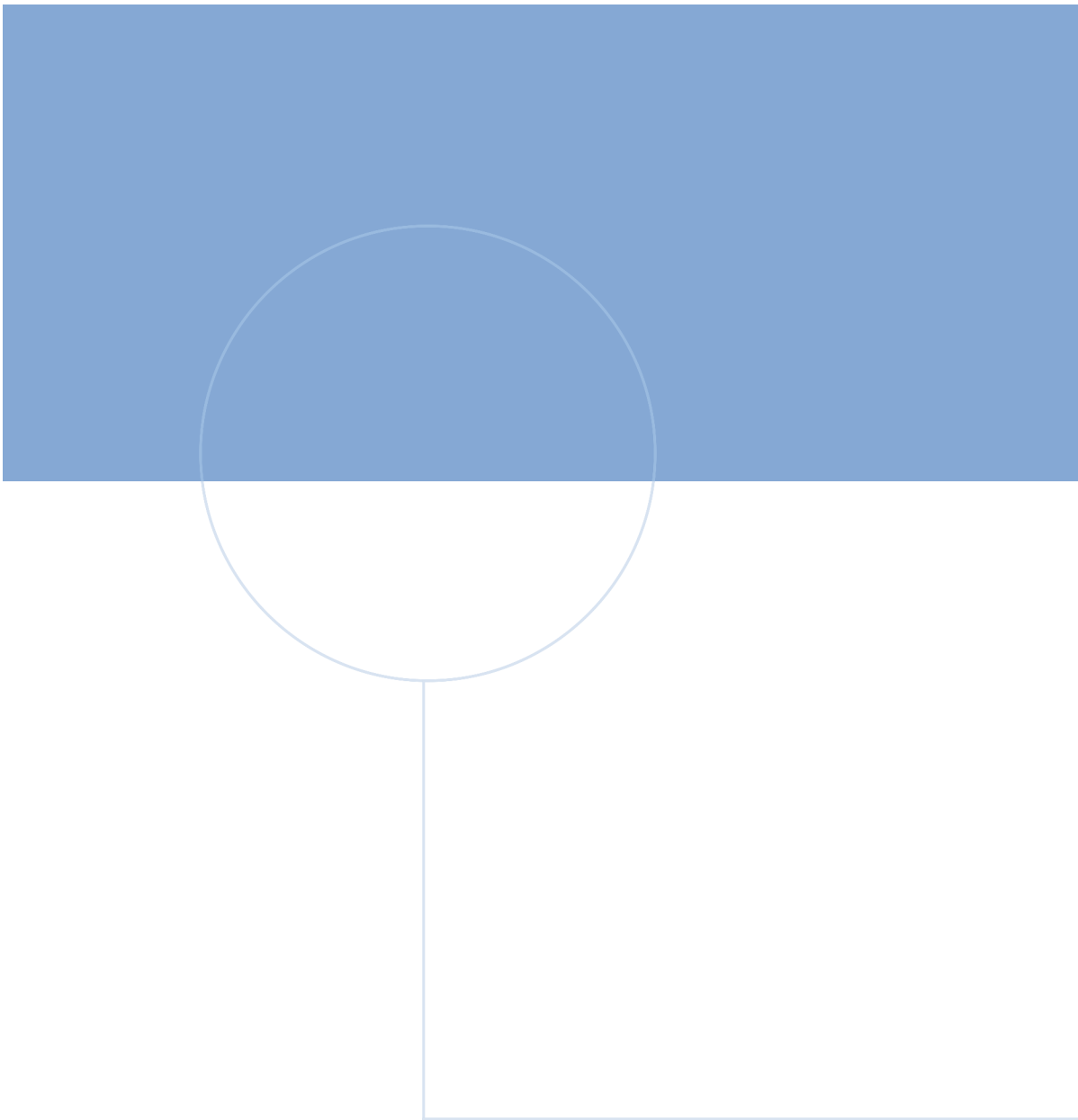

NTNU
Norwegian University of
Science and Technology

CHALMERS
UNIVERSITY OF TECHNOLOGY